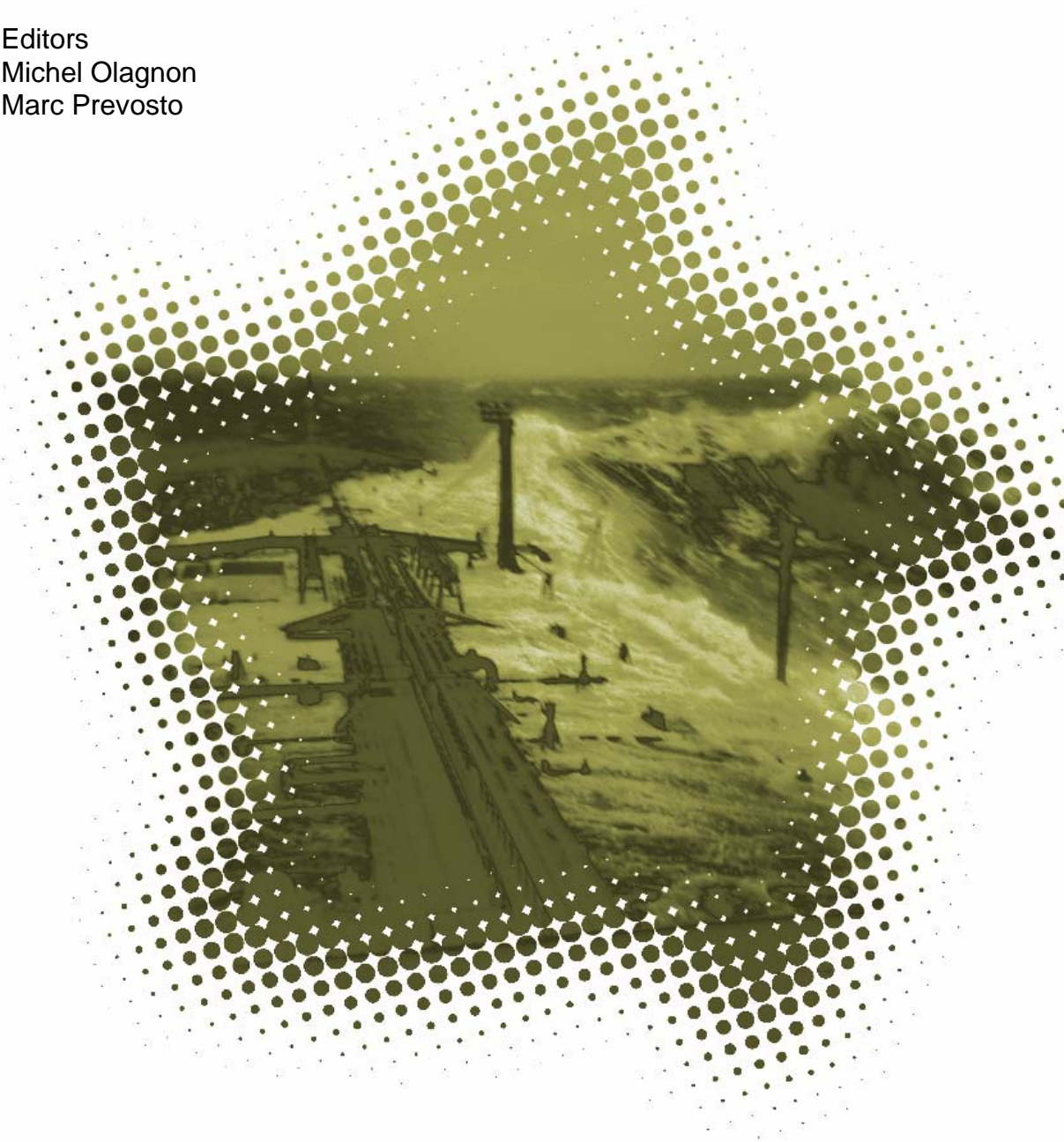


Brest
13-14-15 October 2008

proceedings

Editors
Michel Olagnon
Marc Prevosto



Rogue Waves 2008



Ifremer

Rogue Waves 2008

Michel Olagnon & Marc Prevosto
Editors

Proceedings of a Workshop organized by Ifremer
and held in Brest, France
13-14-15 October 2008 within the Brest Sea Tech Week 2008

See also <http://www.ifremer.fr/web-com/stw2008/rw>

Preface

2008 was the fourth and last year of the 696th Olympiad. It was thus time according to a recent but vivid tradition for researchers, forecasters and industry people to meet at a friendly Rogue Waves workshop in Brest, to discuss their achievements of that elapsed Olympiad and to strengthen their work by exchanges in and around a conference room.

We have been very pleased that many of them did respond with evidence of high-quality work carried out since they had gone home after the previous workshop.

We organized the sessions in five groups:

1. Observations and measurements of actual rogue waves in the ocean.
2. Numerical models.
3. Statistical models.
4. Laboratory investigations.
5. Link with meteorological situation, and risk analyses.

Many authors provided a written paper, and those are assembled in the present e-book. For various reasons, we have not been able to publish it in a printed version, yet we believe that making them available as a freely downloadable e-book on the web can be an acceptable alternative. We would like to remind readers that the workshop was video-recorded, and that most of the presentations are also available at the only expense of registering your identity at <http://www.seatechweek.com/>.

We hope to be able to gather participants again at the end of the 697th Olympiad (2012) to discuss once again their progress on those issues. Yet, we should not forget that the ultimate achievement will be when we can discontinue the Rogue Waves workshops — but nevertheless meet all together at Olympic intervals on some other topics — because we shall then know enough on rogue waves to make the corresponding risks neglectible.

September 2009

Michel Olagnon & Marc Prevosto
Editors of the proceedings
ROGUE WAVES 2008

<http://www.ifremer.fr/web-com/stw2008/rw/>

Organisation

ROGUE WAVES 2008 was organized by the Hydrodynamics and Metocean Group of Ifremer (Institut Français de Recherche pour l'Exploitation de la Mer) and benefitted from the support of Brest Métropole Océane.

It was one of the events of the Brest SeaTechWeek 2008, a week devoted to exchanges between research and industry in marine science and technology.

Our thanks go to all those who supported this workshop by helping finding funding and volunteering their personal time and efforts.

Participants

ARDHUIN Fabrice	SHOM	France	ardhuin@shom.fr
BADULIN Sergei	P.P. Shirshov Institute of Oceanology	Russia	bsi@wave.sio.rssi.ru
BATEMAN William	Lloyds Register	UK	william.bateman@lr.org
BITNER-GREGERSEN Elzbieta	Det Norske Veritas	Norway	E.Bitner-gregersen@dnv.Com
BOMPAIS Xavier	Ifremer	France	xbompais@ifremer.fr
CAVARELI Luigi	ISMAR	Italy	luigi.cavaleri@ismar.cnr.it
CHRISTOU Marios	SHELL	Netherlands	marios.christou@shell.com
DAMY Gilbert	Ifremer	France	gdamy@ifremer.fr
DENCHFIELD Sally	University of Southampton	UK	ssd103@soton.ac.uk
DESORMEAUX Yves	DORIS Engineering	France	desormeaux.y@doriseng.com
DOONG Dong-Jiing	National Taiwan Ocean University	China (Taiwan)	doong@mail.ntou.edu.tw
DUCROZET Guillaume	LMF	France	guillaume.ducrozet@ec-nantes.fr
EWANS Kevin	SHELL	Netherlands	kevin.ewans@shell.com
FAGOT Guillaume	ENERTRAG	France	guillaume.fagot@enertrag.com
FLYNN Jan	SHELL International Exploration & Production	Netherlands	jan.flynn@shell.com
FRANCIUS Marc	LSEET- CNRS Université du Sud	France	francius@univ-tln.fr
GENTY Goery	Tampere University of Technology	Finland	goery.genty@tut.fi
GRAMSTAD Odin	Department of Mathematics University of Oslo	Norway	oding@math.uio.no
GRIGORIEVA Victoria	P.P. Shirshov Inst. of Oceanology	Russia	vika@sail.msk.ru
GUEDE Zakoua	Ifremer	France	zguede@ifremer.fr
GUERIN Charles-Antoine	LSEET/Université de Toulon CNRS	France	charles-antoine.guerin@lseet.univ-tln.fr
HAN Gil-Yong	IACS	UK	gilyonghan@iacs.org.uk
HENNIG Janou	MARIN	Netherlands	j.hennig@marin.nl
HIRAYAMA Katsuya	Port and Airport Research Institute	Japan	hirayama@pari.go.jp
HJELMERVIK Karina	University of Oslo	Norway	karibh@math.uio.no
HONG Keyyong	MOERI	South Korea	kyhong@moeri.re.kr
KJELDTSEN Soren Peter	Trondheim Maritime Academy	Norway	peter.kjeldsen@stfk.no

KROGSTAD Harald	Dept. Mathematical Sciences	Norway	harald.krogstad@math.ntnu.no
KUZNETSOV Sergey	P.P. Shirshov Institute of Oceanology	Russia	kuznetsov@ocean.ru
LE BOULLUEC Marc	Ifremer	France	mlb@ifremer.fr
LE FLOCH Daniel	DIRISI Brest	France	
LEHNER Susanne	DLR	Germany	susanne.lehner@dlr.de
LINDGREN Georg	Mathematical Statistics	Sweden	georg@maths.lth.se
LIU Paul	NOAA/GLERL	USA	paul.c.liu@noaa.gov
LOPATUKHIN Leonid	St.Petersburg State University	Russia	leoni-lop@yandex.ru
MA Qingwei	School of Engineering and Mathematical Sciences	UK	q.ma@city.ac.uk
MAGNUSSON Anne Karin	Norwegian Meteorological Institute	Norway	anne.karin.magnusson@met.no
MAISONDIEU Christophe	Ifremer	France	cmaisond@ifremer.fr
MORI Nobuhito	Kyoto University	Japan	mori@oceanwave.jp
NOUGUIER Frédéric	Institut Fresnel	France	frederic.nouguier@fresnel.fr
OJIEH Nwaka Chucks	Universities of Glasgow & Strathclyde	UK	n.c.ojieh@strath.ac.uk
OLAGNON Michel	Ifremer	France	molagnon@ifremer.fr
ONORATO Miguel	Università di Torino	Italy	miguel.onorato@gmail.com
OSBORNE Alfred	Dipartimento di Fisica	Italy	al.osborne@gmail.com
PREVOSTO Marc	Ifremer	France	mpre@ifremer.fr
RESIO Donald	US Army Corps of Engineers	USA	natalie.s.elwart@usace.army.mil
ROSENTHAL Wolfgang	GAUSS	Germany	rosenthal@gkss.de
SAPRYKINA Yana	P.P. Shirshov Institute of Oceanology	Russia	saprykina@ocean.ru
SHEMER Lev	TEL-AVIV University	Israel	shemer@eng.tau.ac.il
SHIN Seung-Ho	MOERI	South Korea	shinsh@moeri.re.kr
SHRIRA Victor	KEELE University	UK	v.i.shrira@keele.ac.uk
SLUNYAEV Alexey	Institute of Applied Physics	Russia	slunyaev@hydro.appl.sci-nnov.ru
TAMURA Hitoshi	JAMSTEC	Japan	htamura@jasmtec.go.jp
TOLMAN Hendrick	NOAA-NCEP	USA	tammy.braun@noaa.gov
TRULSEN Karsten	Department of Mathematics	Norway	karstent@math.uio.no
WASEDA Takuji	Univ. of Tokyo	Japan	waseda@k.u-tokyo.ac.jp
WINTHER Nina	Storm Weather Center	Norway	nina.winther@storm.no

Contents

Session I.1: Observations

- Olagnon, Michel -- Welcome and **About the Frequency of Occurrence of Rogue Waves** 13
- Krogstad, Harald E. ; Barstow, Stephen ; Mathisen, Jan Petter ; Lønseth, Lasse ; Magnusson, Anne Karin & Donelan, Mark A. -- **Extreme Waves in the Long-Term Wave Measurements at Ekofisk**.....23
- Cavaleri, Luigi ; Bertotti, Luciana -- **The «Voyager» accident - meteorological and marine predictability**34
- Grigorieva, Vika & Gulev, Sergey -- **Extreme waves in visual observations by VOS**...41

Session I.2: Observations (ctd.)

- Hirayama, Katsuya, Kashima, Hiroaki & Hiraishi, Tetsuya -- **Examples of Unexpected High Waves in Shallow Water in Japan**49
- Liu, Paul C. ; Doong, Dong-Jiing ; Chen, Hsuan S. ; Kao, Chia Chuen & Hsu, Yueh-Jiuan G. -- **Freak Waves during a Typhoon**.....59
- Rosenthal, Wolfgang -- **Sea State Statistics and Extreme Waves Observed by Satellite**.....71

Session II.1: Numerical Models

- Gramstad, Odin & Trulsen, Karsten -- **Can swell increase the number of freak waves in a wind-sea?**75
- Badulin, Sergei I. ; Korotkevich, A.O. ; Resio, Don & Zakharov, V.E. -- **Wave-wave interactions in wind-driven mixed seas**77
- Ducrozet, Guillaume ; Bonnefoy, Félicien & Ferrant, Pierre-- **Rogue waves in large-scale fully-nonlinear High-Order-Spectral simulations**87
- Kuznetsov, Sergey & Saprykina, Yana -- **Fine Structure and Peculiarities of Wave Spectra with Benjamin-Feir Instability**99

Session II.2: Numerical Models (ctd.)

- Ojeh, Nwaka -- **RANS/VOF Simulation of an Alternative Extreme Wave**109
- Osborne, Al R. ; Onorato, Miguel & Resio, Don -- **A New Class of Rogue Waves in Shallow Water: Nonlinear Fourier components and Hyperfast Numerical Simulations in the Boussinesq Approximation**111
- Didenkulova, Ira ; Pelinovsky, Efim & Sergeeva, Anna -- **Runup of irregular waves on a plane beach**113

Session II.3: Numerical Models (ctd.)

- Leblanc, S. ; Branger, H. ; Francius, M. ; Golay, F. & Kharif, C. -- **Wind-forced modulations of gravity waves**115
- Mori, Nobuhito ; Onorato, Miguel & Janssen, Peter A.E.M. -- **Directional dispersion effects on kurtosis for freak wave prediction**117
- Ma, Qingwei & Yan, S. -- **Preliminary Simulation of Wind Effects on 3D Freak Waves**127
- Shrira, Victor I. & Geogjaev, Vladimir -- **On 3-D Freak Waves Caused by Modulational Instability**129

Session III: Statistical Models

- Lindgren, Georg & Åberg, S.-- **First order Lagrange models for asymmetric ocean waves**.....133

Fedele, Francesco ; Gallergo, Guillermo ; Benetazzo, Alvise ; Yezzi, Anthony & Tayfun, Mehmet A. -- Euler Characteristics and Maxima of Oceanic Sea States	145
Hjelmervik, Karina & Trulsen, Karsten -- Extreme waves on current jets - are they freak?	155
Shin, Seung-Ho & Hong, Keyyong -- Nonlinear Parameters of Wave Distribution to Characterize Freak Waves	157

Session IV.1: Laboratory

Dudley, J.M. ; Genty, G. ; Dias, F. & Eggleton, B.J. -- Extreme value phenomena in optics: origins and links with oceanic rogue waves	161
Christou, Marios ; Ewans, Kevin ; Buchner, Bas & Swan, Chris -- Spectral characteristics of an extreme crest measured in a laboratory basin	165
Shemer, Lev ; Sergeeva, A. & Slunyaev, Alexey -- Experimental and Numerical Study of Evolution of Statistical Properties of Unidirectional Narrow-Banded Steep Wave Groups	179
Shemer, Lev ; Slunyaev, Alexey & Dorfman, Boris -- Direct Measurements of Temporal Wave Field Evolution in a Laboratory Tank and Comparison with Strongly Nonlinear Simulations	191

Session IV.2: Laboratory (ctd.)

Onorato, M. ; Cavaleri, L. ; Gramstad, O. ; Janssen, P.A.E.M. ; Monbaliu, J. ; Osborne, A.R. ; Serio, M., Stansberg, C.T. ; Toffoli, A. & Trulsen, K. -- Statistical properties of mechanically generated surface gravity waves: a laboratory experiment in a 3D wave basin	199
Waseda, Takuji ; Tamura, Hitoshi & Kinoshita, Takeshi -- Extremely Narrow Spectrum and Freak Wave - an Abnormal Sea State	207
Slunyaev, Alexey ; Ezersky, Alexander ; Mouazé, Dominique & Chokchai, Wuttersack -- Nonlinear Modulations of Standing Long Gravity Waves in a Resonator	209
Denchfield, S.S. ; Murphy, A.J. & Temarel, P. -- A deep-water beach for laboratory generation of abnormal waves	219

Session V.1: Link with meteorological situation and Risk analysis

Annenkov, Sergei Y. & Shrira, Victor I. -- Direct numerical simulation of waves subjected to an abrupt change of wind: evolution of spectra and kurtosis	233
Papadimitrakis, Ioannis & Dias, Frédéric -- Occurrence and Breaking of Extreme Waves in Deep Water. A Stochastic Approach Revisit	235
Lopatoukhin, Leonid & Boukhanovsky, Alexander -- Freak wave as a multivariable extreme (approach to estimation)	247
Tamura, Hitoshi ; Waseda, Takuji & Miyazawa, Yasumasa -- Numerical study of the sea state in the Kuroshio Extension region at the time of an accident	249

Session V.2: Link with meteorological situation and Risk analysis (ctd.)

Kjeldsen, S.Peter -- Risk analysis concentrated on wave crest kinematics	251
Resio, Don T. & Long, Charles E. -- Kurtosis and «Extreme» Wave Probabilities in Very Young Wind-Generated Seas	259
Magnusson, Anne Karin -- Forecasting Extreme Waves in Practice	261
Bitner-Gregersen, E.M., Toffoli, A. ; Onorato, M. & Monbaliu, J. -- Implications of Non-linear Waves for Marine Safety	283



Sessions I. Observations



About the Frequency of Occurrence of Rogue Waves

Michel Olagnon

IFREMER Centre de Brest
B.P. 70, F-29280 Plouzané, France
Michel.Olagnon@ifremer.fr

Abstract. Some articles dealing with rogue waves state in their introduction that rogue waves are more frequent than common statistics would predict (see for instance [12]). However, supporting evidence that taking into account second-order non-linearities would fail to be sufficient to explain the deviation from Rayleigh distribution is very hard to find. To be fair, the opposite thesis, that extreme waves would not be “freak”, is also difficult to validate.

Nearly 20 years ago, we ([10]) did not observe in a large 2 million individual waves dataset more high waves than expected from the Rayleigh distribution. We extended the dataset to about 3.3 million waves in [8] without any change on those conclusions.

In the present study, we analyse the Alwyn dataset, where some authors have detected rogue waves [6, 14] but for which we are not aware of any global statistical analysis. We detail the techniques that we apply to validate the data on the grounds of physical limits on the water velocities, accelerations and other quantities.

We conclude that here again extreme waves are not more frequent than common statistics would predict, and that the problem to be addressed is not the number of their occurrences, but their precise times and locations that are still unpredictable as far as we can tell from the available references.

Introduction

A number of articles dealing with rogue waves state in their introduction that rogue waves are more frequent than statistics would predict (see for instance [12]). To find supporting evidence for this statement, the reader is commonly referred to the introductions of other similar papers or to papers such as that by Dean ([1]) or the Gorm field analysis by Sand *et al* ([11]) in the same workshop.

However, when returning to those insightful papers, one finds out that for instance Bob Dean was very cautious about the statistical significance of the observations, and only concluded that rogue waves might be defined by being more numerous than expected from the Rayleigh distribution and that non-linearities might then be the explanation. Samewise, Sand *et al* analysed waves of 10 to 18 m in only 40 m water depth, and found that those largest waves departed

from linear statistics. Yet, there is no evidence in those papers that taking into account even only second-order non-linearities would fail to be sufficient to explain deviations from Rayleigh distribution, nor indeed to be fair that it would succeed.

We do not infer that there would be lack of evidence that extreme and dangerous waves exist: their gigantic size has been testified by many shipmasters' reports and their dangerousness has been proven by damages on ships and offshore structures, some examples of which are described in Ersdal & Kvitrud (1999) [2] or Kjeldsen (1997) [5]. One should note however that in the very short term, other waves are bound to appear disproportionately small in the vicinity of an extreme one. Whether in a long-term statistical sense such extreme waves are normal waves or abnormal ones is however still an unsolved problem.

Moreover, Robin ([10]) analysed about 2 million individual waves at a location where water depth non-linearities were unlikely to have any significant influence and did not observe more high waves than expected from the Rayleigh distribution. We extended the dataset to about 3.3 million waves in [8] without any change on those conclusions.

The present paper investigates another dataset, in order to help decide whether extreme crest-trough waves are actually more frequent than expected from linear theory. Crest-trough heights distributions are almost unaffected by conventional non-linearities. Of course, if some non-conventional phenomenon occurs, it might also leave crest-trough heights unaffected. Yet, if nothing abnormal is detected on long-term crest-trough heights distributions, we can at least conclude that crest-trough height is not an appropriate parameter to characterize rogue waves.

That dataset analysed here is the Alwyn one, where some authors have detected rogue waves [6, ?] but for which we are not aware of any full statistical analysis. Especially, Wolfram *et al* [14] do not detail the validation and selection processes for the 2762 records used in their bivariate distribution fitting, nor did they conclude about the frequency of extremes.

1 Validation of the dataset

1.1 General description

The initial dataset consists of 71510 20-minute records of water surface elevation by a wave altimeter (EMI monitor) located on the Alwyn North platform in the North Sea, below the flare boom on the south of the platform. Records were periodically made at 5 Hz. Continuous recording was triggered when significant wave height was about or exceeded 3.5 meters. The dataset covers most of the 1994-2005 period, with a few interruptions.

As it is unfortunately usual with marine data, many records show signal histories that can not sensibly correspond to actual water surface elevation ones. Validation is thus necessary, and needs to be at least semi-automated given the high number of records. Care should however be taken in the validation process that criteria should not result in discarding abnormal but actual values.

1.2 Validation of the data

In a first stage, moment statistics (average, standard deviation, skewness, kurtosis) were performed over the signals in each record, and wave identification and count followed by wave statistics (zero-crossing period, $H_{\frac{1}{3}}$, $H_{\frac{1}{10}}$, H_{max} , and the associated periods).

A first selection was made by discarding any record for which either:

- Computation of the moments failed
- Skewness is larger than 5
- Kurtosis is larger than 10
- H_{σ} (4 times standard deviation) is larger than 20 meters
- Identification of the zero-crossing waves failed
- $H_{\frac{1}{3}}$ is less than 1 meter
- T_Z is larger than 25 seconds
- T_Z is smaller than 2 seconds
- $T_{H_{\frac{1}{3}}}$ is larger than 25 seconds
- H_{σ} is more than twice $H_{\frac{1}{3}}$
- $H_{\frac{1}{3}}$ is more than twice H_{σ}

Upon examination of a few of the remaining records, we felt that to carry out moment statistics on the first and second time derivatives of the signal (velocity and acceleration of the water surface elevation) and apply similar criteria would be more efficient than making the above ones more stringent.

The following criteria were added:

- Computation of the moments of the velocity failed
- Standard deviation of the derivative is larger than 10 m/s
- Kurtosis of the derivative is larger than 10
- Random visual examination showed problems
- Computation of the moments of the acceleration failed
- Kurtosis of the acceleration is larger than 10

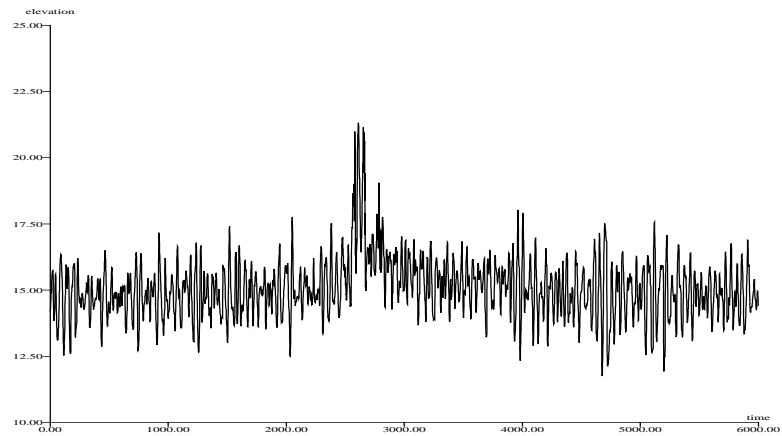


Fig. 1. A signal that visual examination discards

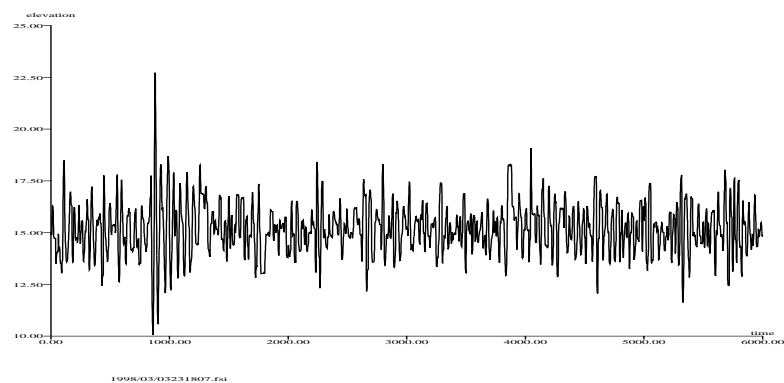


Fig. 2. A signal that visual examination keeps despite doubts

Eventually, the records with the highest ratios $\frac{H_{max}}{H_S}$ in the remaining set were visually examined, and those for which the signal did not look sensible were discarded, until the 100 records with highest ratios were validated. It appeared that many of the visually faulty cases showed a highly varying mean level over the record duration. A moving average over a 2-minute window was thus computed, and those records for which standard deviation of the moving average was more than 0.3 meter were discarded. A typical record that this criterion dis-

cards is shown on figure 1. Visual examination of a dozen of the records discarded according to that criterion randomly selected in the subset where $\frac{H_{max}}{H_s} > 2$ confirmed that the threshold at 0.3 meter only removed invalid time-histories from that subset.

After applying all criteria, only 47426 records remained, *i.e.* 66% of the initial database. The distribution of the records with respect to significant wave height originating from an independent source (ERA-40 and NOAA hindcasts) is shown on figure 3. Malfunctions of the system are more frequent for low H_s than for higher ones, and for routine records than for threshold triggered ones.

Therefore, validation might introduce a bias, with more weight given to high H_s situations. However, statistics of extreme waves for low H_s have little practical use, especially as they can be biased by, for instance, ship wakes and other phenomena of an artificial origin. We can thus consider in the following that the sampling bias towards high H_s is no problem for practical applications.

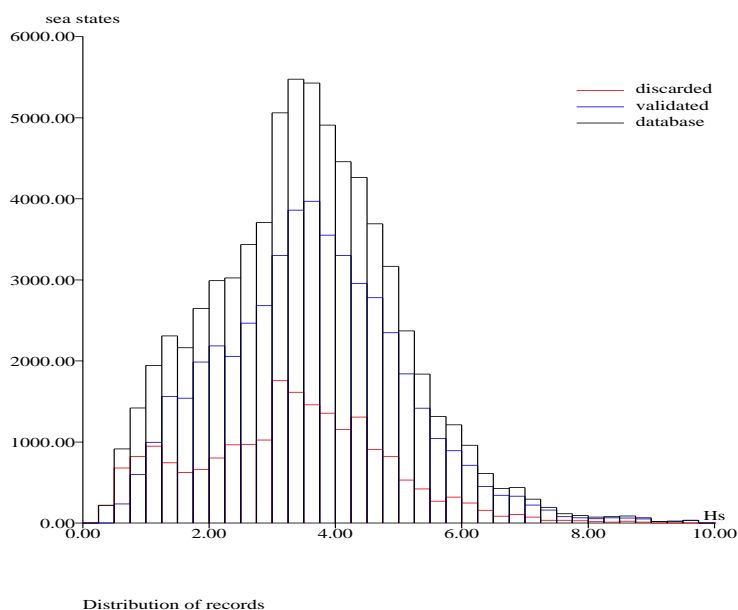


Fig. 3. Distribution of records with respect to hindcast H_s

1.3 Distribution of the ratio $\frac{H_{max}}{H_{1/3}}$

The empirical distribution of the ratio $r = \frac{H_{max}}{H_{1/3}}$ is compared to several Rayleigh approximations, *i.e.* based on the assumption that the maximum height in a record is the same as the the maximum of N_W independent random values distributed with a Rayleigh distribution, where N_W is the number of waves in the record:

$$P(r) = \left(1 - e^{-2r^2}\right)^{N_W}$$

This formula assumes narrow bandwidth, the extremes are slightly reduced when a larger bandwidth is taken into account.

The first approximation assumes that all sea states have the same number of waves, taken as the average ($168=7973268/47426$) over the database. $P(r)$ in the above formula is then the distribution model for all observed ratios.

A further approximation is to assume that $P(r)$ can be replaced by its asymptotic Gumbel limit:

$$P(r) \approx G_l(r) = e^{-e^{-\left(r - \sqrt{0.5 \ln(N_W)}\right) \left(2\sqrt{2 \ln(N_W)}\right)}}$$

Eventually, a reference ‘‘Rayleigh’’ distribution was computed through 2000 simulations of the set of sea states with their actual numbers of waves (independent Rayleigh random values). This simulation also provides a confidence interval for the wave distribution to follow the Rayleigh model, thanks to the quantiles of the simulated cumulative distribution.

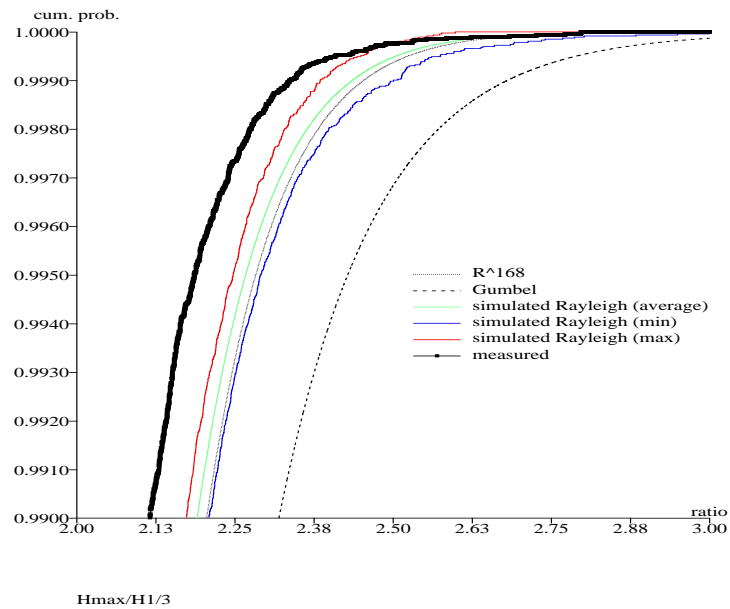


Fig. 4. Distribution of $\frac{H_{max}}{H_{1/3}}$

Figure 4 shows that the R^{168} model does not differ significantly from the average. On the opposite, the Gumbel approximation is much higher, and it may be assumed that the number of waves in a sea state is not sufficient to allow the use of that asymptotic approximation.

The measured ratios are significantly lower than the Rayleigh approximation on most of the database. It can be seen on figure 5, a zoom on the highest part of the previous figure obtained by using Gumbel coordinates, that only the highest ratio in the database matches Rayleigh theory, and on figure 6, another zoom, that those highest measured values are within reasonable confidence limits about the Rayleigh. Thus Rayleigh theory is certainly not underestimating the numbers of extremely high crest-trough waves as long as only a few millions of waves are concerned.

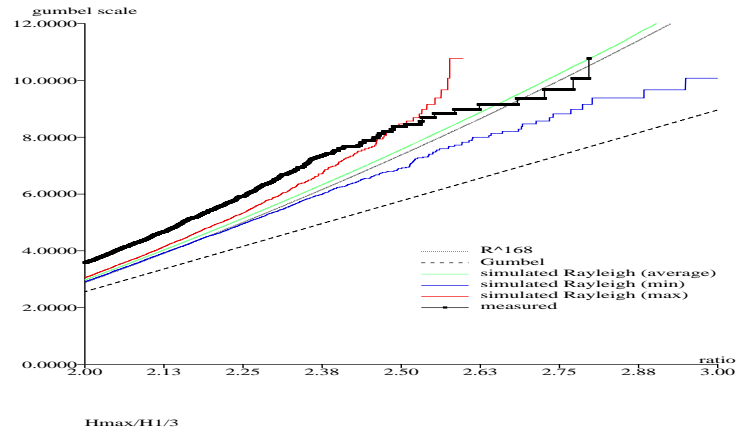


Fig. 5. Distribution of $\frac{H_{max}}{H_{1/3}}$ - Gumbel scale

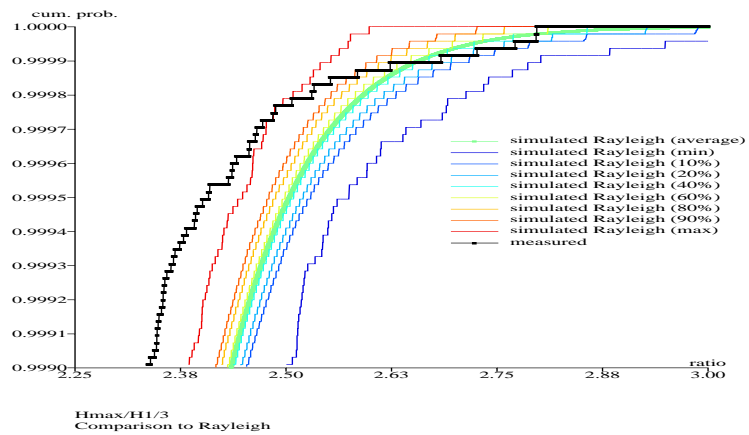


Fig. 6. Distribution of $\frac{H_{max}}{H_{1/3}}$ - zoom

Conclusion

When considering the carefully validated Alwyn database, the overall number of extreme crest-trough wave heights are not in excess of the Rayleigh linear theory predictions.

Crest-trough height alone is thus not an appropriate parameter for characterizing rogue or freak waves.

Rogue or freak waves should on the opposite be characterized by their potential damage, and research should consider the velocities in the wave, the steepness, the pressures on a hull, and similar parameters.

In addition, it should be sought reasons why extreme heights are not expected at the time and place where they occur whereas they are not abnormal from the long term statistics point of view.

References

1. **Dean, R.** "Freak Waves: a Possible Explanation" *Proc. Water Waves Kinematics*, NATO ASI Series E, Vol. 178, pp.609–612.
2. **Ersdal, G. & Kvitrud, A.** "Green sea on Norwegian production ships" *Proc. Airgap Workshop*, HSE/E&P Forum, London 1999.
3. **C. Guedes Soares**, "Spectral Modeling of Sea States With Multiple Wave Systems", *Journal of Offshore Mechanics and Arctics Engineering*, vol.114 1992.
4. **International Association for Hydraulic Research** "List of Sea State Parameters" *Supplement to bulletin* No 52 (1986).
5. **Kjeldsen, S.P.** "Examples of heavy weather damages caused by giant waves" in *Bulletin of the Society of Naval Architects of Japan*, 820, 1997-10, pp. 744–748.
6. **Linfoot, B., Stansell, P. & Wolfram, J.** "On the characteristics of storm waves" *Proc. Int. Offshore and Polar Engineering Conf.*, ISOPE, 2000
7. **Olagnon, M. & Krogstad, H.E.** "Observed short- and long-term distributions of wave steepness", *Proc. Int. Offshore and Polar Engineering Conf.*, Vol. 3, Montréal (1998), pp. 63–70.
8. **Olagnon, M. & van Iseghem, S.** (2000), "Some observed characteristics of sea states with extreme waves", *Proc. 10th International Offshore and Polar Engineering Conf.* ISOPE, 3, pp. 84-90.
9. **Podgórski, K., Rychlik, I., Rydén, J & Sjö, E.** "How big are the Big Waves in a Gaussian Sea ?", *Int. J. of Offshore and Polar Engineering*, Vol.10, No.3, (2000), pp. 161–169.
10. **Robin, A. & Olagnon, M.** "Occurrence of Extreme Waves with respect to Significant Wave Height" *Proc. Offshore Mechanics and Arctic Engineering*, OMAE Vol.2a, 1991, pp. 1–9.
11. **Sand, S.E., Ottesen Hansen N.E., Klinting, P., Gudmestad, O.T. & Sterndorff, M.J.** "Freak Wave Kinematics" *Proc. Water Waves Kinematics*, NATO ASI Series E, Vol. 178, pp.535–550.
12. **Solli, D.R., Ropers, C., Koonath, P., & Jalali, B.** "Optical rogue waves" *Nature*, Vol.450, Dec. 2007, pp. 1054–1057.
13. **van Iseghem, S., Deleuil, G. & Guerin, P.** "Improved characterizations for design waves" *Proc. Int. Offshore and Polar Engineering Conf.*, ISOPE, 2001.
14. **Wolfram, J., Linfoot, B., Stansell, P.** (2000) "Long- and short-term extreme wave statistics in the North Sea" *Proc. Rogue Waves 2000*.

Extreme Waves in the Long-Term Wave Measurements at Ekofisk

Harald E. Krogstad, NTNU¹⁾

Stephen F. Barstow, Jan Petter Mathisen, Lasse Lønseth, Fugro Oceanor AS,
Anne Karin Magnusson, met.no, Mark A. Donelan, Univ. of Miami.

¹⁾harald.krogstad@math.ntnu.no

Abstract. The Ekofisk Reference Data Set (ERDS) is a quality checked wave data set containing more than 100,000 twenty minutes records with significant wave height exceeding 3 meters. A study of crest heights has confirmed earlier findings that second order models appear to agree reasonably well with the data. An attempt to link the occurrence of high waves to spectral or averaged time series parameters has come out negative. A local wavelet-based directional analysis shows that rogue waves in the data material tend to have directions close to the mean wave direction and a low directional spread. The main conclusion is that the observed rogue waves do not appear come from a different population, but rather are rare occurrences within the 2nd order stochastic model.

Introduction

The Ekofisk oil field in the central North Sea holds a unique position for long term wave measurements. Time series wave data exist from six different wave measuring systems for over more than 25 years. On the initiative of the operating oil company at Ekofisk, ConocoPhillips Inc., the data have now been quality checked and compiled into the Ekofisk Reference Data Set, *ERDS* [8]. Currently, ERDS contains over 100,000 twenty minute records with significant wave height exceeding 3 meters, and additional data are added on a yearly basis. One of the systems, the Ekofisk Laser Array, *LASAR*, has been in operation since February 2003. With a continuous 5Hz sampling the system provides directional spectra as well as a reliable surface tracking. ERDS contains numerous individual waves fulfilling the commonly used rogue wave criteria, and these are, in accordance with the terminology in [2], denoted rogue waves in the following.

The paper first reports on a study of the maximum crest heights for the wave records in ERDS compared to 2nd order wave theory. The overall conclusion, applying a simple statistical test, is that Forristall's 2nd order model for crest height can not be rejected by the test for what is believed to be most reliable data. Search for dependence of the maximum crest height on commonly used spectral parameters, like the mean steepness and the spectral widths in frequency as well as in direction, has shown almost no dependence.

A more detailed analysis of the *LASAR* data, also based on sea states with significant wave height (H_s) above 3 meters, has been carried out using the

median elevation from all 4 time series. This eliminates spikes and errors in the data and is a robust estimate of the surface elevation for waves of some size. These data contain 49 rogue waves with a crest height larger than $1.25H_s$ and, at the same time, a wave height exceeding $2H_s$. A visual examination of the directional spectra at the time of these rogue wave events seems to show normal variability. Moreover, their occurrences appear to be completely random. All records containing the rogue waves have also been subject to a local wavelet-based directional analysis. This shows that the local direction of the rogue wave does not differ from the main wave direction, but there is a certain tendency for the waves to occur at low local directional spread. Low local spread is otherwise connected to strong wave groups, but there are also a few occurrences of rogue waves away from obvious wave groups, as well as waves occurring in average spread seas.

Recently, the Benjamin-Feir instability has been suggested as a generation mechanism for rogue waves [5], [12], [4], and [2] and the references therein. However, numerical simulations and recent wave tank experiments suggest that in order to be active, the mechanism requires considerably more unidirectional waves than typical wind wave fields in the open sea. The theory links enhanced kurtosis to an increased occurrence of rogue waves. Somewhat surprisingly, even the LASAR data show a clear positive correlation between the maximum crest and wave heights and the estimated kurtosis based on the same 20 minute time series. However, an analysis of carefully simulated gaussian time series with typical ocean wave spectra and a similar duration demonstrates that the correlation is not real and simply due to correlated sampling variability.

Ekofisk Reference Data Set

The Ekofisk Reference Data Set, covering time series wave data from 1980 to present, has been compiled from various sources and contains, in addition to waves, also wind and wave model data [8]. The raw wave data reside at the environmental data centre at the Norwegian Meteorological Institute (met.no). The sampling frequency is mostly 2Hz, whereas the time series were recorded every third hour from 1986 to 1996, and then continuously from 1997. The data have been subject to extensive quality checks. For the crest height study reported below, spikes and irregularities will be quite serious and it soon became evident that the standard error control used by the operational wave analysis was not sufficient for some of the data sets. Over 80,000 records were visually inspected around the maximum crest height. The check compared the raw data to a band-pass filtered version (0.03 – 0.5Hz), and all records with a significant difference around the maximum crest (indicative of a spike or an irregularity) were discarded from further analysis. A list of the wave instrumentation (some of which used in various locations at Ekofisk) is shown in Table 1. In addition, a WaMoS radar has been in operation at Ekofisk since 1994, but is not considered here. All sea state parameters discussed in the following have been computed from the estimated spectra, *e.g.* $H_s = 4\sqrt{m_0}$. A standard zero-upcrossing analy-

Instrument	Period
Datowell Waverider	June 1980 –
Plessey radar	June 1980 – Sept.1993
Thorn/EMI laser	July 1986 – Aug. 1989
Optech lasers	Nov.1993 – July 2003
Optech Laser Array	Feb. 2003 –
Miros Range Finder	March 2002 – May 2005

Table 1. Wave measurement instrumentation used in the Ekofisk Reference Data Set.

sis has been used for wave and crest heights. The maximum crest height is at the same time the maximum data value in the series measured from the mean.

The Laser Array

The LASAR array consists of four vertically looking OptechTM lasers placed in a square with sides 2.6m, 20 meters above the surface and over a water depth of 70m. It is mounted on the bridge between the Kilo and Bravo platforms situated about one nautical mile north of the Ekofisk complex and measures undisturbed waves from the dominating wave directions at Ekofisk.

The system has been designed by met.no in cooperation with University of Miami, and the data collection is carried out under operational responsibility of ConocoPhillips Inc. The recording uses a continuous 5Hz sampling with a 10^{-3} m vertical resolution. Sampled data are collected in 21 minutes segments with a one minute overlap every 20 minutes. Data for the current investigation have been down-sampled to 1.7Hz each covering exactly 20 minutes. The system is occasionally suffering from poor data quality, which is the main reason why the non-directional wave analysis below has been based on median-averaged recordings.

The ERDS Crest Height Study

The objective of the crest height analysis was to copy the investigation carried out during the WADIC project and reported in [6]. The reason for basing the investigation on the maximum crest height in each 20 minutes record and applying the standard relation for the maximum of independent events also in the case of sequentially correlated wave heights was discussed in [6]. The data material for the crest study covers different time periods up to about 2005.

The Forristall crest height model [3] is based on second order numerical simulations of the surface using a directionally spread JONSWAP spectrum and parametrized in terms of the average *wave steepness*, $s_1 = 2\pi H_s/k_1$, governing the non-linearity, and the *Ursell number*, $Ur = H_s/k_1^2 d^3$, governing the shallow water dependence. Here k_1 is the deep water wave number corresponding to $T_{m01} = m_0/m_1$, and d is the water depth. For a record of duration T , the

maximum crest height distribution is expressed in terms of a Weibull distribution raised to the number of waves:

$$\begin{aligned} P(Cr_{\max}/H_s \leq h) &= \left[1 - \exp\left(- (h/\alpha)^\beta\right) \right]^{T/T_z}, \\ \alpha &= 1/\sqrt{8} + 0.2568s_1 + 0.08Ur, \\ \beta &= 2 - 1.7912S_1 - 0.5302Ur + .2824Ur^2. \end{aligned} \quad (1)$$

The validity of the model for the data at hand has been checked by a statistical procedure based on the Kolmogorov-Smirnov test. The output from the test is a probability stating how reasonable it is that the selected data set fits the model. It is important to note that the extent to which the data conform to the model depends on the size of the data set. For a small data set some deviations will not be statistically significant for rejecting the model. On the contrary, a large data set will make the test flag even quite minor deviations. The test is easy to carry out; if Forristall's model holds, the statistic

$$U = \left[1 - \exp\left(- \left(\frac{Cr_{\max}/H_s}{\alpha}\right)^\beta\right) \right]^{T/T_z} \quad (2)$$

should be uniform on the interval $[0, 1]$. Space prevents us from going too much into details, but the results conform well with the findings in [6]. As has been consistently observed in similar intercomparisons, the Waverider stands out with maximum wave crests even below the benchmark Gaussian result, and thus far below the Forristall model. This is attributed to the quasi-Lagrangian behavior of the buoy and also to a tendency of avoiding narrow peaks in a directional sea, see [9], Sec. 5. The Miros Range Finder also shows crest heights below the Forristall model. The laser systems and the Plessey radar agree with the model, with minor deviations going either side for various selections of data.

As the test considers all data, it might be asked whether there may be real outliers, that is, individual waves outside the crowd. Fig. 1 puts the focus on the very highest waves by displaying the empirical probability of exceedance for nine of the data sets. The ratio Cr_{\max}/H_s is adjusted for different number of waves in the record by the factor $\sqrt{\log N_0/\log N}$, where N is the actual number of waves in the record, and N_0 a mean. The red curve is the fixed reference

$$P(Cr_{\max}/H_s > h) = 1 - \left(1 - e^{-\left(\frac{h}{0.38}\right)^2} \right)^{128} \quad (3)$$

meant as an aid to judge the data distribution. The deviations for the Waverider and Miros Range Finder at North Flare are obvious. The Optech lasers situated on the North and South Flares show a slight excess of high waves, and more on North Flare than on South Flare. Photos have shown that very high waves can produce a lot of spray when going through the constructions upwind of the measuring point at these sites, and North Flare observations might also be influenced by reflected waves from the concrete wall around the Ekofisk tank.

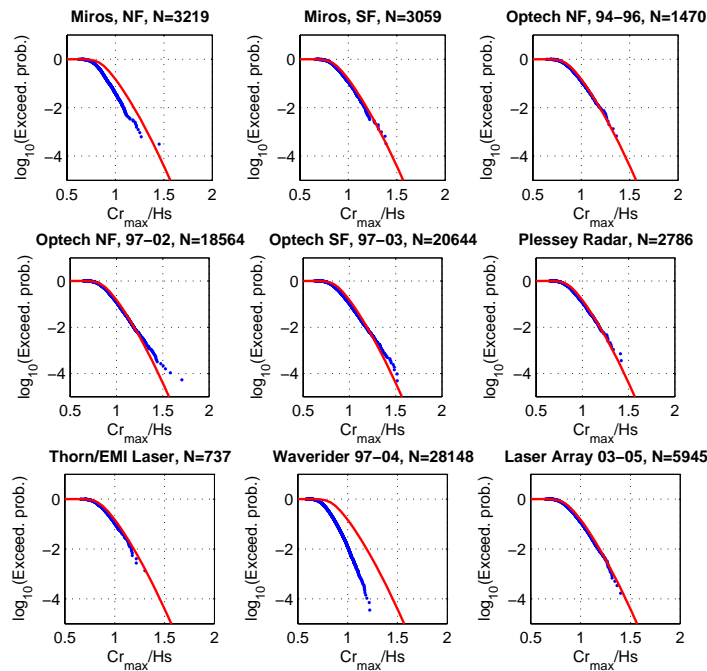


Fig. 1. Observed probability of exceedance of the ratio Cr_{max}/Hs for 20 minute records, $Hs \geq 3m$ (Data every three hours before 1997, otherwise every 20 minutes). The red curve is the fixed reference mentioned in the text. NF and SF refer to the north and south flare towers, i.e. the locations of the sensors.

In conclusion, apart from the North Flare Optech laser data, the data show no obvious signs of what could be denoted *true* rogue waves.

The crest study has again put focus on the behavior of the various instrument systems for crest measurements. It has also revealed that the maximum crest height is a delicate parameter with respect to spikes and data errors, and that the analysis indeed needs a careful error control.

Extreme Waves in the LASAR Data Set

LASAR provides directional spectra as well as an accurate surface profiling based on the median time series from the four lasers. For the period February 2003 – November 2007, there are a total of 14,679 twenty minute records with H_s exceeding 3m. The maximum crest height to significant wave height, Cr_{max}/H_s , has been compared to three common measures for the wave steepness

and the spectral widths:

$$s = \frac{H_s}{\frac{g}{2\pi} T_p^2}, \quad \nu = \sqrt{\frac{m_2 m_0}{m_1^2} - 1}, \quad \sigma_{T_p} = \sqrt{2 \left(1 - \left(a_1 (T_p)^2 + b_1 (T_p)^2 \right) \right)} \quad (4)$$

Note that the steepness parameter here uses T_p instead of T_{m01} in the crest study, whereas $\nu = \left\langle (f - \bar{f})^2 \right\rangle^{1/2} / \bar{f}$ is the RMS relative width of the frequency spectrum, and σ_{T_p} is the directional spread at the spectral peak. The result is shown in Fig. 2. Although a very weak increase in Cr_{\max}/H_s is seen for

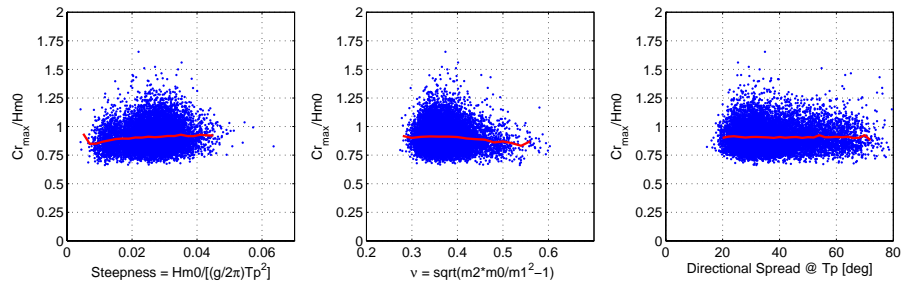


Fig. 2. Normalized crest height vs. the overall steepness and the spectral widths in frequency and direction. The red curves are binned averages.

steeper waves, no significant dependence is seen for the directional width. A slight increase in the ratio is also seen for decreasing RMS width of the frequency spectrum, down to about $\nu = .35$.

Theory, numerical simulations and wave tank experiments have linked high kurtosis to an increased occurrence of high waves (See discussion and further references in [2]). However, it appears that this correspondence weakens as the directional spread increases, and is assumed to be minor for realistically spread ocean waves. Nevertheless, by comparing Cr_{\max}/H_s and H_{\max}/H_s for 20 minute records to the kurtosis and skewness estimated from the same records, a clear correlation occurs for kurtosis and some even for skewness, as shown in Fig. 3. A similar scatter plot has also been presented in [10]. Since this behavior is somewhat unexpected, the same analysis was carried out using carefully simulated gaussian time series with typical wave spectra and the same 20 minute duration. This demonstrated that the correlation between the height and the kurtosis is only due to correlated sampling variability. In fact, comparing estimates obtained from measured neighboring records removed all traces of a real correlation. The same conclusion was reached for data from the Frigg field in [11], after computing the kurtosis with and without the highest wave included.

A total of 105 waves in the LASAR data set fulfill the $H/H_s \geq 2$ criterion, and 85 the $Cr/H_s \geq 1.25$ criterion. Both criteria are satisfied for 49 waves, which

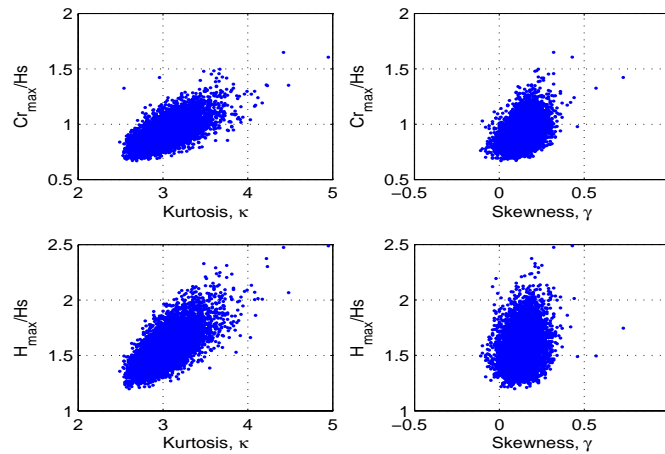


Fig. 3. Observed (spurious) correlation between the maximum crest and wave height, and the kurtosis and skewness for 20 minute LASAR wave records. See the text for the explanation.

are denoted *double* rogue waves in the following. Because of the data quality of the individual series, directional spectra exist for only 43 of the waves.

The most extreme wave is shown in Fig. 4. The significant wave height is over 9 meters with $Cr/H_s = 1.56$ and $H/H_s = 2.42$. Relatively speaking, the wave is more extreme than the famous Draupner wave. However, only 8 of the 43 double rogue waves have H_s exceeding 5 meters. Both narrow and multiple-peaked directional spectra exist for the double rogue wave records, and the variability does not seem to be significantly different from what is normal for the site. As also observed previously, the occurrence of a rogue wave appears to be quite random, e.g., the wave shown in Fig. 4 is a solitary rogue wave occurrence during an almost three-day long major storm period. The conclusion is that it is difficult to predict the occurrence of rogue waves from spectral and integrated time series properties alone.

The spectral analysis treats the data over the duration of the record in a uniform way, and is unable to resolve time localized events such as the passage of strong wave groups and transient waves. On the contrary, the alternative Directional Wavelet Method [1] resolves the temporal variations down to the wave group time scale. In the Local Triplet Analysis, three laser series are transformed into equivalent heave/slope records and the Morlet continuous wavelet transform replaces the discrete Fourier transform [7]. The method has previously shown consistent results when applied to LASAR data [7], where in particular time averaged local estimates of the spectrum and directional parameters closely fit the estimates from the standard spectral analysis. The local wavelet and triplet analysis for an excerpt around the extreme wave in Fig. 4 is shown in Fig. 5.

It is observed that directional spread drops from an average of 25° to below 10° near the occurrence of the rogue wave. For other cases in the data material the drop is even more dramatic. Even if the majority of the double rogue waves cases show a similar drop in directional spread around their occurrence, there are also a few situations with no obvious changes in the spread. Low local spread is otherwise connected to strong wave groups, but there are also occurrences of rogue waves away from obvious wave groups. None of the double rogue waves have propagation directions significantly different from the dominating wave direction.

Conclusions

The Ekofisk Reference Data Set (ERDS) is currently containing more than 100,000 twenty minute records with significant wave height exceeding 3 meters. A study of crest heights compared to existing second order theory and covering data up to about 2005 revealed some instrumental differences, but no major deviations between what is generally considered to be the most reliable instruments. The analysis also confirmed earlier findings, based on similar statistical tests, that Forristall's second order model appears to agree well with the data. It may, however, still be argued that the test as well as the model are rather crude, and exceptional situations could be drowned in the vast amount of normal sea states.

The present study has not been able to link favorable conditions for high waves strongly to spectral or averaged time series parameters. Similar conclusions were found in [10].

The local wavelet-based directional analysis shows that the rogue waves tend to occur during low local directional spread, but a completely consistent picture is not seen. It is however observed that none of the double rogue waves have propagations directions significantly different from the prevailing wave direction.

The main conclusion at the moment is thus that the observed rogue waves here do not seem to come from a different population, but rather are rare occurrences within the 2nd order stochastic model.

Acknowledgments

We would like to offer our special thanks to Dave Peters of ConocoPhillips Inc. for his help and encouragement throughout the project.

References

1. Donelan, MA, WM Drennan, and AK Magnusson: Nonstationary analysis of the directional properties of propagating waves, *J. Phys. Ocean.*, **26** (1996), pp. 1901–1914.
2. Dysthe K, HE Krogstad, and P Müller: Oceanic Rogue Waves, *Ann. Rev. of Fluid Mech.*, Vol. 40 (2008) pp. 287–310.
3. Forristall, G.: Wave Crest Distributions: Observations and Second Order Theory, *J. Phys. Ocean.*, **30** (2000) pp. 1931 – 1943
4. Gramstad O, K Trulsen: Influence of crest and group length on the occurrence of freak waves, *J. Fluid Mech.*, **582** (2007) pp. 463 – 472.
5. Janssen, PAEM: Nonlinear four wave interaction and freak waves. *J. Phys. Ocean.*, **333** (2003) pp. 863–84.
6. Krogstad HE, SF Barstow: Analysis and applications of second-order models for maximum crest height, *J. Offshore Mech. Arctic Eng.*, **126** (2004) pp. 66–71.
7. Krogstad HE, AK Magnusson, MA Donelan: Wavelet and Local Directional Analysis of Ocean Waves, *Int. J. Offs. Polar Eng.* **16** (2006) pp. 97–103.
8. Lønseth, L: *Ekofisk Reference Data Set 1980 – 2005*. Fugro OCEANOR report No. C55060/4026/R2 (2006) (*confidential*).
9. Magnusson AK, MA Donelan, WM Drennan: On Estimating Extremes in an Evolving Wave Field, *Coastal Eng.*, **36**, (1999) pp. 147–163.
10. Magnusson AK, E Bitner-Gregersen, JC Nieto Borge: Analysis of Extreme Waves in the MAXWAVE Database, *Proc. MAXWAVE Final Meeting*, Geneva, Switzerland (2003).
11. Olagnon M, M Prevosto: Are rogue waves beyond conventional predictions? *Proc. 14th ‘Aha Huliko’ Hawaii Winter Workshop, Honolulu* (2005), ed. P Müller, D Henderson.
12. Socquet-Juglard H, KB Dysthe, K Trulsen, HE Krogstad, J Liu: Probability distributions of surface gravity waves during spectral changes, *J. Fluid Mech.*, **542** (2005) pp. 195–216.

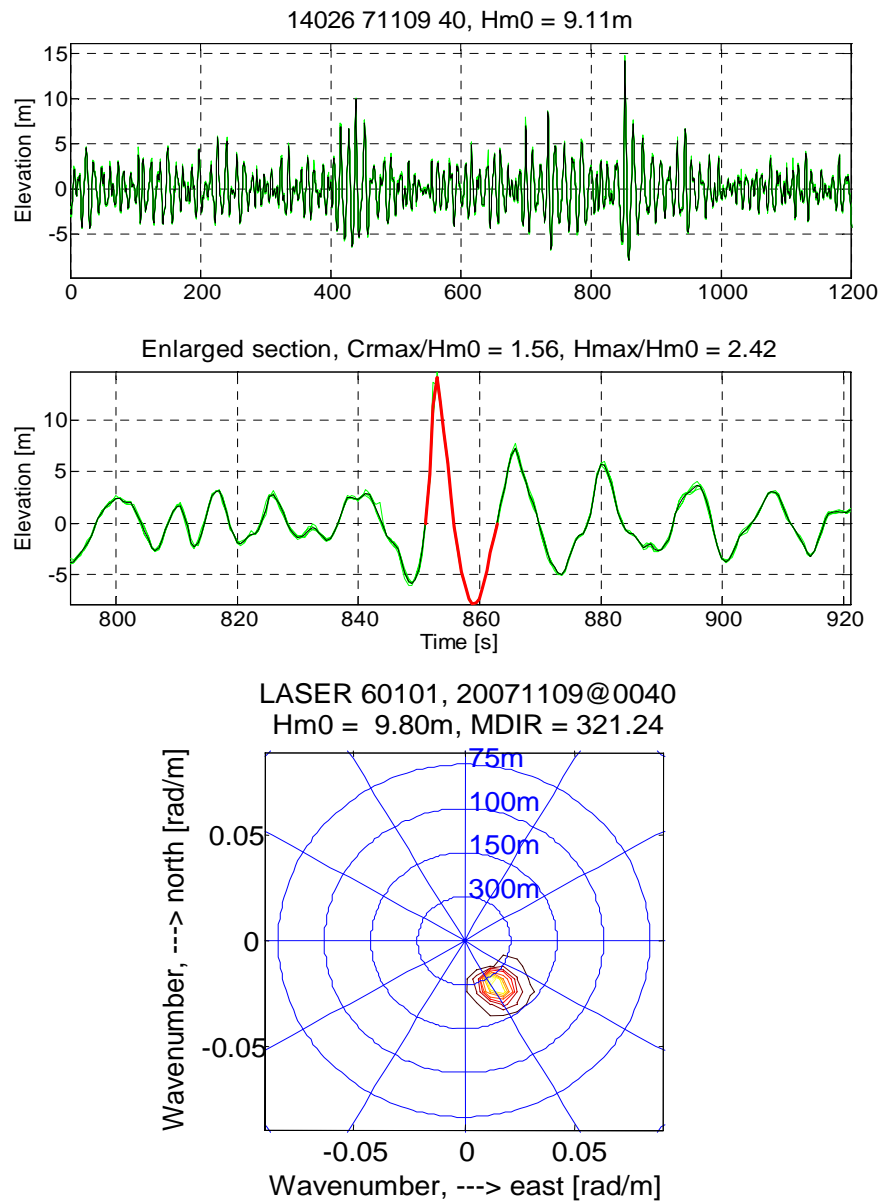


Fig. 4. The highest "double" rogue wave in the data material. *Top:* Full 20 minutes time series. *Middle:* Expanded section around the wave. *Bottom:* Wavenumber spectrum. (Note a difference in H_s ($= H_{m0}$) from the median time series as compared to the mean spectra from the directional analysis).

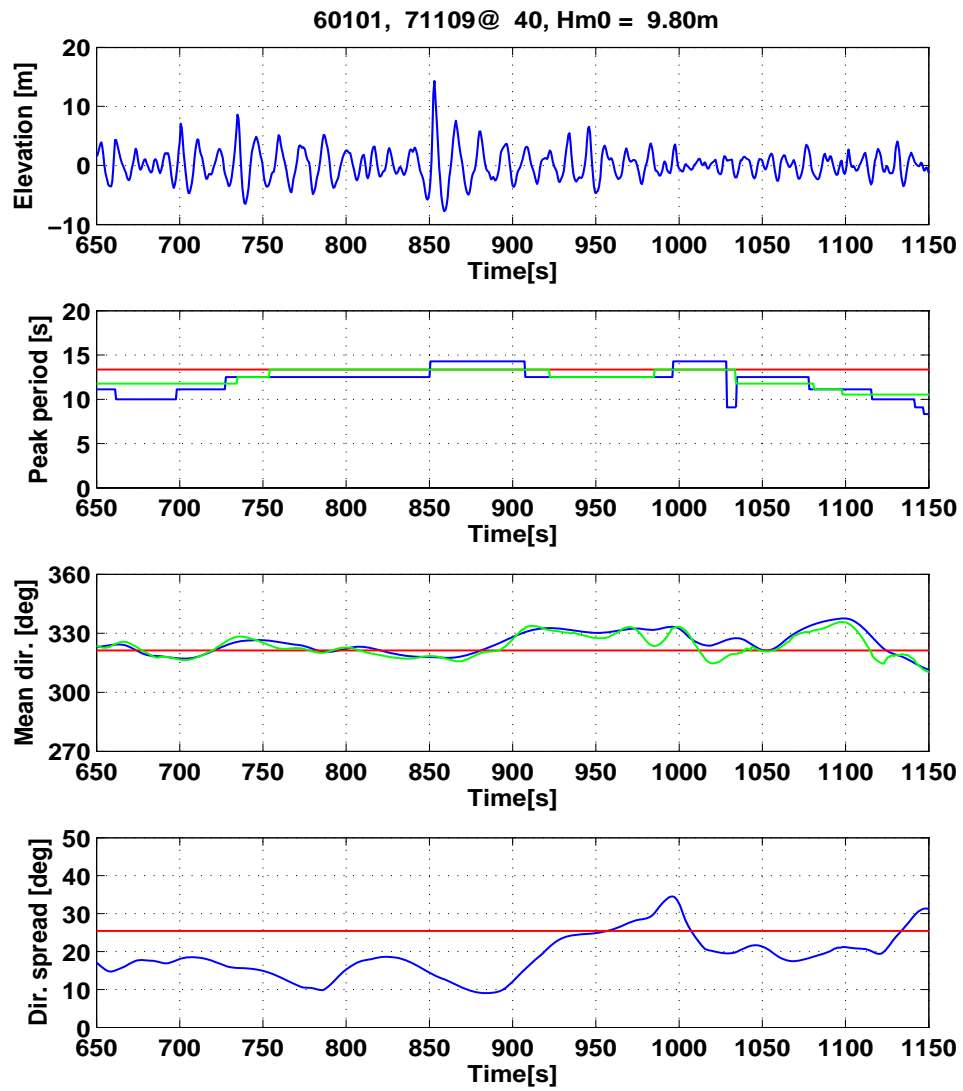


Fig. 5. Local directional analysis for the major rogue wave. *Green*: DWM-analysis; *blue*: local triplet analysis; *red*: standard spectral estimate.

Rogue Waves 2008 - 3rd Int. Workshop

Brest, France, 13-14 October 2008

Luigi Cavaleri and Luciana Bertotti

Institute of Marine Sciences, Venice, Italy

The “Voyager” accident – meteorological and marine predictability

Abstract

On February 14, 2005 the cruise ship “Voyager” en route from Tunis to Barcelona came across a severe Mistral storm. In particular the ship was hit by one or more high waves that broke the windows of the control deck. The consequent flooding of the ship control system brought her to a halt, forcing the crew to send out a distress call. After many hours the crew managed to restart one of the engines and she slowly made her way to the closest harbour.

The storm had been well forecast, as shown by comparison of the forecasts and the later analysis. Besides the passes of the QuikSCAT and Jason satellites at the right time and position provided direct measurement of the local wind and wave conditions at the time of the accident. This provided a direct check of the hindcast results, hence full availability of all the conditions, e.g. spectra, for the evaluation of the possibility of a freak wave encounter.

We have evaluated this possibility using linear and second order theories, and considering the nonlinear instability plus some recent related results obtained in a wave channel. While the probability is negligible in the first two cases, it turns out that the last approach suggests a substantial encounter probability of the estimated height of the wave that caused the damage.

We discuss the attitude that a ship master has to consider while facing these situations. The available evidence suggests that very large wave heights, compared to the significant ones, are not as rare as it was once believed, but part of the conditions a ship master expects while facing a storm.

1 – The fact

On February 14, 2005 the cruise ship “Voyager” en route from Tunis to Barcelona came across a severe Mistral storm. The storm was from the northern sector, with a very intense and gusty wind, typical of the situation. Waves were then estimated at about ten metre significant wave height. From what derived from later reports, at a certain moment the ship was hit by one or more high waves that broke the windows of the control deck, well high above the floating line. The consequent flooding of the ship control system brought her to a halt, forcing the crew to send out a distress call. One of the reports about the call shows well the terrible conditions the ship was in:

“Battered by storm

A high wave smashing through the windows of the bridge and damaging electronics is thought to have caused the power cut.

The distress call from the ship said it was taking on water and was in ‘terrible condition’, UK coastguards reported.

*They received the message just after 0900 GMT on Monday, via the Gimi.
The French coastguards told the BBC that the ship was not on fire and not in danger of sinking.
Two tugs – one Spanish and one French – are travelling to the stricken vessel and hoping to tow it into a French port, they said.
The V Ships spokesman said they would be there within 14 hours.
Several aircrafts have also been sent to the scene.
Most of the passengers ...”*

After many hours the crew managed to restart one of the engines and she slowly made her way to the closest harbour in Sardinia.

The event, amply reported in the specialised literature, prompted a detailed analysis of the storm to derive the height of the waves that could reasonably be expected in that situation.

2 – Analysis of the storm

At the time the European Centre for Medium-Range Weather Forecasts (ECMWF, Reading, U.K.) was using the operation T511 meteorological model, corresponding to about 40 km resolution. A direct inspection of the forecast fields clearly shows that the storm had been well forecast. However, due to the underestimate of the surface wind fields typical of the enclosed basins, also the derived wave heights were expectable underestimated. See Cavaleri and Bertotti (2006) for a thorough discussion on the subject. To go into more details Bertotti and Cavaleri (2008, henceforth referred to as BC1) analysed the storm with higher resolution. They carried out a series of short (12 hours) forecasts at T799 resolution (about 25 km) starting at 12 hour interval from the available analyses. Assembling all the forecast together provided a uninterrupted sequence of higher resolution wind fields at three hour interval, suitable for the following wave evaluation. At this aim they used the WAM model (Komen et al., 1994) at 0.25 degree resolution. A second hindcast was done using the COAMPS winds, a high-resolution model used at the Fleet Numerical Meteorology and Oceanography Center (FNMOC, Monterey, California, USA).

The wind and wave resulting data were further refined making use of two lucky passes of the QuikSCAT scatterometer and the Jason-1 altimeter that crossed the area practically at the time of the accident. A cross comparison between the model and measured wind speeds and wave heights led to a very good calibration of the model data, providing a very accurate description of the situation in the area in the morning of February 14. Figure 1 shows the wave field in the area between the Balearic islands and Sardinia at 09 UTC. Isolines are at 1 m interval (significant wave height). The arrows, whose length is proportional to the local wave height, indicate the mean wave direction, the ellipse shows the area where the ship was located. This map has been obtained using the COAMPS winds. Use of the ECMWF winds leads to a more extended storms towards the South, but with more or less the same wave heights in the zone limited by the ellipse. As a matter of fact, there are uncertainties on the her actual position. In practice the best estimate in BC1 for the wave conditions at the time of the accident was between 8 and 10 m significant wave height (depending on the actual position of the ship).

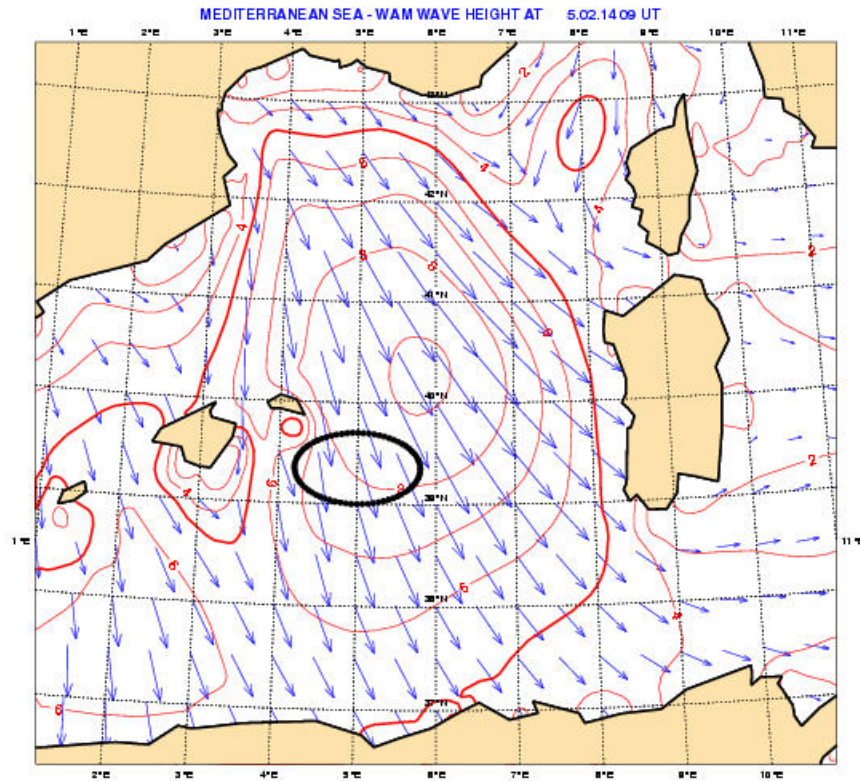


Figure 1 – Wave field at 09 UTC 14 February 2005. The area is the Western Mediterranean Sea. Isolines at 1 m interval. Arrows show significant wave height and mean direction. Wave field obtained using COAMPS winds. The ellipse shows the approximate position of the cruiser “Voyager” at the time of the accident (after BC1)..

A good example of the quality of the hindcasts is given in Figure 2 where the modelled H_s along the marked cross section (ground track of the Jason-1 altimeter) are compared with the corresponding measured values. We note that more to the South the two hindcasts diverge (as specified, ECMWF somehow anticipated the storm), but all the results are consistent where our present interest is focused. During the model runs not only the integrated wave values, but also the full 2D spectra were saved in the area of interest to be later used for the extreme analysis.

3 – Statistics

Some of the various reports from onboard the ship referred to waves up to 14 m high. A direct use of the standard Rayleigh distribution quickly shows that, given the local conditions, such wave height had to be quite common. In any case a 14 m high waves could not damage the ship at the height where the control room is located. Bertotti and Cavaleri (2008b, henceforth referred to as BC2) hypothesised that indeed it was a 14 m crest that hit the ship, and moved therefore to analyse the corresponding probability. At this aim, apart from the linear theory, they considered the Tayfun distribution (1980). The related results are shown in Table 1. Focusing for the time being on the first four lines, we see that a 14 m crest is extremely unlikely, as easily guessed, when considering the linear theory, but coming into the real of the, although remote, possibilities when we base our considerations on the Tayfun distribution. Indeed, if in the area of 10 m H_s , an encounter every 14 days is something to take into account.

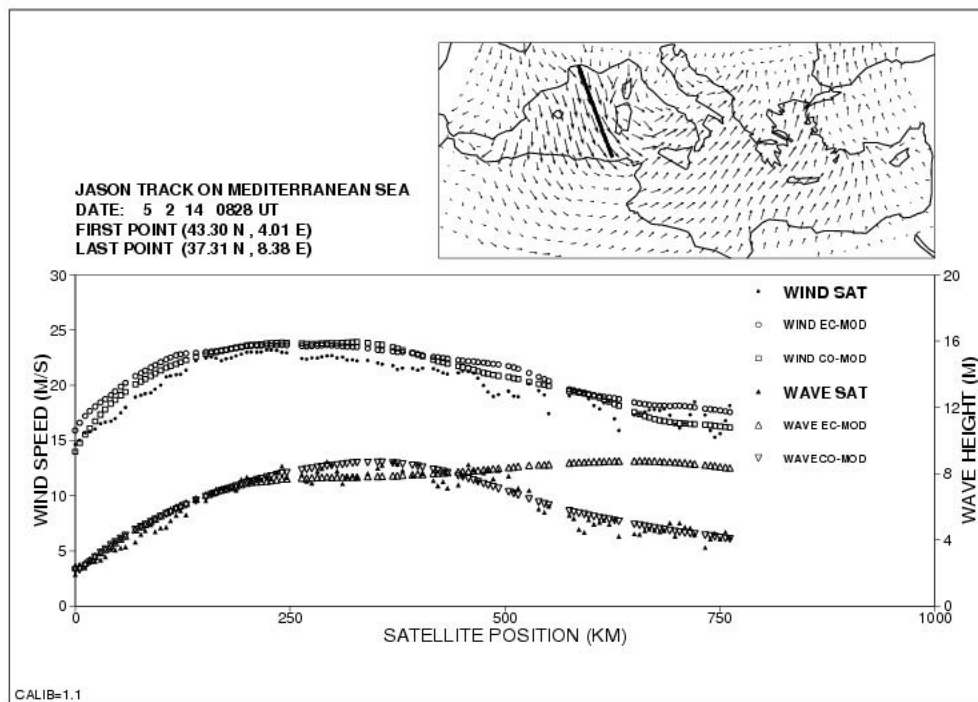


Figure 2 – Comparison between Jason altimeter wind speeds and wave heights and corresponding model results. EC-MOD = ECMWF and CO-MOD = COAMPS. The ground track and the overall wind field are shown in the smaller upper right figure (after BC1).

However, things get much worse when we consider the possible highly nonlinear effects. Onorato et al (2006) explored the modulational instability in a random sea based on the nonlinear Schrödinger equation (NLS), showing that this could indeed lead to much higher wave and crest heights. Their results are shown in Figure 3, where it is evident that the higher the considered height, the larger the difference between the NLS results and the alternative theories. The implications are summarised in the lower two lines of Table 1 where we see that, if in a 10 m H_s sea (the data are disposal are not sufficient for the 8 m H_s estimate), a 14 m crest encounter is to be expected on the average every 20 hours.

4 – General discussion

Ships are built according to certain principles dictated by an internationally accepted authority. If they are correctly built, then, if something happens, this is generally considered as a “freak” event, i.e. something out of the normally expected range (we do not discuss here the specific sea faring capability). However, these well established rules are based on information that is revealing itself as obsolete. The freak wave, the unexpectedly high wave in the middle of much lower wave conditions, is something that is no more part of the myths, of the fairy tales told by sailors. The extremely large number of data presently available in the open ocean, either from platforms and wave measuring buoys or from satellites, have definitely shown that these events are indeed real, and they must be considered as part of what could be encountered at sea.

The point we raise is that, while the official rules provide the ground on which a captain can officially take his decisions, the now widely known evidence of possible freak waves, strongly supported by theory and devoted experiments (see, e.g., Onorato et al, 2006), should be considered

Table 1 – Encounter probability of a 14 m high wave crest for different significant wave heights H_s and according to different theories. Tayfun is second order theory, NLS is modulational instability based on nonlinear Schrödinger equation. N is the average number of waves = $1/\text{Probability}$ between two encounters. Time is the corresponding elapsed time. Based on the wave conditions present at the time and location of the “Voyager” accident. The available data do not cover the case NLS-8 (after BC2).

theory	H_s (m)	Probability	N waves	Time
linear	8	0.23×10^{-10}	0.44×10^{11}	10,000 years
linear	10	0.15×10^{-6}	0.65×10^7	3 years
Tayfun	8	0.45×10^{-7}	0.22×10^8	7 years
Tayfun	10	10^{-5}	10^5	14 days
NLS	8	-	-	-
NLS	10	0.17×10^{-3}	6000	20 hours

when at sea. In the case of the “Voyager”, while on a global perspective a 10 m high sea (H_s) is not exceptional, the existing possibility of very high crests capable to damage the ship should be taken into account. While we can still argue about the numbers, for instance the experiments by Onorato et al. (2006) have been done in a wave flume without taking the directional spreading into account, qualitatively the available evidence strongly suggests that indeed the encounters with these events are much more common than once believed and, which is the relevant point, than what implicitly embedded into the present construction rules. The estimates of the intensity of, e.g., the 100-year storm in the various parts of the world have been steadily increasing during the last 20-30 years while data were accumulating and the more and more refined models were producing numerical evidence. We strongly believe that it is about time that the construction rules of the ocean going ships are updated. This will be extremely expensive and not easy, and it should therefore be carefully planned, but it is a step we have to face in a not far future.

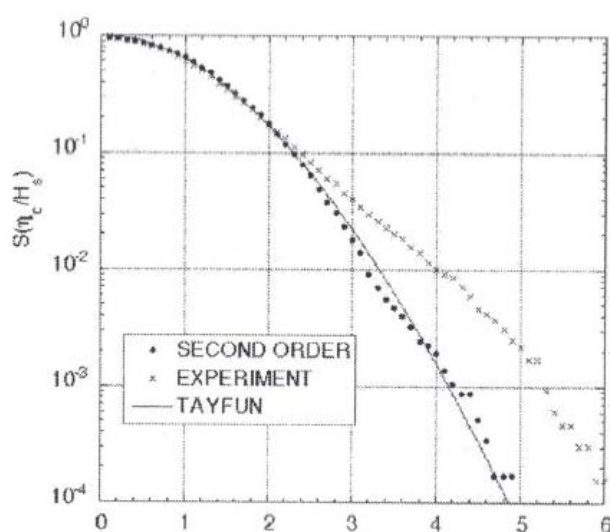


Figure 3 – Encounter probability of a wave crest expressed (abscissa) as multiple of the standard deviation of the sea surface (after Onorato et al., 2006).

References

- Bertotti, L., and L.Cavaleri, 2008a, Analysis of the Voyager storm, *Ocean Engineering*, Vol.**35**, 1, pp.1-5.
- Bertotti, L., and L.Cavaleri, 2008b, The predictability of the “Voyager” accident, *Nat.Hazards Earth Syst.Sci.*, **8**, pp.533-577.
- Cavaleri, L., and L.Bertotti, 2006, The improvement of modelled wind and wave fields with increasing resolution, *Ocean Engineering*, Vol.**33**, 5-6, pp.553-565.
- Komen, G.J., L.Cavaleri, M.Donelan, K.Hasselmann, S.Hasselmann, and P.A.E.M.Janssen, 1994, *Dynamics and Modelling of Ocean Waves*, Cambridge University Press, 532 pp.
- Onorato, M., A.R.Osborne, M.Serio, L.Cavaleri, C.Brandini, and C.T.Stansberg, 2006, Extreme waves modulational instability and second order theory: wave flume experiments on irregular waves, *J.Mech: B Fluids*, **25**, 5, pp.586-601.
- Tayfun, M.A., 1980, Narrow-band nonlinear sea waves, *J.Geoph.Res.*, 85, pp.1548-1552.

Extreme waves in visual wave observations by VOS

Vika Grigorieva and Sergey K. Gulev

P.P. Shirshov Institute of Oceanology, Russian Academy of Sciences, Moscow, Russia

vika@sail.msk.ru <http://www.sail.msk.ru>

Being a disastrous phenomenon, extreme waves (including those classified as rogue waves) are critically important for marine structures. Although there are many works on the theory of rogue waves [e.g. 1, 2, 3, 10, 11, 12, 13], their physics is still poorly understood and they are hardly detectable in different wind wave data. Furthermore, we have very tentative estimates of rogue waves and in most wave data it is hard to discriminate between the observational truth and the measurement artifacts of different nature when very high waves are in question. In this paper we will analyse the collection of visual observations worldwide in order to quantify the most extreme wave cases and to identify their nature.

Besides model hindcasts, satellite and buoy measurements Voluntary Observing Ship (VOS) data represent now an important source of global wave information, including that of extreme wave events. There is a general concern that VOS observations are quite inaccurate and, therefore, are hardly applicable for quantitative wind wave analysis. However this concern results primarily from a poor knowledge of the actual errors and uncertainties inherent in the VOS wave observations. This accuracy was more or less quantified during the last years and many errors and uncertainties were either minimized or removed from the VOS collection [5]. Visual wave observations were extensively used for the description of climatological characteristics of wind waves [5, 6, 7] and for the assessment of the long term tendencies in wave parameters [8, 9]. However, they were not yet employed for the analysis of freak waves. We used these data to quantify the highest observed wave cases in the World Ocean during the last century and to further attribute them to the wind storms, potentially freak waves, or observational artifacts.

Voluntary observing ships provide massive visual wave information worldwide covering the period from 1885 onwards [14, 15]. Before 1950 marine officers reported the highest wave component (sea or swell) and its upper value was limited by 16 m according to the existing coding system. From 1950s observers started to report separately wind sea height and swell height estimates. Furthermore, the coding system was changed and allowed for the detection of the maximum wave height up to 25 meters for both sea and swell. From our collection of more than several million reports we selected all cases reporting wave height exceeding 15 meters. Altogether, after 1950 there has been found more than 1000 of such cases for seas and about 3000 cases for swells (Fig.1). Importantly, we considered separately the subsets of reports providing information about all wave parameters (wind sea and swell heights, their periods and directions) and of incomplete reports which provide typically only one wave parameter (e.g. wind sea height). In the first instance we consider wave statistics based on all selected reported without any census.

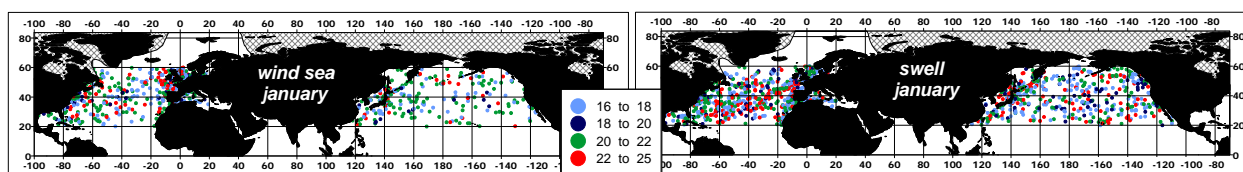


Fig.1 Extreme wind sea (left panel) and extreme swell (right panel), m, Northern Hemisphere, January, 1950-2006

Figure 2 shows the occurrence histograms of the extreme wind wave and swell heights, their periods, wind speed for all selected extreme cases (i.e. reported wave height is higher than 15 m). Additionally we also estimated the occurrences of wave periods, steepness and wave lengths. Furthermore, wave parameters were analyzed within the radius of 100 km around the location of extreme wave report.

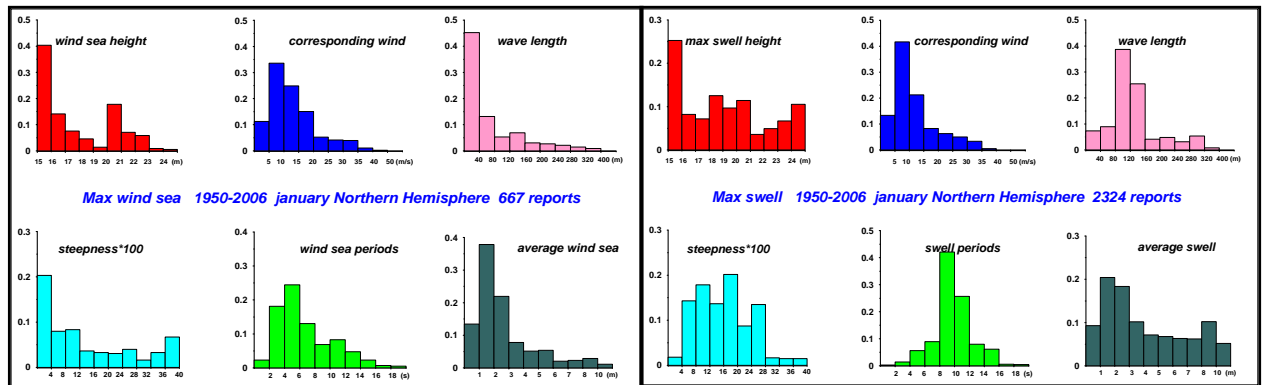


Fig.2 Occurrence histograms for the wind sea (left panel) and swell (right panel), characteristics over the Northern Hemisphere for January (1950-2006).

Preliminary results derived from the subset of all selected extreme cases show quite reliable probability distributions for the whole range of wave parameters implying that the distribution of extreme wave characteristics should now represent the tails of these distributions. Maximum wind speed changes from 5 to 10 m/s, with the wave lengths being about 40 meters for the wind sea and 80-160 m for swell (70% of total subset). Corresponding wave periods change in a wide range from 1 to 25 seconds with the peak of probability at 5 seconds for seas and at 8-10 seconds for swell. We have to note, however, that wave periods are considered to be the most uncertain parameters in VOS and their errors can reach of 30 % from average values.

Two-dimensional occurrence distributions of extreme wave cases and corresponding wind speed are presented in Figure 3. They demonstrate the bimodal structure implying 2 maxima of the occurrences at wave heights of 15-16 m and 20-21 m. Multiply analysis of coding errors nevertheless confirmed the existence of this structure. Very tentatively we can hypothesize that the first maximum is associated with the high waves originating from wind storms and the second one results from the observational artifacts or the freak waves. Analysis of the wave steepness derived from the estimates of wave heights and periods allows for the discrimination of some observational artifacts.

Usually wave steepness is defined as $\delta = H_w / \lambda = 2 * \pi * H_w / (g * P_w^2)$, where H_w is wind sea height, λ is wave length, P_w is wind sea period, g is the gravitational acceleration. According to the wave theory $\delta > 1/7$ results in increasing wave steepness and the loss of stability, forcing wave breaking. In the case of multi-system sea, however, wave height and wave length are statistical parameters computed from the wave spectra. This implies some uncertainty in this definition. For instance for some extreme cases identified in the VOS data steepness can reach unrealistic values, particularly due to uncertainties in the estimation of wave periods. For example, for $P_w = 1$ sec $\delta \approx 0.64 H_w$. Therefore, we consider this criterion to be effective enough and adopted it for the further analysis.

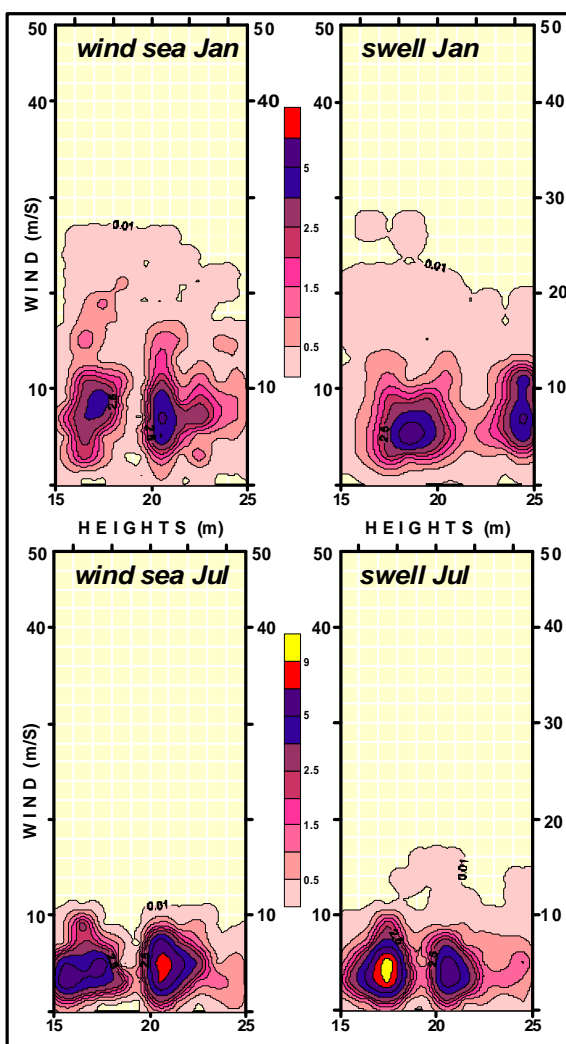


Fig.3 Two-dimensional probability distributions of the wind sea heights and wind speed for January and July over the Northern Hemisphere

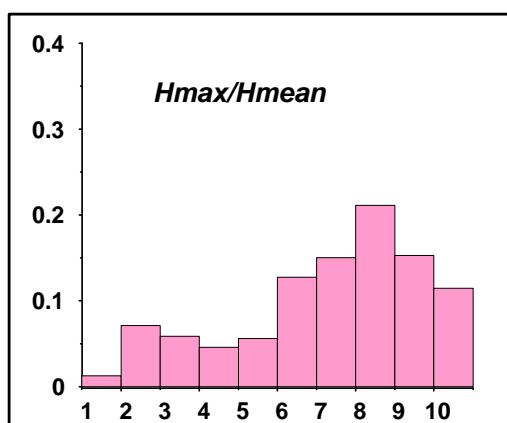


Fig. 4 Histogram of the ratio η for the Northern Hemisphere, January 1950-2006

One of the key parameters used for the detection and quantification of the rogue waves is the ratio between maximum and the averaged wave height in the record. We used this criterion, taking the average value from all observations within the radius of 100 kilometers from location of maximum. In this case we consider the ratio $\eta = H_{max}/H_{mean}$ where H_{max} is the reported extreme wave height and H_{mean} is the average over all simultaneous reports within 100 km radius. Occurrence histograms for these mean estimates are presented in Figure 4. Usually the threshold of $\eta=2$ is considered for the detection of extreme cases, the values of $\eta>4-5$ are

identified very seldom. The occurrence histogram of η (Fig.4) show that the ratio varies from 1 to 25 with the peak values of 8-9. Thus, this ratio is not effective enough for the detection of the observational artifacts and we need another criterion to check our data quality.

In the next step we performed an accurate quality control of the selected extreme wave cases. First, we selected only the reports providing information about all wave parameters (wind sea and swell heights and periods) and excluded incomplete reports which provide frequently only one wave parameter. This census resulted in the reduction of the number of reports by about 30%. Then we excluded the reports without wind speed and reports which give suspicious characteristics of the wave steepness. We used the threshold of 0.2 for wind sea steepness and of 0.15 for swell steepness. This limitation broke up to 80% reports. Finally 129 extreme wind sea cases and about 800 extreme swell cases were left for the further analysis.

The frequency distributions derived from this subset show already quite significant differences from those derived from the whole census (Fig.5). For the wind waves they show one major maximum at 15-16 m with the smaller secondary one at more than 20 meters. Remarkably the wind speed distribution is represented by the wide plateau with the modal values varying within 5-35 m/sec. However, when we consider the extreme swells, the two maxima in the distributions remain, being still centered at the same values (15-16 and 20-21 meters).

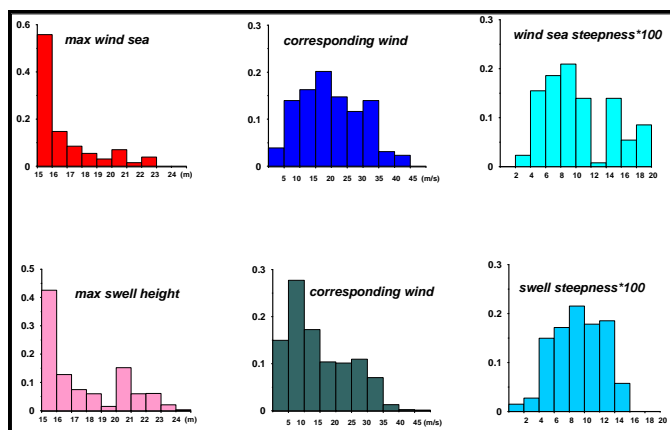


Fig.5 Occurrence histograms after the quality control for the wind sea (upper pictures) and swell (down pictures) parameters, Northern Hemisphere, January 1950-2006

In the next instance we analyzed individual cases in order to attribute extremes to the storm conditions, artifacts or freak waves. For the seas we requested that storm wind speed for all cases exceeds at least 10 m/sec and that the sea level pressure should be deeper than 1002 hPa. These requirements eliminated about 98% of all reports which can be with a high probability associated with severe storms. After that the rest consisted of few cases (e.g. 19 cases for January). They are located in the Northern hemisphere mid latitudes and few in the Atlantic tropics where then are likely associated with the tropical cyclone development. All these cases report wind waves higher than 16 meters with the highest waves (of 22 meters and more) identified in the eastern mid-latitudinal Atlantic and northeast Pacific.

The data from these reports were further analyzed with respect to the wave age [4]:

$$a = C_p / V_{ef},$$

where C_p is deep water phase speed at spectral peak, which is derived from the peak wave period P_w as

$$C_p = (g/2\pi) P_w.$$

Here g is the gravitational acceleration, $V_{ef} = V_{10} * \cos \theta$ is the component of the wind in the wave direction, θ is the angle between wave and wind directions (in 95% cases those angle are equal), V_{10} is the wind at 10 m anemometer height and neutral stability. For all extreme seas wave age $a > 1.2$. So, those reports are either observational artifacts or swell, which was reported as wind sea.

Furthermore, we performed a detailed synoptic analysis of all cases with extreme wind waves using SLP and wind speed data from the NCEP/NCAR re-analysis. Reanalysed winds and SLP also do not hint on the extremes in the VOS data. Thus, extreme heights which passed the quality control of wind waves can not be attributed to the freak waves.

Similar analysis of extreme swells is much more complicated, since swell does not depend on the local wind and, thus, local wind cannot be used as additional information for the analysis. We first limited our analysis to the cases when extreme swell is associated with wind sea height smaller than 5 meter. This is reasonable, because high wind seas of 10-15 meters are unlikely to be associated with simultaneously high swells. In other words, sailors cannot accurately identify these cases and discriminate high wind seas and high swells. Secondly, we eliminated from the analysis all cases of extreme swells identified in the marginal seas or in the regions where the fetch is short enough to provide swell growth up to extreme values. Next, for every report of extreme swell we analyzed visual swell reports in the vicinity of about 200 km from this point. We required that the neighboring swell reports should imply swells of at least higher than monthly mean values. All these procedures filtered out substantial amount of reports and left for the further analysis about 1% cases of extreme swells. In the Northern Hemisphere about 50% of extreme swell cases were identified in the North Atlantic and North Pacific mid latitudes and subtropics where they can be attributed to the propagation of the swell parcels from storms. Tropical cases can be associated with the propagating swells from the tropical cyclone systems.

For the Southern Hemisphere the number of extreme wind sea and swell cases is generally smaller than for the Northern Hemisphere (Fig.6). This can be reasonably explained by generally smaller number of observations here compared to the Northern Hemisphere. Altogether there have been identified 86 cases of extreme wind seas of which the quality control procedures left 9 cases to be further considered with confidence. For swell data we first selected 227 extreme cases of which only 7 cases were left after the critical analysis.

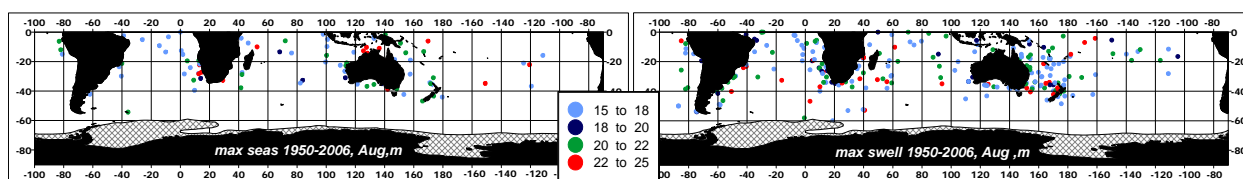


Fig.6 Extreme wind sea (left panel) and extreme swell (right panel), m, Southern Hemisphere, January, 1950-2006

The further analysis of wave age and synoptic situations revealed that all extreme wind seas in the South Ocean can be attributed to either severe storm conditions or observational errors. None of the remained 7 extreme swell reports was found to be suspicious.

This work was focused on the explanation of extreme waves in the VOS-collection. These waves do not influence the global climatology, but may play an important role in the extreme wave statistics. We tried to find signatures of the known freak events in VOS data and to show that not all 25 meter heights are the observational artifacts. The VOS collection does not include any reports to be verified with such events as the New Year Wave and the extreme wave in the south-east Africa region. Nevertheless, one report was found near the location of the catastrophe

on 15 February 1982 near the Grand Banks of Newfoundland (Lawton G.) This report fits to all our requirements. Remarkably, it reports swell with the height of 15 meters, period of 15 sec and the length of 351 m implying steepness of 0.04. The corresponding wind sea height was 5 m with the period being 6 sec.

We also analyzed wave reports over all well-known banks with specific topography and wave regime. Only the data from the Dogger Bank and Chatham rise (Fig. 7) have been accepted for analysis after the quality control. We have to stress, however, that the period reported (about 17 seconds), should be considered with caution. Although the analysis of synoptic situation shows strong gradients of sea level pressure in this location, we do believe that wind sea of 15 meters height and 9 sec period can be considered as a reliable indication of the storm in this area.

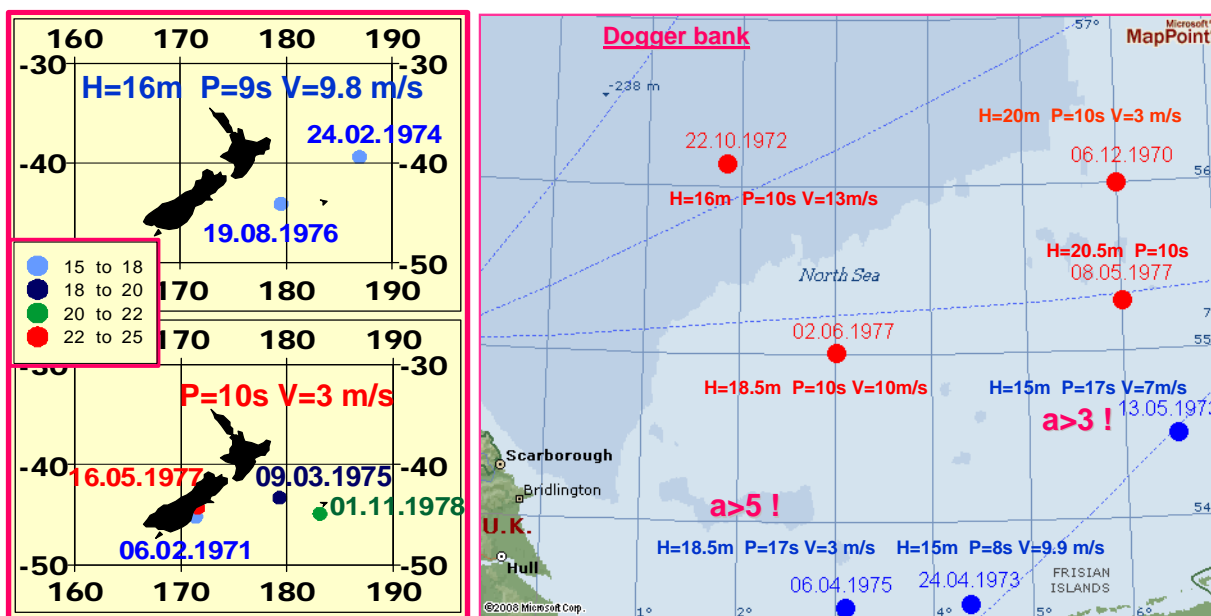


Fig. 7 Left panel: Extreme cases on the Chatham rise. Wind sea data are shown on the top and swell data are in the bottom panel. Right panel: extreme cases on the Dogger-bank. Blue color indicates wind sea, red color stands for the swell data.

Considering Chatham rise, we can conclude that extreme wind sea estimates are quite reliable for this region, although extreme swells are likely overestimated. However, we can argue that South Ocean provides conditions for long enough fetch and, therefore, hypothesize that extreme swell can also contribute to the freak events.

Our analysis of extreme wave heights in the VOS collection over the last several decades shows that VOS data when properly quality controlled and pre-processed can be capable of capturing even single extreme wave events. Among all extreme wind waves in the VOS collection about 20% can be attributed to wind wave storms and more than 80% are considered as observational artifacts. Frequency distributions of extreme wave heights clearly show maxima peaked at 15-16 meters and 20-21 meters and these maxima hold even after very strict quality control, indirectly hinting on the existence of freak events in the VOS records. At the same time we have to stress that all data reporting extreme swells are highly doubtful. However, few cases (about 1-2% of identified events) can really be considered as confirmation of extremely high swells, potentially of the freak nature.

References

1. Annenkov S., Badulin S. Multi-wave resonance and Formation of High-Amplitude Waves in the Ocean. Proceedings of a Workshop "Rogue waves". Brest, France, 2000, p.205-214.
2. Boukhanovsky A.V., Lopatoukhin L.I., Rozhkov V.A. Approaches, experience and some results of wind wave climate investigations. III. Exterme and freak waves. (in Russian) Saint-Petersburg University, 2006, volume 7,issue 1, pp. 58-70
3. Davidan I.N., Lopatoukhin L.J., Wind waves in the World ocean. Saint Petersburg (Russia): Hydromet. Publishing; 1985. 278. [In Russian].
4. Dobson, F.W., S.D.Smith, and R.J.Anderson, Measuring the relationship between wind stress and sea state in the open ocean in the Presence of swell. *Atmosphere-Ocean*, 32, 61-81, 1994.
5. Gulev, S.K., V.Grigorieva, A.Sterl, and D. Woolf, 2003: Assessment fo the reliability of wave observations from voluntary observing ships: insights from the validation of a global wind wave climatology based on voluntary observing ship data. *J. Geophys. Res. – Oceans*, 108(C7), 3236, doi:10.1029/2002JC001437
6. V.Grigorieva, S.Gulev and A.Sterl: Global climatology of wind waves based on VOS observation. *Symposium Internatiol "In route to GODAE",205-206, 2002,Biarritz*
7. Gulev, S.K., V. Grigorieva, K.M.Selemenov, and O. Zolina, 2003: Evaluation of surface winds and waves from volunatary observing ship data. *Advances in Applications of Marine Climatology*, WMO, Geneva, 53-67
8. Gulev, S.K. and V. Grigorieva, 2004: Last century changes in ocean wind wave height from global visual wave data. *Geophys. Res. Lett.*, 31, L24302, doi: 10.1029/2004GL021040
9. Gulev, S.K. and V. Grigorieva, 2006: Variability of the winter wind waves and swell in the North Atlantic and North Pacific as revealed by the Voluntary Observing Ship data, *J. Climate*, 19, p. 5667-5685
10. Lopatoukhin L.J., Rozhkov V.A., Ryabinin V.E., Swail V.R, Boukhanovsky A.V., Degtyarev A.B. Estimation of extreme wind wave heights.// World Meteorological Organisation (WMO). WMO/TD-No. 1041, 2000, JCOMM Technical Report, 71p.
11. Lopatoukhin, L.J., Boukhanovsky, A.V., 2004, "Freak Wave Generation and their Probability", *International Shipbuilding Progress*, vol. 51, no. 2/3, pp. 157-171.
12. Pelinofsky E., Kharif T., Talipova T., Damiani T. Nonlinear Wave Focusing as a Mechanism of the Freak Wave Generation in the Ocean. Proceedings of a Workshop "Rogue waves". Brest, France, 2000, p.193-204.
13. Rogue waves 2000. Proceedings of a Workshop organized by Ifremer. Brest, France. 29-30 November. 2000. 396p.
14. Woodruff, S. D., H. F. Diaz, J. D. Elms, and S. J. Worley, COADS release 2. Data and metadata enhancements for improvements of marine surface fluxfields, *Phys. Chem. Earth*, 23, 517– 526, 1998.
15. Woodruff, S. D., S. J. Worley, J. A. Arnott, H. F. Diaz, J. D. Elms, M. Jackson, S. J. Lubker, and D. E. Parker, COADS Updates and the Blend With the UK Meteorological Office Marine Data Bank, in *Achievements in Marine Climatology*, edited by V. Swail, pp. 23– 31

Examples of Unexpected High Waves in Shallow Water in Japan

Katsuya Hirayama¹, Hiroaki Kashima², and Tetsuya Hiraishi³

¹ Wave Group, Marine Env. and Eng. Dept., Port and Airport Research Institute,
3-1-1 Nagase, Yokosuka, Japan

hirayama@pari.go.jp

² Wave Group, Marine Env. and Eng. Dept., Port and Airport Research Institute,
3-1-1 Nagase, Yokosuka, Japan

kashima@pari.go.jp

³ Marine Env. and Eng. Dept., Port and Airport Research Institute,
3-1-1 Nagase, Yokosuka, Japan

hiraishi@pari.go.jp

Abstract. The examples of unexpected high waves observed in Japan are introduced and confirmed whether a freak wave was occurred or not by analyzing those datasets. The kurtosis has great relationship with the occurrence possibility of a freak wave according to a theory. It could grow up in shallow water due to nonlinear wave shoaling, but the ratio of the maximum wave height to the significant wave height was still smaller than 2. As for the occurrence of unexpected high waves in shallow water, it is more influence that swell groups banded in narrow range on frequency have beat in their profile and can be concentrated due to refraction and shoaling in relatively deeper water.

1 Introduction

Many Japanese harbors are directly facing to the Pacific Ocean or the Japan Sea where both high wind waves and long swells are sometime occurred due to heavy storms. The breakwaters and seawalls have been designed to prepare such some expected high waves attacking. However, some severe coastal disasters have occurred in these days due to unexpected high waves (Fig. 1). The common characteristics of them are that their periods are relatively long.

These long swells grow up under the typhoons in the Pacific Ocean or the winter storms in the Japan Sea. Fortunately, these were observed by the NOWPHAS, that is, Nationwide Ocean Wave information network for Ports and HARbourS (Fig. 2). For examples, the 14.2s swell was observed in Fushikitoyama port facing to the Japan Sea when the breakwater and the seawall were severe damaged on February in 2008, the 14.2s swell was also observed along the Shonan coast facing to the Pacific Ocean when the seawalls were broken down on September in 2007, and the 14.5s swell was observed in Kuji port facing to the Pacific Ocean when the big parapets on the revetment were moved on September in 2006.

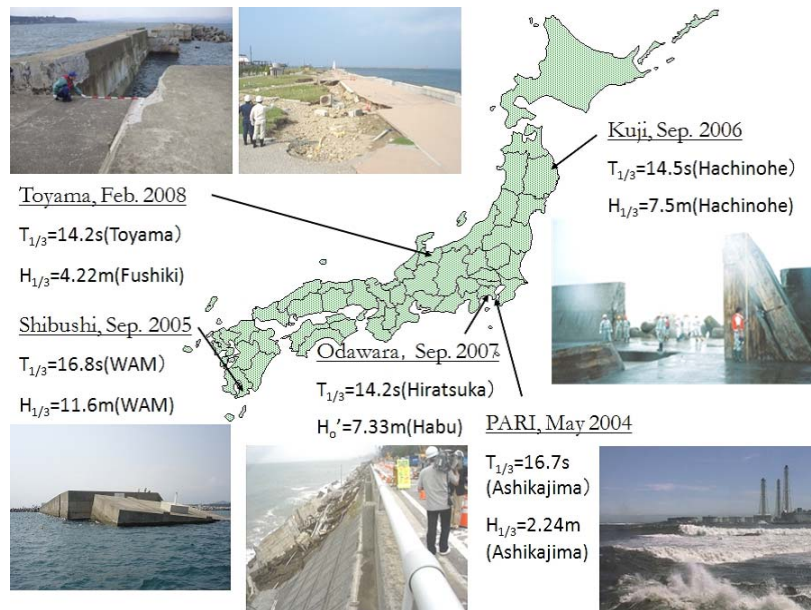
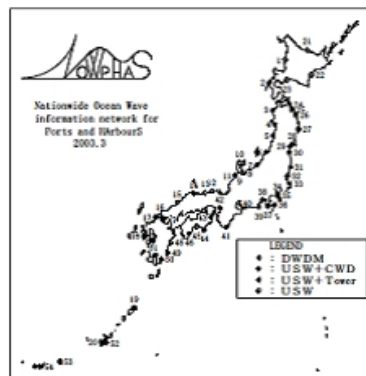


Fig. 1. Examples of coastal disaster in Japan



(a) NOWPHAS Network



(b) DWDM Seabed Installed Sensor

Fig. 2. Nationwide Ocean Wave information network for Ports and Harbours

The linear wave transformations including the refraction and the diffraction are mainly evaluated in the harbor design so far. However the nonlinearity of wave shoaling is also important in shallow water especially for long waves because their relative water depth is shallower than short waves. In addition, swell groups banded in narrow range on frequency have beat in their profile and can be also concentrated due to refraction in relatively deeper water. Moreover it could be supposed that the interaction between waves and currents also generate high waves in the fields where incident waves collide with river currents or tidal flows, but this phenomenon is not mentioned in this paper.

The examples of the unexpected high waves observed in Japan are introduced and they are confirmed whether a freak wave was observed or not by analyzing those datasets. In Sect. 2 the definition of the freak wave is reviewed and the theory on the occurrence probability of a freak wave proposed by Mori and Janssen ([1], [2], [3], [4], [5]) is verified by carrying out some tests in a basin. In Sect. 3 the shallow water effects are discussed. The unexpected wave appeared in Kurihama bay is introduced and the characteristics of the observed wave train are investigated with some parameters. And Fushikitoyama port which suffers from the long swell locally called "YORIMAWARI-NAMI" is picked up and the occurrence probability of a freak wave in shallow water is discussed by using a Boussinesq-type wave transformation model. Finally, the conclusions are made in Sect. 4.

2 Theory of Freak Waves and Its Verification

It has been already well-known that a freak wave can be occurred both linear and nonlinear focusing in deep water (ex. [6], [7], [8]). The definition of the freak wave is that the maximum wave height; H_{\max} is greater than 2 times of the significant wave height; H_s in wave train.

$$H_{\max}/H_s > 2 \quad (1)$$

2.1 Occurrence Probability of Freak Wave

It has been suggested that four-wave interactions enhance the occurrence probability of a freak wave ([9]). Moreover, Mori and Janssen have suggested that quasi-resonant four-wave interactions may influence the statistical properties of deep water surface gravity waves such as a freak wave, and the kurtosis and *BFI* (Benjamin-Feir Index) are index of nonlinear focusing of the freak wave generation.

$$P_{freak} = 1 - \exp [-N e^{-8} \{1 + (\mu_4 - 3)\}] \quad (2)$$

where P_{freak} is the occurrence probability of a freak wave, N is the number of waves, and μ_4 is the kurtosis.

Thus, the occurrence probability of a freak wave can be expected by analyzing the datasets obtained in field observations, model experiments, or numerical

simulations. Now, some verifications of the theory are carried out in our experimental basin.

2.2 Verification by Generation in Experimental basin

Firstly the uni-directional wave trains were generated in the flume which has the length of 35m, the width of 0.6m, and the depth of 1.3m. The wave maker can generate irregular waves with absorbing the reflected waves, and the wave absorbing structure installed at the opposite side can control the reflection coefficients in less than 0.1 against 1.0s period waves in deep water.

Fig. 3 shows the variations of the kurtosis measured through the direction of wave train propagation, as the wave train generated in condition that $H/L=0.04$ and $\gamma=1, 3.3, 10$. Here, γ is the peak amplified ratio of JONSWAP spectrum and x is the distance from the wave maker. It is confirmed that the kurtosis of the wave trains can grow up in propagation as γ is greater than 3.3 (normally $\mu_4=3.0$ with Gaussian distribution). Hence, the occurrence probability of a freak wave increases in case that the spectrum banded in narrow range on frequency (such a swell's spectrum) propagates in enough distance in deep water.

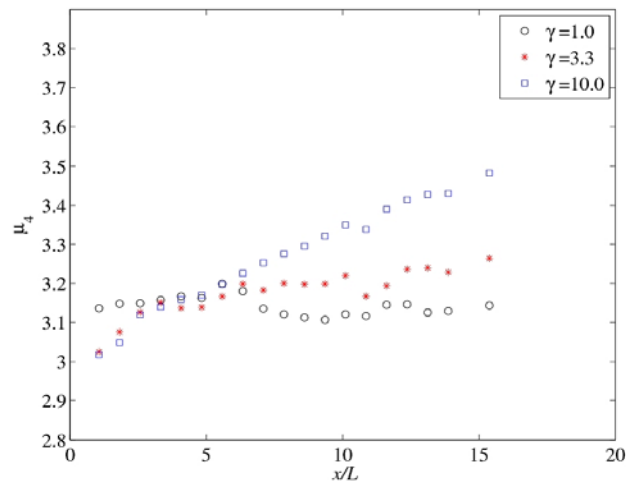


Fig. 3. Variation of the kurtosis with propagating in deep water. ($T=1s$, $H/L=0.04$)

By the way, the directional effects on the generation of a freak wave are investigated by model experiments (ex. [10]) and numerical simulations (ex. [11], [12]). According to them, the kurtosis of a wave train decreases as their directionality increased.

Then, secondary the multi-directional waves train were generated in the basin which has the length of 42m, the width of 18m, and the depth of 1.3m. The wave maker can generate multi-directional irregular waves with absorbing the oblique

reflected waves, and the wave absorbing structures installed around the basin can control the reflection coefficients in less than 0.2 against 1.0s period waves in deep water. The layout of them with the installation of wave gauges is shown in Fig. 4. And the generated wave conditions are listed in Table. 1. Fig. 5(a)

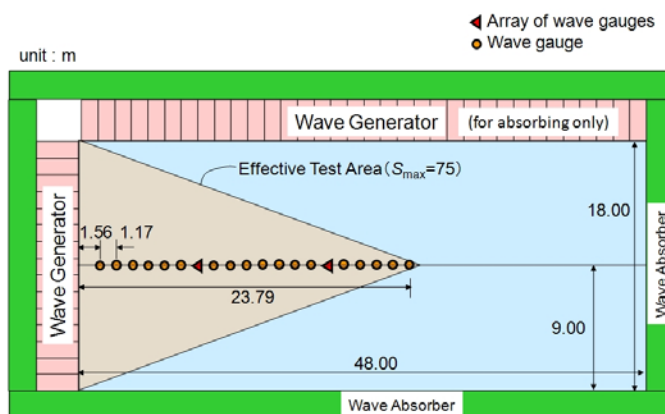


Fig. 4. Layout of the wave maker, wave absorbing structures and wave gauges

Table 1. Generated wave conditions ($T=1s$)

case	S_{max}	h (m)	γ	H/L	comments
1	999	0.8	10	0.04	uni-direction
2	150	0.8	10	0.04	multi-direction
3	75	0.8	10	0.04	multi-direction

shows the variation of the kurtosis and Fig. 5(b) shows the variation of the ratio of H_{max} to H_s , measured through the principal direction of wave train propagation against each number of waves as $S_{max}=999$ (uni-direction). Here, S_{max} is the parameter of directional spreading and y is the distance from the wave maker. In the same way, the variations of the kurtosis and the ratio of H_{max} to H_s are shown in Fig. 6 as $S_{max}=150$, and Fig. 7 as $S_{max}=75$.

Though the wave generated as $S_{max}=999$ in the basin is same to the wave generated as $\gamma=10$ in the flume, these results are not corresponding. The reason is considered that the reflected waves might exist in the basin because the wave absorbing structures did not enough work due to relatively short thickness. However, the variation of the kurtosis still increases through the propagating direction (Fig. 5(a)) and the ratio of H_{max} to H_s also increases through the propagating direction and with the greater number of waves (Fig. 5(b)).

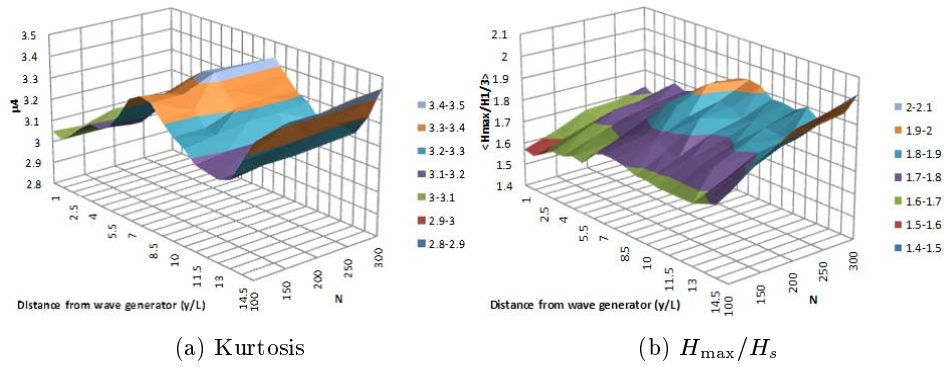


Fig. 5. variations of the kurtosis and ratio of H_{max} to H_s as $S_{max}=999$

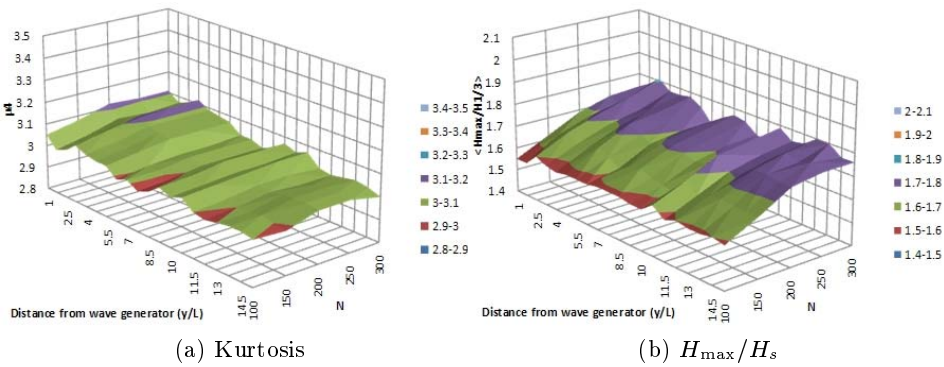


Fig. 6. variations of the kurtosis and ratio of H_{max} to H_s as $S_{max}=150$

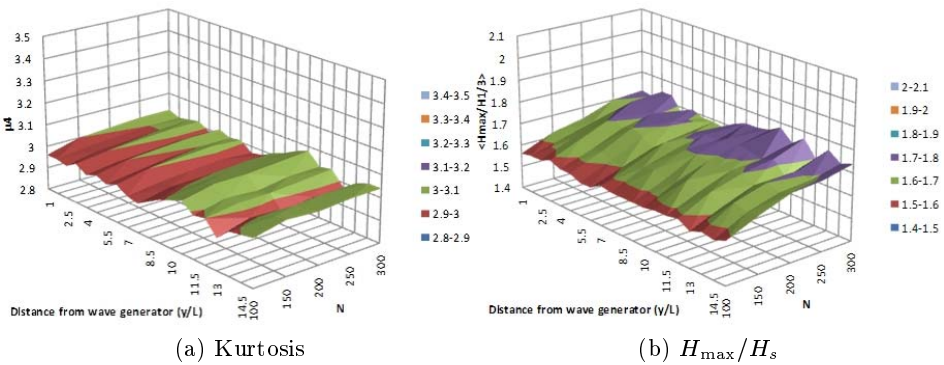


Fig. 7. variations of the kurtosis and ratio of H_{max} to H_s as $S_{max}=75$

In case that $S_{\max}=150$ and $S_{\max}=75$, the variations of both the kurtosis and the ratio of H_{\max} to H_s are almost constant through the principal propagating direction as shown in Fig. 6 and Fig. 7. On the other hand, the ratios of H_{\max} to H_s grow up with the greater number of waves in the range of the Rayleigh distribution. Hence, it is confirmed that both the kurtosis and the occurrence probability of a freak wave on the wave trains decreases as their directionality increased.

3 Shallow water effects on freak waves

The shallow water effects on freak waves are discussed by Onorato and Janssen ([13]). Then, this paper makes another approach to them with both the several field observations shown in Fig. 1 and the numerical simulations using a weak nonlinear wave transformation model.

3.1 Swell Grouping Observed in Shallow water

At the Kurihama bay facing to the mouth of Tokyo bay, it was observed that the wave group of swell whose significant period was 16.7s were suddenly shoaling and breaking in shallow water. They were observed at Ashikajima station in NOWPHAS and watched from the coast.

Fig. 8 shows the overviews of propagation of swell wave and the wave train observed at Ashikajima station (on the depth of 20m). This is understood that the calm sea surface appeared at the node of wave profile and the severe sea surface appeared at the beat. Such a case looks like the high waves suddenly occurred in shallow water. However, the ratio of H_{\max} to H_s obtained by an-

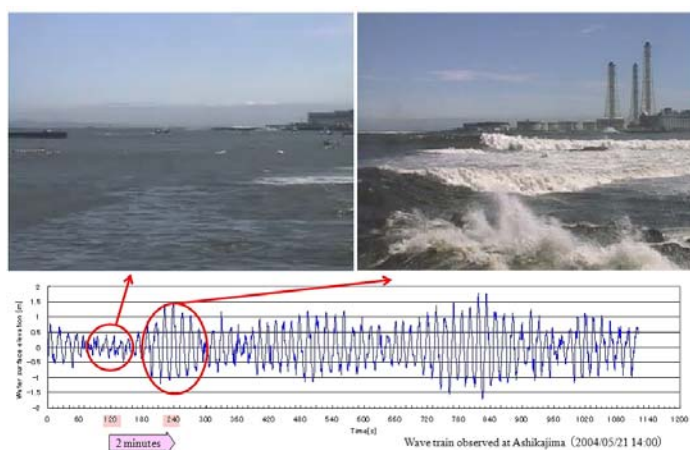


Fig. 8. Observed swell group in Kurihama bay

alyzing this dataset was still smaller than 2 and the value of kurtosis was also normal (around 3), though the profile of the spectrum was very sharp (which corresponds to the JONSWAP spec-trum with $\gamma=10$). Then, it can be judged that these observed high waves are not a freak wave.

By the way, that wave train should be observed 1-2 hours before at Habu station (on the depth of 50m) where located in offshore of Tokyo bay. The directional and frequency spectra observed around that time are shown in Fig. 9. These figures indicate that the directionality of the observed swell reduces the occurrence probability of a freak wave though the profile of the spectrum is also very sharp.

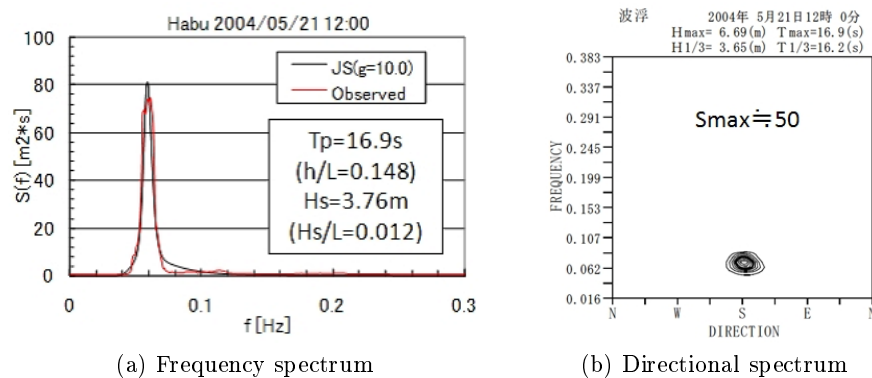


Fig. 9. Observed directional and frequency spectra in Habu station

3.2 Wave Concentration due to Bathymetry

Both the breakwater and the seawall in Fushikitoyama port were damaged by the swell whose period was 14.2s and height was 4.42m. This wave train propagated from Northern East with growing up through the long fetch in the Japan Sea. The Toyama bay in front of Fushikitoyama port has much complicated bathymetry that a lot of deep valleys penetrate to the coastal line (Fig. 10(a)). The swell can be refracted and shored on such relatively deeper shoals between the valleys. Then, the reproduction of wave transformation is carried out by using the Boussinesq-type wave transformation model produced by Hirayama ([14]), assuming the incident wave spectrum as JONSWAP with $\gamma=10$ and the offshore water depth as 150m constant which is almost deep water for the incident wave (Fig. 10(b), (c)). These calculations are carried out with or without considering the breakwater in order to verify the influences due to the reflected waves. Fig. 10(b) shows that the significant wave height is partially concentrated in front of the damaged breakwater and seawall due to wave refraction and shoal-

ing on the deeper capes. Moreover, the concentration of wave height appears more clearly as shown in Fig. 10(c) because of the reflected waves superposing.

Fig. 11 shows the variations of significant wave height; H_s , the kurtosis; μ_4 , and the ratio of H_{max} to H_s through the Line-2 which defined in Fig. 10(a). Fig. 11(a) shows that the kurtosis increases with the significant wave height increasing, but the ratio of H_{max} to H_s is almost constant in shallow water though it increases in deep water. Hence, a freak wave is also not occurred in this case. On the other hand, it is difficult to verify the occurrence of a freak wave in Fig. 11(b) because the reflected waves are disturbing the variations of these parameters.

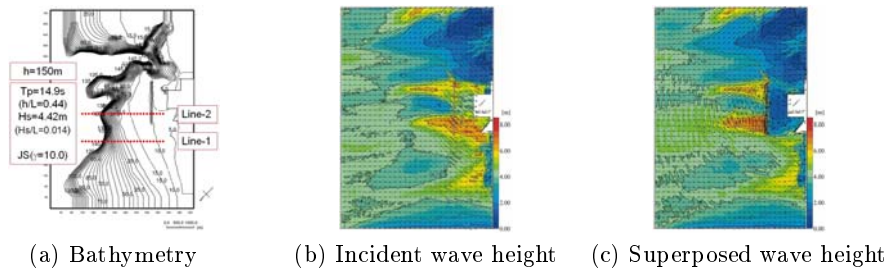


Fig. 10. Swell transformation on complicated bathymetry in Fushikitoyama port

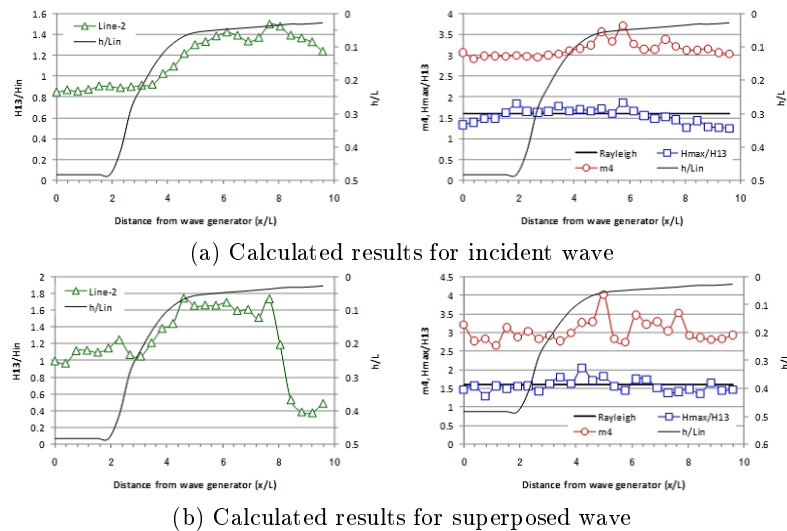


Fig. 11. Variations of significant height; H_s , kurtosis; μ_4 , and H_{max}/H_s through Line-2

4 Conclusions

The occurrences of a freak wave are verified by comparing the statistical properties obtained in field observations and numerical simulations in shallow water with the theory. The freak wave seems to not occur in these cases because the shallow water effects reduce the kurtosis enhanced by four-wave interactions though the refraction and shoaling increase the kurtosis enhanced by weak non-linearity, and the reflected waves disturb the variations of the kurtosis and the ratio of H_{\max} to H_s .

References

1. Mori, N. and P. Janssen: Freak wave and nonlinear wave interaction, Annual Journal of Coastal Engineering, JSCE, Vol.52 (2005) pp.131-135 (in Japanese).
2. Mori, N. and P. Janssen: On kurtosis and occurrence probability of freak waves, Journal of Physical Oceanography, 36, 7, (2006) pp.1471-1483.
3. Mori, N., M. Onorato, and P. Janssen: Freak Wave Prediction and its Validity, Annual Journal of Coastal Engineering, JSCE, Vol.53 (2006b) pp.306-310 (in Japanese).
4. Mori, N., P. Janssen, and M. Onorato: Directional Effects on Freak Wave Prediction, Annual Journal of Coastal Engineering, JSCE, Vol.54 (2007) pp.96-100 (in Japanese).
5. Mori, N., P. Janssen, and K. Kawaguchi: Developing freak wave prediction model with directional effects and its validation, Annual Journal of Coastal Engineering, JSCE, Vol.55 (2008) pp.111-115 (in Japanese).
6. Yasuda, T., N. Mori and K. Ito: Freak waves in a unidirectional wave train and their kinematics, Proc. of the 23th Int. Conf. on Coastal Eng., Vol.1, ASCE, Venice (1992) pp.751-764.
7. Onorato, M., A. R. Osborne, M. Serio, and S. Bertone: Freak waves in random oceanic sea states, Physical Review Letter, 86 (2001) pp.5831-5834.
8. Trulsen, K. and K. Dysthe: Freak waves-A three-dimensional wave simulation. In Proceedings of the 21st Symposium on Naval Hydrodynamics, (1997) pp.550-558.
9. Janssen, P.: Nonlinear four-wave interactions and freak waves, Journal of Physical Oceanography, 33, 4 (2003) pp.863-884.
10. Waseda, T.: Impact of directionality on the extreme wave occurrence in a discrete random wave system, In 9th International Workshop on Wave Hindcasting and Forecasting Sep.24-29, Victoria, Canada, 2006.
11. Dysthe, K., K. Trulsen, H. Krogstad, and H. Socquet-juglard: Evolution of a narrow-band spectrum of random surface gravity waves, The Journal of Fluid Mechanics, vol. 478 (2003) pp. 1-10.
12. Gramstad, O and K. Trulsen: Influence of crest and group length on the occurrence of freak waves, The Journal of Fluid Mechanics, vol. 582 (2007) pp. 463-472.
13. Janssen, P and M. Onorato: The Intermediate Water Depth Limit of the Zakharov Equation and Consequences for Wave Prediction, Journal of Physical Oceanography, 37, 10 (2007) pp.2389-2400.
14. Hirayama, K.: Utilization of numerical simulation on nonlinear irregular wave for port and harbor design, Technical Note of The Port and Airport Research Institute, No.1036, (2002), 162p.

Freak Waves during a Typhoon

Paul C. Liu¹, Dong-Jiing Doong², Hsuan S. Chen³,
Chia Chuen Kao⁴, and Yueh-Jiuan G. Hsu⁵

¹ NOAA Great Lakes Environmental Research Laboratory, Ann Arbor, Michigan, USA

² National Taiwan Ocean University, Keelung, Taiwan

³ NOAA National Centers for Environmental Prediction, Camp Spring, Maryland, USA

⁴ National Cheng Kung University, Tainan, Taiwan

⁵ Marine Meteorology Center, Central Weather Bureau, Taipei, Taiwan

Abstract: *This paper presents a search for freak waves from wave measurement data made in the northeastern coastal water of Taiwan during Typhoon Krosa, October 2007. Not knowing what to expect, we found rather astonishingly that there were more freak wave types during the build-up of the storm than we ever anticipated. We also developed an empirical wave grouping approach to identify freak waves from time series wave data, as the conventional approach of defining freak waves as $H_{max}/H_s > 2$ is ineffective to discern all the conspicuous cases.*

Introduction

Freak (freak or rogue) waves were first recognized by Draper (1964) nearly four and one-half decades ago. But it has only been in recent years that the concept of and term freak (freak or rogue) wave has become common in the media and has been mentioned frequently as a possible cause in a plethora of relevant, semi-relevant, or even irrelevant events. For the ocean wave studies, however, freak waves remain under-explored beyond a number of theoretical as well as empirical conjectures. We still do not really know where, when, why, and how freak waves occur in nature. As in many severe storm cases where freak waves were implicated, we do not even know how to differentiate between a freak wave and a storm generated wave, or if they can exist simultaneously.

In one of the most tragic shipping disasters, the loss of the bulk carrier *MV Derbyshire* during Typhoon Orchid in September 9, 1980 in Western Pacific south of Japan, all hands (42 crew and two wives) on board perished. There were two official investigations into the possible cause. Perhaps Faulkner (2000) summarized the findings of all those investigations best by his postulate that “a steep elevated abnormal wave probably collapsed the forward hatch covers during Typhoon Orchid.” As one of the appointed assessors who examined all possible loss scenarios along with available underwater survey of the wreckage and laboratory experiments, Faulkner’s finding is certainly irrefutable. The postulate of the cause of a steep abnormal wave, however, while entirely conceivable will remain to be a speculative conjecture unless actual measurement or veracious evidence can be manifested.

There are also other similar disasters in the later part of 20th Century, for instance, the sinking of the *SS Edmund Fitzgerald* during a gale storm in eastern Lake Superior on November 10, 1975 with 29 crew members onboard (NTSB, 1978); and the wreck of the semi-submersible, offshore rig *Ocean Ranger* during a storm linked to a major Atlantic

cyclone while drilling in the Grand Banks area on the North American continental shelf on February 15, 1982 with 84 crew members onboard (Royal Commission, 1984). In both cases they seemed to have happened suddenly, there were no survivors, and thus there is speculation that they were overwhelmed by the force of a freak wave.

Are there freak waves during a hurricane, typhoon, or severe storm? In this paper we expect to answer this question by using wave measurements made in the northeastern coastal waters of Taiwan during the Typhoon Krosa in October 2007.

The Typhoon Krosa

In the early days of October 2007, a tropical depression that originated east of the Philippines in the Western Pacific Ocean, rapidly intensified to become Typhoon Krosa. It was later upgraded to a Category 4-equivalent super typhoon as it advanced northwestward toward Taiwan. Its track momentarily hovered and made a small loop back out to sea over the northeastern coastal waters of Taiwan before making landfall on October 6, 2007 (Figure 1). There were several moored buoys deployed around Taiwan where wave conditions during Krosa were summarily recorded. In particular, the buoy located at longitude $121^{\circ}55'30''\text{E}$ and latitude $24^{\circ}50'57''\text{N}$ in 38 m water depth recorded a very large trough to crest maximum wave height of 32.3 m, which could be the highest known H_{\max} ever recorded (Liu, et al. 2008). The buoy was located near the small Gueishantao Island (Figure 5), 12 km offshore of the northeast coast town of Suao, which was located close to the center of Krosa.

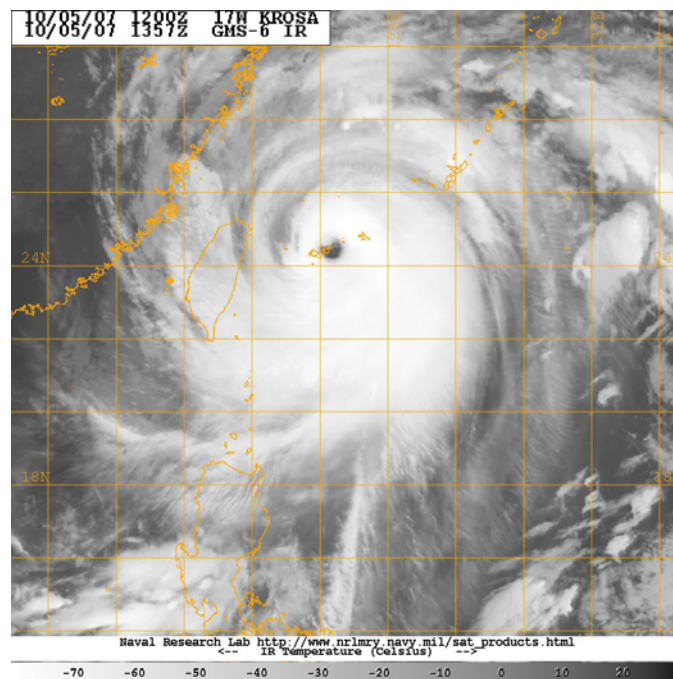


Figure 1. Typhoon Krosa approaching Taiwan.

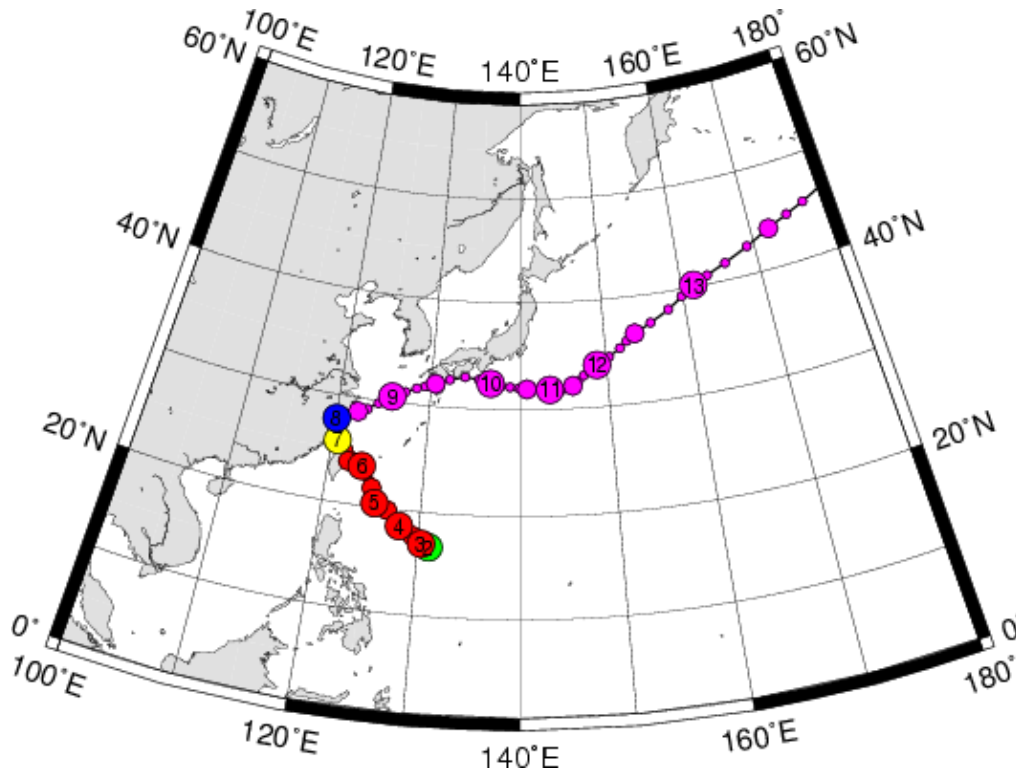


Figure 2. The track of Typhoon Krosa. The colored circles show the strength and location of the typhoon center. The number inside represents the date of occurrence. (Color code: Magenta : Extratropical Cyclone; Blue : Tropical Depression; Green : Tropical Storm; Yellow : Severe Tropical Storm; Red : Typhoon.)

Figure 2 gives the detailed track and the corresponding central pressure record of the Typhoon Krosa as given in the web site <http://agora.ex.nii.ac.jp/digital-typhoon/summary/wnp/s/200715.html.en>. It is shown that Krosa followed a fairly steady northwestern path toward northeast Taiwan, while the central pressure deepened as wind intensity gradually strengthened to 70 m/s (140 kt) just before making landfall on October 6, 2007.

The wave measurement

The Central Weather Bureau (CWB) of Taiwan has been constantly developing, deploying, and maintaining moored 2.5 meter circular discus hull foam buoys (Figure 3) in the coastal waters around Taiwan Island for meteorological and marine measurements including ocean wave measurement since 1997. The buoys were designed for reliable operations, with wave following characteristics, and are lightweight for convenient and safe land and sea transportability. Currently there are nine buoys in operation, all are equipped with heave, pitch, and roll accelerometers sampled at 2 Hz frequency for 10 minutes duration each hour. In this paper we are concentrating on the one buoy located at longitude 121°55'30"E, and latitude 24°50'57"N in 38 m water depth in the lee of the small offshore Gueishantao Island (Figure 4). The buoy is located 12 km offshore of the

northeast coast of Taiwan, which was closest to the center path of Typhoon Krosa prior to its landfall. The wave conditions during the onward movement of Krosa at this buoy location, as represented by the ocean surface fluctuations inferred from the recorded heave displacements, are used in this paper in search of possible occurrences of freak waves during the passage of the typhoon.



Figure 3. A deployed CWB Buoy.



Figure 4. The buoy location near Gueishantao off the northeast coast of Taiwan.

The portrait of a freaque wave

What are freaque waves and how do we identify them? These seemingly, simple-minded questions are still lacking unified, clear-cut answers. Currently, information is limited to descriptions of the waves at best. It is usually described or displayed as one singular, unexpected wave profile characterized by an extraordinarily large and steep trough or crest over the others in the field. Freaque waves were not being regarded as part of the ocean wave process during most of the second half of the 20th Century, while vigorous growth in ocean wind wave research endeavors were flourishing. All the currently available wave measurements, as well as the conventional wave measurement systems, have been based on and primarily designed for ocean waves that are presumed to be from a stationary Gaussian random process that basically negates the existence of the kind of freaque waves we are considering. But that does not necessarily mean freaque waves have never been measured. The well-known North Sea freaque wave records of Gorm field (Sand et al., 1990) and Draupner platform (Haver, 2004) were both discovered from conventional wave measurements. The wave profile from the Draupner platform, as shown in the upper left panel of Figure 5, has been widely recognized and generally identified as the exemplary depiction of a freaque wave. Since it is also generally construed that freaque waves can happen any time and in any part of the world's oceans, there must be more Gorm/Draupner-like freaque waves being recorded but that simply have not been discovered or noticed.

The time series plot of the ocean surface fluctuation shown in the upper left panel of Figure 5 is widely considered as the portrait of a freaque wave, also known as the Draupner freaque wave. We see that it clearly does not fit the conventional conceptualization that expects the ocean surface as a Gaussian random process. This is shown by the discord in the cumulative distribution between the Gaussian process and the Draupner data on the upper right panel of Figure 5, especially at the high end. In contrast, measurement at the same sensor one hour later, as shown in the two bottom panels, displays a more customary time series plot and a nearly accordant Gaussian cumulative distribution.

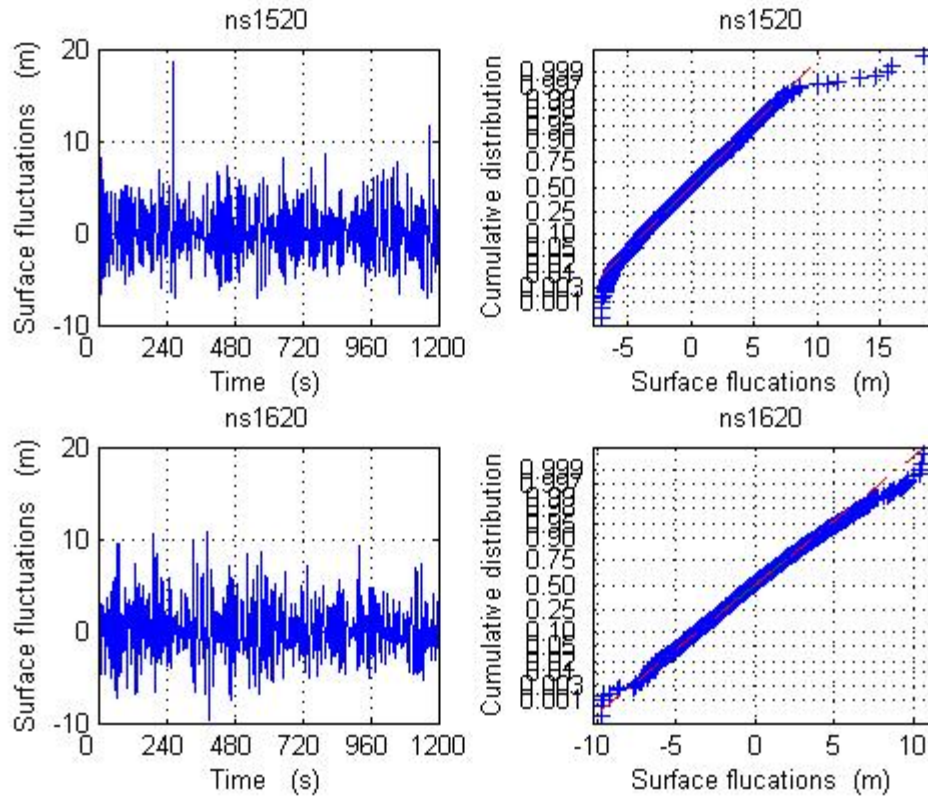


Figure 5. Two wave data recorded on January 1, 1995 at Draupner platform. The upper left panel is considered to be the standard portrait of a freak wave.

As the discovery and recognition of the Draupner freak wave time series shown above was basically through visual means, other generally objective approaches of recognizing freak waves have also been employed. One frequently used approach is to examine the ratio H_{\max} / H_s , the maximum wave height, H_{\max} in the time series to the significant wave height, H_s , which we feel should be more appropriately called the standard deviation wave height since it is given by $4 \times$ standard deviation in the data. For the Gaussian random process, the zero-upcrossing or zero-downcrossing wave heights usually follow a Rayleigh distribution where statistically H_{\max} should be at most twice the H_s , thus it is frequently thought that cases with $H_{\max} / H_s > 2$ are freak waves. One of the well-known equations that correlates H_{\max} / H_s with the number of zero-upcrossing or zero-downcrossing waves needed in the data for it to occur is

$$H_{\max} / H_s = [\ln(N)/2]^{1/2} \quad (1)$$

where N is the number of waves encountered in the data.

Another minor approach that has only been used for reference purposes is to check into the kurtosis of the data set. The kurtosis for a perfect Gaussian process is 3. Larger kurtosis values signify a greater departure from Gaussian. As shown in Figure 6, the Draupner freak wave has a kurtosis of 4.0648, but an hour later, without the freak wave, the kurtosis is 3.2842.

In search of freaque waves during Krosa

We started by visually examining the wave time series data recorded at Gueishantao buoy during the build up of Typhoon Krosa prior to landfall on Taiwan, October 3 – 6, 2007. We looked at each data set during this period for Draupner-like cases and are rather astonished to have found more cases than we ever expected. The results are shown in Figure 6 where the vertical red bars denote the cases that were visually recognized cases, and two samples of the Draupner-like freaque wave time series plots and their corresponding test of Gaussian probability distributions, similar to Figure 5, are shown in the Figure 7.

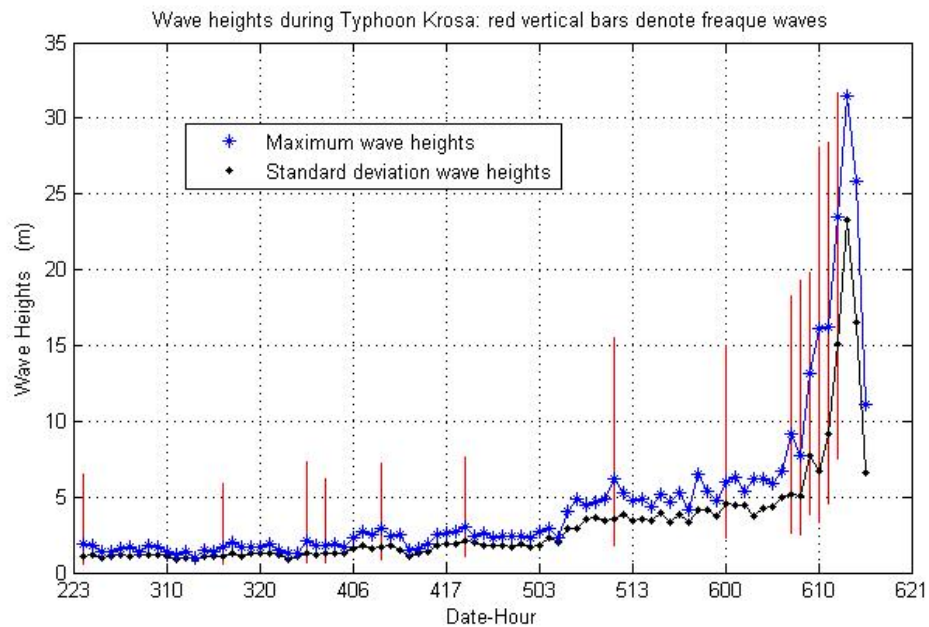


Figure 6. Time history of wave heights during Typhoon Krosa. For the three digit numbers on the abscissa, the first number is the day of October and the next two digits give the corresponding hour. The red vertical bars denote where freaque waves might have occurred.

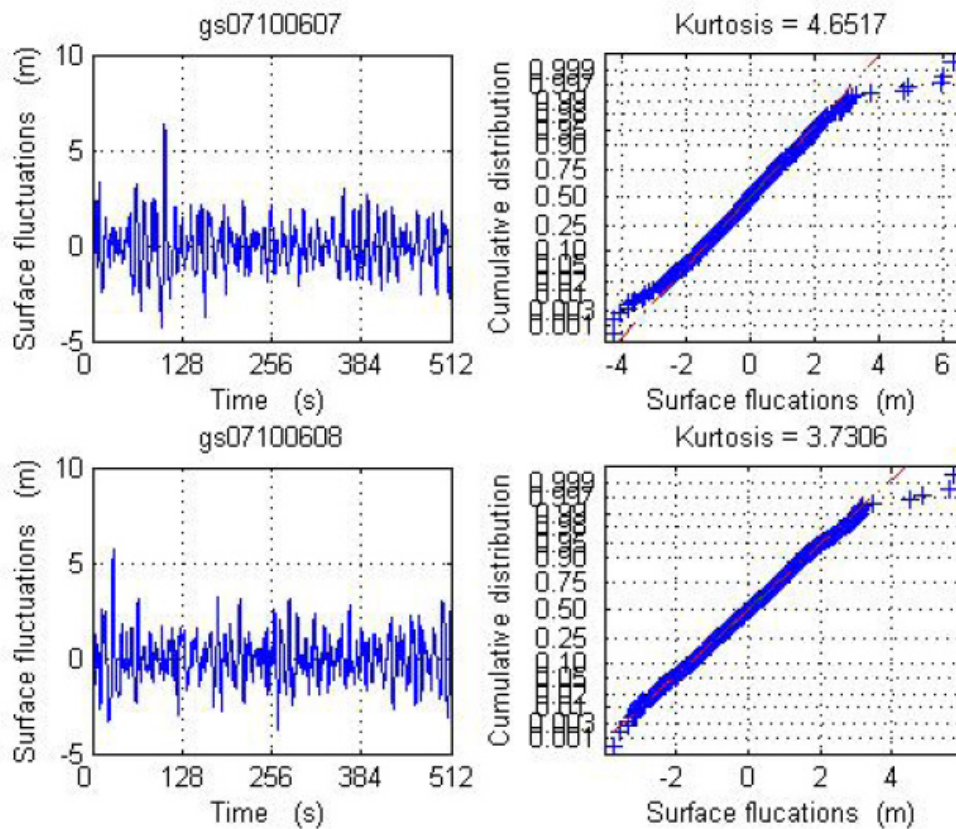


Figure 7. Two samples of Draupner-like freak wave cases found during Typhoon Krosa.

This part of the exercise is necessarily intuitive and subjective. Not all cases are as dramatically pronounced as the Draupner case. They are, in our visualization, at least potential freak wave cases. With a few exceptions, their corresponding kurtosis and their departure from Gaussian distribution tend to sustain our subjective visual choice. Clearly visual picks tend to find more cases than the conventional indicators. But who is in position to quibble which one really is or is not a true freak wave when we don't even have a tangible definition for it yet?

Circumscribing freak wave cases

We proceed next to examine conventional approaches to circumscribe freak waves. As alluded earlier the widely used approach is the use of the ratio of maximum wave height versus significant wave height in a given time series wave data. Based on the assumption of Gaussian and Rayleigh distribution theories, a ratio larger than 2 is generally regarded as possibly a freak wave case. However, some ambiguity is implicated with this approach. One is that the size of time series data has never been specified. Different time length of data invariably leads to different results. The other is that the significant wave height, usually defined as the average of the highest one third wave heights in the data, has been mostly represented by four times the standard deviation in the data – again

a result of the assumption of Gaussian and Rayleigh distributions. The significant wave height, $H_{1/3}$, and the standard deviation wave height, H_s , are not always the same as we see in Figure 8 here. The North Sea data, represented by the points labeled as ns1520 and ns1620, show that H_{\max}/H_s and $H_{\max}/H_{1/3}$ are basically close. But the Gueishantao data show that H_{\max}/H_s tend to underestimate $H_{\max}/H_{1/3}$ by about 15 percent. This is possibly because The Draupner platform is in the deep North Sea, whereas Gueishantao buoy is more in the nearshore area which could be affected by shoaling effects. As a result, we see that there are 3 cases of H_{\max}/H_s greater than 2, whereas 6 cases of $H_{\max}/H_{1/3}$ greater than 2. But our visually picked freaque wave cases seem to be indifference to the demarcation nevertheless, as there are plenty of cases show freaque wave occurrences with either ratios below 2 as shown by the data points of freaque wave cases enclosed by red circle in Figure 8.

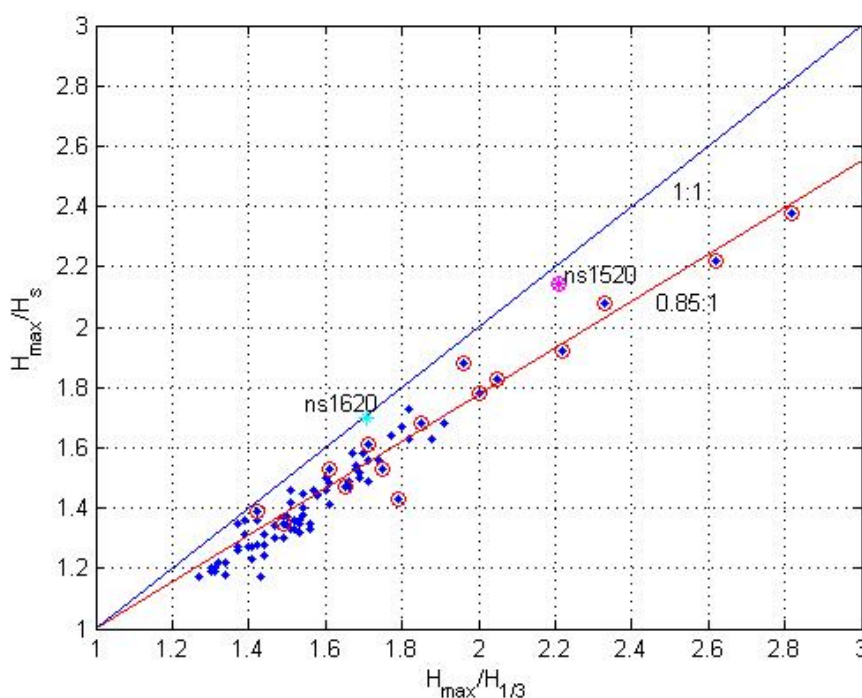


Figure 8. Correlation of the ratios of H_{\max}/H_s with $H_{\max}/H_{1/3}$. The blue line represents the 1:1 perfect fit. The red line is a best eyeball fit, 0.85:1 in this case. The points with a red circle around are the visually picked freaque wave cases.

We have also examined the data in connection with equation (1) discussed earlier that shown the theoretical relation between the ratio of wave heights and the number of trough-to-crest wave heights in the data. It is of interest and may even be comforting to note that the measured data fit the theoretical relation reasonably well for the most part. With one or two exceptions most of the identified freaque wave cases are clearly not part of the theoretical curve as expected. It is encouraging to see that while Gaussian and Rayleigh distributions can be useful in general but they are just not capable of representing cases when freaque waves are present. Furthermore, we found when $H_{1/3}$ and H_s are not comparable, $H_{1/3}$, rather than H_s , should be used in the analysis.

A new freaque index

To further devise a viable approach to justify our subjective visual identification of freaque waves from the available data, we constructed a simple new empirical freaque wave index based on examining groupings of 18 consecutive waves. This is a purely empirical venture, we have not yet been able to put it in analytical form. The idea stems from the popularly fabled notion that every 7th wave is the highest. We generalize it into the consideration of a group of 18 consecutive wave heights. Clearly a freaque wave, being considered as unusually larger than those in its proximity both in time and space, should be rising up from one of these groups. Thus for every 1024 data point time series in the Typhoon Krosa wave data set, we looked at every group of 18 consecutive zero-crossing wave heights in the time series, and calculated the ratio of maximum to mean wave heights among them in each group. The highest of all these calculated ratios is the *group index for 18 waves* in that time series. The results are presented in Figure 10. It was through intuition and trial and error that led us to the size of 18 waves and a demarcation of 2.95, plotted as the middle red line in Figure 9, as best substantiated our visual picks. As shown in Figure 9 it is likely any time series data with a freaque index over 2.95 will contain a freaque wave.

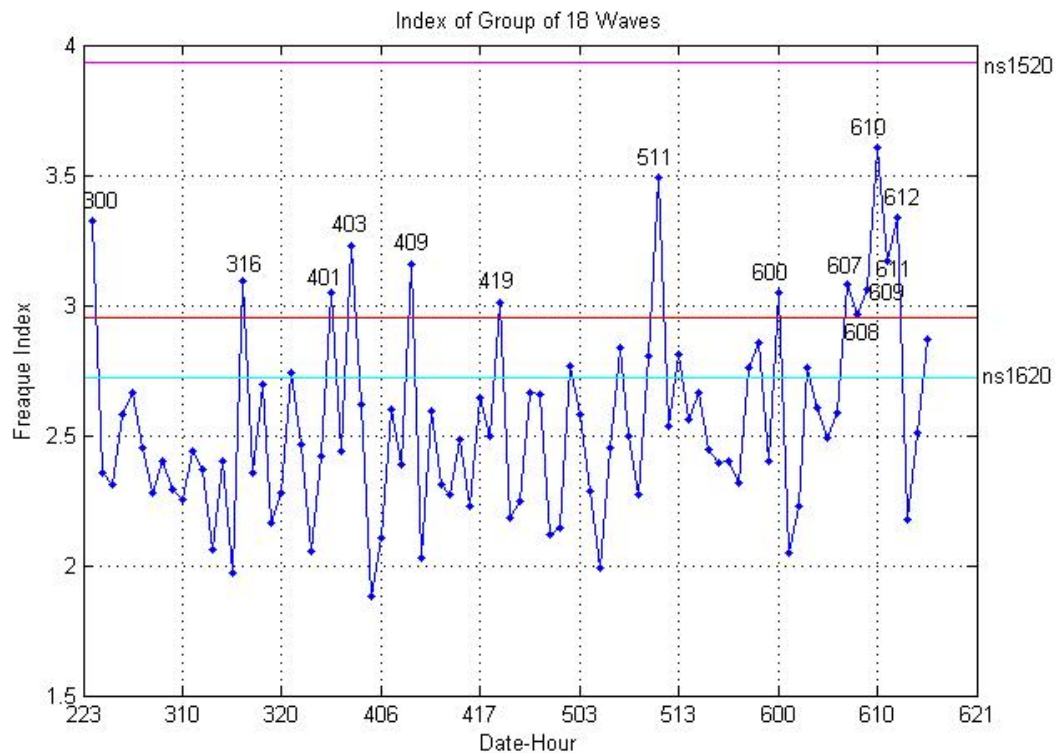


Figure 9 Calculated freaque index corresponding to the data shown in Figure 7.

As an independent corroboration, we calculated the freaque index for the North Sea Draupner data sets shown in Figure 10 as respective horizontal lines. The widely recognized freaque wave case occurred at hour 1520, January 1, 1995 that data produced a freaque index 3.9 shown as the top ns1520 line, whereas the hour 1620 case without a freaque wave produced a freaque index of 2.7, shown by the lower ns1620 line. Both fit our postulated criteria well. We are reasonably confident that this new freaque index will emerge as a viable, encompassing index for searching and exploring freaque waves.

Concluding remarks

Without any preconceived notion regarding whether or not freaque waves can occur during a typhoon or hurricane, we are surprised and encouraged that we are able to positively ascertain that their occurrences are clearly manifested. Although at this stage we are not certain that our findings can be generalized to all typhoons or hurricanes, we feel that it is quite possible that MV *Derbyshire* might have encountered an abnormal freaque wave during the 1980 Typhoon Orchid before their demise.

How often that freaque waves occur is still a question that has yet to be satisfactorily answered. A widely reported news item regarding a brief three-week radar satellite study carried out by the German Aerospace Centre in 2003 in which they found 10 monster waves around the world, ranging from 26 m to 30 m in height and concluded that “it looks as if freaque waves occur in the deep ocean far more frequently than the traditional linear model would predict.” Liu and Pinho (2004) studied wave measurements made from Campos Basin off the Brazil coast in South Atlantic Ocean also concluded that freaque waves are “more frequent than rare.” The Liu and Pinho study was based on cases that fulfill $H_{\max} / H_s > 2$. Now that we have also found freaque wave cases for H_{\max} / H_s less than 2, we can certainly expect that what we are now considering as freaque waves may just be an integral part of the ocean surface process.

So in the midst of still more uncertainties along with more results for each new study, we wish to echo the recent call by Liu et al. (2008) for the need for more concerted wave measurements throughout the world’s oceans since “Without tangible measurements, no amount of modeling or theoretical simulations can truly divulge the reality of what is really happening during the passing of a typhoon or hurricane.”

Acknowledgement

We wish to thank S. Haver of Statoil, Norway for generously providing the North Sea Draupner wave data. This is GLERL Contribution no. 1505.

References

Draper, L., 1964: "Freak" Ocean Waves, *Oceanus*, X:4. Reprinted in *Rogue Waves 2004: Proceedings of a Workshop*.

Faulkner, D., 2000: Rogue Waves – Defining their characteristics for marine design, *Rogue Waves 2000: Proceedings of a Workshop*.

Haver, S., 2004: A possible freak wave event measured at the Draupner Jacket January 1, 1995, *Rogue Waves 2004: Proceedings of a Workshop*.

Janssen, P.A.E.M., 2003: Nonlinear four-wave interactions and freak waves, *J. Phys. Oceanogr.*, Vol. 33, 863-884.

Liu, P. C., H. S. Chen, D.-J. Doong, C. C. Kao, and Y.-J. G. Hsu, 2008: Monstrous ocean waves during Typhoon Krosa, *Annales Geophysicae*. Vol. 26, 1327-1329.

Liu, P. C. and U. F. Pinho, 2004: Freak waves - more frequent than rare! *Annales Geophysicae*, Vol. 22, 1839-1842.

National Transportation Safety Board (NTSB), 1978: Marine Accident Report SS EDMUND FITZGERALD Sinking in Lake Superior on November 10, 1975.

Royal Commission, 1984: Report One: The loss of the Semisubmersible Drill Rig Ocean Ranger and its crew. Canadian Government Publishing Centre.

Sand, S. E., N.E.O.Hansen, P.Klinting, O.T.Gudmestad and M.J.Sterndor, 1990: Freak wave kinematics. In *Water Wave Kinematics*, NATO ASI Series E, 178, Kluwer Academic, 535–550.

SEA STATE STATISTICS AND EXTREME WAVES OBSERVED BY SATELLITE

Wolfgang Rosenthal
GKSS, Geesthacht, Germany
Wolfgang.Rosenthal@gkss.de

For the design of ships as well as for the investigation of ship accidents it is important to have knowledge about both the two dimensional spectral wave properties as well as extreme value statistics of ocean waves. Although numerical wave models have reached a high level of accuracy, they still have weaknesses with respect to the details of the 2-D wave spectrum. Furthermore standard models like WAM provide estimates of the 2-D wave spectrum, i.e., second order sea state statistics and therefore lack information on individual wave properties and the occurrence of extreme events.

In this study the potential of global Synthetic Aperture Radar (SAR) wave mode data acquired by the European satellites ERS-2 and ENVISAT to investigate ship accidents is discussed and compared to altimeter data and ECMWF model results. These data are acquired independent of light and weather conditions on a global scale.

Using ENVISAT ASAR and altimeter data sea state is analysed in the area between parallel tracks that are 300 km apart.

Different ocean wave parameters like significant wave height and wave periods are derived from the SAR data. The potential role of the respective wave conditions for some recent accident is discussed in detail. This includes in particular the analysis of cross sea conditions, groupiness and extreme events.



Sessions II. Numerical Models

ROGUE WAVES 2008, Brest 13–14 October 2008

Can swell increase the number of freak waves in a wind-sea?

Odin Gramstad and Karsten Trulsen

University of Oslo, Department of Mathematics, P.O.Box 1053 Blindern, NO-0316 Oslo, Norway

Longuet–Higgins & Stewart (1960) predicted that short gravity waves riding on a much longer wave will have locally shorter wavelengths and larger amplitudes close to the crests of the long wave, and correspondingly longer wavelengths and smaller amplitudes near the troughs of the long wave. Assuming irregular short waves riding on a monochromatic swell, we have derived modifications to the Gaussian and Rayleigh distributions appropriate for the type of wave–swell interaction described by Longuet–Higgins & Stewart. According to this theory we anticipate that both the kurtosis and the intensity of freak waves should increase, but for realistic swell this effect is small.

Taking the analysis one step further, we ask if the nonlinear modulation of short gravity waves is affected by a swell in such a way that the statistics of extreme waves can be different from the Longuet–Higgins & Stewart modification. A partial answer was given by Regev, Agnon, Stiassnie & Gramstad (2008) who suggested that swell represents a perturbation capable of provoking nonlinear modulations that produce freak waves. However, the same amount of freak waves was also seen to occur through nonlinear modulations provoked by perturbations different from swell.

We have derived extensions of the Zakharov equation and the Dysthe nonlinear Schrödinger equation suitable for describing the long-term evolution of directional short gravity waves riding on swell of arbitrary direction. The latter model was used for Monte–Carlo simulations from which we have extracted statistics of extreme waves (Gramstad 2006). Our results indicate that the intensity of freak waves in a wind-sea is hardly affected by swell at all.

GRAMSTAD, O. 2006 *Kan dønning framprovosere ekstreme bølger i vindsjø?* Master thesis (in Norwegian), University of Oslo.

REGEV, A., AGNON, Y., STIASSNIE, M. & GRAMSTAD, O. 2008 Sea-swell interaction as a mechanism for the generation of freak-waves (*submitted*).

LONGUET–HIGGINS, M. S. & STEWART, R. W. 1960 Changes in the form of short gravity waves on long waves and tidal currents. *J. Fluid Mech.* **8**, 565–583.

Wave-wave interactions in wind-driven mixed seas

Sergei I. Badulin¹, Alexander O. Korotkevich², Donald Resio³
and Vladimir E. Zakharov^{4,5,6}

¹ P.P.Shirshov Institute of Oceanology, Moscow, Russia
badulin@ioran.ru

² Landau Institute for Theoretical Physics, Moscow, Russia
alexander.korotkevich@gmail.com

³ Waterways Experimental Station, Vicksburg, Mississippi, USA
Donald.T.Resio@usace.army.mil

⁴ University of Arizona, USA,
zakharov@math.arizona.edu

⁵ P.N. Lebedev Physical Institute, Russia,

⁶ Waves and Solitons, LLC, USA

Abstract. Effect of anomalously strong interaction of long and short waves is studied in the context of observed peculiarities of wind-wave spectra in the mixed seas. Very short times of this interaction makes questionable the kinetic equation approach itself to this problem. At the same time, the evolution within the kinetic description appears to be consistent both qualitatively and quantitatively with solutions for the weakly nonlinear dynamical equations for water waves. The impact of the found fast transitional effects on problems of wind-driven sea monitoring and forecasting is discussed.

1 Introduction

Sea waves are observed quite often as the so-called mixed seas, i.e. as locally generated wind waves superimposed on relatively long remotely generated swell. Manifestations of this interaction are seen in effects of steering wind waves by swell [1, 2], visible suppression of wind waves and the swell enhancement [3].

Experimental studies [3, 2] give a solid background that, in words by I. Young [3], ‘well indicate that the non-linear wave-wave interaction term is actually stronger than the representations which are implemented in, even the most sophisticated, research models’. In this paper we propose ‘the least sophisticated model’ of evolution of mixed seas. The essence of the model is in taking nonlinear transfer in wave spectra into account ‘in full’. Thus, we follow the line of the cited papers [2, 3] where authors emphasized crucial role of non-linear wave-wave interactions.

The results of our modelling show quite good qualitative and quantitative agreement with observations by Young [3] at extreme wind conditions in hurricanes. These results are also consistent with measurements by Kahma & Petter-

son [2] in the Baltic Sea where steering effect of long (swell) waves on wind-driven waves is also related to the leading role of nonlinear transfer in wave spectra.

Two key points of our study should be stressed at the very beginning. First, the applicability of the statistical description in the sense of weakly non-linear kinetic equation (the Hasselmann equation [4]) is found to be questionable for the problem of the mixed sea. We use this approach as soon as the observed peculiarities of wave spectra appear to be consistent with conventional ‘normal’ wind-sea features [3]. At the same time, we realize definitely the problem of validity of this approach for the problem under discussion where evolution occurs at very short times, formally, beyond the kinetic approach paradigm. To check validity of our conclusions we compared the kinetic equation solutions with one for weakly nonlinear dynamical equations for water waves [5, 6]. We found that both approaches give very close results.

The second point concerns physics itself observed by [3]. Locally generated wind waves appear to be indiscernible in the mixed sea in terms of one-dimensional spectra. Directional spectra shows the presence of the wind waves in the remotely generated swell background but in many cases ‘there is a continuous smooth transition in direction between the dominant low-frequency swell and the higher frequency components aligned with the local wind direction’ [3]. This shows strong non-locality of resonant interactions between waves of very different scales (long swell and relatively short wind waves). This non-locality is also essential for large angles between directions of swell and wind-driven constituent (say, in case of counter-propagating waves) providing strong energy exchange between different spectral peaks. Nevertheless, these peaks keep their ‘identities’ due to strong wave-wave interactions within each peak. Directional bi-modality is observed in such cases. We treat features of the mixed sea found in our numerical study and in the cited experimental papers as manifestations of strong nonlinear transfer in wave spectra rather than of wind forcing and wave dissipation. The problem of strong wave-wave interactions in the mixed sea can be related to dynamics of rogue waves quite naturally. The characteristic scales of the transitional effects in the mixed sea appears to be between relatively slow evolution of waves due to wind forcing and freak wave events which time scales can be comparable with wave periods.

In § 2 we remind some basic features of wind-wave growth [7, 8] and formulate ‘the least sophisticated’ duration-limited spectral model of swell–wind-wave coupling. Results of numerical analysis of four reference cases [3] within the Hasselmann equation [4] are given in § 3. The applicability of the statistical description is discussed in § 4 where dynamical and kinetic equations are solved for a ‘camel-like’ initial spectrum. Conclusions are presented in § 5.

2 Interaction of swell and wind sea within the kinetic approach

The Hasselmann equation [4, 9, 10]

$$\frac{\partial N_{\mathbf{k}}}{\partial t} + \nabla_{\mathbf{k}} \omega_{\mathbf{k}} \nabla_{\mathbf{r}} N_{\mathbf{k}} = S_{nl} + S_f \quad (1)$$

describes evolution of wave action spectral density $N(\mathbf{k}, t)$ (or wave energy spectral density $E(\mathbf{k}, t)$) due to four-wave nonlinear resonant interactions (the so-called collision integral S_{nl}) and external forcing S_f . This equation plays an important role both as a theoretical foundation of wave forecasting models and as a model of weak turbulence theory. A number of hypotheses underlies relevance of this equation to the problem of spectral evolution of wind-driven seas. The most important one is dealing with scaling of this equation: parameter of nonlinearity – wave steepness is assumed to be small

$$\varepsilon = ak \ll 1 \quad (2)$$

and, hence, solutions of (1) have time scaling $T_{Hass} \sim \varepsilon^{-4}$. The latter impose constraints on external forcing term S_f which is generally small due to smallness of ratio of air and water densities responsible for wind forcing. Additionally, it implies a proximity of solutions of the Hasselmann equation (1) to an inherent state where nonlinear transfer is, in a sense, minimal and provide the correct weakly nonlinear scaling (2). This minimization of nonlinear transfer term does not mean its smallness as compared with external forcing term $S_f = S_{in} + S_{diss}$ that describes a net effect of wave input S_{in} and dissipation S_{diss} . On the contrary, the nonlinear transfer appears to be a leading mechanism of wind wave spectral evolution due to strength of nonlinear relaxation to the inherent state. This concept of leading nonlinearity has been developed recently in [7, 12, 8, 13].

Numerical solutions of (1) in fig. 1 (see [7] for details of numerical approach) illustrate basic features of wind-wave evolution due to leading role of nonlinear transfer in case of swell: at large time wave spectra are tending to self-similar behavior with a universal spectral shapes and with weakly turbulent high-frequency tails described by basic Zakharov-Filonenko solutions [14]. It should be stressed that the Pierson-Moskowitz spectrum which is close to an ‘inherent’ wave spectrum has been taken as initial condition at $t = 0$: such evolution appeared to be quite slow, spectral peak frequency changes by 25% only for 256 hours.

Fig. 2 shows the case when the initial condition appears to be very far from an ‘inherent’ state of wave spectra. This state is a superposition of two swell solutions of (1) obtained from the same initial condition at $t = 0$ for different times. Evolving independently (without interaction of components) these two peaks can merge into single peak at rather long time. Fig. 2 shows how peak-to-peak nonlinear interactions can precipitate these peaks merging: solutions for the initially camel-like spectra are shown in solid lines, surrogate spectra composed of two swell spectra evolving independently are given by dashed lines. Right fig. 2 shows nonlinear transfer term S_{nl} of the camel-like spectrum at

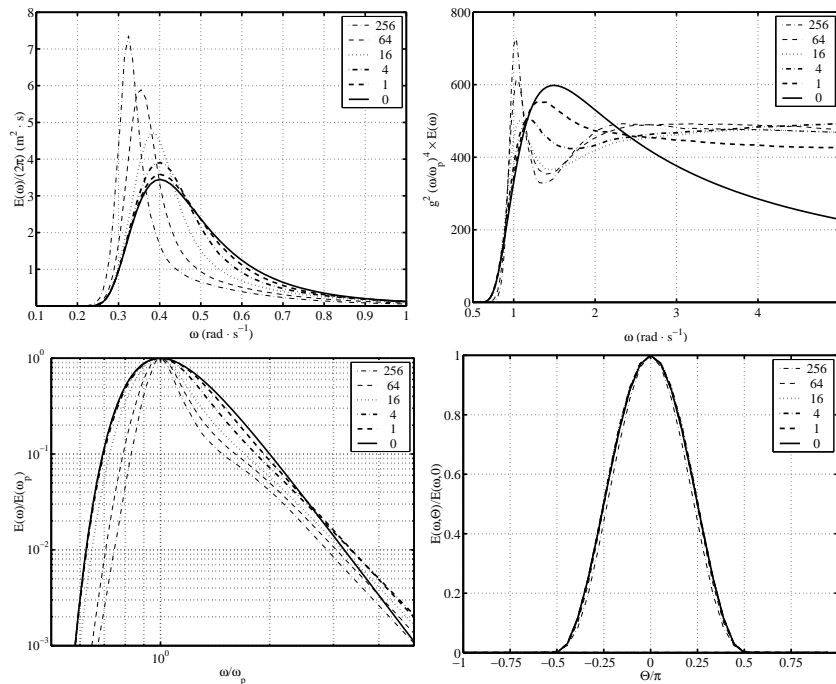


Fig. 1. Duration-limited evolution of initially matured wind sea [11] for long times (in hours in legends) with no input and dissipation. a) – Energy spectrum; b) – compensated spectra; c) – non-dimensional energy spectra; d) – angular distribution at spectral peak frequency ω_P . Tendency to universality is seen in frequency and angular distributions.

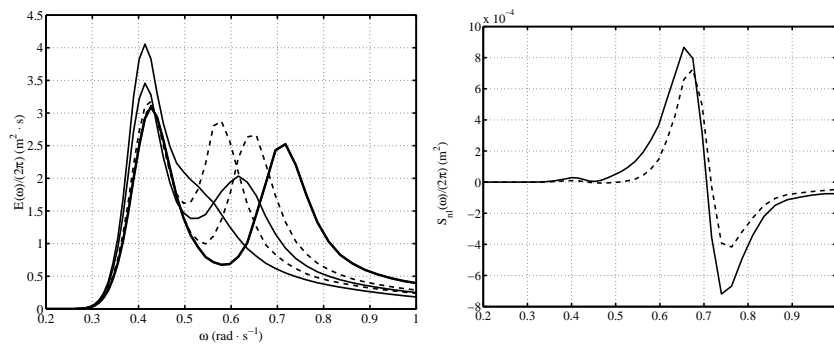


Fig. 2. Left panel – duration-limited evolution of camel-like spectrum from initial state ($E^{(1)} + E^{(2)}$) (solid lines) against ‘surrogate’ spectra obtained as linear superpositions of $E^{(1)}$ and $E^{(2)}$ evolving independently (dashed lines), times are 0, 1.8 and 6.6 hours. Right panel – nonlinear transfer term S_{nl} averaged in angle for camel-like spectrum ($E^{(1)} + E^{(2)}$) (solid line) and a ‘surrogate’ collision term ($S_{nl}^{(1)} + S_{nl}^{(2)}$) (dashed) at $t = 0$.

$t = 0$. Non-locality of resonant wave-wave interactions is seen fairly well in this example: they redistribute effectively the energy of peaks that leads to degradation of high-frequency peak and apparent enhancement of the low-frequency one. The direction of the evolution is consistent with mechanism of inverse cascade described by Zakharov [15] in sixties.

3 Duration-limited evolution of the mixed sea and observations by Young (2006)

Examples of the previous section gives an idea to model effects observed in the mixed sea within the simplest model of duration-limited wave growth. To consider cases described by Young [3] we create two constituents of the mixed sea as solutions of the Hasselmann equation (1). Like in previous section we take linear superposition of the solutions as an initial condition for our numerical run. To specify physics of such mixed sea we compare further evolution of the camel-like spectrum and one of superposition of non-interacting swell and wind-waves.

In this paper we present numerical study of cases presented by Young [3]. We fix wind speed for our mixed sea $U_{10} = 20$ m/s, spectral peak frequency $f_p = 0.09$ Hz and wind-sea component peak $f_{2p} = 1.92$ Hz. Thus, our low frequency component has wave age parameter $U_{10}/C_p \approx 1.15$ and wind waves are associated with rather young waves $U_{10}/C_p \approx 2.46$. The significant height of the superposition of the resulting wave systems $H_s = 8$ m was also very close to cases of Young [3].

A critical point of the proposed setup is the choice of external forcing term S_f . Conventional parameterizations of the term (see sect. 3.2 in [7]) for the case of hurricane winds are questionable. We reserve this point for further studies and focus our efforts on nonlinear wave-wave interactions which effect in the problem discussed appears to be evident. Thus, we follow Young's note on the effect of nonlinear transfer: 'It appears that the shape stabilizing processes giving rise to the spectral form are largely independent of local wind forcing'. We fix basic parameters of wind sea for all the cases by Young [3] and change direction of long waves relatively to the wind only.

3.1 Case C – close propagation of swell and wind waves

We start with Young's case C (fig. 3). Direction of swell was 30° relatively to the wind. The evolution of the initial camel-like spectrum is shown in fig. 3. The effect of peak interaction appears to be surprisingly strong: the wind wave peak is absorbed completely by low frequency (swell) peak for less than 100 periods of short (wind) waves. Further evolution has essentially slower rates as seen from figs. 3 for 2000 seconds (approximately 400 periods, bottom row). Independent evolution of fractions of the camel-like spectra is shown by dashed lines. One can see a dramatic difference: short wave spectral peak continues to grow due to wind forcing while being 'mixed' with swell it disappears for quite short time. Long wave (swell) peak grows slightly due to wind (dashed lines) but

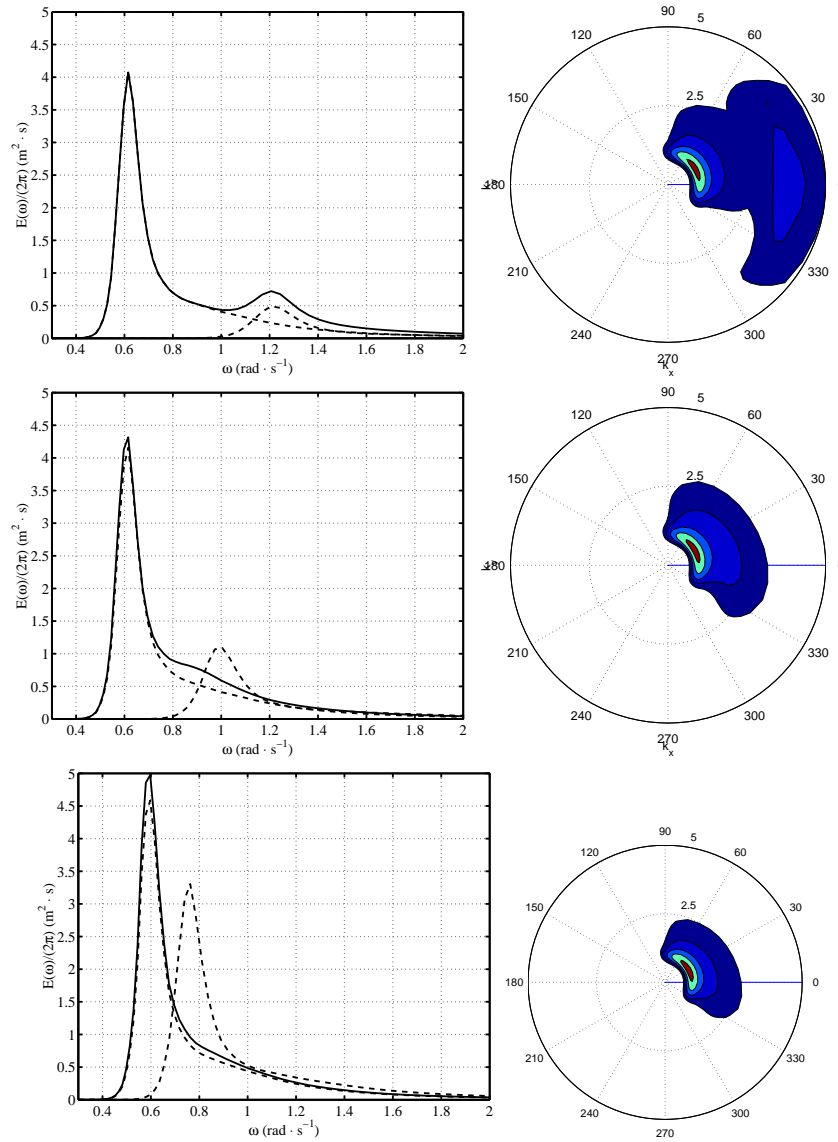


Fig. 3. Duration-limited evolution of camel-like spectrum, Young's case C. Energy frequency (left column) and directional spectra (right column) are shown for times $t = 0$ s (top), $t = 522$ (middle) and $t = 2000$ seconds. Fractions of the initial spectrum evolving independently under the same wave input are shown by dashed lines.

in the mixed sea (solid lines) it gains energy from short waves due to nonlinear interactions. This absorption of short waves that are mostly affected by wind leads to dramatic reduction of wave input. This result is illustrated fairly well by charts for directional spectra in fig. 3: the steering effect of swell component on short wind waves is clearly seen, short waves deviate from wind direction.

3.2 Case D – counter-propagating wind waves and swell

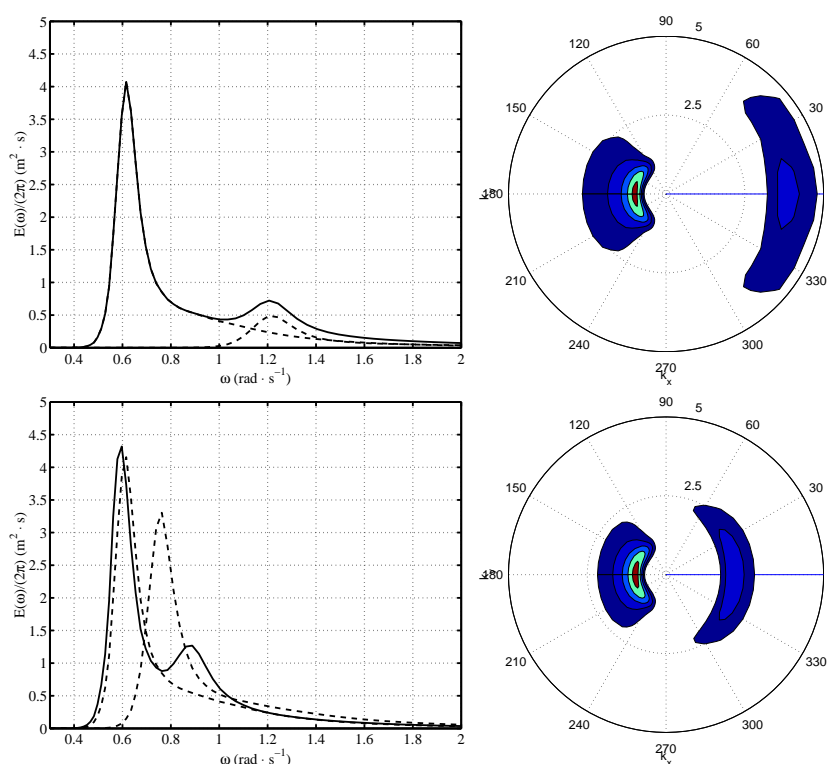


Fig. 4. Duration-limited evolution of camel-like spectrum, Young's case D. Energy frequency spectra (left column) and directional energy spectra (right column) are shown for times $t = 0$ s (top), $t = 2000$ (bottom) seconds. Solutions for one-peak fractions of the initial spectrum are shown by dashed lines.

In view of results of previous paragraph the case D of counter-propagating swell and wind waves can be considered as an opposite extreme case of the mixed sea dynamics. Wind waves gain energy from the wind, while swell does not (we use the simplest parameterizations of wave input where wave damping due to opposite wind is not taken into account). Starting with the same one-dimensional frequency spectrum as in case C (fig. 4) we see again quite different,

as compared with independent evolution of spectra constituents, evolution. Wind wave component is losing energy and is tending to vanish in the swell background (left column fig. 4). At the same time, we see a weak growth and relatively fast downshift of low-frequency peak. Again, the high-frequency waves supply low frequency peak indirectly through nonlinear transfer.

The absorption of high-frequency peak has an important impact on evolution of mixed sea: it reduces dramatically wave input if we follow conventional scheme of wave generation when the wave input is provided mainly by young waves. As a result the mixed wind sea develops at lower rates as compared with purely wind sea in both cases C and D (figs. 3, 4). Note, that the known mechanisms of wave input reduction at high winds consider peculiarities of air-sea interaction that affects aerodynamical properties of sea surface [16, 17]. The presented physical effect is dealing with wave properties only: steering effect of long waves change short wave field essentially and, thus, reduce the resulting wave input.

3.3 Young's cases A, B – directional bi-modality of the mixed sea

Cases A and B described in Young's paper [3] show no qualitatively new features of the mixed sea. The effect of rather fast absorption of wind-wave peak by swell component remains apparent in frequency spectra but one can see pronounced bi-modality in directional spectra. This bi-modality is observed for maximal duration of wave development in our numerical runs – 1 day.

4 Camel-like spectra within the dynamical equations for water waves

The validity of the kinetic description for the evolution of camel-like spectra has been checked in simulations within the weakly nonlinear dynamical equation. The numerical approach is described in recent papers [5, 6]. For the problem of camel-like spectra greater grids have been used up to the finest currently possible 512×4096 points in rectangular coordinate domain.

Simulation setup followed the kinetic equation simulation described in sect. 2. The dynamical equations were solved for an initial surface elevation $\eta(\mathbf{x})$ with gaussian spectrum and randomly distributed phases of Fourier-harmonics. A camel-like state was composed of two solutions of the problem at different sufficiently long times (of order of 100 wave periods) when spectral evolution becomes reasonably slow, i.e. consistent with the kinetic equation time scaling. The spectrum of the resulting camel-like state obtained within the dynamical approach then was smoothed for simulation within the kinetic Hasselmann equation. At the moment the case of co-propagating long and short wave constituents was simulated only.

Spectra of solutions at different times are presented in fig. 5. The effect of very fast absorption of short-wave fraction by long-wave peak is reproduced in this simulation fairly well. Comparison of evolution of camel-like spectra within the dynamical and kinetic approaches showed qualitative and, more, quantitative

agreement of results: short-wave peak disappeared completely for a few dozen of wave periods only. This agreement seems to be very important for wave forecasting models that uses simplified representation of wave-wave interactions. Taking wave-wave interactions into account ‘in full’ can make these models to be valid for adequate description of the transitional effects of mixed seas presented in this study.

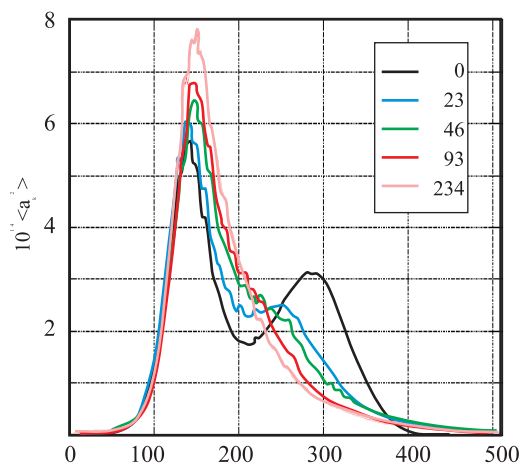


Fig. 5. Evolution of camel-like spectra within the dynamical weakly nonlinear equations. Time in initial periods of short-wave peak is shown in legend.

5 Conclusions

Finalize this paper by summarizing our results.

- Wave-wave interactions in the mixed seas can be strong due to non-locality of these interactions. Fast transitional effects of steering wind waves by swell are observed within the simplest duration-limited model. The time scales of these effects can be comparable with times of rogue wave events;
- Kinetic description becomes formally invalid to describe these fast transitional effects;
- At the same time, as comparison with dynamical approach shows, the formally invalid kinetic equation gives qualitatively correct and quantitatively close results.

In case of mixed seas we likely have a class of strong dynamical effects which time-scales are well between slow evolution of wave spectra and very fast freak wave events. This is a challenging problem of wind sea forecasting.

The work was supported by ONR grant N00014-06-C-0130, US Army Corps of Engineers grant W912BU-08-P-0143, INTAS-8014, RFBR N07-05-00648, 07-05-92211, 08-05-00648, 08-05-13524-ofi-c and Russian Academy Program 'Topical problems of nonlinear dynamics'. This support is gratefully acknowledged.

References

1. Nguy, D.: Observations on the directional development of wind-waves in mixed seas. Master of science in mechanical engineering, University of Washington (1998) Technical report APL-UW-TR9802.
2. Pettersson, H.: Wave growth in a narrow bay. PhD thesis, University of Helsinki (2004) [ISBN 951-53-2589-7 (Paperback) ISBN 952-10-1767-8 (PDF)].
3. Young, I.R.: Directional spectra of hurricane wind waves. *J. Geophys. Res.* **111** (2006) doi:10.1029/2006JC003540
4. Hasselmann, K.: On the nonlinear energy transfer in a gravity wave spectrum. Part 1. General theory. *J. Fluid Mech.* **12** (1962) 481–500
5. Zakharov, V.E., Korotkevich, A.O., Pushkarev, A.N., Resio, D.: Coexistence of weak and strong wave turbulence in a swell propagation. *Phys. Rev. Lett.* **99**(164501) (2007)
6. Korotkevich, A.O., Pushkarev, A.N., Resio, D., Zakharov, V.E.: Numerical verification of the weak turbulent model for swell evolution. *Eur. J. Mech. B/Fluids* **27**(361) (2008) doi:10.1016/j.euromechflu.2007.08.004.
7. Badulin, S.I., Pushkarev, A.N., Resio, D., Zakharov, V.E.: Self-similarity of wind-driven seas. *Nonl. Proc. Geophys.* **12** (2005) 891–946
8. Badulin, S.I., Babanin, A.V., Resio, D., Zakharov, V.: Weakly turbulent laws of wind-wave growth. *J. Fluid Mech.* **591** (2007) 339–378
9. Hasselmann, K.: On the nonlinear energy transfer in a gravity wave spectrum. Part 2 Conservation theorems; wave-particle analogy; irreversibility. *J. Fluid Mech.* **15** (1963) 273–281
10. Hasselmann, K.: On the nonlinear energy transfer in a gravity wave spectrum. P. 3. *J. Fluid Mech.* **15** (1963) 385–398
11. Komen, G.J., Hasselmann, S., Hasselmann, K.: On the existence of a fully developed wind-sea spectrum. *J. Phys. Oceanogr.* **14** (1984) 1271–1285
12. Badulin, S.I., Babanin, A.V., Pushkarev, A.N., Resio, D., Zakharov, V.E.: Flux balance and self-similar laws of wind wave growth. In: 9th International workshop on wave hindcasting and forecasting. (2006) <http://waveworkshop.org/9thWaves/Papers/Badulin.pdf>.
13. Badulin, S.I., Babanin, A.V., Resio, D., Zakharov, V.: Numerical verification of weakly turbulent law of wind wave growth. In Borisov, A.V., Kozlov, V.V., Mamaev, I.S., Sokolovskiy, M.A., eds.: IUTAM Symposium on Hamiltonian Dynamics, Vortex Structures, Turbulence. V. 6, IUTAM Bookseries. Springer (2008) 175–190.
14. Zakharov, V.E., Filonenko, N.N.: Energy spectrum for stochastic oscillations of the surface of a fluid. *Soviet Phys. Dokl.* **160** (1966) 1292–1295
15. Zakharov, V.E.: Problems of the theory of nonlinear surface waves. PhD thesis, Budker Institute for Nuclear Physics, Novosibirsk, USSR (1966)
16. Kudryavtsev, V.N.: On the effect of sea drops on the atmospheric boundary layer. *J. Geophys. Res.* **111** (2006) C07020
17. Makin, V.K.: A note on drag of the sea surface at hurricane winds. *Boundary-Layer Meteorol.* **115**(1) (2005) 169–176

Rogue waves in large-scale fully-non-linear High-Order-Spectral simulations

Guillaume Ducrozet, Félicien Bonnefoy & Pierre Ferrant

Laboratoire de Mécanique des Fluides - UMR CNRS 6598
École Centrale de Nantes
1, rue de la Noë, 44321 Nantes, France
guillaume.ducrozet@ec-nantes.fr, felicien.bonnefoy@ec-nantes.fr,
pierre.ferrant@ec-nantes.fr

Abstract. This study is devoted to the simulation of 3D directional wave fields with a fully-non-linear potential-flow model. This model is based on the High-Order-Spectral (HOS) method in the consistent form of West et al. [14]. The accuracy and efficiency of this model give access to the fully-non-linear evolution of large domains during long period of time. Besides, the recent efficient parallelization of the code (see Ducrozet et al. [5]) allows us to run parametric studies. In this paper, the occurrence of extreme waves is investigated within sea-states of different characteristics.

Introduction

Extremely large waves are named freak or rogue waves when their height or crest amplitude exceed the significant wave height by a factor 2.2 or 1.4 respectively. Several ships and platforms have been confronted to such destructive waves in the last decades (see *eg.* Didenkulova et al. [2] for a review of the accidents involving freak waves in 2005). However, accurate simulations of this 3D highly non-linear process is still very challenging. Different mechanisms of formation of such events have been pointed out such as wave focusing, wave-current interactions, non-linear wave interactions, ... (see Kharif and Pelinovsky [8] for a review). We focus in this paper on the long-time evolution of wave fields in deep water without wind and current.

Many numerical models have been developed to study the freak waves occurrence in the last fifty years. The pioneering work of Philipps who studied the energy exchange resulting from wave interaction in the framework of a weakly-non-linear method, was followed by other numerical tools accounting for more and more complexity. Zakharov [15] described the full time evolution equations of the wave system which have been later solved using reduced expressions limited to four-wave or five-wave interactions (see *eg.* Stiassnie and Shemer [12]). The Non-Linear Schrödinger (NLS) equation (arising when the narrow-band assumption of the wave spectrum is added to the previous model) has also been widely used in this topic (see Trulsen and Dysthe [13] for the latest enhanced

version (Broad-Modified NLS - BMNLS) allowing broader bandwidth and fourth order in wave steepness). However, as noticed in Kharif and Pelinovsky [8], rogue waves present large amplitudes, high steepness, and short duration. This breaks the assumptions of weak non-linearity and narrow-banded spectrum. An interesting approach can then be to use time-domain fully-non-linear potential models. Nonetheless, such numerical simulations are today still very challenging. Indeed, the Boundary Element Method (BEM), classically employed within the latter class of methods, remains too slow to reproduce square kilometers of ocean long-time evolution.

Consequently, our study is based on an alternative approach, the High Order Spectral (HOS) method, proposed by West et al. [14] and Dommermuth and Yue [4]. This method allows the fully-non-linear simulation of gravity waves evolution within 3D periodic domains. With respect to classical time-domain models such as the BEM, this spectral approach presents the two assets of its fast convergence and its high computational efficiency (by means of Fast Fourier Transforms FFTs), allowing to accurately simulate long-time 3-D sea state evolutions with fine meshes.

Firstly, we present the model used which is a parallelized version of the order consistent HOS model of West et al. [14]. Specific attention has been paid to aliasing matter and numerical efficiency. A parallel version of the code (Ducrozet et al. [5]) is used, allowing fully-non-linear simulations of tens of square kilometers during hundreds of periods without prohibitive CPU cost. The initial condition is defined (through a given wave spectrum) and we let it evolve during long simulation time looking at natural appearance of rogue events. Typically, 100 km² of ocean are simulated over 500 peak periods (*i.e.* \simeq 1 h and 45 min.). The second part of the present paper is devoted to a parametric study of the influence of the mean steepness of the wavefield, *i.e.* Benjamin-Feir Index (BFI), on these extreme events occurrence. Comparisons between linear theory and our fully-non-linear simulations are provided and will point out the main importance of non-linearities.

1 Formulation

In this section we briefly present the HOS method used in the following large-scale simulations. The initialization of the wavefield is exposed as well as the approach employed to detect the rogue waves. A recent paper, Ducrozet et al. [6], shows the ability of this model to simulate freak waves appearance and a first parametric study on the influence of directionality on freak waves occurrence was proposed. We refer to this paper for more details about the HOS method.

1.1 Hypothesis and equations

We consider an open periodic fluid domain D representing a rectangular part of the ocean of infinite depth $h \rightarrow \infty$. We choose a cartesian coordinate system with

the origin O located at one corner of the domain. Horizontal axes are aligned with the sides of the domain and (L_x, L_y) represent the dimensions in x - and y -directions respectively. \mathbf{x} stands for the (x, y) coordinates. The vertical axis z is orientated upwards and the level $z = 0$ corresponds to the mean water level (see Fig. 1).

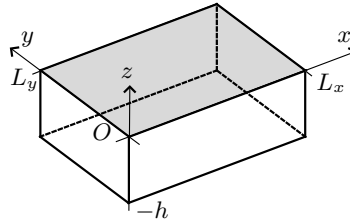


Fig. 1. Sketch of the domain with coordinate system

The fluid is assumed incompressible and inviscid. The wave-induced motion of the fluid is described by an irrotational velocity and we assume that no wave-breaking occurs. Under these assumptions, the flow velocity derives from a velocity potential $\phi(\mathbf{x}, z, t)$ satisfying the Laplace's equation inside the fluid domain D .

$$\Delta\phi = 0 \quad \text{inside } D \quad (1)$$

Following Zakharov (1968), the fully-non-linear free surface boundary conditions can be written in terms of surface quantities, namely the single-valued free surface elevation $\eta(\mathbf{x}, t)$ and the surface potential $\phi^s(\mathbf{x}, t) = \phi(\mathbf{x}, \eta, t)$.

$$\frac{\partial\phi^s}{\partial t} = -g\eta - \frac{1}{2}|\nabla\phi^s|^2 + \frac{1}{2}(1 + |\nabla\eta|^2) \left(\frac{\partial\phi}{\partial z}\right)^2 \quad (2)$$

$$\frac{\partial\eta}{\partial t} = (1 + |\nabla\eta|^2) \frac{\partial\phi}{\partial z} - \nabla\phi^s \cdot \nabla\eta \quad (3)$$

both expressed on $z = \eta(\mathbf{x}, t)$ with $W = \partial\phi/\partial z(\mathbf{x}, \eta, t)$. The unknowns η and ϕ^s are then time-marched with a 4th order Runge-Kutta scheme with an adaptative step-size control. The only remaining unknown in Eqs (2) and (3) is the vertical velocity W which is evaluated by the order-consistent HOS scheme of West et al. [14].

1.2 High-Order-Spectral method

The HOS method consists in expanding the velocity potential located at the *exact* free surface position in a combined power of η and Taylor series about the mean water level $z = 0$ prior to compute its vertical derivative. The products

involving $\nabla\eta$ and W in Eqs. (2) and (3) are evaluated thanks to the order consistent formulation of West et al. [14].

This method is based on an iterative process (up to the so-called HOS order M) to evaluate the vertical velocity W . This quantity W is the only one that is approximated in the free surface boundary conditions whose non-linearities are otherwise fully accounted for. The non-linear terms are conserved and the boundary conditions expressed on the exact free surface position $\eta(\mathbf{x}, t)$.

The HOS formulation provides a very efficient FFT-based solution scheme with numerical cost growing as $N \log_2 N$, N being the number of modes. An acceleration procedure, based on an analytical integration of the linear part of the equations, has also been implemented. Non-linear products are evaluated in the spatial domain with special care paid to dealiasing while derivatives are evaluated in the Fourier domain.

Periodic boundary conditions are applied in both direction x and y to the unknowns η , ϕ^s and the potential ϕ . These conditions added to the infinite depth condition as well as the Laplace's equation (1) are used to define the spectral basis functions on which ϕ is expanded. The unknowns η and ϕ^s are accordingly expanded on the Fourier basis.

Finally, notice that a parallel version of the code has been recently developed which allows the use of memory-distributed supercomputers. More details about the parallelization and particularly about its great efficiency can be found in Ducroz et al. [5]. Simulations presented later on have been performed with this parallel version.

1.3 Initial condition

The initial wavefield is defined by a directional wave spectrum $S(\omega, \theta) = \psi(\omega) \times G(\theta)$ where the frequency spectrum is chosen as a modified JONSWAP one (space and time are normalized respectively with scales $\tilde{L} = 1/k_p$ and $\tilde{T} = \sqrt{L/g}$ where k_p is the peak wavenumber).

$$\psi(\omega) = \alpha g^2 \omega^{-5} \exp\left(-\frac{5}{4} \left[\frac{\omega}{\omega_p}\right]^{-4}\right) \gamma \exp\left[-\frac{(\omega - \omega_p)^2}{2\sigma^2 \omega_p^2}\right] \quad (4)$$

with ω_p the angular frequency at the peak of the spectrum and

$$\alpha = 3.279E, \quad \gamma = 3.3, \quad \sigma = \begin{cases} 0.07 & (\omega < 1) \\ 0.09 & (\omega \geq 1) \end{cases} \quad (5)$$

The dimensionless energy E of the wavefield is related to the significant wave height H_s by $H_s \simeq 4\sqrt{E}$. The directionality function is defined by:

$$G(\theta) = \begin{cases} \frac{1}{\beta} \cos^2\left(\frac{\pi\theta}{2\beta}\right), & |\theta| \leq \beta \\ 0, & |\theta| > \beta \end{cases} \quad (6)$$

with β a measure of the directional spreading. In the following, we study only long crested wave fields, with $\beta = 0.26$ which corresponds to a directional spread

of 14.9° or almost equivalent to directional function $\cos^{2s}(\theta)$, with $s = 45$.

Then, the initial free surface elevation η and free surface velocity potential ϕ^s are computed from this directional spectrum definition by a superposition of linear components with random phases. It is to notice that a linear initialization of a fully-non-linear simulation can lead to numerical instabilities. Thus, the relaxation scheme of Dommermuth [3] is used at the beginning of the computation for the transition from the linear wavefield to the *realistic* fully-non-linear one.

1.4 Detection of rogue waves

The rogue waves are generally defined as waves whose height H exceeds the significant wave height H_s by a given factor (typically 2.2) or waves whose crest height A_c exceeds H_s in a given proportion. To apply such a criterion, we have to define and measure the waves height or crest height from the free surface elevation η . Firstly, we define the wave height in our 3D simulations as the height of a wave in the mean direction of propagation. Then, we perform a zero up-and-down crossing analysis on each mesh line aligned with the x -axis which is the mean direction of propagation of our wavefield. Afterwards, a transverse zero up-and-down crossing analysis is performed, along the y -axis this time. This double zero-crossing analysis allows us to extract each 3-D wave and to describe it in both horizontal directions with its wavelength λ_x , crest length λ_y and also the crest and trough heights. The significant wave height is calculated from the standard deviation σ of the free surface elevation η ($H_s = 4\sigma$). Among the detected waves, we are able to locate the freak events, determine their dimensions and characteristics by applying one of the above criteria.

For instance, Fig. 2 shows a typical evolution of the ratio $\max(H)/H_s$ for a simulation with a steepness $\varepsilon = 0.1$. One can notice that the threshold 2.2 is overshoot several times, each one being a rogue wave.

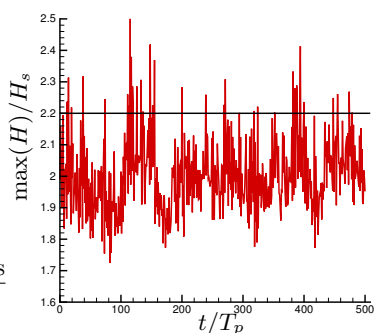


Fig. 2. Evolution of $\max(H)/H_s$ for $\varepsilon = 0.1$.

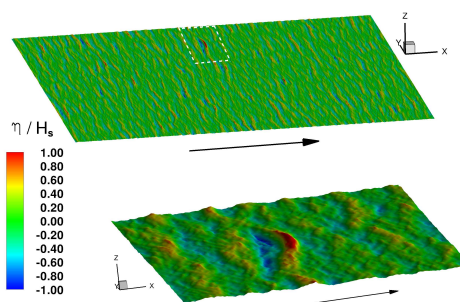


Fig. 3. Example of freak event

Once the freak wave is detected inside the domain, it is possible to analyze its shape, crest and trough height, *i.e.* all its characteristics. An example of detected extreme event is presented on Fig. 3. Top part of the figure represents the whole simulated domain (the white square encloses the detected extreme event) while the bottom part is a zoom on this event which exhibits a ratio $H/H_s = 2.48$.

The arrows indicate the mean direction of propagation of the wavefield while the colors give the free surface elevation. The freak wave (which height is 12.7 m for $H_s = 5.12$ m if we choose $T_p = 12.5$ s) is a huge wave crest followed by a deep trough. One can see the exceptional feature of this wave compared to the surrounding waves.

2 Influence of the mean steepness

Using the numerical model described in the previous sections, we study the influence of the mean steepness of the wave field on the formation of freak waves during the evolution of a given wave spectrum. Thus, one lets evolve this given initial 3D sea-state which is analyzed to extract different waves and study their properties. Firstly, the linear theory for the freak waves occurrence in 3D wavefields is briefly exposed. Then, the set of simulations used to study the influence of mean steepness is presented. We notice the importance of spectral broadening during simulations, leading to an enhanced linear theory, and finally, we present the results obtained, pointing out the influence of non-linearities in the rogue waves phenomenon.

The following numerical conditions are common to all the performed simulations:

- Domain area: $L_x \times L_y = 42\lambda_p \times 42\lambda_p$, with λ_p the peak wavelength,
- Number of modes: $N_x \times N_y = 1024 \times 512$,
- HOS order $M = 5$, full dealiasing,
- Duration of simulations: $500 T_p$ (with T_p being the peak period).

The energy density E will be defined later.

2.1 Linear model

Baxevani and Rychlik [1] studied the probability of occurrence of extreme events in a Gaussian framework. Particularly, they provided an upper bound for the probability of wave crests height (A_c) exceeding a given level u in a region of space during a period of time. This upper bound is given by the following equation:

$$\begin{aligned}
 P[A_c > u] &\leq P[X(0) > u] + \left(\frac{L_x}{\lambda_x} + \frac{L_y}{\lambda_y} + \frac{T}{T_z} \right) e^{-8u^2/H_s^2} \\
 &+ \sqrt{2\pi} \left(N_t + N_y \sqrt{1 - \alpha_{xt}^2} + N_x \sqrt{1 - \alpha_{yt}^2} \right) \frac{4u}{H_s} e^{-8u^2/H_s^2} \\
 &+ 2\pi N \sqrt{1 - \alpha_{xt}^2 - \alpha_{yt}^2} \left(\frac{4u}{H_s} \right)^2 e^{-8u^2/H_s^2}
 \end{aligned} \tag{7}$$

where T_z is the average wave period and for our purpose, $N = L_x L_y T / (\lambda_x \lambda_y T_z)$, $N_x = L_y T / (\lambda_y T_z)$, $N_y = L_x T / (\lambda_x T_z)$ and $N_t = L_x L_y / (\lambda_x \lambda_y)$. The parameters α_{xt} and α_{yt} accounts for drift velocity; we have $\alpha_{xt} = 0.89$ as we use a JONSWAP spectrum and $\alpha_{yt} = 0$ due to symmetry of the directional spreading. We invite to refer to Baxevani and Rychlik [1] for details concerning this equation. We notice here that they also pointed out the influence of the spreading of waves on these occurrences: considering waves moving along one direction (i.e. 2D calculations) can lead to substantial underestimations.

Consequently, to be consistent with this formulation, the definition of freak waves has to be adapted to define the corresponding exceedance on the ratio $\max(A_c)/H_s$. Taking as basis the observation of Guedes Soares et al. [10], one chooses to use the vertical asymmetry parameter: $\max(A_c) \geq 1.4H_s$. Thus, one evaluates the return period of such a wave (i.e. the time required to record such a wave within our simulation domain) from equation (7). We obtain that in a linear framework, in a domain like the one simulated here ($42\lambda_p \times 42\lambda_p$), the return period of rogue waves is $360T_p$ or equivalently $\simeq 60.000$ waves. That is to say, the linear theory predicts that a freak wave can eventually appear during our 500 T_p simulations. For the comparisons made with the linear theory of Baxevani and Rychlik, the analysis of this ratio $\max(A_c)/H_s$ is chosen as a detection criterium for the extreme events.

2.2 Description of the non-linear simulations

We performed simulations with varying steepness as reported in Tab. 1. It is to notice that a small filtering is applied to the most extreme case ($E = 5 \cdot 10^{-3}$) to prevent from wave breaking during simulations: this explains the slight differences one could observe at beginning of simulations (Fig. 5). Table 1 contains the mean steepness of the wave field $\varepsilon = k_p \bar{a}$, with $\bar{a} = (2 \langle \eta^2 \rangle)^{1/2}$ (i.e. $\varepsilon = k_p H_s / 2\sqrt{2}$) and the Benjamin-Feir Index (BFI) defined by

$$BFI = \frac{2\varepsilon}{\sigma_\omega}$$

where σ_ω is the bandwidth of the spectrum. This index plays a key role in the wave-wave interactions (Alber, 1978) and characterizes the stability of wave trains.

2.3 Spectral broadening

During the evolution of the wavefield, we observe that the non-linear wave interactions induce changes in the wave spectrum. As it has been previously studied with several numerical methods (for instance with advanced NLS models in Socquet-Juglard et al. [11]) the spectrum broadens in the transverse direction and the spectrum peak is downshifted. Figure 4 shows a typical evolution of the spectrum for a steepness $\varepsilon = 0.1$. The left part of the figure presents the initial

E	ε	BFI
$5 \cdot 10^{-5}$	0.01	0.10
$5 \cdot 10^{-4}$	0.032	0.33
$1 \cdot 10^{-3}$	0.045	0.46
$2 \cdot 10^{-3}$	0.063	0.65
$3 \cdot 10^{-3}$	0.077	0.80
$5 \cdot 10^{-3}$	0.10	1.03

Table 1. Simulations parameters

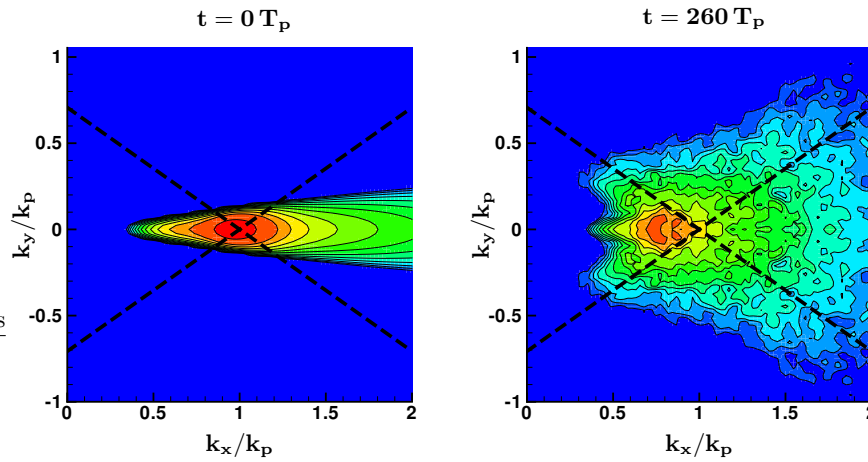


Fig. 4. Spectral broadening for a long crested wavefield with $\varepsilon = 0.1$

wave elevation spectrum while the right part depicts this spectrum after $260 T_p$ of propagation.

The most unstable directions with respect to the transverse Benjamin Feir (BF) instability (defined as $k_y = \pm 2^{-1/2}k_x$) are also shown in Fig. 4. It clearly appears that the spectral broadening occurs mainly along these directions. This emphasizes the influence of the BF mechanism in the spectrum evolution. Fig. 5 presents the evolution of the measured mean transversal wavelength λ_y (normalized by peak wavenumber k_p) versus normalized time t/T_{BF} for different steepness ε where the BF time-scale T_{BF} is defined as $T_{BF} = T_p \varepsilon^{-2}$. We observe that the curves for varied steepness all collapse together and a simple fit to the data would be $\lambda_y(t) = \lambda(t=0) \exp[-t/T_{BF}]$.

The drastic reduction of the mean transversal wavelength is again related to the BF mechanism as it is to be linked with the spectrum broadening. Note that the fully-non-linear HOS model gives access to times greater than T_{BF} (during which main changes occur in the spectrum) and therefore can predict the long

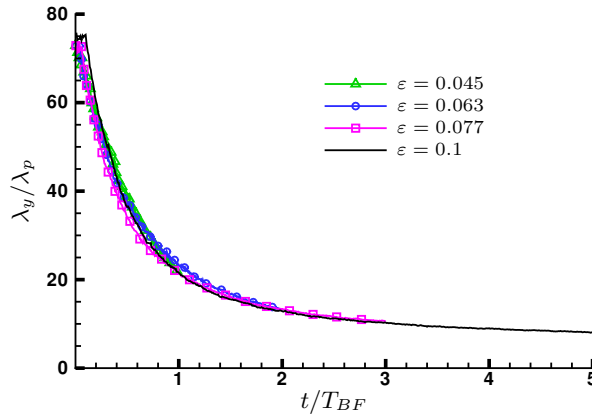


Fig. 5. Evolution of λ_y with BFI time for different choices of E

term behavior of the wavefield, after the BF spectral changes have occurred. This is one of the main advantage to work with the HOS method compared to classically used NLS models.

2.4 Enhanced linear model

The main features of the wavefield are widely modified by non-linear effects, resulting in a large influence on the probability of occurrence of freak waves. For instance, the number of waves N we detect in the domain is strongly related to λ_y and its modification will affect the linear prediction in Eq. (7). On the other hand, we have observed that the mean wavelength in the main direction λ_x remains almost unchanged. Consequently, for better comparisons with our non-linear simulations, we try to enhance the linear model of Baxevani and Rychlik [1] in the following way.

We take into account the temporal change of the transverse wavelength and we estimate a return period that evolves during the simulation $T_{return}(t)$. We can then estimate the number of freak waves by dividing the duration of the simulation $T_{sim.}$ by the previous return period. This gives with $T_{return}(t)$ obtained from Eq. (7) with varying N, N_x, N_y, N_t

$$n_{enhanced} = \frac{T_{sim.}}{\int_0^{T_{sim.}} \frac{T_{return}(t)}{T_{sim.}} dt} \quad (8)$$

2.5 Discussion

Table 1 compares the number of detected freak waves in the non-linear HOS simulations with the prediction from the linear theory of Baxevani and Rychlik [1] (with λ_y estimated at $t = 0$) and the enhanced version described previously.

ε	Number of freak waves			ε	Number of freak waves		
	simulation	linear	enhanced		simulation	linear	enhanced
0.01	2	1.4	1.3	0.063	17	1.4	3.4
0.032	6	1.4	2.0	0.077	36	1.4	4.5
0.045	9	1.4	2.4	0.1	36	1.4	4.9

Table 2. Detected freak events and linear predictions

First, the smallest steepness $\varepsilon = 0.01$ shows similar results for the linear theory, the enhanced one and the HOS simulation. As expected, such a steepness leads to a linear wavefield whose spectrum is nearly unchanged during the 500 peak periods. This observation validates both the HOS model at low steepness and the detection process for the freak events. As the steepness increases, the spectrum broadening and the resulting decrease in transverse crest length affects the probability of occurrence of freak waves. Both the measurements made with the HOS wavefields and the enhanced theory predict a greater number of extreme events. The non-linear simulations shows however an even greater probability of occurrence than what the enhanced theory does. The spectral broadening that we take into account through the modification of λ_y is not the only factor governing the formation of extreme events.

Besides, it is interesting to remark that Fig. 2 shows that extreme events appear also after $t > T_{BF}$ *i.e.* after the initial main BF spectral changes. This figure also indicates, at first sight, that the probability of occurrence is of the same order during the whole simulations, lasting in this case up to $t = 5T_{BF}$ (some freak waves are detected at every stage of the propagation). Consequently, the different results claiming that the occurrence of large waves is associated with rapid spectral development (or instability) (cf. *eg.* experiments of Onorato et al. [9] or numerical simulations of Dysthe et al. [7]) are not recovered clearly here: several rogue waves appear after the main spectral development. Thus, maybe other non-linear mechanisms lead to these freak waves. The precise understanding of the phenomenon conducting to the formation of a freak wave is still on-going work.

Conclusion

This paper presented some fully-non-linear simulations of large scale domains. We studied more particularly the formation of rogue waves in the computational domain during long time simulations. The influence of the mean steepness of the

wave field (or equivalently the BFI) on the freak waves occurrence probabilities is analysed.

Simulations are performed with the HOS method on a large domain (typically 100 km^2) during $500 T_p$. The initial wave field is defined by a directional JON-SWAP spectrum and its fully-non-linear propagation during time is computed. Then, the wave pattern is analysed to detect freak waves appearing inside the domain. In order to assess the correctness of our resolution, we take as reference the work of Baxevani and Rychlik [1] which gives the probabilities of occurrence of freak waves inside a domain during a period of time in a Gaussian (i.e. linear) framework. However, the non-linear evolution of the wave field induce several changes in the wave spectrum, particularly a spectral broadening with a peak down-shifting. This has to be taken into account and consequently leads to an enhanced version of the linear prediction of Baxevani and Rychlik [1]. For the almost linear case, both theories and HOS simulations are in concordance and assess the reliability of our fully-non-linear simulations as well as the method of detection of freak events. Then, when the non-linearity of the wave field is enlarged, it appears clearly in the HOS simulations that the number of rogue waves observed is also widely increased and consequently greatly deviates from the linear theory. Furthermore, the enhanced linear theory predicts a correct increase of this number of freak waves with the steepness but to a lesser extent. Thus, other non-linear effects than the spectral broadening are influent on the occurrence of freak waves. Besides, our simulations indicate that extreme events appear also after $t > T_{BF}$ i.e. after the initial main BF spectral changes. The understanding of the precise physical mechanisms leading to these freak waves (during and after the main spectral changes) is still under way and seems a really important point to clarify. Is there a long-time link between freak waves formation and BF mechanism and/or what are the other non-linear mechanisms leading to such rogue waves ?

References

1. A. Baxevani and I. Rychlik. Maxima for gaussian seas. *Ocean Engng.*, 33:895–911, 2006.
2. I. I. Didenkulova, A. V. Slunyaev, E. N. Pelinovsky, and C. Kharif. Freak waves in 2005. *Nat. Hazards Earth Syst. Sci.*, 6:1007–1015, 2006.
3. D.G. Dommermuth. The initialization of nonlinear waves using an adjustment scheme. *Wave Motion*, 32:307–317, 2000.
4. D.G. Dommermuth and D.K.P. Yue. A high-order spectral method for the study of nonlinear gravity waves. *J. Fluid Mech.*, 184:267 – 288, 1987.
5. G. Ducrozet, F. Bonnefoy, and P. Ferrant. Analysis of freak waves formation with large scale fully nonlinear high order spectral simulations. In *Proc. 18th Int. Symp. on Offshore and Polar Engng.*, Vancouver, Canada, July 2008.
6. G. Ducrozet, F. Bonnefoy, D. Le Touzé, and P. Ferrant. 3-D HOS simulations of extreme waves in open seas. *Nat. Hazards Earth Syst. Sci.*, 7(1):109–122, 2007.
7. K. Dysthe, H. Socquet-Juglard, K. Trulsen, H. E. Krogstad, and J. Liu. “Freak” waves and large-scale simulations of surface gravity waves. In *Proc. 14th ‘Aha Huliko’ a Hawaiian Winter Workshop*, Honolulu, Hawaii, January 2005.

8. C. Kharif and E. Pelinovsky. Physical mechanisms of the rogue wave phenomenon. *Eur. J. Mech., B/Fluids*, 22:603–634, 2003.
9. M. Onorato, A.R. Osborne, M. Serio, L. Cavaleri, C. Brandini, and C.T. Stansberg. Extreme waves and modulational instability: wave flume experiments on irregular waves. <http://arxiv.org/abs/nlin.CD/0311031>, 2004.
10. C. Guedes Soares, Z. Cherneva, and E.M. Antao. Characteristics of abnormal waves in north sea storm sea states. *Appl. Ocean Res.*, 25:337–344, 2003.
11. H. Socquet-Juglard, K. Dysthe, K. Trulsen, H. E. Krogstad, and J. Liu. Probability distributions of surface gravity waves during spectral changes. *J. Fluid Mech.*, 542:195–216, 2005.
12. M. Stiassnie and L. Shemer. On modifications of the zakharov equation for surface gravity waves. *J. Fluid Mech.*, 143:47–67, 1984.
13. K. Trulsen and K. B. Dysthe. A modified nonlinear schrödinger equation for broader bandwidth gravity waves on deep water. *Wave Motion*, 24:281–289, 1996.
14. B.J. West, K.A. Brueckner, R.S. Janda, M. Milder, and R.L. Milton. A new numerical method for surface hydrodynamics. *J. Geophys. Res.*, 92:11803 – 11824, 1987.
15. V. Zakharov. Stability of periodic waves of finite amplitude on the surface of a deep fluid. *J. Appl. Mech. Tech. Phys.*, pages 190–194, 1968.

Fine Structure and Peculiarities of Wave Spectra with Benjamin – Feir Instability

Sergey Kuznetsov¹ and Yana Saprykina¹

¹ P.P. Shirshov Institute of Oceanology, Russian Academy of Sciences, Nakhimovskii prospect, 36, Moscow, 117997, Russia
kusnetsov@ocean.ru, saprykina@ocean.ru

On the base of analysis of field and laboratory experiments the fine structure of wave spectra with nonlinear instability is investigated. It was found that on deep water most of storm waves have two-three sidebands in wave spectra possible due to nonlinear instability of waves. The waves of each of these sidebands have the own wave group structures, which are different from the group structure of waves of frequency band of the main spectral peak. To define several wave group structures a new spectral technique – spavelet - was applied. The envelopes of waves of different frequency bands have different periodicity. The superposition of these envelopes and coincidence in time and space of maximum of waves of different frequency bands leads to formation of the extreme or freak waves. The effect of downshifting of main peak of spectrum is discussed.

1 Introduction

Studying and the description of changes of heights of storm waves is important for navigation and for an estimation of impact on coast and technical constructions in a coastal zone. Most interesting are knowledge about highest waves, so-called “extreme waves” and “freak waves”.

Last years investigation have shown, that in general there is two main reasons of occurrence of extreme waves:

1) an influence on waves of natural factors. For example, influence of hurricanes and tornados; interaction of waves and currents or influence of bathymetry during wave propagation (refraction, reflection);

2) interactions between waves. First of all, it is linear superposition of wave groups of the various wave systems propagating in different directions, and in one, for example, at the effect of focusing caused by a dispersion and nonlinear focusing [1], [2].

Many researchers note connection between existence of wave group structure characterizing irregularity of waves in height and appearance of extreme waves, including freak waves [3]. But the physical origin of an irregularity of waves is still unknown and it is not clear, whether it due to random phases of waves or it is a result of nonlinear instability. A possible role of nonlinear instability (so called Benjamin-

Feir or modulation instability) in formation of an irregularity of waves by different researchers was mentioned (see, for example, [4], [5], [6]).

There are many papers in which specific solutions “breathers” or “unstable modes” generating in presence of modulation instability numerically and theoretically are found and discussed [7], [8]. Existence of “unstable modes” was proved using nonlinear Fourier analysis also [9]. Each of “unstable modes” has its own unique dynamics and can appear and disappear on the short distance of waves transformation.

However, physical mechanisms of formation of an irregularity and, accordingly, wave group structure and its change in process of developing and changing of type of nonlinear instability are studied insufficiently. The exact mechanism of formation of extreme waves at existence of wave group structure till now is not clear also.

The purpose of this investigation is on the basis of field and laboratory data to investigate peculiarities of wave regimes with nonlinear instability and define mechanisms of formation of extreme and freak waves in point of view of formation and evolution of wave group structure.

2 Extreme Waves in Nature

Southern Branch of P.P. Shirshov Institute of Oceanology performed in 1996 – 2003 field experiment on Black sea near Gelendzhik town. Waverider buoy (DATAWELL, Netherlands) have been anchored on distance of 4 miles from the coast in open sea on 85 m depth, that for all measured data were corresponded to deep water conditions [10]. Buoy transferred measured data by radio channel. Buoy displacement in space with time discretization 0.78 s and duration 20 min were registered every hour at storm and swell waves and every 3 hours at other wave conditions.

In this field experiment the most extreme storm was registered on 2 February 2003. Duration of storm was about 5 hours; the maximum height of waves was 11-12 m and mean height of waves - 4.5 – 5 m. Wind speed during this storm according to a meteorological data in blast was about 21 m/s and mean wind speed was about 15 m/s.

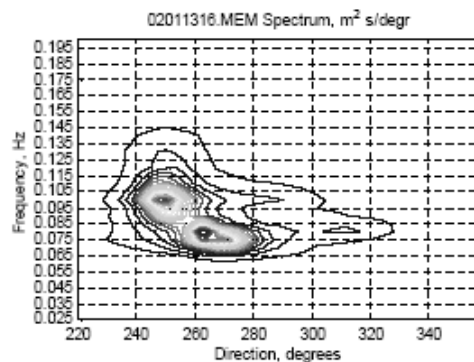


Fig. 1. Angular-frequency spectrum of storm waves, 1 p.m., 2 February, 2003.

The angular-frequency spectra of wave are narrow-banded that allows to consider a storm as only wind waves and to search the reasons of occurrence of extreme waves in internal structure of waves, and, for example, not in an interference of several systems of waves with a different direction of movement or systems of waves of the different nature (Fig. 1).

Time evolution of wave parameters and of wave spectrum are shown on Fig.2. It is visible that the frequency of the main spectral peak shifts down to low frequency part of spectrum (from 0.14 up to 0.8 Hz) and evolution of maximum wave height correlates well with this process.

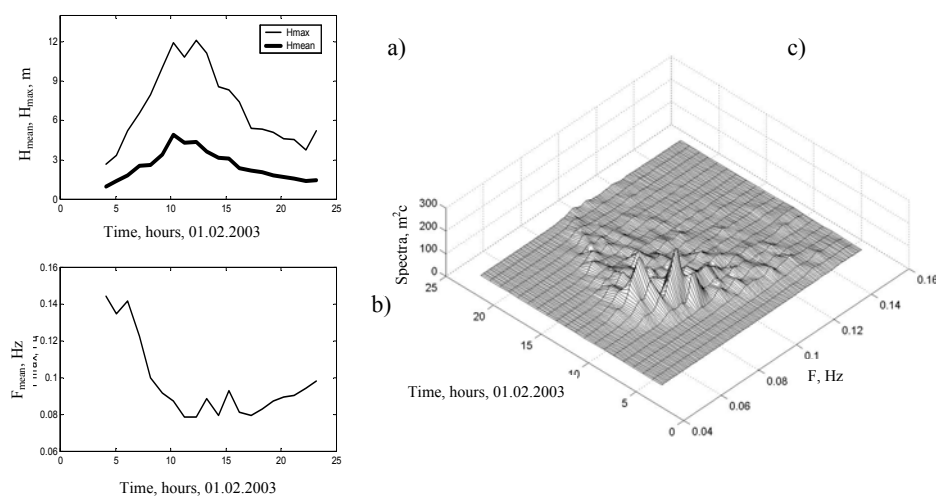


Fig. 2. Time evolution of mean and maximum height of waves (a), mean frequency of waves (b) and wave spectrum (c) during storm of 2 February 2003.

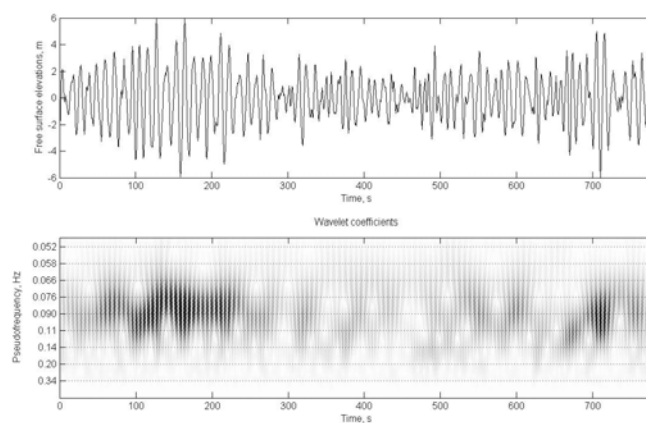


Fig. 3. Fragment of wave record with extreme wave and its wavelet transform. Beginning of the fragment corresponds to 10.18 a.m. 2 February, 2003

Let us consider this storm in detail to understand how extreme waves were formed and what parameters, except for height, distinguish them from usual waves.

To analyze how frequency structure of the extreme waves differs from structure of other waves, wavelet-transform of wave records representing development of a wave spectrum in time, have been applied [11]. Dependences of wavelet coefficients on frequency scales and on time show, that all observable individual extreme waves have much wider band of frequencies in the crest, than neighboring waves (Fig. 3).

Fourier spectrum of this 20-minute wave record constructed with high resolution is shown in fig.4a. According performed high resolution spectral analysis of field data the similar shape of a spectrum is typical for all observed storms in this experiment: the maximum of wave spectrum consist from two or several close located maximums which can be caused by Benjamin-Feir instability. All of this storm waves have well visible wave group structure when low waves are alternated with high waves (Fig. 3a). It is convenient to investigate the wave group structure by using of envelopes of waves [12].

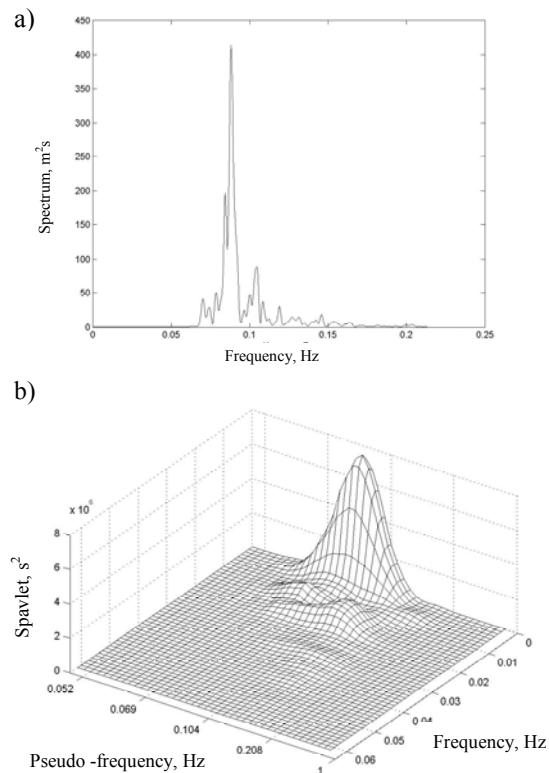


Fig. 4. A wave spectrum (a) and spawlet (b) of 20-minute wave record 10.15 p.m. 2 February, 2003.

Because the smoothed modules of wavelet coefficients of any frequency band are the envelope of waves of this frequency band, let us to investigate the group structure of waves in details by spavelet-analysis [13]. A spavelet is a set of spectra of modules of wavelet coefficients of different scales (pseudo-frequencies) or, by other words, of spectra of envelopes of waves of different scales. The spavelet-analysis has shown, that waves of different frequency bands have the different spectral structure of envelopes, i.e. various wave group sub-structure (Fig. 4b). So waves of a frequency band of the main spectral maximum (close to 0.088 Hz, Fig. 4a) have rather slowly fluctuating of envelopes (the biggest peak of spavelet on pseudo-frequencies of 0.088 Hz, frequencies <0.005 Hz). Waves of a frequency band of overtones of the basic wave movement (peak of a spectrum on frequency of 0.103 Hz, Fig. 4a) have envelope with frequency of fluctuations of 0.02 Hz (Fig. 4b, pseudo-frequency of 0.104 Hz, frequency of 0.02 Hz). The similar structure we can see at low sideband frequency (about 0.07 Hz). Thus, it is visible, that Benjamin-Feir nonlinear instability (or modulation instability) forms inside of initial waves the own group structure of overtones of the basic wave movement, and extreme waves are formed during the moment of superposition in time as maximums of waves of different frequency scales, and their maximums of envelopes.

To show this effect clearly, we made a numerical filtration of investigated wave record on two frequency bands (a limit between two basic peaks of a spectrum of waves is at frequency 0.95 Hz). At the moments of coincidence of crests of waves of different frequency bands and accordingly different wave group structures arise extreme waves (88 s and 125 s on Fig. 5).

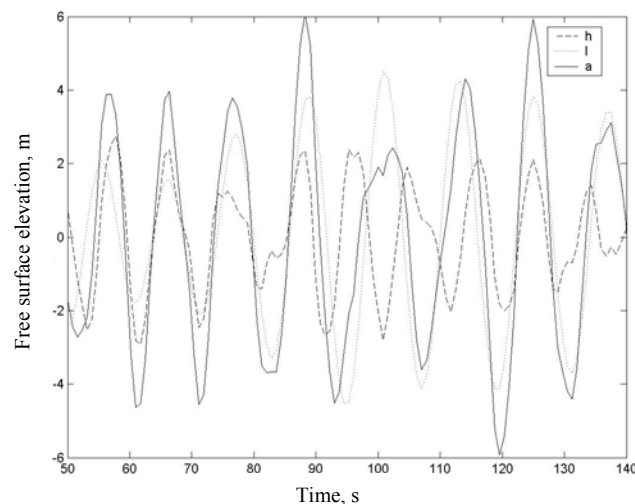


Fig. 5. A fragment of wave record (a), its high frequency (h) and its low-frequency (l) components. The beginning of wave record is at 10.18 p.m., February 2, 2003.

Note, that such special fine structure of wave spectra and spavelets near main peak frequency was a feature most of investigated storms waves observed during this field

experiment in Black Sea. It testifies that nonlinear instability, arising during nonlinear waves transformation, is the inherent feature of most regimes of storm waves.

So we can conclude that spectra of storm waves have fine structure near the main peak frequency, produced by modulation instability. Energy distribution on sidebands frequencies (characteristic frequency scales) alternates in time. It testifies the complexity of wave group structure. A possible mechanism of formation of extreme or freak waves is a superposition of maximums of waves of different frequency scales having different wave group structure.

3 Extreme Waves in Laboratory Flume

To check our assumption about mechanism of formation of extreme waves due to Benjamin-Feir instability consider a typical examples of transformation of initially bichromatic waves (waves with simple wave group structure) on deep water. Laboratory experiment was carried out in water flume of Institute of Hydroengineering of the Polish Academy of Sciences (Gdansk), in 2005. The total length of flume is 64 m, depth - 1.4 m. Initially bichromatic waves with frequencies from 0.5 up to 2.5 Hz and different heights over constant depth were modelled. For measurements of water surface elevations 15 gauges were used, which were placed every 3 m from 4 up to 47 m of flume length. The wave records were from 2 up to 6 min, with sampling frequency 200 Hz.

On Fig. 6 the example of changes of waves and their spectra on different distances of flume are shown. It is well visible as initial regular groups of bichromatic waves are transformed to completely irregular waves. The beginning of formation of an irregularity corresponds to appearance of Benjamin-Feir nonlinear instability, visible on a spectrum as additional small peaks around of main spectral maximums provided by initial harmonics.

We can see that spectrum becomes wider during the wave propagation. According to Janssen [14] the reason of it is nonlinear quasi-resonant interactions of harmonics arising due to instability and the initial harmonics make wider an initial spectrum of waves and frequency of a maximum of a spectrum shifts to low frequencies. This downshifting process is discrete, both on frequency, and in time and its characteristic frequency scale is equal to a difference between frequencies of instability and the maximum of a spectrum, and time scale is characteristic time of nonlinear interaction between these frequencies.

Note, that during wave transformation in flume there are various types of instability. For example, originally nonlinear instability (modulation instability) had smooth character and visible groups of waves had almost identical structure. But from some time (distance 13 m), character of instability abrupt changes, the visible group structure of waves becomes complicated and then one group of waves becomes unlike another (for example, on distance 20 m). Because at the same time occurs fast change of shape of spectrum characterizing by downshifting of main frequency it is possible to define this process as ‘spectral instability’. The next development of an irregularity of waves under influence of instability leads to formation of separate extreme high waves, which visually are distinguished from existing wave group structure (distances

32 and 35 m). When spectrum of waves becomes “stable” again (fig.6, distances 41, 45, 47 m) no separate extreme waves are visible.

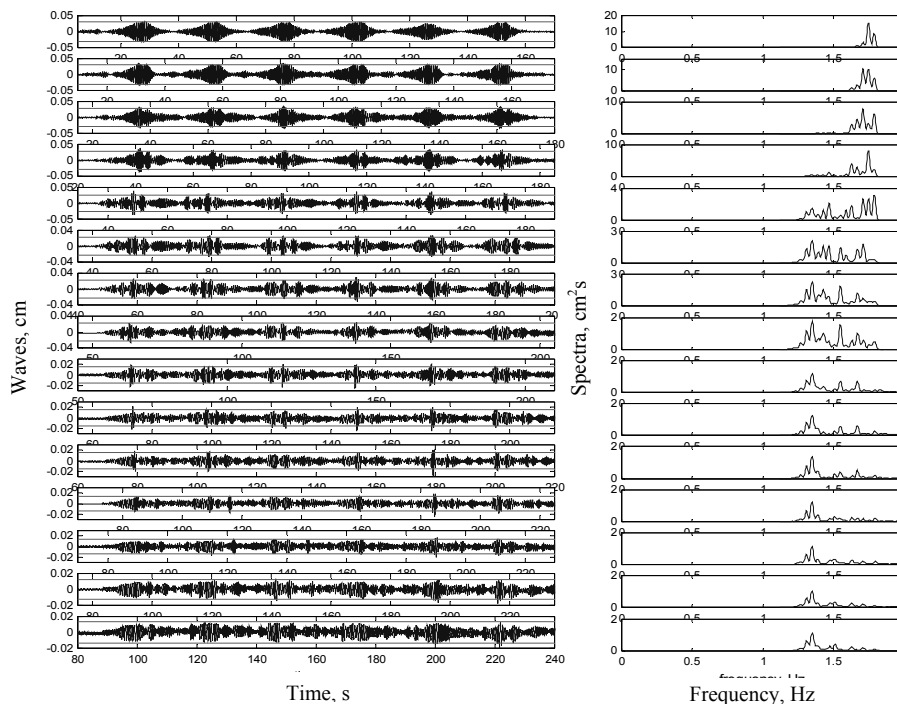


Fig. 6. Evolution of initial bichromatic waves (left) and its spectra (right) with amplitude of maximal waves 7 cm, frequency 1.84 and 1.87 Hz (from upper to down). Thin line - $2H_{sig}$.

Let us apply wavelet and spavelet analyses to waves shown on Fig.6. In Fig. 7b and Fig.8b the modules of wavelet-coefficients on distances 20 and 32 m, accordingly, are shown by intensity of color. It is well visible that distribution of energy on the frequency scales close to frequency of a maximum of a spectrum of waves as in case of natural waves strongly alternates in time and is various for different frequency scales (pseudo-frequencies). It confirms complex character of change of group structure of considered waves and shows simultaneous presence of several wave group structures with closed frequencies scales.

The presence of a few group structures is testified by the spavelet-analysis also (Fig. 7c and Fig. 8c). It is visible, that waves of near frequency scales (main peak and close located maximums) have different spectral structure of envelopes, and, hence, they have various wave group structures.

More in details, waves of a frequency band of the main spectral maximum (frequency scale of pseudo-frequency 1.3 Hz, Fig.8c) have rather slowly fluctuating envelope (the biggest peak of spavlet is about 0.04 Hz). Waves of a frequency bands corresponding to additional maximums of wave spectrum (for example, additional

peak of wave spectrum on 0.2 Hz and corresponding peak of spavelet on pseudo-frequency of 1.5 Hz on Fig.8c) have envelopes with other frequency of fluctuations. Thus, it is shown, that nonlinear instability of waves forms own wave group structure inside of initially existing group structure waves.

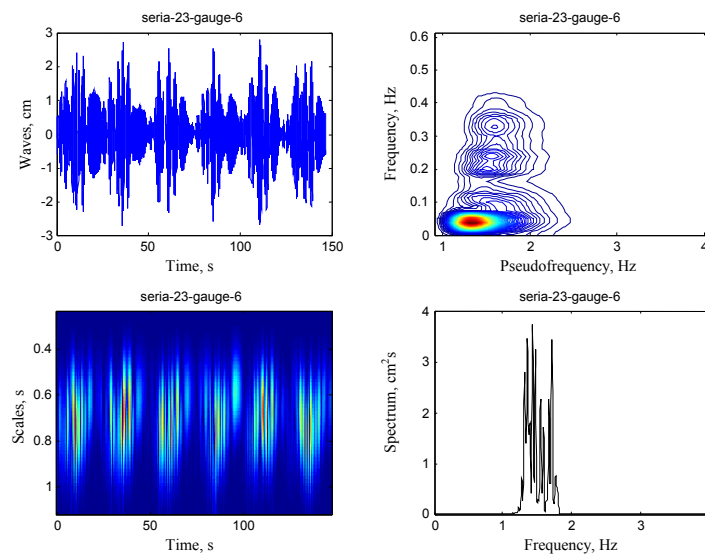


Fig. 7. Waves (a), wavelets (b), spavelet (c) and wave spectra for series 23, distance 20 m.

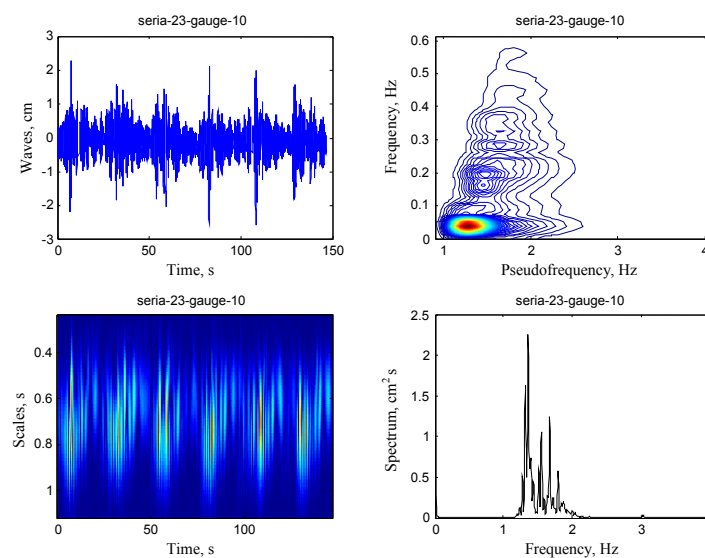


Fig. 8. Waves (a), wavelets (b), spavelet (c) and wave spectra for series 23, distance 32 m.

Dependences of wavelet coefficients of various scales on time show, that all observable individual extreme waves have much wider band of frequencies in the crest, than neighboring waves (Fig.7b, 8b) and extreme waves are formed during the moment of superposition in time as maximums of waves of different frequency scales, and their maximums of envelope. These several group structure can be associated with “unstable modes” and mutual application of wavelet and spavelet analysis allow physically detect it in wave records.

A numerical filtration of wave record (series 23, distance 32 m) on two frequency bands (a limit is between two basic peaks of a spectrum of waves) shows that at the moments of coincidence of crests of waves of different frequency bands and accordingly different wave group structures (or different “unstable modes”) there are extreme waves (90 s, Fig. 8a and Fig. 9). This mechanism of formation of extreme waves exists in the nature and is described in previous section (see also [15]).

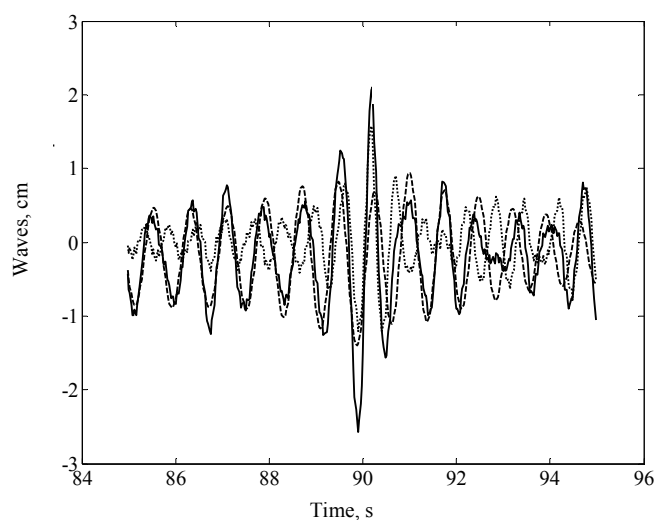


Fig. 9: Formation of extreme waves at the moment of coincidence of maximums of waves of different frequency bands (series 23, distance 32 m). Continuous line – waves, dotted line- high frequency part of waves, dashed line – low frequency part of waves corresponding to frequency scales of nonlinear instability.

4 Conclusions

It was shown that in deep water nonlinear instability of waves lead to the existence of two-three sidebands that looks as the additional peaks near the main spectral peak. The waves of these sidebands have the group structures, which are different from the group structure of waves of frequency band of main spectral peak. Superposition in time and space of wave maximum of each wave system provides formation of the extreme (freak) waves. Different wave group structures are formed due to nonlinear instability (modulation instability and “spectral” instability) at the moments of main

frequency downshifting. The process of frequency downshifting is discrete in both time and frequency. A frequency step is equal to minimum of scales of nonlinear instability, and time step – to time of nonlinear quasi-resonant interaction.

Acknowledgements

The authors are grateful to W. Sulisz for the opportunity to perform laboratory experiment. This work were supported by Russian Foundation for Basic Research , project № 08-05-00648, and by the Russian Federal Program "World Ocean", contract № 01.420.1.2.0006.

References

1. Pelinovsky E, T. Talipova, C. Khariff : Nonlinear-dispersive mechanism of freak wave formation in shallow water. *Physica D*. Vol.147 (2000) 83-94.
2. Mori, N., Yasuda T.: Effects of high order nonlinear wave-wave interactions on deep-water waves. Proceedings of "Rogue Waves 2000" (2000) 181-192.
3. Chien, H., C. Kao, L. Chuang: On the characteristics of observed coastal freak waves. *Coastal Engineering Journal*. Vol. 44, N 4 (2002) 301-309.
4. Yuen, H.C, B.M. Lake: Nonlinear dynamics of deep-water gravity waves. *Advances in applied mechanics*. Vol.22 (1987) 67-229.
5. Tulin M.P., T. Waseda: Laboratory observations of wave group evolution, including breaking effects, *Journal of Fluid Mechanics*. 378 (1999) 197-232.
6. Infeld E, G. Rowlands: *Nonlinear waves, solitons and chaos*. Cambridge, University press. (2000).
7. Dysthe, K.B., Trulsen, K.: Note on breather type solutions of NLS as a model for freak waves. *Physica Scripta*. 82 (1999) 48-52.
8. Osborne, A.R., M. Onorato, M.Serio: The nonlinear dynamics of rogue waves and holes in deep-water gravity wave trains. *Physical Letters. A* 275 (2000) .385-393.
9. Osborne, A.R., M. Onorato, M.Serio: Nonlinear Fourier analysis of deep-water, random surface waves: theoretical formulation and experimental observations of rogue waves, Aha Huliko'a Hawaiian Winter Workshop 2005 (2005).
10. Kosyan R.D., B.V. Divinskiy, O.V. Pushkarev: Measurements of parameters of wave processes in the open sea near Gelendzhik. The Eight Workshop of NATO TU-WAVES/Black Sea, METU, Ankara, Turkey, 17-18 Apr. (1998) 5-6.
11. Torrence C., G.P. Compo: A practical guide to wavelet analysis. *Bulletin of American Meteorological Society*. Vol. 79. N 1 (1998) 61-78.
12. Saprykina Ya, Kuznetsov S.: Transformation of irregular waves and wave groups due to breaking and nonlinear processes. Proceeding of 29th International Conference on Coastal Engineering. World Scientific. (2005) 282-294.
13. Petenko I.V.: Advanced combination of spectral and wavelet analysis ("spavlet analysis"). *Boundary-Layer Meteorology*. Vol.100 (2001) 287-299.
14. Janssen P.A.E.M.: Nonlinear Four-Wave Interactions and Freak Waves. *J. Physical Ocean*. 33, 863, (2003) 863-884.
15. Kuznetsov S.Yu., Ya.V. Saprykina, R.D. Kos'yan, O.V. Pushkarev: Formation Mechanism of Extreme Storm Waves in the Black Sea. *Doklady Earth Sciences*, 408, No. 4 (2006) 570–574.

Abstract for the Rogue Waves 2008 Workshop, Brest, France

RANS/VOF Simulation of an Alternative Extreme Wave

Nwaka Ojeh (University of Strathclyde)

In this work, two different kinds of extreme waves are generated. First is the traditional "new-wave" which represents the most-probable highest wave in a sea-state. Second, we generate an alternative extreme wave which is not necessarily the highest wave in the sea-state (JONSWAP spectrum of the same H_s and T_z) but is the most-probable shape of the steepest wave, by aligning the fronts rather than the crests (traditional new-wave) of component waves in the spectrum. Using a RANS/VOF model partially validated by experimental results, we investigate and compare the properties of the two types of extreme waves. It was observed that although the steepest wave is not as high as the traditional new-wave, it was more non-linear than the traditional new-wave. The 5th order new-wave theory proposed by Walker et al (2004) was also used to simulate the water surface elevation of both waves. While the theory was able to predict the wave elevations reasonably well in the case of the traditional new-wave, it significantly under-predicted the elevation of the steepest wave. This suggests that non-linearity can be more than simply wave-heights and wave-front steepness also needs to be taken into account when determining the critical wave in a given sea-state. It is therefore shown that the highest wave in a sea-state is not necessarily the critical wave rather an alternative extreme can occur which though not being the highest is more non-linear.

Abstract for the Rogue Waves 2008 Workshop, Brest, France

A New Class of Rogue Waves in Shallow Water: Nonlinear Fourier components and Hyperfast Numerical Simulations in the Boussinesq Approximation

Al R. Osborne, Miguel Onorato, Don Resio

A new theoretical and numerical analysis of directionally spread shallow water waves has been conducted. As a consequence we have developed a nonlinear Fourier decomposition of shallow water wave trains which is based upon many directional cnoidal wave trains (at leading order they are solutions to the Kadomsev-Petvishvili or the 2+1 Gardner equations) which nonlinearly interact with one another. The fully spread directional spectrum is based upon a Riemann matrix formulation which uses multi-dimensional Fourier series to compute the surface elevation out to the Boussinesq approximation. We find that a new type of rogue wave is observed in these shallow water sea states which is not related to the Benjamin-Fier instability. Instead the rogue evens arise by the formation of Mach stems at the locus of two crossed cnoidal waves. We give a nonlinear spectral decomposition which allows us to find the actual cnoidal waves that cause the rogue event in a random sea state. We also show how the numerical algorithm executes about 1000 times faster than typical Boussinesq simulations.

Runup of irregular waves on a plane beach

Ira Didenkulova^{1,2)}, Efim Pelinovsky²⁾ and Anna Sergeeva²⁾

¹⁾ Institute of Cybernetics, Tallinn University of Technology, Tallinn, Estonia;

²⁾ Institute of Applied Physics, Nizhny Novgorod, Russia

The freak wave phenomenon is usually discussed for the open sea (Olagnon and Athanassoulis, 2001; Kharif and Pelinovsky, 2003). Such unusual waves are observed also in the coastal zone and the probability of their appearance is rather high. One of the first works (Sand et al, 1990) already presents data of freak wave observations in the shallow part of the North Sea (on the depth of 20 m). Chien et al. (2002) report about 140 freak wave events in the coastal zone of Taiwan in the past 50 years (1949–1999) that caused loss of 500 people and destruction of 35 ships. According to (Didenkulova et al, 2006) 2/3 of the freak wave events occurred in 2005 were observed onshore. Thus a freak wave attacked the breakwater in Kalk Bay (South Africa) on August 26, 2005 and washed off the breakwater people. Two months later on October 16, 2005, two freak waves induced panic at Maracas Beach (Trinidad Island, Lesser Antilles), when a series of towering waves, many more than 25 feet high (maximal height of 8 m), flooded the beach, carried sea-bathers, vendors and lifeguards, running for their lives. Thus, analysis of freak waves on a coast is an important task for practice. Here we will investigate distribution functions of the runup height and velocity on a beach, assuming that distribution functions in the coastal zone are known and waves do not break. The analytical shallow water theory, described in (Synolakis, 1987; Didenkulova et al, 2007) is used as theoretical model.

According to (Didenkulova et al, 2007) the water displacement and water flow on the shoreline ($x = 0$) within the linear theory can be expressed as

$$\eta(t, x = 0) = \int \left(\frac{16\pi^2 h}{g\alpha^2} \right)^{1/4} \omega^{1/2} A(\omega) \exp \left[i \left(\omega(t - \tau) + \phi(\omega) + \frac{\pi}{4} \right) \right] d\omega, \quad (1)$$

$$u(t, x = 0) = \frac{1}{\alpha} \int \left(\frac{16\pi^2 h}{g\alpha^2} \right)^{1/4} \omega^{3/2} A(\omega) \exp \left[i \left(\omega(t - \tau) + \phi(\omega) + \frac{3\pi}{4} \right) \right] d\omega, \quad (2)$$

where A and ϕ are spectral amplitudes and phases, ω is the basic frequency of the incident wave

$$\eta(t, x = L) = \int A(\omega) \exp[i(\omega t + \phi(\omega))] d\omega, \quad (3)$$

given at the distance $x = L$ from the shore and τ is travel time to the coast. Rigorous solutions of the nonlinear shallow-water system can be obtained from Eqs. (1) and (2) with the use of Riemann transformation of time, see papers cited above. It is important to mention that series (10)-(11) can be used to calculate positive and negative runup amplitudes in the nonlinear theory also but not moments and distribution functions of the water displacement at the shoreline.

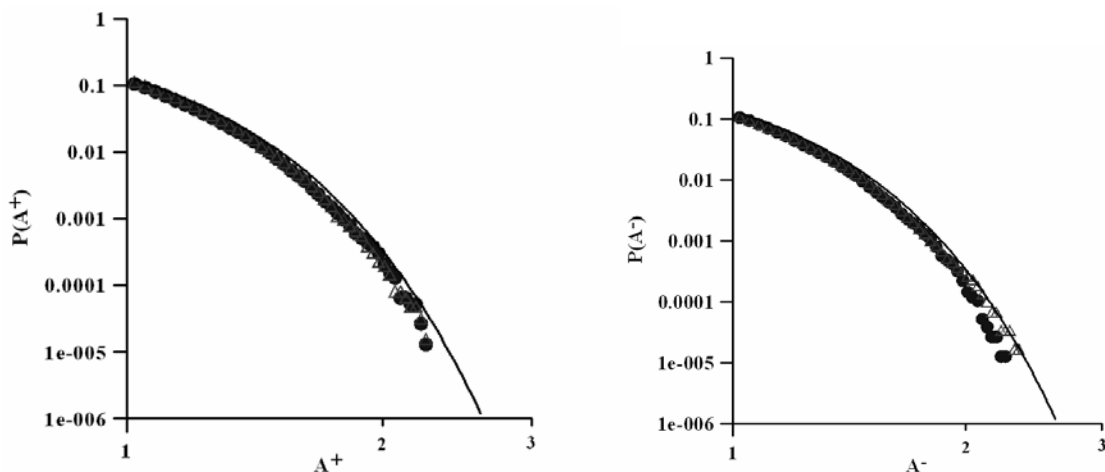


Fig. 1. Distribution functions of maximal positive (left) and negative (right) amplitudes for incident wave (triangles) and shoreline displacement (circles); solid line corresponds to the Rayleigh distribution

So, the wave runup on a plane beach leads to increasing of the probability of the large-amplitude waves, and freak wave phenomenon should be taken into account in the coastal protection.

References

- Chien H., Kao C-C., Chuang L.Z.H.** On the characteristics of observed coastal freak waves. *Coastal Engineering Journal*, 2002, vol. 44, No. 4, 301-319.
- Didenkulova, I.I., Slunyaev, A.V., Pelinovsky, E.N., and Charif, Ch.** Freak waves in 2005. *Natural Hazards and Earth System Sciences*, 2006, vol. 6, 1007-1015.
- Didenkulova I., Pelinovsky E., Soomere T., Zahibo N.** Runup of nonlinear asymmetric waves on a plane beach. *Tsunami and Nonlinear Waves* (Ed: Anjan Kundu), 2007, 173-188.
- Kharif C., Pelinovsky E.** Physical mechanisms of the rogue wave phenomenon. *European J Mechanics / B – Fluid*, 2003, vol. 22, No. 6, 603-634.
- Olagnon M., Athanassoulis G.A.** (Eds.), *Rogue Waves 2000*. France: Ifremer, 2001.
- Sand S.E., Hansen N.E., Klinting P., Gudmestad O.T., Sterndorff M.J.** Freak wave kinematics. In: Torum, A., Gudmestad, O.T. (Eds.), *Water wave kinematics*. Kluwer, Dordrecht, 1990, 535-549.
- Synolakis, C.E.** The runup of solitary waves. *J. Fluid Mech.*, 1987, vol. 185, 523-545.

WIND-FORCED MODULATIONS OF GRAVITY WAVES

S. LEBLANC¹, H. BRANGER³, M. FRANCIUS¹, F. GOLAY², C. KHARIF³

¹LSEET/CNRS/INSU, ²IMATH, Université de Toulon, France

³IRPHE/CNRS, Universités d'Aix-Marseille, France

Summary The effect of wind on modulational instability of gravity waves is presented. A forced nonlinear Schrödinger equation that governs the evolution in deep water of weakly nonlinear packets of surface gravity waves under wind forcing is derived. Stokes waves are shown to grow exponentially following Miles' linear mechanism, while modulational instability becomes explosive. These analytical results are completed by numerical simulations and experiments showing the amplification of modulations by wind. Therefore, we suggest that wind boosts the formation of rogue waves.

INTRODUCTION

In 1957, Miles [1] discovered a linear mechanism for the amplification of infinitesimal wavy disturbances at the interface between air and water when wind blows. Ten years later, Benjamin and Feir [2] and Zakharov [3] discovered independently the modulational instability of a finite amplitude wave train. While the modulational instability has been observed both experimentally and numerically [4], the effect of wind on this latter remains a matter of controversy. Indeed, experimental results show either suppression [5] or enhancement [6] of modulations, while numerical models predict either amplification [7] or downshifting [8].

THE FORCED NLS EQUATION AND EXPLOSIVE MODULATIONS

Theoretically, some progress has been made recently for modulational instability under wind forcing [9]. Let

$$\eta(x, t) = \text{Re}\{a(x, t)e^{i(kx - \omega t)}\} + O(|a|^2) \quad (1)$$

be the surface elevation of a narrow-banded gravity wave packet modulated around a carrier wave with wavenumber $|k|$ and frequency $\omega = \sqrt{g|k|}$, that propagates in deep water under the forcing of a steady wind with velocity profile $U(z)$ along the x -direction, and such that $U(0) = 0$. Let $\delta = \rho_a/\rho_w$ be the density ratio between air and water ($\delta = 1.29 \times 10^{-3}$), both assumed inviscid. The amplitude of the wave packet is governed by the forced NLS equation [7, 8, 9]

$$i(\partial_t a + c_g \partial_x a) - (\omega/8k^2)\partial_{xx} a - (\omega k^2/2)|a|^2 a = \frac{1}{2}\omega(\alpha + i\beta)a, \quad (2)$$

where $c_g = \partial_k \omega$ is the group velocity, and α and β are real numbers defined such that $\alpha + i\beta = \delta(\chi'_0/k + U'_0/\omega - 1)$, using the notation $f'_0 = (\partial_z f)|_{z=0}$. The function $\chi(z)$ solves Rayleigh equation in the air ($z > 0$):

$$(U - c)(\chi'' - k^2\chi) - U''\chi = 0, \quad c = \omega/k, \quad (3)$$

with boundary conditions $\chi(0) = 1$ and $\chi(\infty) = 0$. Integration of (3) yields $\beta = 0$ except if there exists a critical height z_c such that $U_c = U(z_c) = \omega/k$. In that case, according to Miles [1], $\beta = -\pi\delta U''_c|\chi_c|^2/|kU'_c|$ so that $\beta > 0$ for usual wind profiles ($U''(z) < 0$). Therefore, the wave with wavenumber k grows exponentially with time in the linear regime.

In the weakly nonlinear regime, it is convenient to recast (2) as

$$2iA_T - \frac{1}{4}A_{XX} - |A|^2 A = i\beta A, \quad (4)$$

where $T = \omega t$, $X = k(x - c_g t)$, and $A(X, T) = ka(x, t)e^{i\omega\alpha t}$. If $\beta = 0$ (no wind forcing), the usual NLS equation is recovered and Stokes wave is described by the homogeneous solution $A(T) = R_0 e^{i(\Theta_0 - R_0^2 T/2)}$. With wind forcing ($\beta > 0$), Stokes wave becomes $A(T) = R_S(T)e^{i\Theta_S(T)}$ where: $R_S(T) = R_0 e^{\beta T/2}$ and $\Theta_S(T) = \Theta_0 - \frac{1}{2}R_S^2(T)/\beta$ so that it grows exponentially with time without saturation.

If we now disturb this solution by setting $|A(X, T)| = R_S(T)(1 + \lambda(T) \cos(KX))$, Eq. (4) yields, upon linearization:

$$\lambda''(T) + \gamma(\gamma - R_0^2 e^{\beta T})\lambda(T) = 0, \quad \gamma = \frac{1}{8}K^2. \quad (5)$$

If $\beta = 0$, the disturbance grows exponentially when $0 < \gamma < R_0^2$: this is the modulational instability [2, 3]. If $\beta > 0$, the solution of (5) may be expressed in terms of modified Bessel function and, for large time [9]:

$$\lambda(T) \sim 2e^{f(T)}/\sqrt{2\pi f(T)}, \quad f(T) = 2\gamma^{\frac{1}{2}}R_0 e^{\beta T/2}. \quad (6)$$

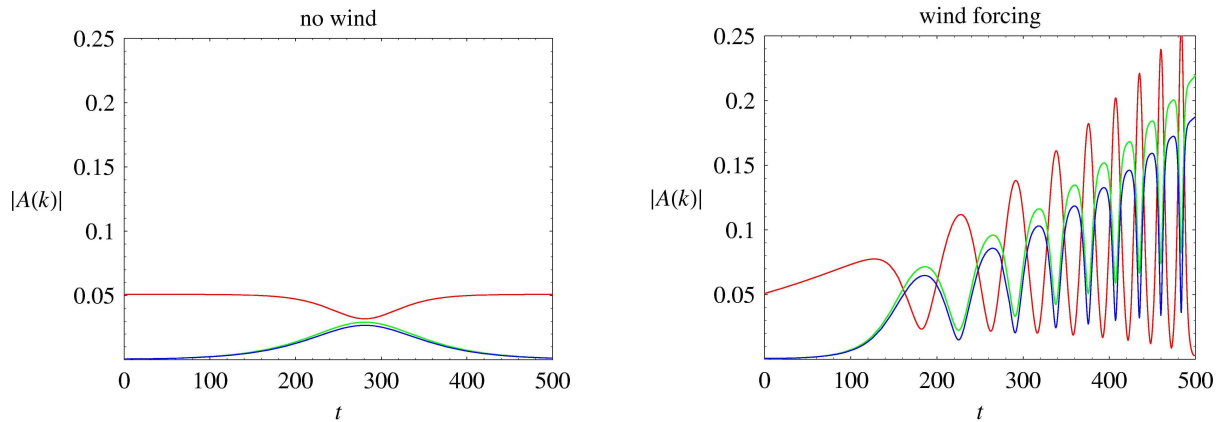
Thus, the modulations grow *superexponentially* under fair wind. The growth is however so rapid that nonlinear effects not considered here should rapidly interact. This is perhaps the reason why this surprising behavior have not been observed in experiments. Furthermore, the validity of the present approach is restricted to steepnesses $|ka|$ of order $\sqrt{\delta}$; above, higher order approximations or numerical computations are needed.

NUMERICAL COMPUTATIONS AND EXPERIMENTAL RESULTS

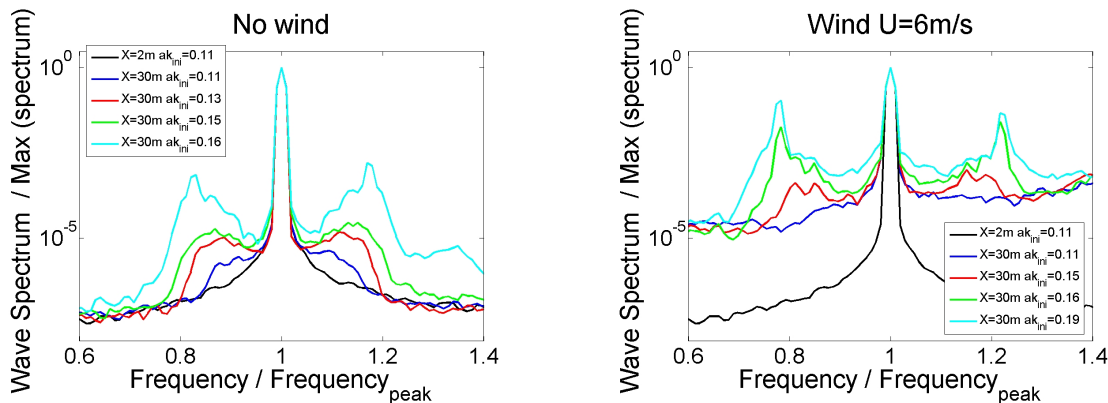
To test the validity of the linear results mentioned above, numerical simulations of the forced Zakharov equation [7]:

$$i\partial_t A_{\mathbf{k}} - \omega_{\mathbf{k}} A_{\mathbf{k}} - \int_{\mathbf{k}+\mathbf{p}=\mathbf{q}+\mathbf{r}} T_{\mathbf{k},\mathbf{p},\mathbf{q},\mathbf{r}} A_{\mathbf{p}}^* A_{\mathbf{q}} A_{\mathbf{r}} d\mathbf{p}d\mathbf{q}d\mathbf{r} = \frac{1}{2}\omega_{\mathbf{k}}(\alpha_{\mathbf{k}} + i\beta_{\mathbf{k}})A_{\mathbf{k}}, \quad (7)$$

have been performed for three modes. Here, $A_{\mathbf{k}}$ is Zakharov canonical variable [3] and T is Krasitskii's nonlinear transfer term. Figure below on the left shows the evolution of a Stokes wave with steepness 0.1 and wavenumber $|\mathbf{k}| = 1.97 \text{ m}^{-1}$ (in red), disturbed by two sideband disturbances (blue and green) that grow with time owing to modulational instability and then decreases in a recurrent way [4]. In the presence of wind (right), Stokes waves in red starts to grow exponentially with rate $\frac{1}{2}\omega\beta$ according to the theory exposed previously (here, $\beta \approx 7.5 \times 10^{-3}$). Then, the two disturbances (blue and green) grow suddenly much faster than Stokes wave, in fact close to the predicted superexponential growth. Then, nonlinearity makes its job, resulting in the acceleration of the cycles of modulation/demodulation. At larger times, energy must saturate either by breaking or by quenching of the wind profile [10], effects that are taken into account neither in (2) nor in (7). Such effects are actually under investigation, as far as computations based on the fully coupled Euler equations.



Experiments have been conducted in the large air-sea interaction facility of the IRPHE laboratory in Marseille. The water tank is 40 m long, 3 m wide, 1 m deep and the height of the aerodynamical flow above the water surface is 1.5 m. The wind velocity can be adjusted from 0.5 to 14 m/s. Mechanical waves in the frequency range 1 to 2 Hz with various amplitudes can be generated by a completely immersed wavemaker. We performed several runs with regular mechanical generated waves, with different steepness. Experiments were first conducted without wind, then with a $U = 6 \text{ m/s}$ wind blowing over the paddle waves. Waves were recorded with two capacitance wave gauges located at 2 m and 30 m away from the wavemaker. The last two figures show the normalized frequency spectrum of the water elevation for different initial wave steepness. Obviously, at 30 m away from the wavemaker, there is a large increase of the Benjamin-Feir side-band instabilities due to the presence of the wind.



- [1] Miles J.W.: On the generation of surface waves by shear flows. *J. Fluid Mech.* **3**:185, 1957.
- [2] Benjamin T.B., Feir J.E.: The disintegration of wave trains on deep water. *J. Fluid Mech.* **27**:417, 1967.
- [3] Zakharov V.E.: Stability of periodic waves of finite amplitude on the surface of a deep fluid. *J. Appl. Mech. Tech. Phys.* **2**:190, 1968.
- [4] Dias F., Kharif C.: Nonlinear gravity and capillary-gravity waves. *Ann. Rev. Fluid Mech.* **31**: 301, 1999.
- [5] Bliven L.F. *et al.*: Experimental study of the influence of wind on Benjamin-Feir sideband instability. *J. Fluid Mech.* **162**:237, 1986.
- [6] Waseda T., Tulin M.P.: Experimental study of the stability of deep-water wave trains including wind effects. *J. Fluid Mech.* **401**:55, 1999.
- [7] Krasitskii V.P., Makin V.K.: Stochastization of surface gravity waves generated by an induced pressure field. *Okeanologia* **27**:905, 1987.
- [8] Hara T., Mei C.C.: Frequency downshift in narrow-banded surface waves under the influence of wind. *J. Fluid Mech.* **230**:429, 1991.
- [9] Leblanc S.: Amplification of nonlinear surface waves by wind. *Phys. Fluids* **19**:101705, 2007.
- [10] Janssen P.A.E.M.: The interaction of ocean waves and wind. *Cambridge University Press*, 2004.

Directional dispersion effects on kurtosis for freak wave prediction

Nobuhito Mori, Miguel Onorato and Peter A.E.M. Janssen

Disaster Prevention Research Institute, Kyoto University,
Gokasho, Uji 611-0011, Japan mori@oceanwave.jp

Università di Torino, Dip. di Fisica Generale,
Via P. Giuria, 1 - Torino 10125, Italy
onorato@ph.unito.it

European Centre for Medium-Range Weather Forecasts,
Shinfield Park, Reading RG2 9AX, UK
Peter.Janssen@ecmwf.int

Abstract. Based on the Monte Carlo simulation of the two-dimensional Nonlinear Schrödinger equation, the dependence of the kurtosis on the directional energy distribution is examined numerically. The parametric survey is carried out to obtain the behavior of kurtosis as functions of Benjamin-Feir index and directional spread in directional sea states. As directional dispersion effect becomes significant, the kurtosis monotonically decreases in comparison with the unidirectional waves. A parametrization of the kurtosis estimated from directional spectra is here proposed.

Nomenclature

BFI	Benjamin-Feir Index
MCNLS	Monte Carlo simulation of Nonlinear Schrödinger equation
A	Wave amplitude
T	Wave period
ϵ	Wave steepness
ω	Angular frequency [rad]
θ	Direction [rad]
μ_4	Fourth order moment of surface elevation
κ_{40}	Fourth order cumulant of surface elevation ($\kappa_{40} = \mu_4 - 3$)
σ_ω	Frequency spectrum bandwidth
σ_θ	Directional spectrum bandwidth
δ_ω	Normalized frequency spectrum bandwidth by characteristic angular frequency
δ_θ	$= \sigma_\theta$
σ	Directional spread

1 Introduction

Freak wave studies started in the late 80's [1] and the high-order nonlinear effects on the freak waves were discussed in the early 90's Coastal Engineering Conference [2, 3]. The evidence of freak wave generation in the real ocean were reported by analyzing field data of the North Sea [4], the Sea of Japan [5, 6] and the Gulf of Mexico [7]. Due to the many research efforts, the occurrence of freak waves, their mechanism and detailed dynamic properties are now becoming clear. The state of the art on freak waves is summarized in [8].

Freak wave generation is sometimes discussed in the context of the Benjamin-Feir instability [9]. Janssen (2003) [10] found that the ratio between the steepness, a measure of the nonlinearity and the spectral band-width, a measure of the dispersion, is an important parameter for determining the probability of finding a large wave. After Janssen (2003) [10] this ratio between nonlinearity and dispersion has been named the Benjamin-Feir-Index, BFI:

$$\text{BFI} = \frac{\sqrt{2} \epsilon}{\Delta} \quad (1)$$

$$\kappa_{40} = \frac{\pi}{\sqrt{3}} \text{BFI}^2 \quad (2)$$

where ϵ and Δ are the characteristic wave steepness and bandwidth of frequency spectrum, and κ_{40} is the fourth order cumulant of the surface elevation which equals to kurtosis minus three, respectively. The final result is that the kurtosis depends on the square of the BFI. The role of the skewness in the wave height distribution is less important with respect to kurtosis. The skewness comes usually as a result of second order corrections (bound modes) and is weakly affected by the dynamics of free waves [11]. In Mori and Janssen (2006) [12] the formal relations between the kurtosis, the exceedance probability for wave height and occurrence probability of freak wave have been discussed. The kurtosis enters in the distribution function as a correction to the Rayleigh distribution: when the kurtosis tends to three, the expected Gaussian values, then the distribution function tends to the Rayleigh distribution. In this context, the changes in the kurtosis can be evaluated once the evolution of the wave spectrum is known. These analytical frame works were verified by the large scale wave experiments with unidirectional waves and well predicts the spatial developments of the kurtosis, the wave height distribution and the maximum wave height distribution in the wave tank [13]. Thus, an accurate estimation of kurtosis is important for freak wave prediction. However, recent works based on numerical simulations of envelope equations [14–17] and wave tank experiments [18, 19] have pointed out the influence of directional dispersion on the kurtosis evolution in deep-water. These results show that the directional dispersion effects suppress the kurtosis enhancement in directional sea states. Therefore, it is required a general expression of kurtosis estimation from the directional spectra, quantitatively.

The purpose of the present paper is to present a formula for the kurtosis as an extension of Eq.(1) and Eq.(2) including directional dispersion effects. First,

the Monte Carlo simulations using the cubic nonlinear Schrödinger equation with two dimensional Gaussian spectra are described. Second, the kurtosis estimation formula in the directional sea states is proposed,

2 Numerical method and conditions

For a weakly nonlinear narrow band wave train, the two-dimensional Nonlinear Schrödinger equation (NLS2D) equation can be derived from the potential Euler equation. The NLS2D has the following form:

$$i \left(\frac{\partial A}{\partial t} + \frac{\omega_0}{2k_0} \frac{\partial A}{\partial x} \right) - \frac{\omega_0}{8k_0^2} \frac{\partial^2 A}{\partial x^2} + \frac{\omega_0}{4k_0^2} \frac{\partial^2 A}{\partial y^2} - \frac{1}{2} \omega_0 k_0^2 |A|^2 A = 0 \quad (3)$$

where k_0 and ω_0 are the principal wave number and the angular frequency, respectively, and A is the wave envelope and is related to the free surface as follows:

$$\eta(x, y, t) = A(x, y, t) \exp[i(k_0 x - \omega_0 t)] + c.c. \quad (4)$$

In the past it has been found [20] that the instability region for a plane wave solution of the NLS2D equation is unbounded; as a result numerical simulations of the NLS2D show an unphysical energy leakage towards high wave numbers. A higher order Nonlinear Schrödinger equation in two horizontal dimensions has been derived by Trulsen and Dysthe (1996) [21]. The NLS2D is valid on the Benjamin-Feir time scale, i.e. $t \ll O(1/\omega_0 \epsilon^2)$, while the higher order NLS2D is valid on a much longer time scale than the original NLS2D [14]. Our aim is here to investigate the formation of extreme waves on a time scale of the Benjamin-Feir instability in the weakly nonlinear directional sea states, therefore to reduce the computational cost, we have used the NLS2D equation.

A series of runs has been carried out to obtain statistically stable relations of kurtosis with different initial conditions. The computational domain was set to $128L_0 \times 128L_0$ in both x and y directions where L_0 is the characteristic wave length. Wave numbers are normalized by k_0 both in k_x and k_y direction. The initial condition for the simulations is provided by the following two-dimensional Gaussian spectrum:

$$E(\omega, \theta) d\omega d\theta = \frac{1}{2\pi\sigma_\omega\sigma_\theta} \exp \left\{ -\frac{1}{2} \left[\left(\frac{\omega - \omega_0}{\sigma_\omega} \right)^2 + \left(\frac{\theta - \theta_0}{\sigma_\theta} \right)^2 \right] \right\} \quad (5)$$

where θ is directions, σ_ω and σ_θ are measure of spectrum width both ω and θ , and θ_0 is the principal wave direction. The initial wave steepness was set at 0.07 to keep a weakly nonlinear condition, and $\theta_0 = 0$ was selected for simplicity. According to previous studies, the normalized spectrum bandwidth can be expressed as

$$\delta_\omega = \frac{\sigma_\omega}{\omega_0} \quad (6)$$

$$\delta_\theta = \sigma_\theta \quad (7)$$

In addition, the directional spread s of Eq.(5) can be obtained analytically.

$$s = \Delta_\theta = \sqrt{\int d\theta \theta^2 D(\theta)} = \sigma_\theta \quad (8)$$

where $D(\theta)$ is directional distribution. Therefore, σ_θ of Eq.(5) is equal to the standard directional spread and is measured in radians.

Changing σ_ω and σ_θ (BFI and σ_θ from 0 to 1 with step of 0.05, respectively), a series of 300 ensemble with the same initial condition except initial phases was conducted each case. The total number of simulations were 120,000 to obtain following results. The Monte Carlo simulations using the Nonlinear Schrödinger equation will be denoted MCNLS for simplicity hereafter. The MCNLS can gives good relationship between BFI and kurtosis in comparison with the Zakharov equation for the unidirectional waves with relatively small BFI (BFI < 1, see Janssen (2003) [10]).

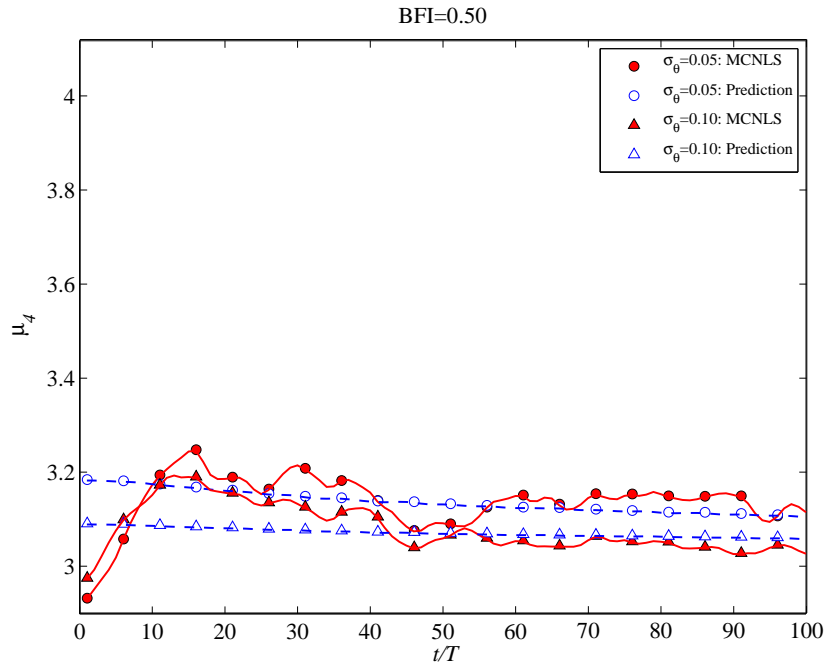
3 Kurtosis estimation by MCNLS

Fig.2 shows examples of temporal evolution of the kurtosis. The solid lines in Fig.2 are instantaneous values of the kurtosis calculated from the surface elevation; the dashed lines are the prediction using what we call the *effective* BFI, *i.e.* the BFI calculated from Eq.(1) where the spectral bandwidth is estimated only in the main direction of propagation. For the small BFI, see panel (a), the kurtosis changes are smaller with respect to the large BFI condition in panel (b). This results is consistent with previous results obtained for unidirectional waves. The values of the kurtosis significantly increase on a time scale of 10 to 40 periods and then decrease. Similar results are observed for unidirectional wave simulations. The difference between $\sigma_\theta = 0.05$ and $\sigma_\theta = 0.10$ is significant for BFI=1.0 but it is less relevant for BFI=0.5. The maximum value of the kurtosis calculated from the initial spectrum using the *effective* BFI is in fairly good agreement with numerical simulations

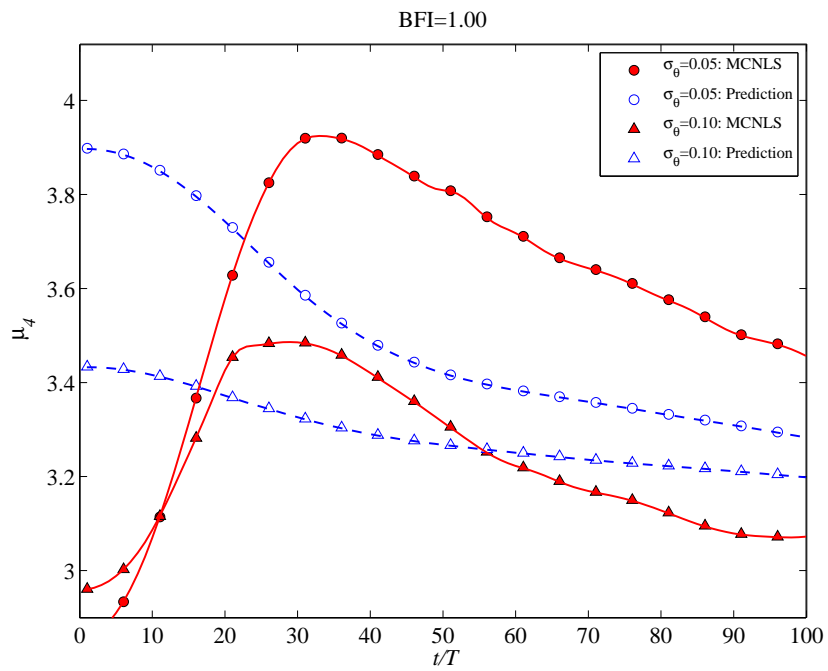
Fig.3 shows the maximum value of the kurtosis obtained from MCNLS as a function of BFI and σ_θ (a similar plot is shown in [17] with different variables) . As the directional dispersion effects become significant ($\sigma_\theta \rightarrow 1$), the kurtosis decreases. The reduction of kurtosis is monotonic as σ_θ increases. Similar results were obtained numerically [17] and experimentally [18, 19].

As shown in Fig.2, the expected value of kurtosis in the directional wave states can be estimated by Eq.(1), if we used *effective* BFI. Following this idea, it is assumed that only the principal direction of spectrum components contributes to the kurtosis change. Assuming the 2D Gaussian spectra as Eq.(5), starting from Eq.(5) and considering only the main direction of propagation, we can derive the effective BFI for the 2D Gaussian spectrum

$$\text{BFI}_0 = \frac{\text{BFI}}{(2\pi)^{1/4} \sigma_\theta^{1/2}}. \quad (9)$$



(a) BFI = 0.5 (circle: $\sigma_\theta = 0.05$, triangle: $\sigma_\theta = 0.10$)



(b) BFI = 1.0 (circle: $\sigma_\theta = 0.05$, triangle: $\sigma_\theta = 0.10$)

Fig. 1. Time evolution of kurtosis (solid line: instantaneous kurtosis from wave profile, dashed line: estimated kurtosis by Eq.(1) from wave spectra)

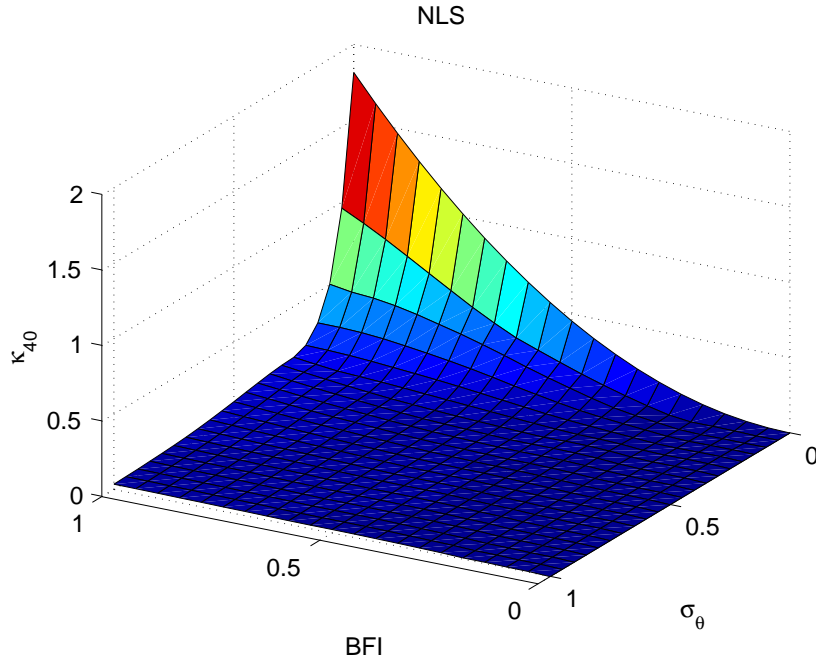


Fig. 2. The ensemble averaged maximum value of kurtosis dependence on BFI and σ_θ by MCNLS for multi-directional waves

Substituting Eq.(9) into Eq.(1) yields:

$$\kappa_{40} = \frac{\pi}{\sqrt{3}} \text{BFI}_0^2 = \frac{\pi}{\sqrt{6\pi}} \frac{\text{BFI}^2}{\sigma_\theta} \quad (10)$$

Thus, the kurtosis is proportional to the inverse of σ_θ . Keeping the similar relation to Eq.(10) but introducing two empirical coefficients to fit Fig.3 more accurately, we have

$$\kappa_{40} = \frac{\pi}{\sqrt{3}} \text{BFI}^2 \left(\frac{1}{1 + b\sigma_\theta} \right)^c \quad (11)$$

where $b=7.68$ and $c=2.06$ are the empirical coefficients and were estimated by the least-square method. The empirical curve is shown in Fig.3. The maximum difference between the kurtosis simulated by the MCNLS and Eq.(11) is less than 0.1 and it corresponds to an error of about 3% in average and 10% error maximum. Eq.(11), therefore, represents a useful estimation of the kurtosis from directional spectra.

As indicated above figures, the kurtosis changes in time. To verify the kurtosis estimation formula, BFI and σ_θ relation by the field data, it is difficult to observe such an evolution and only time-averaged characteristic can be obtained by field observations. Fig.4 shows the mean and standard deviation of the

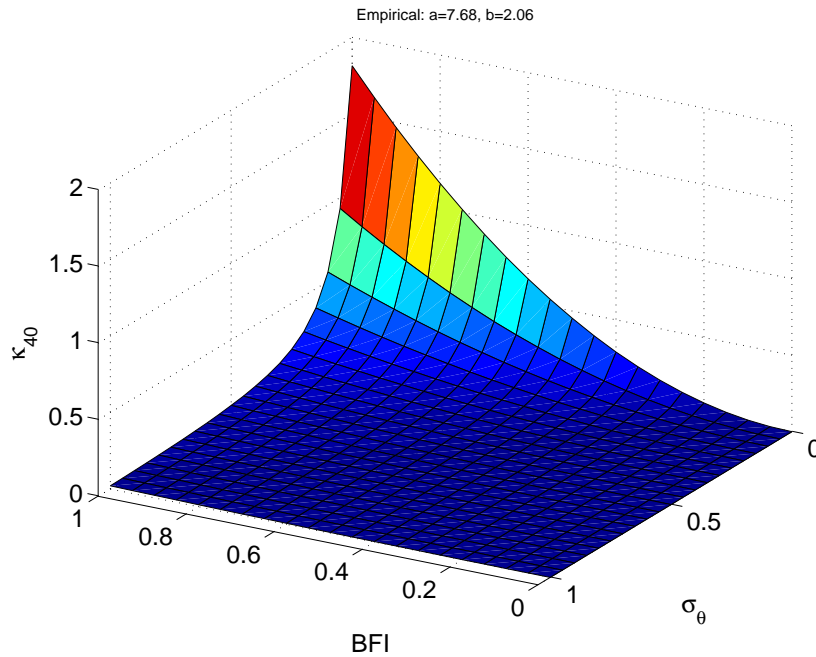


Fig. 3. The empirical fit for Fig.3

kurtosis obtained from the MCNLS as functions of BFI and σ_θ . Basically, they are quite similar distribution and magnitude. Therefore, the kurtosis during the propagation can be changed significantly. On the other hand, the mean of kurtosis is much smaller than its maximum value (see Fig.3). These temporal features of the kurtosis make the verification of the theory by field observations very difficult.

4 Conclusion

In this study, the directional dispersion effects on the kurtosis have been investigated. Based on numerical simulations of the Nonlinear Schrödinger equation, a formula for the kurtosis has been presented for directional sea states as functions of BFI and directional spectrum bandwidth (or directional spread). The reduction of the kurtosis is monotonic as the directional bandwidth σ_θ increases.

The careful and quantitative validation of the kurtosis estimation in fields will be required near future.

Acknowledgment

This work was partially supported by Grant-in-Aid for Scientific Research by JSPS.

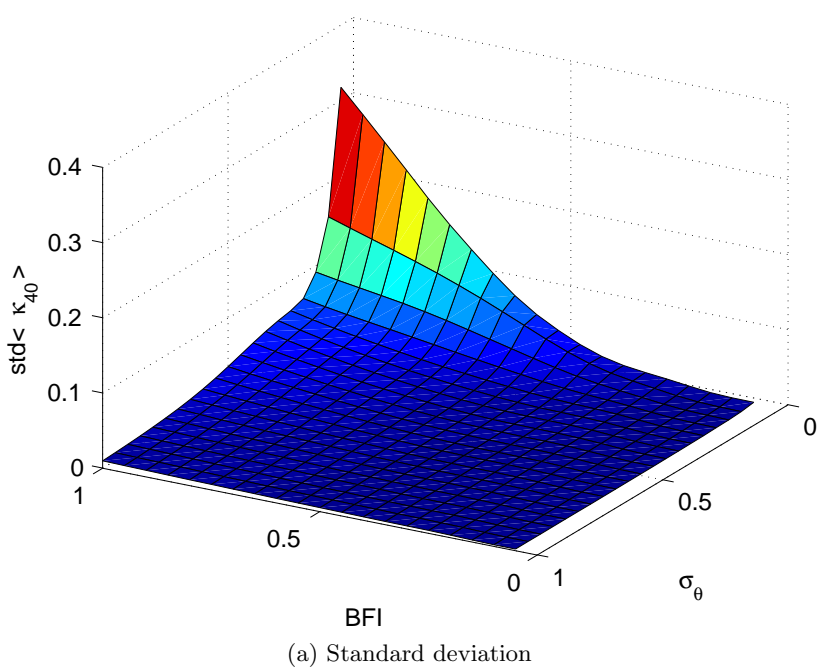
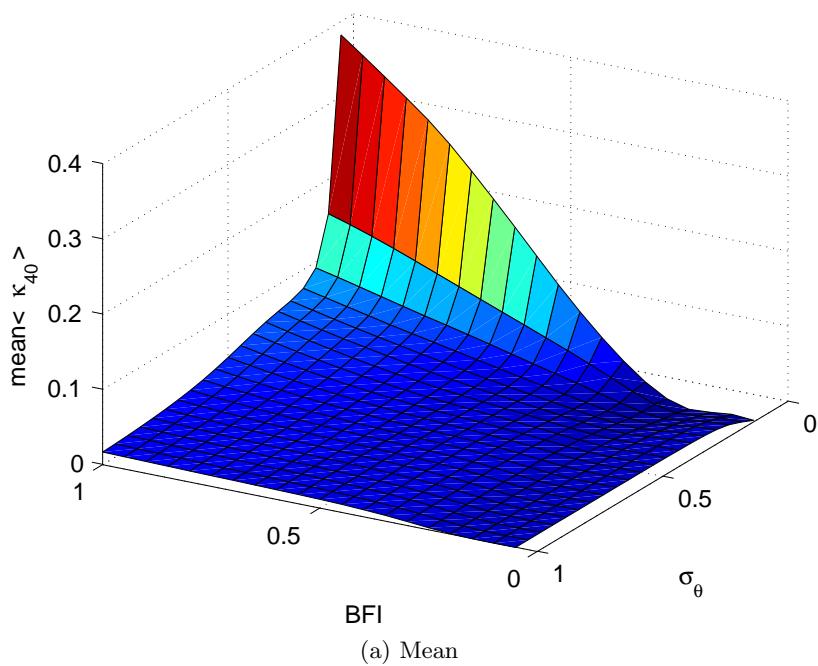


Fig. 4. Dependence of mean and standard deviation of kurtosis on BFI and σ_θ by MCNLS

References

1. R.G. Dean. Freak waves: a possible explanation. In A. Tørum and O.T. Gudmestad, editors, *Water wave kinematics*, pages 609–612. Kluwer Academic Pub., 1990.
2. T. Yasuda, N. Mori, and K. Ito. Freak waves in a unidirectional wave train and their kinematics. In *Proc. of the 23th Int. Conf. on Coastal Eng.*, volume 1, pages 751–764, Venice, 1992. ASCE.
3. T. Yasuda and N. Mori. High order nonlinear effects on deep-water random wave trains. In *International Symposium: Waves-Physical and Numerical Modelling*, volume 2, pages 823–332, Vancouver, 1994.
4. G. Guedes Soares, Z. Cherneva, and E.M. Antao. Characteristics of abnormal waves in North Sea storm sea steas. *Applied Ocean Research*, 25:337–344, 2003.
5. T. Yasuda and N. Mori. Occurrence properties of giant freak waves the sea area around Japan. *Journal of Waterway, Port, Coastal, and Ocean Engineering*, 123(4):209–213, 1997.
6. T. Yasuda, N. Mori, and S. Nakayama. Characteristics of giant freak waves observed in the Sea of Japan. In *Waves97*, pages 482–495, Virginia, VA, 1997.
7. G. Guedes Soares, Z. Cherneva, and E.M. Antao. Abnormal waves during hurricane Camille. *Journal of Geophysical Research*, 109:C08008, 2004.
8. K. Dysthe, H.E. Krogstad, and P. Müller. Oceanic Rogue Waves. *Annual Review of Fluid Mechanics*, 40:in print, 2008.
9. M. Onorato, A.R. Osborne, M. Serio, and S. Bertone. Freak waves in random oceanic sea states. *Physical Review Letters*, 86(25):5831–5834, 2001.
10. Peter A.E.M. Janssen. Nonlinear four-wave interactions and freak waves. *Journal of Physical Oceanography*, 33(4):863–884, 2003.
11. M. Onorato, A.R. Osborne, and M. Serio. On deviations from Gaussian statistics for surface gravity waves. In *Proceedings Rogue Waves, Hawaiian Winter Workshop*, pages 79–83, 2005.
12. N. Mori and P.A.E.M. Janssen. On kurtosis and occurrence probability of freak waves. *Journal of Physical Oceanography*, 36(7):1471–1483, 2006.
13. N. Mori, M. Onorato, Peter A.E.M. Janssen, Alfred R. Osborne, and Marina Serio. Exceedance probability for strongly nonlinear long crested waves. *Journal of Geophysical Research*, page doi:10.1029/2006JC004024, 2007.
14. K.B. Dysthe, K. Trulsen, H.E. Krogstad, and H. Socquet-Juglard. Evolution of a narrow-band spectrum of random surface gravity waves. *Journal of Fluid Mechanics*, 478:1–10, 2003.
15. H. Socquet-Juglard, K. Dysthe, K. Trulsen, Krogstad H.E., and Liu J. Probability distribution of surface gravity waves during spectral changes. *Journal of Fluid Mechanics*, 542:195–216, 2005.
16. M. Onorato, A.R. Osborne, and M. Serio. Extreme wave events in directional, random oceanic sea states. *Physical Review Letters*, 96:No.014503, 2006.
17. Odin Gramstad and Karsten Krulsen. Influence of crest and group length on the occurrence of freak waves. *Journal of Fluid Mechanics*, 582:463–472, 2007.
18. T Waseda. Impact of directionality on the extreme wave occurrence in a discrete random wave system. In *The 9th Wave Workshop*, page 10p., 2006.
19. M. Onorato, L. Cavaleri, S. Fouques, O. Gramstad, and P. A. E. M. Janssen. Statistical properties of mechanically generated surface gravity waves: a laboratory experiment in a 3d wave basin. *Journal of Fluid Mechanics*, page in press, 2009.
20. H.C. Yuen and B.M. Lake. Nonlinear dynamics of deep-water gravity waves. *Advances in Applied Mech.*, 22:67–327, 1982.

21. K. Trulsen and K.B. Dysthe. A modified nonlinear Schrödinger equation for broader bandwidth gravity waves on deep water. *Wave Motion*, 24(3):281–289, 1996.

Preliminary Simulation of Wind Effects on 3D Freak Waves

Q.W. Ma (q.ma@city.ac.uk) and S. Yan (s.yan@city.ac.uk)
School of Engineering and Mathematical Sciences, City University, UK

Introduction

Freak waves have attracted a lot of attention from scientists and engineers as they pose a real threat to human activities in oceans. A great deal of effort has been made to experimentally and numerically study the generation mechanisms and the physical properties of freak waves (e.g. Baldock, Swan & Taylor, 1996; She, Greated & Easson, 1997). Detailed reviews may be found in Kharif & Pelinovsky (2003). However, effects of wind, as a main source of wind wave field, have received less attention, though evidence has indicated that freak waves are often accompanied by strong winds. Only very recently, the possible effects of wind on freak waves have been considered by Giovanangeli et al (2004), Touboul et al. (2006) and Kharif et al. (2008), performing experimental and numerical analysis. Their numerical analysis is based on the fully nonlinear potential flow theory (FNPT) with the wind effects modelled by empirical wind pressure on the free surface (Jerreys' sheltering formula). Using the numerical model, they investigated the wind effects on freak waves due to spatio-temporal focusing mechanism and modulational instability. Although they presented very impressive results, these are all for two-dimensional cases and their numerical model could not take full account of viscous effect. Our work focuses on wind effects on 3D freak waves with considering the viscosity in a more precise way. Some progress in this direction is reported here.

Numerical Approach and Results

The approach adopted in our work is to combine the StarCD with our QALE-FEM method based on the FNPT model. The StarCD solves general Reynolds-Averaged Navier-Stokes equations for air and water by using the finite volume method. The free surface is identified by using the Volume of Fluid (VOF) method. The software can fully consider viscous effect without need of empirical model for pressure. However, it is not computationally efficient, particularly in cases with a large domain. Furthermore, it can suffer from numerical diffusion, spuriously removing the energy from waves. The QALE-FEM, recently developed by the authors of this paper, has been successfully used to model 2D and 3D freak waves without winds and has been proved to be very efficient for nonlinear waves (Yan & Ma, 2008). The main idea of our approach is that in the area where waves are small or wind effects can be accurately modelled by Jerreys' sheltering formula, our QALE-FEM model is applied while in the area where wind effects require more precisely modelling, the StarCD is employed. This approach can take advantages of both models and overcome their drawbacks. To achieve this needs to tackle several challenges, such as how to combine the StarCD with the QALE-FEM, when or where to start use of StarCD and so on. We are on the way toward the goal. Some intermediate results are presented in abstract and more results will be discussed in the workshop.

The first case is about 3D directional focusing freak waves generated using a snake-type wavemaker with parameters of $N_\theta=30$, $\theta_{\max}=45^\circ$, $\omega_i=1.0$ and $a_i=0.01$. The details of the freak wave generation and corresponding parameters may be found in Fochesato, Grilli & Dias (2008) and (Yan & Ma, 2008). The numerical tank has length of $22d$ and width of $30d$, where d is the water depth. The wind speed is taken as $4\sqrt{gd}$. The main purpose of this case is to preliminarily look at the property of wind effects on 3D freak waves. Therefore the QALE-FEM is applied for the whole domain (the area for StarCD code is 0) with wind effects modelled by Jerreys' sheltering formula modified for 3D waves. Fig.1 illustrates the free surface profile at $\tau \approx 29\sqrt{d/g}$. To show the wind effect, the corresponding result without wind is also plotted in the figure. It can be seen that the wind mainly and significantly affects the high wave crests in the 3D freak waves.

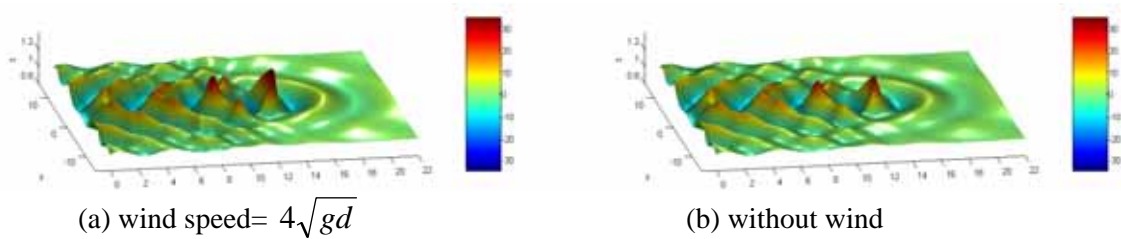


Fig.1 3D freak waves with or without wind blowing at $\tau \approx 29\sqrt{d/g}$
 ($N_\theta=30$, $\theta_{\max}=45^\circ$, $\omega_i=1.0$ and $a_i=0.01$, colour bar representing ζ/a_i)

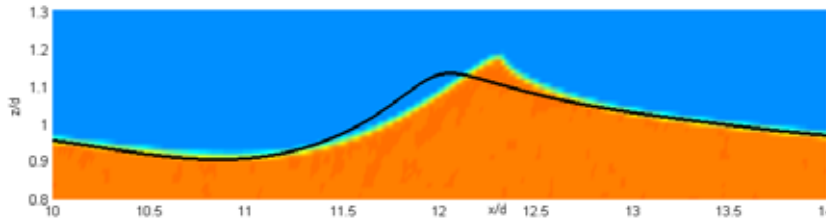


Fig. 2 2D freak wave profiles at $\tau \approx 56\sqrt{d/g}$ with or without wind blowing
 (solid curve: wind speed=0; yellow column: wind speed= $2\sqrt{gd}$)

In the second case, a 2D spatio-temporal freak wave is generated by a piston wavemaker. The detail of the motion of the wavemaker can be found in Ma (2007). 32 individual wave components with frequency ranging from $0.8683\sqrt{g/d}$ to $1.8865\sqrt{g/d}$ and amplitude of $0.00465d$ are used. The length of tank is $20d$. The StarCD is used in range of $5 < x < 15$ and the QALE-FEM is applied in other areas. Fig. 2 shows the free surface profiles for the case without wind and for the case with wind at a speed of $2\sqrt{gd}$. The result demonstrates that under action of wind, the wave becomes higher, steeper, breaking earlier and more asymmetrical about the crest point.

Acknowledgement

This research is supported by Leverhulme Trust, UK (F/00353/G), for which the authors are most grateful.

Reference

- Baldock, TE, Swan, C, Taylor, PH (1996). "A laboratory study of non-linear surface waves on water," *Philos. Trans. R. Soc. London, Ser. A*, Vol.354, pp.1-28.
- Fochesato C, Grilli, ST, and Dias, F, (2007). "Numerical modelling of extreme rogue waves generated by directional energy focusing," *Wave Motion* Vol 44, pp 395–416.
- Giovanangeli, JP, Kharif, C., Pelinovsky, E., (2004) "Experimental study of the wind effect on the focusing of transient wave groups", *Rogue Wave 2004*, Brest, France (<http://www.ifremer.fr/web-com/stw2004/rw/>).
- Kharif, C, Pelinovsky, E, (2003). "Physical mechanisms of the rogue wave phenomenon," *Eur. J. Mech. B / Fluid.*, 22, 603-634.
- Kharif, C., Giovanangeli, JP., Touboul, J., Grare, L., Pelinovsky, E., (2007) "Influence of wind on extreme wave events: Experimental and numerical approaches," *Journal of Fluid Mechanics*, 594, 209 – 247, 2008.
- Ma, QW, (2007). "Numerical Generation of Freak Waves Using MLPG_R and QALE-FEM Methods," *CMES*, Vol.18, No.3, pp.223-234.
- She, K, Greated, CA, and Easson, WJ (1997). "Experimental study of three-directional breaking wave kinematics," *Appl. Ocean Res.*, Vol 19, pp 329-343.
- Touboul, J, Giovanangeli, JP, Kharif, C and Pelinovsky, E (2006). "Freak waves under the action of wind: experiments and simulations," *Eur. J. Mech. - B/Fluids*, Vol. 25, pp. 662-676.
- Yan, S., Ma, QW, (2008), "Nonlinear Simulation of 3D Freak Waves Using a Fast Numerical Method", *Proceedings of Int. Offshore and Polar Engng. Conf. (ISOPE2008)*, Vancouver.

On 3-D Freak Waves Caused by Modulational Instability

Victor I. Shrira

Dept. of Mathematics, Keele University, UK

and

Vladimir Geogjaev

Shirshov Institute for Oceanology, Moscow, Russia

One of the very few physical mechanisms identified so far as responsible for formation of freak waves in the absence of "special external factors" is the modulational (Benjamin-Feir) instability. Sufficiently narrow-banded wave fields are known to be modulationally unstable. The issue was extensively studied theoretically and numerically (e.g. [Tanaka(1990), Osborne et al.(2000), Onorato et al.(2001), Slunyaev et al.(2002), Dyachenko & Zakharov(2005), Janssen(2003)]), who showed that, indeed, the BF instability might lead to emergence of freak waves. There is also some experimental evidence suggesting a link between the probability of freak waves and the BF instability. However most of the theoretical studies were confined to one dimensional models and what happens in two spatial dimensions is still very poorly understood.

In the present work we study essentially three-dimensional freak waves which emerge as a result of the modulational instability within the framework of the Davey-Stewartson (DS) equation for water of moderate depth [Davey & Stewartson(1974)]. The set of assumptions is standard: ideal fluid, narrow-band wave packet, deterministic setting, asymptotic expansion in powers of small nonlinearity parameter. Although the model is weakly nonlinear it captures the basic physics of the phenomenon. Often the particular classes of the exact solutions of the 1-D nonlinear Schrödinger equation (the Akhmediev and Ma breathers and their limiting case the Peregrine soliton) are viewed as plausible weakly nonlinear 'prototypes' to freak waves (see, e.g., [Dysthe & Trulsen(1999)]). The question we investigate is how such solutions interact in 3D system when several different modulations propagate all having different angles with respect to the group velocity of the packet. By constructing an exact 'N-breather' solution we investigate the properties and peculiarities of such interactions.

References

- [Davey & Stewartson(1974)] DAVEY, A. & STEWARTSON, K. 1974 On three-dimensional packets of surface waves. *Proc. R. Soc. London A* **338**, 101–110.
- [Dyachenko & Zakharov(2005)] DYACHENKO, A.I. & ZAKHAROV V. E. 2005 Modulational instability of Stokes waves \rightarrow freak wave. *JETP Lett.* **81**, 255-259.
- [Dysthe & Trulsen(1999)] DYSTHE, K. B. & TRULSEN, K. 1999 Note on breather type solutions of the NLS as models for freak-waves. *Phys. Scripta* **T82**, 48–52.
- [Janssen(2003)] JANSSEN, P. A. E. M. 2003 Nonlinear four-wave interactions and freak waves. *J. Phys. Oceanogr.* **33**, 863–884.
- [Onorato et al.(2001)] ONORATO, M. OSBORNE, A. R., SERIO, M. & BERTONE, S. 2001 Freak waves in random oceanic sea states. *Phys. Rev. Lett.* **86**, 5831–5834.

- [Osborne et al.(2000)] OSBORNE, A.R., ONORATO, M. & SERIO, M. 2000 The nonlinear dynamics of rogue waves and holes in deep-water gravity wave trains. *Phys. Let. A* **275**, 386–393.
- [Peregrine(1983)] PEREGRINE, D. H. 1983 Water waves, nonlinear Schrödinger equations and their solutions. *J Austr. math. Soc. Ser. B* **25**, 16–43.
- [Slunyaev et al.(2002)] SLUNYAEV, A., KHARIF, C., PELINOVSKY, E. & TALIPOVA, T. 2002 Nonlinear wave focusing on water of finite depth. *Physica D* **173**, 77-96.
- [Tanaka(1990)] TANAKA, M. 1990 Maximum amplitude of modulated wave train. *Wave Motion* **12**, 559–568.



Sessions III. Statistical models

First order Lagrange models for asymmetric ocean waves

Georg Lindgren & Sofia Åberg

Mathematical Statistics, Lund University

Box 118, SE-221 00 Lund, Sweden

Georg.Lindgren@matstat.lu.se

WWW home page: <http://www.maths.lth.se/matstat/>

Abstract. The first order stochastic Lagrange wave model is a simple and realistic alternative to the linear Gauss wave model. However, while the produced waves are crest-trough asymmetric, they are still statistically front-back symmetric. This symmetry depends on a simple correlation structure between the vertical and horizontal components in the simplest Lagrange model. We present a physically motivated modification that is able to generate also front-back asymmetry. We further give expressions for the exact statistical distributions of several important slope characteristics that illustrate the asymmetry, for instance the space slope at the time of a level crossing.

Introduction

Wave front steepness is one of the many characteristics that have to be considered in the safety analysis of marine vessels and structures. In general, measures of crest-trough and front-back asymmetry of irregular waves are notoriously difficult to derive from the common stochastic wave models. Empirically, asymmetry properties has drawn considerable interest, in particular when more or less continuously sampled data from offshore platforms have become available. The stochastic Lagrange model is a promising model, that agrees with observations and allows theoretical analysis of many statistical properties.

A thorough study of irregular, stochastic, Lagrange models was made by Gjørund in [5], and the theory was further developed in [3] and [13].

In a series of recent papers, [1, 2, 6, 7, 9], Lindgren and Åberg have derived the exact statistical distributions of many wave characteristics, including steepness/slope, both for the space formulation, and for the time formulation.

In this paper we describe a modified Lagrange model with forced correlation between the vertical and horizontal components. The main message is that the statistical correlations between the vertical and horizontal movements uniquely determine the exact skewness and asymmetry distributions in the stochastic Lagrange model. We restrict the analysis to unidirectional 2D waves.

1 Stochastic Lagrange models

1.1 The Gauss-Lagrange model

A Lagrange wave is a stochastic version of a Miche wave, the depth dependent modification of a Gerstner wave; [4, 11]. It describes the vertical and horizontal movements of individual water particle as functions of time t and original horizontal location u , the *reference co-ordinate*. In the first order model, components with different frequencies and wave numbers act independently, and their effects are added. We consider here only particles on the free water surface.

The *stochastic Lagrange model* is obtained by letting the vertical and horizontal displacements be correlated random processes. The vertical process, which describes elevation above the still water level and is denoted $W(t, u)$, is taken as a Gaussian process with mean zero, and so is the horizontal location, denoted $X(t, u)$. Hence, a more complete name is *Gauss-Lagrange model*.

Expressed verbally, in the stochastic Lagrange model, a particle with still water location $(u, 0)$ has, at time t , the stochastic coordinates $(X(t, u), W(t, u))$, and the height of the surface at location $X(t, u)$ is therefore equal to $W(t, u)$. The Gauss-Lagrange model is completely defined by the covariance functions

$$r^{ww}(t, u) = \text{Cov}(W(0, 0), W(t, u)) = \int_0^\infty \cos(\kappa u - \omega t) S(\omega) d\omega,$$

and $r^{xx}(t, u) = \text{Cov}(X(0, 0), X(t, u))$, $r^{wx}(t, u) = \text{Cov}(W(0, 0), X(t, u))$. Here, $S(\omega)$ is the *orbital spectrum*, and wave number $\kappa > 0$ and wave frequency $\omega > 0$ satisfy the dispersion relation, $\omega^2 = g\kappa \tanh \kappa h$, with water depth h , and g denoting the gravitational constant.

1.2 The free stochastic Lagrange model

The *free Gauss-Lagrange wave model* is the stochastic version of the Miche waves. The horizontal displacement process $X_M(t, u)$ is obtained as a linear filtration of the vertical process $W(t, u)$ with amplitude and phase response function

$$H_M(\omega) = i \frac{\cosh \kappa h}{\sinh \kappa h}, \quad (1)$$

where the subscript M stands for *Miche filtration*; [3]. Expressed as stochastic Fourier integrals, the relation between the vertical and horizontal processes is

$$W(t, u) = \int_{-\infty}^{\infty} e^{i(\kappa u - \omega t)} d\zeta(\omega),$$

$$X_M(t, u) = u + \int_{-\infty}^{\infty} e^{i(\kappa u - \omega t)} H_M(\omega) d\zeta(\omega),$$

where the complex Gaussian process $\zeta(\omega)$ has orthogonal increments such that $E(d\zeta(\omega) \cdot \overline{d\zeta(\omega')}) = \frac{1}{2} S(|\omega|)$, if $\omega = \omega'$. The cross-covariance function between the vertical and horizontal process is

$$r_M^{wx}(t, u) = \int_0^\infty \cos(\kappa u - \omega t + \pi/2) \frac{\cosh \kappa h}{\sinh \kappa h} S(\omega) d\omega.$$

1.3 The Lagrange model with linked components

In the free Lagrange model the water particles move according to the simplified hydrodynamic laws of motion, unaffected by outer forces, resulting in stochastically front-back symmetric waves. For wind driven waves this is unrealistic, and one would like to include some external influence in the interaction. A flexible approach is to replace (1) by a general response function, $H(\omega) = \rho(\omega) e^{i\theta(\omega)}$, leading to the cross-covariance function of the form

$$r^{wx}(t, u) = \int_0^\infty \cos(\kappa u - \omega t + \theta(\omega)) \rho(\omega) S(\omega) d\omega,$$

and a spectral representation with frequency dependent phase shift,

$$X(t, u) = u + \int_{-\infty}^\infty e^{i(\kappa u - \omega t + \theta(\omega))} \rho(\omega) d\zeta(\omega).$$

A physically motivated relation is obtained by letting the horizontal acceleration depend on the height, e.g. to take $X(t, u)$ as the solution to an equation

$$\frac{\partial^2 X(t, u)}{\partial t^2} = \frac{\partial^2 X_M(t, u)}{\partial t^2} - \alpha W(t, u),$$

with $\alpha > 0$. With $G(\omega) = \frac{-\alpha}{(-i\omega)^2}$, the response function will then be

$$H(\omega) = H_M(\omega) + G(\omega) = i \frac{\cosh \kappa h}{\sinh \kappa h} - \frac{\alpha}{(-i\omega)^2} = \rho(\omega) e^{i\theta(\omega)}.$$

1.4 Time and space waves

The *space wave* is obtained as the parametric curve $u \mapsto (X(t_0, u), W(t_0, u))$, by keeping time $t = t_0$ fixed. A complication is that there may occur double points, where $X(t_0, u_1) = X(t_0, u_2)$ with $u_1 \neq u_2$ and $W(t_0, u_1) \neq W(t_0, u_2)$. The space wave is defined implicitly through the relation $L(t_0, X(t_0, u)) = W(t_0, u)$, and explicitly, if there is only one $u = X^{-1}(t_0, x)$ satisfying $X(t_0, u) = x$, as $L(t_0, x) = W(t_0, X^{-1}(t_0, x))$.

The *time wave* is obtained as measurements of the free water level $L(t, x_0)$ at a fixed location in space with co-ordinate x_0 , viz. as the curve $t \mapsto W(t, X^{-1}(t, x_0))$, provided that the inverse $X^{-1}(t, x_0) = \{u; X(t, u) = x_0\}$ is unique.

1.5 The example model

We will illustrate the theory on a model with Pierson-Moskowitz (PM) orbital spectrum, with spectral density

$$S(\omega) = \frac{5H_s^2}{\omega_p(\omega/\omega_p)^5} e^{-\frac{5}{4}(\omega/\omega_p)^{-4}}, \quad 0 < \omega < \omega_c,$$

with significant wave height $H_s = 4\sqrt{\text{Var}(W(t, u))} = 7$ m, peak frequency ω_p , and peak period $T_p = 2\pi/\omega_p$. We assume a finite cut off frequency $\omega_c = 32/T_p$ to obtain finite spectral moments. The *steepness* parameter, H_s/T_p^2 , is important for the front-back asymmetry, and we illustrate the distributions for very steep, steep, and moderately steep waves with $T_p = 12, 14, 16$ s. We do the calculations for different depths, $h = 8, 32, 64, \infty$ m and three different degrees of linkage, $\alpha = 0, 0.4, 0.8$, where $\alpha = 0$ means “no linkage”.

2 Wave characteristics

2.1 Observable characteristics

There are many wave characteristic distributions that are of importance in ocean engineering practice, and they can all be derived exactly from the correlation properties. In different applications one can identify many different quantities related to the wave profiles. Some are described by their statistical distribution when waves are sampled at a constant sampling rate. Others are coupled to level crossings and the wave profile when the wave reaches some specified level. We list five variables of special interest that we analyse in the examples:

- (AS) **Asynchronous slopes in space:** This is the distribution of the space slope $L_x(t_0, x)$ observed at equidistant sampling of the space wave.
- (AT) **Asynchronous slopes in time:** This is the distribution of the time slope $L_t(t, x_0)$ observed at constant rate sampling of the time wave.
- (SS) **Slope in space at level crossings in space:** This is the distribution of the space slope $L_x(t_0, x)$ observed only at the up- or downcrossings of a fixed level v by the space wave $L(t_0, x)$, (*synchronous sampling in space*).
- (TT) **Slope in time at level crossings in time:** This is the distribution of the time slope $L_t(t, x_0)$ observed only at the up- or downcrossings of a fixed level v by the time wave $L(t, x_0)$, (*synchronous sampling in time*).
- (ST) **Slope in space at level crossings in time:** This is the distribution of the space slope $L_u(t, x_0)$ observed at the instances when the time wave reaches level v . Note that this is the slope of the moving wave front that may hit a deck of an offshore construction.

The observable statistical distributions in the different cases are defined as the asymptotic, long run, empirical distributions.

2.2 Model characteristics

To find the theoretical statistical distribution of the observable characteristics in cases (US)-(ST) we need to express the corresponding quantities in terms of the vertical and horizontal processes, $W(t, u)$ and $X(t, u)$. We derive the model variables in terms of the partial time and space derivatives, which we denote as $X_t(t, u) = \partial X(t, u)/\partial t$, $X_u(t, u) = \partial X(t, u)/\partial u$, $W_t(t, u) = \partial W(t, u)/\partial t$, $W_u(t, u) = \partial W(t, u)/\partial u$, etc.

Consider first the time wave. The Lagrange time wave satisfies the relation $L(t, X(t, u)) = W(t, u)$. By differentiating with respect to t , we obtain $\frac{\partial L(t, X(t, u))}{\partial t} = W_t(t, u) = L_t(t, X(t, u)) + L_u(t, X(t, u)) X_t(t, u)$. By differentiating with respect to u , we obtain further, $W_u(t, u) = L_u(t, X(t, u)) X_u(t, u)$, giving the fundamental definition of the time wave slope at location $X(t, u)$,

$$L_t(t, X(t, u)) = W_t(t, u) - W_u(t, u) \frac{X_t(t, u)}{X_u(t, u)}. \quad (2)$$

Equation (2) is a mathematical identity, and if $X^{-1}(t, x_0)$ is uniquely defined it also gives the unique slope of the Lagrange time wave $L(t, x_0)$ at location x_0 . If there are multiple u -values such that $X(t, u) = x_0$, we define $L_t(t, x_0)$ by (2) for each of these u -values.

We also need the slope of the space wave observed at time t_0 . The space wave is implicitly defined by $L(t_0, X(t_0, u)) = W(t_0, u)$, or explicitly, if there is only one $u = X^{-1}(t_0, x)$ satisfying $X(t_0, u) = x$, by $L(t_0, x) = W(t_0, X^{-1}(t_0, x))$. For each of the solutions, the slope is defined by

$$L_x(t_0, x) = \frac{W_u(t_0, u)}{X_u(t_0, u)}. \quad (3)$$

3 Asynchronous slopes, exact results for (AS) and (AT)

The asynchronous slopes are obtained by *asynchronous sampling*, for example equidistant in time or in space, and their model representatives are defined by (2) and (3). To find the slope distributions at a location x_0 at time t_0 one has to identify the reference coordinate for the particle that occupies position x_0 at time t_0 , i.e. to find the solution(s) to the equation $X(t_0, u) = x_0$. Due to the stationarity in time and space we can take $t_0 = 0, x_0 = 0$.

Now, $X(0, u)$ is a Gaussian process with parameter u , with non-constant mean u , and stationary covariance function $r^{xx}(0, u) = \text{Cov}(X(0, 0), X(t, u))$. The slope distributions in time or space are equal to the distribution of the representations (2) and (3), respectively, under the condition that u is a point of crossing of the level 0 by the process $X(0, u)$. To reduce the effect of multiple solutions as much as possible, we consider only upcrossings.

The number of solutions to $X(0, u) = 0$ is random, with a small probability of there being more than one, and so are the reference coordinates of the solutions. To formulate the long run distribution, we define the counters $N^+ = \# \{u; X(0, u) = 0, \text{ upcrossing}\}$, and

$$N^T(a, b) = \# \left\{ u; X(0, u) = 0, \text{ upcrossing}, \right. \\ \left. a < W_t(0, u) - W_u(0, u) \frac{X_t(0, u)}{X_u(0, u)} \leq b \right\}, \\ N^S(a, b) = \# \left\{ u; X(0, u) = 0, \text{ upcrossing}, a < \frac{W_u(0, u)}{X_u(0, u)} \leq b \right\}.$$

The distribution functions of the asynchronous slopes in time and space, are then $F(L_T \leq x) = \frac{\mathbf{E}(N^T(-\infty, x))}{\mathbf{E}(N^+)}$ and $F(L_S \leq x) = \frac{\mathbf{E}(N^S(-\infty, x))}{\mathbf{E}(N^+)}$.

Define the indicator functions

$$I^{(T)}(a, b) = I \left\{ a < W_t(0, u) - W_u(0, u) \frac{X_t(0, u)}{X_u(0, u)} \leq b \right\}, \quad (4)$$

$$I^{(S)}(a, b) = I \left\{ a < \frac{W_u(0, u)}{X_u(0, u)} \leq b \right\}, \quad (5)$$

and let $p_u(0, z)$ be the density of $\mathbf{U}(0, u) = (X(0, u), X_u(0, u))$ at $(0, z)$.

Theorem 1 ([8]). *The observable distributions of the asynchronous time and space slopes in the Gauss-Lagrange model are given by,*

$$F(L_S \leq y) = \frac{1}{\mathbf{E}(N^+)} \int_{u=-\infty}^{\infty} \int_{z=0}^{\infty} z p_u(0, z) \mathbf{E} \left(I^S(-\infty, y) \mid \mathbf{U}(0, u) = (0, z) \right) dz du, \quad (6)$$

$$F(L_T \leq y) = \frac{1}{\mathbf{E}(N^+)} \int_{u=-\infty}^{\infty} \int_{z=0}^{\infty} z p_u(0, z) \mathbf{E} \left(I^T(-\infty, y) \mid \mathbf{U}(0, u) = (0, z) \right) dz du, \quad (7)$$

with $\mathbf{E}(N^+) = \int_{u=-\infty}^{\infty} \int_{z=0}^{\infty} z p_u(0, z) dz du$. The expectations in (6)–(7) are easily found by conditional simulation of the three-dimensional Gaussian vector $(W_t(t, u), W_u(t, u), X_t(t, u))$ given that $\mathbf{U}(0, u) = (0, z)$.

Example 1. We use the Pierson-Moskowitz (PM) orbital spectrum described in Section 1.5 and simulate the vertical and horizontal components. From these we construct space and time waves and observe the slopes. We also compute, by Monte Carlo simulation of the expectations, the exact cumulative distribution functions.

We simulated 50 replicates of space and time waves, with length 2048 m and 2048 s, respectively. Table 1 shows the estimated skewness (with standard error) for three water depths, and three degrees of linking dependence. The skewness (A) and kurtosis excess (B) in the observed slopes are used as an estimate of the theoretical skewness of the slopes and deviation from normality, (with subscript $i = S, T$ indicating space or time waves), $A_i = \mathbf{E}(L_{slope}^3) / \text{Var}(L_{slope})^{3/2}$, $B_i = \mathbf{E}(L_{slope}^4) / \text{Var}(L_{slope})^2 - 3$.

Figure 1 shows cumulative space slope distributions for the nine combinations of depth and linking. As seen the slope distribution deviates significantly from normality, even in the symmetric case with infinite water depth. For time waves, the skewness is not as extreme as for space waves (not shown here).

Table 1. Estimated skewness and kurtosis excess with standard errors of asynchronous slope distributions, PM orbital spectrum with $H_s = 7\text{m}$, $T_p = 11\text{s}$.

Depth		$\alpha = 0$	$\alpha = 0.4$	$\alpha = 0.8$
$h = \infty$	$A_S =$	0.0 (0.02)	-0.3 (0.02)	-0.6 (0.03)
	$A_T =$	0.0 (0.01)	0.5 (0.01)	0.9 (0.02)
	$B_S =$	0.2 (0.03)	0.4 (0.05)	1.2 (0.14)
	$B_T =$	0.1 (0.02)	0.4 (0.05)	1.4 (0.07)
$h = 64$	$A_S =$	0.0 (0.02)	-0.3 (0.02)	-0.7 (0.03)
	$A_T =$	0.0 (0.01)	0.5 (0.01)	0.9 (0.02)
	$B_S =$	0.1 (0.04)	0.3 (0.05)	1.3 (0.16)
	$B_T =$	0.1 (0.02)	0.5 (0.03)	1.4 (0.09)
$h = 8$	$A_S =$	0.0 (0.02)	-1.1 (0.08)	-2.6 (0.12)
	$A_T =$	0.0 (0.03)	0.8 (0.05)	1.5 (0.08)
	$B_S =$	0.8 (0.08)	5.2 (0.66)	17.2 (1.41)
	$B_T =$	1.1 (0.08)	2.3 (0.26)	5.0 (0.29)

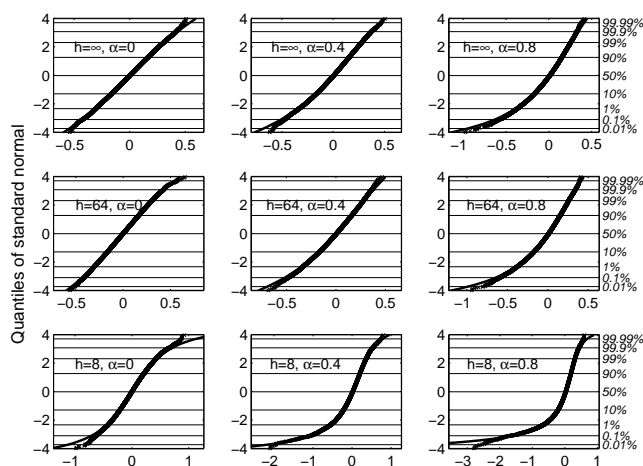


Fig. 1. Cumulative distribution functions (CDF) on normal probability paper for asynchronous slopes in Lagrange space waves. Crosses = simulated data, solid line = theoretical CDF.

4 Asymmetry in space waves, case (SS)

The distribution of the space wave slope at a crossing of the level v is the distribution of the ratio (3), conditioned on the event that u is a v -crossing point in the vertical Gaussian process $W(t_0, u)$. Now, it is wellknown that the derivative of a Gaussian process, observed only at crossings of a fixed level, has a two-sided Rayleigh distribution. Observed at upcrossings or downcrossings, the derivatives have a positive or negative Rayleigh distribution, respectively.

In the following theorem, R and U are two independent random variables, with densities, respectively, $f_R(r) = \frac{|r|}{2} e^{-r^2/2}$, and $f_U(u) = \frac{1}{\sqrt{2\pi}} e^{-u^2/2}$, i.e. R has a two-sided Rayleigh distribution and U is standard normal. The notation $X \stackrel{\mathcal{L}}{=} Y$ means that the random variables X and Y have the same distribution.

Theorem 2 ([1, 9]). *The distribution of the space derivatives in (3), under the condition that u_k is a v -crossing point in $W(t_0, u)$, can be expressed as*

$$W_u(t_0, u_k) \stackrel{\mathcal{L}}{=} R\sqrt{r_{uu}^{ww}},$$

$$X_u(t_0, u_k) \stackrel{\mathcal{L}}{=} 1 + v \frac{r_{0u}^{wx}}{r^{ww}} + R \frac{r_{uu}^{wx}}{\sqrt{r_{uu}^{ww}}} + U \sqrt{r_{uu}^{xx} - \frac{(r_{0u}^{wx})^2}{r^{ww}} - \frac{(r_{uu}^{wx})^2}{r_{uu}^{ww}}},$$

and hence the slope of the Lagrange space wave at a v -crossing has the representation

$$L_x(t_0, x_k) \stackrel{\mathcal{L}}{=} \frac{R\sqrt{r_{uu}^{ww}}}{1 + v \frac{r_{0u}^{wx}}{r^{ww}} + R \frac{r_{uu}^{wx}}{\sqrt{r_{uu}^{ww}}} + U \sqrt{r_{uu}^{xx} - \frac{(r_{0u}^{wx})^2}{r^{ww}} - \frac{(r_{uu}^{wx})^2}{r_{uu}^{ww}}}}. \quad (8)$$

The distributions at an upcrossing or at a downcrossing are obtained by replacing the two-sided Rayleigh variable by a one-sided, positive and negative, respectively. An explicit formula for the probability density can be found in [9].

As seen in the denominator in (8), the front-back asymmetry depends on the covariance

$$r_{uu}^{wx} = \int_0^\infty \kappa^2 \cos(\theta(\omega)) S(\omega) d\omega,$$

between the spatial derivatives of the vertical and horizontal processes. If it is zero the slope distribution at an upcrossing is just the mirror of that at a downcrossing. If non-zero the Rayleigh variable in the nominator also influences the denominator and makes the slope distribution asymmetric. In the free Lagrange model the phase shift is 90° and the covariance is 0.

Example 2: Figure 2 shows how the the cumulative distribution functions (CDF) for the upcrossing and downcrossing slopes in Lagrange space waves with $\alpha = 0.4$, depend on the crossed level, and on the water depth and wave steepness.

5 Asymmetry in time waves, cases (TT), (ST)

The time wave level crossings at position x_0 are more complicated than the space wave crossings, since one has to follow the vertical and horizontal variations of the random particle that happens to be located at x_0 as time changes. Thus, a crossing of the level v occurs at time t_k if there is a particle with reference coordinate, which we denote by u_k , such that $W(t_k, u_k) = v$ and $X(t_k, u_k) = x_0$. To solve problems (TT), (ST), we have to find the conditional distribution of

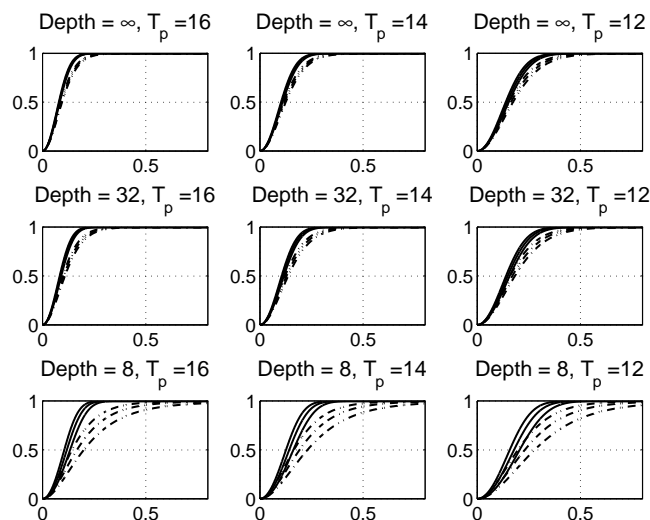


Fig. 2. CDF for slopes at upcrossings (solid) and negative slopes at downcrossings (dash-dotted) of levels -1, 0, 1, for linked Lagrange space waves with $\alpha = 0.4$. (Smallest slope at level -1, largest at level +1.)

the time slope, defined by (2), and space slope, defined by (3), conditioned on the crossing event, just defined.

By a remarkable generalization of Rice's formula for the number of level crossings, Mercardier, [10], has given the tool for how to find conditional distributions like the ones we seek. To formulate the theorem, we define

$$D = |W_t(0, u)X_u(0, u) - W_u(0, u)X_t(0, u)|,$$

and write $q_u(v, x)$ for the density of $\mathbf{V}(0, u) = (W(0, u), X(0, u))$, evaluated at (v, x) .

Theorem 3 ([1, 7]). (a) *The distribution function for slopes at upcrossings of the level v in the Lagrange time wave, is given by,*

$$F_v^{TT+}(y) = \frac{1}{\mathbf{E}(N^+)} \int_{-\infty}^{\infty} g_y^{TT+}(u) q_u(v, x_0) du,$$

where

$$g_y^{TT+}(u) = \mathbf{E}(D \times I^{(T)}(0, y) \mid \mathbf{V}(0, u) = (v, x_0)), \quad (9)$$

and $\mathbf{E}(N^+) = \int_{-\infty}^{\infty} g_{\infty}^{TT+}(u) q_{W(0, u), X(0, u)}(v, x_0) du$.

(b) *The cumulative distribution of slopes at downcrossings is obtained by replacing the indicator function $I^{(T)}(0, y)$ by $I^{(T)}(-y, 0)$, properly adjusting the \leq sign. The distribution for space slope, (ST), at time crossings is found by replacing (4) by (5) in (9).*

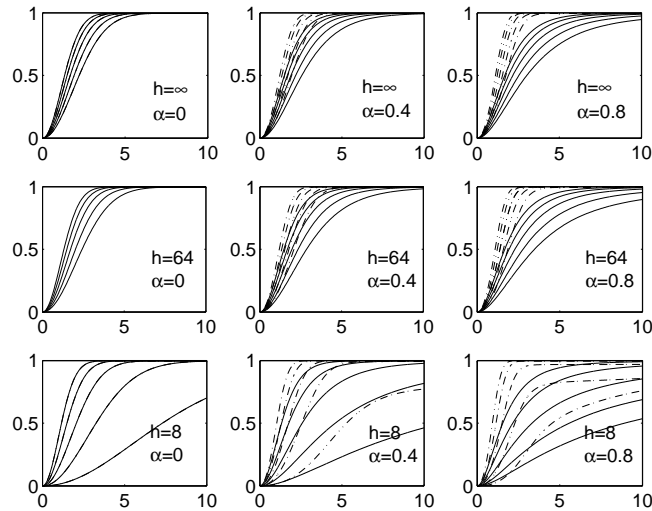


Fig. 3. Cumulative distribution functions for time wave slopes (absolute values) at time wave crossings of different levels. Slope CDF at upcrossings (solid lines) and at downcrossings (dash-dotted lines). Levels $v: [-1, 0, 1, 2, 3] \times \sigma$, $4\sigma = H_s$. Largest absolute values correspond to highest level. Orbital spectrum is PM with $T_p = 12s$.

Example 3: Figures 3 and 4 illustrate cases (TT) and (ST), i.e. distributions of slopes in time and space, respectively, observed at up- and downcrossings of different levels. The case (ST), space slopes at time wave crossings, has drawn some interest in the study of rogue waves. It is related to the problem of relation between time wave formulation and the properties of observed wavelength troughs in space, in particular the question of “a hole in the sea” ahead of extreme waves. A common technique to approach this problem is the Fourier snapshot method, described in [12]. The space-time analysis presented in this paper might be an adequate method for genuinely asymmetric waves.

6 Concluding remark

The main message is that the full covariance structure of horizontal and vertical water particle velocities can be the basis for a statistical analysis of crest-front asymmetry of real ocean waves. Besides observational data also data from Monte Carlo experiments of fully non-linear waves models should be of interest.

References

1. Aberg, S.: Wave intensities and slopes in Lagrangian seas. *Adv. Appl. Probab.* **39** (2007) 1020–1035.
2. Aberg, S. and Lindgren, G.: Height distribution of stochastic Lagrange ocean waves. *Probab. Eng. Mech.*, **23** (2008) 359–363.

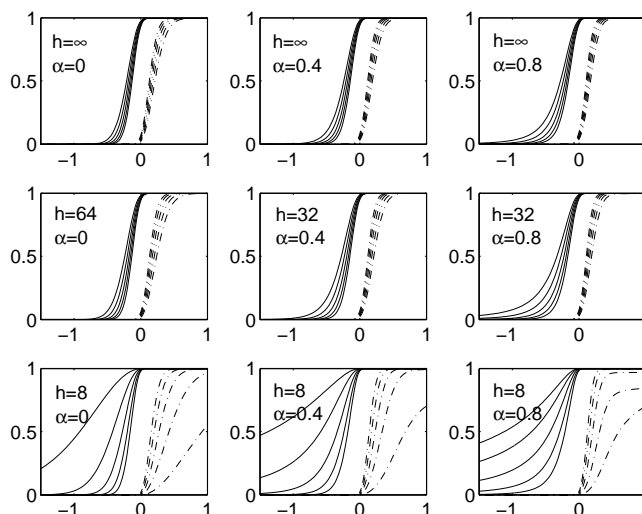


Fig. 4. Cumulative distribution functions for space wave slopes at time wave crossings of different levels. Slope CDF at upcrossings (solid lines) and at downcrossings (dash-dotted lines). Levels $v: [-1, 0, 1, 2, 3] \times \sigma$, $4\sigma = H_s$. Most extreme values correspond to highest level. Orbital spectrum is PM with $T_p = 12s$.

3. Fouques, S., Krogstad, H.E. and Myrhaug, D.: A second order Lagrangian model for irregular ocean waves. *J. Offshore Mech. Arctic Eng.*, **128** (2006) 177–183.
4. Gerstner, F.J.: Theorie der Wellen. *Ann. Phys.* **32** (1809) 420–440.
5. Gjøvund, S.H.: A Lagrangian model for irregular waves and wave kinematics. *J. Offshore Mech. Arctic Eng.*, **125** (2003) 94–102.
6. Lindgren, G.: Slepian models for the stochastic shape of individual Lagrange sea waves. *Adv. Appl. Probab.* **38** (2006) 430–450.
7. Lindgren, G. Slope distributions in front-back asymmetric stochastic Lagrange time waves. Submitted.
8. Lindgren, G. Exact asymmetric slope distributions in Gauss-Lagrange ocean waves. Submitted.
9. Lindgren, G. and Aberg, S.: First order stochastic Lagrange models for front-back asymmetric ocean waves. *J. Offshore Mech. Arctic Eng.*, in press.
10. Mercardier, C.: Numerical bounds for the distributions of the maxima of some one- and two-parameter Gaussian processes. *Adv. Appl. Probab.*, **38** (2006) 19–170.
11. Miche, M.: Mouvements ondulatoires de la mer on profondeur constante ou décroissante. Forme limit de la houle lors de son déferlement. Application aux digues marines. *Ann. Ponts Chassées*, **114** (1944) 25–78.
12. Rydén, J., van Isegem, S., Olagnon, M. and Rychlik, I.: Evaluating height-length joint distributions for the crests of ocean waves. *Appl. Ocean Res.*, **24** (2002) 189–201.
13. Socquet-Juglard, H., Dysthe, K.B., Trulsen, K., Fouques, S., Liu, J. and Krogstad, H.: Spatial extremes, shape of large waves, and Lagrangian models. In *Proc. Rogue Waves, Brest, 2004*. Available at <http://www.ifremer.fr/web-com/stw2004/rw/fullpapers/krogstad.pdf>.

Euler Characteristics and Maxima of Oceanic Sea States

Francesco Fedele¹, Guillermo Gallego², Alvise Benetazzo³, Anthony Yezzi²,
and Mehmet A. Tayfun⁴

¹ School of Civil and Environmental Engineering,
Georgia Institute of Technology, Savannah campus, USA

² School of Electrical and Computer Engineering,
Georgia Institute of Technology, Atlanta campus, USA

³ Protecno S.r.l, Padua ITALY

⁴ College of Engineering, Kuwait University, Kuwait

Abstract. We propose a novel Variational Wave Acquisition Stereo System (VWASS) that exploits new stereo reconstruction techniques for accurate estimates of the space-time dynamics of oceanic sea states. The rich information content of the acquired three-dimensional video data is exploited for predictions of directional spectra and large waves over an area by means of the Euler Characteristics of random fields. The broader impact of these results for oceanic applications is finally discussed.

1 Introduction

The prediction of large waves is typically based on the statistical analysis of time series of the wave surface displacement retrieved from wave gauges, ultrasonic instruments or buoys at a fixed point P of the ocean. However, the largest wave crest predicted in time at P underestimates the highest crest expected over the nearby area. Indeed, large waves travel on top of wave groups, and the probability that the group passes at its apex through P is practically null. The large crest height recorded in time at P is simply due to a group that focuses nearby P forming a larger wave crest in space. Can we thus predict the largest wave expected over a given area?

In this paper, we address this question by proposing a novel variational Wave Acquisition Stereo System (VWASS) for the reconstruction of the water surface of oceanic sea states. The rich information content of the acquired three-dimensional video data is exploited to obtain reliable estimates of the expected global maximum (largest crest height) over an area using the Euler Characteristic (EC) of random excursion sets (Adler 1981, Adler & Taylor 2007). The paper is structured as follows. We first discuss the mathematical formulation of VWASS and introduce the EC of excursion sets (Adler 1981)

$$A_{\eta,h} = \{(x, y) \in S : \eta(x, y) > h\} \quad (1)$$

of a two dimensional (2D) random field η defined over an area S . The EC of $A_{\eta,h}$ is then related to the expected number of maxima and h -upcrossings over

S . We then analyze the EC of the excursion sets of the spatial snapshots η of oceanic sea states acquired via VWASS. We present new estimates from video data of both directional wave spectra and empirical exceedance probabilities of the global maximum of η over S . The broader impact of these results to oceanic applications is finally discussed.

2 The Stereo Variational Geometric Method

The reconstruction of the wave surface from stereo pairs of ocean wave images is a classical problem in computer vision commonly known as the correspondence problem (Ma et al. 2004). Its solution is based on epipolar geometry techniques that find corresponding points in the two images, from which one obtains the estimate of the real point in the three dimensional terrestrial coordinate system. The Wave Acquisition Stereo System (WASS) developed by Benetazzo (2006) utilizes the “epipolar algorithm” for the space-time reconstruction of the sea surface. However, this approach may fail to provide a smooth surface reconstruction because of “holes” corresponding to unmatched image regions (Ma et al. 2004, Benetazzo 2006). For example, this can occur when, at a given point on the water surface, the same amount of light is received from all possible directions and reflected towards the observer causing a visual blurring of the specularities of the water. This is typical of cloudy days, and the water surface is said to support a Lambertian radiance function (Ma et al. 2004). We address this problem by proposing a novel formulation of WASS based on variational principles (VWASS). Under the assumptions of a Lambertian surface, following the seminal work by Faugeras & Keriven (1998), the 3-D reconstruction of the water surface is obtained in the context of active surfaces by evolving an initial surface through a PDE derived from the gradient descent flow of a cost functional designed for the stereo reconstruction problem.

To be more specific, the energy being *maximized* is the normalized cross correlation between the image intensities obtained by projecting the same water surface patch onto both image planes of the cameras. It is clear that such energy depends on the shape of the water surface. Therefore, the active surface establishes an evolving correspondence between the pixels in both images. Hence, the correspondence will be obtained by evolving a surface in 3-D instead of just performing image-to-image intensity comparisons without an explicit 3-D model of the target surface being reconstructed.

To infer the shape of the water surface $\eta(x, y)$ at the location (x, y) over an area S , we set up a cost functional on the discrepancy between the projection of the model surface and the image measurements. As previously announced, such cost is based on a cross correlation measure between image intensities, which will be noted as $E_{\text{data}}(\eta)$. We conjecture that, to have a well-posed problem, a regularization term that imposes a geometric prior must also be included, $E_{\text{geom}}(\eta)$. We consider the cost functional to be the (weighted) sum:

$$E(\eta) = E_{\text{data}}(\eta) + E_{\text{geom}}(\eta) . \quad (2)$$

In particular, the geometric term favors surfaces of least area:

$$E_{\text{geom}}(\eta) = \int_{\eta} dA . \quad (3)$$

The data fidelity term may be expressed as

$$E_{\text{data}}(\eta) = \int_{\eta} \left(1 - \frac{\langle I_1, I_2 \rangle}{|I_1| |I_2|} \right) dA , \quad (4)$$

where η is the wave surface region within the field of views of both cameras, and $\langle I_1, I_2 \rangle$ is the cross-correlation between the image intensities I_1 and I_2 . To find the surface η that minimizes E , we start from an initial estimate of the surface at time $t = 0$, η_0 , and set up a gradient flow based on the first variation of E that will make the surface evolve towards a minimizer of E , hopefully converging to the desired water surface shape. Based on the theorem in Faugeras & Keriven (1998) that says that for a function $\Phi : \mathbb{R}^3 \times \mathbb{R}^3 \rightarrow \mathbb{R}_+$ and the energy

$$E = \int_{\eta} \Phi(\mathbf{X}, \mathbf{N}) dA , \quad (5)$$

where \mathbf{N} is the unit normal to η at \mathbf{X} , the flow that minimizes E is given by the evolution PDE

$$\eta_t = \beta \mathbf{N} , \quad (6)$$

where η_t is the derivative of η with respect to a fictitious time variable and the speed β in the normal direction to the surface that drives the evolution is

$$\beta = 2H(\Phi - \Phi_{\mathbf{N}} \cdot \mathbf{N}) - \Phi_{\mathbf{X}} \cdot \mathbf{N} - \text{trace}((\Phi_{\mathbf{X}\mathbf{N}})_{T_{\eta}} + d\mathbf{N} \circ (\Phi_{\mathbf{N}\mathbf{N}})_{T_{\eta}}) . \quad (7)$$

All quantities are evaluated at the point $\eta = \mathbf{X}$ with normal \mathbf{N} to the surface. H denotes the mean curvature. $\Phi_{\mathbf{X}}, \Phi_{\mathbf{N}}$ are the first-order derivatives of Φ , while $\Phi_{\mathbf{N}\mathbf{X}}, \Phi_{\mathbf{N}\mathbf{N}}$ are the second-order derivatives. $d\mathbf{N}$ is the differential of the Gauss map of the surface and $(\cdot)_{T_{\eta}}$ means “restriction to the tangent plane T_{η} to the surface at $\eta = \mathbf{X}$ ”. Note that our proposed energy (2) can be expressed in the form of (5) if $\Phi = (1 - \langle I_1, I_2 \rangle / (|I_1| |I_2|)) + \alpha$, where α is just a weight for the geometric prior. In practice, we use the flow based on the first-order derivatives of Φ because it provides similar results to those of the complete expression, but saves a significant amount of computations,

$$\eta_t = (2H(\Phi - \Phi_{\mathbf{N}} \cdot \mathbf{N}) - \Phi_{\mathbf{X}} \cdot \mathbf{N}) \mathbf{N} . \quad (8)$$

The level set framework has been adopted to numerically implement (8). For the technical description of the variational stereo algorithm implementation we refer to Gallego et al. (2008). We have tested the variational reconstruction algorithm using a set of images, shown in Fig. 1, acquired by Benetazzo (2006) on a water depth of 8 meters. Fig. 2 shows the successful reconstructed surface and the associated directional wave spectrum. Hereafter, we introduce the concept of the Euler characteristic (EC) that will be applied to predict the expected number of large maxima in oceanic sea states exploiting the high statistical content of the acquired video data via VWASS.

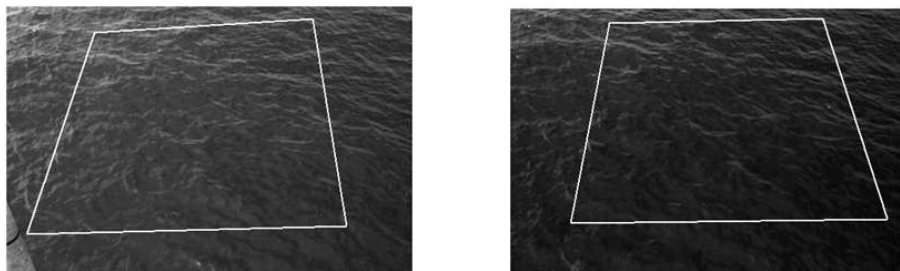


Fig. 1. Input stereo pair images to the algorithm. The rectangular domain ($8 \text{ m} \times 8.7 \text{ m}$) of the reconstructed surface or elevation map (right column) has been superimposed. The height of the waves is in the range $\pm 0.2 \text{ m}$.

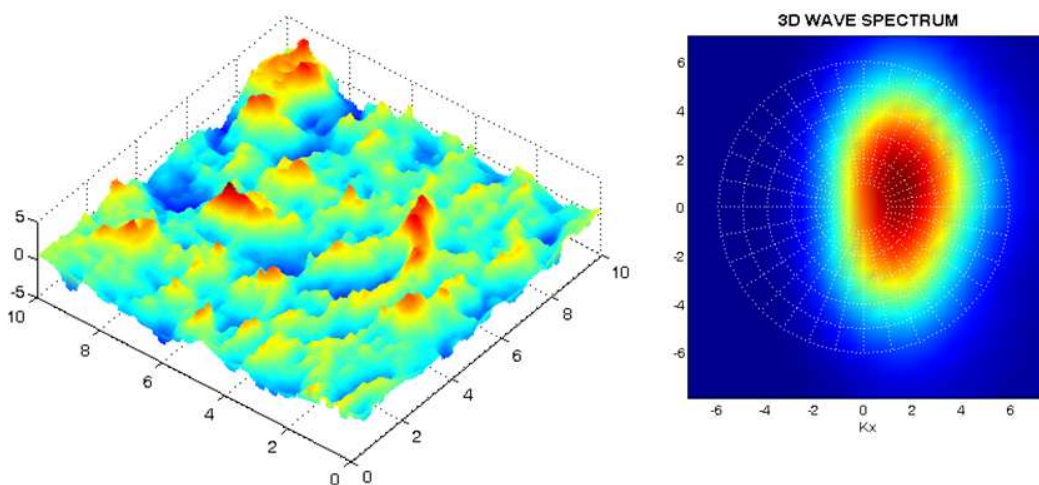


Fig. 2. (left) Reconstructed normalized wave surface η via VWASS with zero mean and unit variance (horizontal axis units are in meters). (right) estimate directional wave spectrum of η (axis units are in meter^{-1}).

3 Euler Characteristic of Random Excursion Sets

In algebraic topology, the **Euler characteristic** EC is classically defined for polyhedra according to the formula

$$EC = V - E + F \quad , \quad (9)$$

where V, E , and F are respectively the numbers of vertices, edges and faces in the given polyhedron. The same definition given in (9) can be adapted to 2D surfaces which are the focus of this paper. In this case, the EC is also equivalent to the difference between the number connected components (CC) and holes (H) of the given set, viz.

$$EC = \#CC - \#H \quad . \quad (10)$$

For a generic 2D set Σ with complicated regions, computing the EC from the definition (10) presents some challenges. A computationally efficient approach can be devised based on (9). Following Adler (1981), we first define a Cartesian mesh grid Γ with cell size $\Delta x \Delta y$ that approximates the complicated domain of the given set Σ . The $EC(\Gamma)$ is then computed as follows. Denote F as the number of squares (faces) composing Γ , E_h (E_v) as the number of horizontal (vertical) segments between two neighboring mesh points and V the number of grid points. The $EC(\Gamma)$ then follows from (9) setting $E = E_h + E_v$. As the grid cell size $\Delta x \Delta y$ tends to zero, $EC(\Gamma) \rightarrow EC(\Sigma)$. For example, for a square $EC = 4 - 4 + 1 = 1$ according to (9), which is in agreement with (10) since there is only 1 connected component and no holes.

As an example, consider a zero-mean Gaussian field Z with unit variance and its excursion set $A_{Z,z}$, i.e. the sub-region where Z exceeds the threshold z . The set $A_{Z,1}$ is illustrated in Fig. 3. The mesh grid Γ approximating the set is also superimposed on $A_{Z,1}$. In this case, $EC(\Gamma) = 20$ since $A_{Z,1}$ is mainly a collection of connected components, or local maxima in agreement with (10). In general, the EC of an excursion set depends very strongly on the threshold. If this is low, then EC counts the number of holes in the given set. If the threshold is high, then all the holes tend to disappear and the EC counts the number of connected components, or local maxima of the random field. For a stationary Gaussian field η , an exact formula for the expected value of EC , valid for any threshold, was discovered by Adler (1981). For 2D Gaussian fields defined over the region S

$$\overline{EC(A_{\eta,h})} = A_S (2\pi)^{-3/2} \sigma^{-2} |A|^{1/2} \xi e^{-\xi^2/2} \quad , \quad (11)$$

where $\overline{(\cdot)}$ means expectation, $\xi = h/\sigma$ is the normalized threshold amplitude, σ is the standard deviation of η , A_S is the area of region S , A is the covariance matrix of the gradient $\nabla\eta$, and $A_{\eta,h}$ is the excursion set defined in (1). If this set touches the boundary of the area S , correction terms need to be added (Worsley 1995), but hereafter these will be neglected without losing accuracy in the final results. Why is the EC of random excursion sets relevant to oceanic applications?

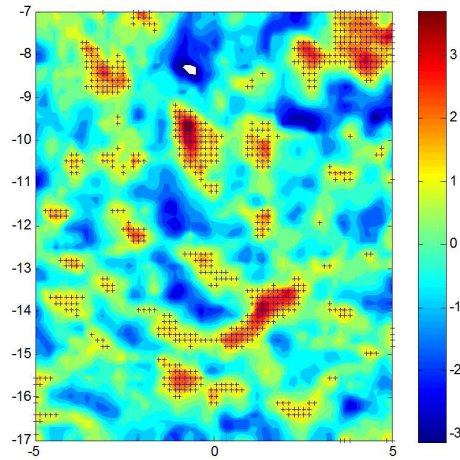


Fig. 3. Excursion set at $z = 1$ of a Gaussian field Z with mean zero and unit variance and superimposed mesh grid Γ which approximates $A_{Z,1}$.

Previous works (Adler 1981, Adler & Taylor 2007) have shown that the probability that the global maximum of a random field η exceeds a threshold h is well approximated by the expected EC of the excursion set $A_{\eta,h}$, provided the threshold is high. Indeed, as the threshold h increases, the holes in the excursion set disappear until each of its connected components includes just one local maximum, and the EC counts the number of local maxima. For very large thresholds, the EC equals 1 if the global maximum exceeds the threshold and 0 if it is below. Thus, the $EC(A_{\eta,h})$ of large excursion sets is a binary random variable with states 0 and 1. As $h \rightarrow \infty$,

$$\Pr\left(\max_{P \in S} \eta(P) > h\right) = \Pr\left(EC(A_{\eta,h}) = 1\right) = \overline{EC(A_{\eta,h})}. \quad (12)$$

Piterbarg (1995) also derived (12) by studying large Gaussian maxima over an infinite area. If η represents realizations of oceanic sea states at fixed time (snapshots), then the global maximum of η is the largest wave crest expected over the area S . Thus, (12) provides the basis for accurate estimates of exceedance probabilities of large waves by means of the EC of excursion sets of video images retrieved via VWASS (see Fig. 2). A consequence of (12) is that, for $h \gg 1$

$$EX_{\max}(h) \approx \overline{EC(A_{\eta,h})}, \quad (13)$$

that is, the expected number EX_{\max} of large local maxima equals that of the EC of large excursion sets.

3.1 Upcrossings and Maxima of Random Fields

Note that for one-dimensional (1D) random processes, the EC of excursion sets counts the number of upcrossings. Thus, (13) simply states that the expected

number of large maxima equals that of large h -upcrossings, implying the well known one-to-one correspondence between h -upcrossings and maxima at large thresholds. For 2D random fields this correspondence does not hold since upcrossings are contour levels. However, the definition of a 2D upcrossing is somehow vague. Can we define an appropriate 2D h -upcrossing for random fields so that the correspondence with large maxima is also one-to-one?

The answer to this question follows from the seminal work of Adler (1976) on generalizing upcrossings to higher dimensions. Without loosing generality, consider the Gaussian field η on a Cartesian coordinate system (t, s) so that the covariance matrix A of $\nabla\eta$ is diagonal with spectral moments m_{tt} and m_{ss} , $m_{tt} > m_{ss}$, and $|A| = m_{tt}m_{ss}$. Note that the t -axis is along the principal direction θ (with respect to the original x axis) where the second spectral moment along θ attains its maximum. The partial derivatives $\partial_t\eta$ and $\partial_s\eta$ of η are thus uncorrelated and stochastically independent. With this setting in mind, a 2D h -upcrossing occurs at a point $P \in S$ if *i*) a 1D h -upcrossing occurs along t ($\eta = h, \partial_t\eta > 0$ at P) and *ii*) η attains a 1D local maximum along s , i.e. η is convex along s ($\partial_s\eta = 0, \partial_{ss}\eta < 0$ at P). Note that the extra condition (*ii*) is necessary so that, locally at P , η is a crescent function. Further, this definition does not depend on the particular choice of the coordinate axes, and for large thresholds each 2D upcrossing corresponds uniquely to a large local maximum of η . Indeed, following Rice logics (Adler 1981), the expected number of 2D h -upcrossings is given by the following generalized Rice formula

$$EX_+(h) = A_S \int_{w_2=-\infty}^0 \int_{w_1=0}^{\infty} w_1|w_2| \cdot p(\eta = h, \partial_t\eta = w_1, \partial_s\eta = 0, \partial_{ss}\eta = w_2)dw_1dw_2 \quad (14)$$

where $p(\cdot)$ is the joint probability density function (pdf) of $\eta, \partial_t\eta, \partial_s\eta, \partial_{ss}\eta$. For an exact solution of (14) we refer to Adler (1981). As $h \rightarrow \infty$, a simple asymptotic solution can be derived as follows. By Gaussianity, $\partial_t\eta$ and $\partial_s\eta$ are independent of each other and from $\partial_{ss}\eta$ and η . This implies that

$$EX_+(h) = A_S \int_0^{\infty} w_1 p(\partial_t\eta = w_1)dw_1 \cdot p(\partial_s\eta = 0) \int_{-\infty}^0 |w_2| p(\eta = h, \partial_{ss}\eta = w_2)dw_2 \quad (15)$$

The first integral on the left is equal to $\sqrt{m_{tt}/(2\pi\sigma^2)}$, and the term within square brackets equals the expected number, per unit length along s , of 1D local maxima with amplitude h . This is given, for large h , by $\sqrt{m_{ss}/(2\pi\sigma^2)}\xi e^{-\xi^2/2}$, with $\xi = h/\sigma$ as a dimensionless threshold. Noting that $|A| = m_{tt}m_{ss}$ is invariant by any axis rotation, we conclude that in general $EX_+(h)$ of (15) equals $EC(A_{\eta,h})$ of (11). Thus, as $h \rightarrow \infty$,

$$EX_+(h) \approx EX_{\max}(h) \approx \overline{EC(A_{\eta,h})} \quad (16)$$

This proves the existence of a one-to-one correspondence between 2D upcrossings and large maxima as in 1D processes. Adler's result (11) is thus relevant for applications because large upcrossings or maxima of random fields can be counted by simply estimating the Euler characteristic of their excursion sets.

4 Euler Characteristics of Oceanic Sea States

We extend (11) to deal with the expected EC of excursion sets of spatial snapshots of oceanic sea states measured via VWASS (see Fig. 2). To properly model oceanic nonlinearities (Fedele 2008, Fedele & Tayfun 2009), we follow Tayfun (1986) and define the wave surface η_{nl} over S as

$$\eta_{nl} = \eta + \frac{\mu}{2}(\eta^2 - \hat{\eta}^2) , \quad (17)$$

where $\mu = \lambda_3/3$ is the wave steepness, which relates to the skewness λ_3 of η_{nl} , and $\hat{\eta}$ is the Hilbert transform of a normalized Gaussian field η . For $\xi = h/\sigma \gg 1$, the excursion regions where $\eta_{nl} \geq \xi$ include just isolated local maxima. So, the structure of the excursion set can be related to the surface field locally to a maximum of η_{nl} with amplitude greater or equal to ξ . Assume that this occurs at $t = t_0$ and $s = s_0$. Then, the wave surface locally around that maximum is described by the nonlinear conditional process

$$\eta_{nc} = \{ \eta_{nl}(t, s) \mid \eta_{nl}(t_0, s_0) \geq \xi \} . \quad (18)$$

From (17) it is clear that the nonlinear quadratic component of η_{nl} is phase-coupled to the extremes of the Gaussian η . So, a large maximum of η_{nl} greater or equal to ξ occurs simultaneously when η itself is at a large maximum with an amplitude greater or equal to, say ξ_1 . Thus, the conditional process (18) is equivalent to the simpler process (Tayfun & Fedele 2007, Fedele & Tayfun 2009)

$$\eta_{nc} = \{ \eta_{nl}(t, s) \mid \eta_{nl}(t_0, s_0) \geq \xi_1 \} = \xi_1 \Psi + \frac{\mu}{2} \xi_1^2 (\Psi^2 - \hat{\Psi}^2) \text{ for } \xi_1 \gg 1 , \quad (19)$$

where $\Psi(t - t_0, s - s_0)$ is the normalized covariance of η . From (19), the large maximum of η_{nl} occurs at $t = t_0$ and $s = s_0$, where $\Psi = 1$ and $\hat{\Psi} = 0$, with amplitude

$$\xi = \xi_1 + \frac{\mu}{2} \xi_1^2 . \quad (20)$$

Thus, from (11) the expected EC of the excursion set $\{ \eta_{nl} \geq \xi \}$ equals that of the EC of the excursion set $\{ \eta \geq \xi_1 \}$ of the linear η , that is

$$\overline{EC(A_{\eta_{nl}, h})} = A_S (2\pi)^{-3/2} \sigma^{-2} |A|^{1/2} \xi_1 e^{-\xi_1^2/2} , \quad (21)$$

where ξ_1 satisfies the quadratic relation (20). In Figure 4 there are plotted the observed EC against the theoretical expected Gaussian EC (11) and the Tayfun EC (21) for the oceanic video data collected via VWASS shown in Fig. 2. The data agree with the nonlinear theoretical model (21).

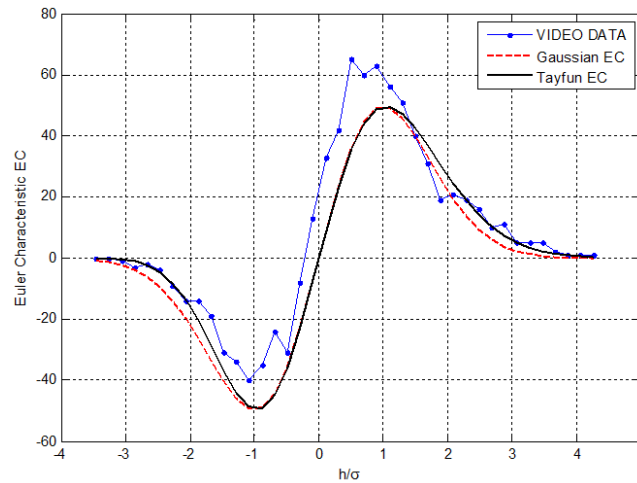


Fig. 4. Comparisons between theoretical models and the observed *EC* of the oceanic video data collected via VWASS (see Fig. 2).

5 Conclusions

We have proposed a novel variational image sensor (VWASS) for the stereo reconstruction of wave surfaces. The rich information content of the acquired three-dimensional video data is exploited to compute reliable estimates of both the directional wave spectrum and the expected global maximum (largest crest height) over an area. These estimates are of relevant significance in the offshore industry. In particular, the expectation of high waves over relatively small areas has important implications for a proper design of the air gap under the deck of fixed offshore structures (Forristall 2006). Localized damages have sometimes been observed on the lower decks of platforms after storms. We speculate that these failures may be due to a design that underestimates the largest water height expected over the area covered by the offshore structure. Thus, modern design criteria should account for the expected maximum of the water surface over a given area that could hit the platform deck. Offshore industry can thus benefit from the synergy of VWASS technologies and statistical tools based on Euler Characteristics that provide predictions of the largest wave height expected over an area and the associated spectral properties.

6 Acknowledgments

The authors would like to acknowledge Hailin Jin for providing source code that was partly used to obtain the results shown in this paper. Alvise Benetazzo is also grateful to Professor Ken Melville and Luc Lenain, of the Scripps Institution of Oceanography (SIO), San Diego, for the support received. We also thank Harald

Krogstad for useful discussions and suggestions. This work was partially supported by the 2007 Scale Space Methods and Variational Methods in Computer Vision (SSVM) best numerical paper award offered by CINECA-Italy.

References

- Adler, R.J. 1976 On generalising the notion of upcrossings to random fields. *Adv. App. Prob.* **27**(4):789-805.
- Adler, R.J. 1981 *The Geometry of Random Fields*, New York: John Wiley.
- Adler, R.J., Taylor, J.E. 2007 *Random fields and geometry*. Springer Monographs in Mathematics Springer, New York.
- Benetazzo, A. 2006 Measurements of short water waves using stereo matched image sequences. *Coastal Engineering* **53**:1013-1032.
- Faugeras O., Keriven R. 1998 Variational principles, surface evolution, pde's, level set methods and the stereo problem. *IEEE Trans. on Image Processing* **7**(3):336-344.
- Fedele, F., Tayfun, M.A. 2009 Nonlinear wave groups and crest statistics. *J. Fluid Mech.* **620**,221-239
- Fedele, F. 2008 Rogue Waves in Oceanic Turbulence. *Phys. D* **237**(14-17):2127-2131 .
- Forristall, G.Z. 2006 Maximum wave heights over an area and the air gap problem. OMAE2006-92022 paper, *Proc. ASME 25th Inter. Conf. Off. Mech. Arc. Eng.*, Hamburg, Germany.
- Gallego G, Benetazzo A., A. Yezzi, Fedele F. 2008 Wave spectra and statistics via a variational wave acquisition stereo system. OMAE2008-57160 paper, *Proc. ASME 27th Inter. Conf. Off. Mech. Arc. Eng.*, Estoril, Portugal.
- Ma, Y. Soatto, S., Kosecka, J., Shankar Sastry, S., 2004 *An invitation to 3-D vision: from images to geometric models*. Springer-Verlag New York.
- Piterbarg V. 1995 *Asymptotic Methods in the Theory of Gaussian Processes*. American Mathematical Society, ser. Translations of Mathematical Monographs, **148**, 205pp.
- Tayfun, M.A. 1986 On narrow-band representation of ocean waves. Part I: Theory. *J. Geophys. Res.*, **1**(C6):7743-7752.
- Tayfun, M.A., Fedele F. 2007 Wave height distributions and nonlinear effects. *Ocean Eng.* **34**(11-12):1631,1649.
- Worsley, K.J. 1995 Boundary corrections for the expected Euler characteristic of excursion sets of random fields, with an application to astrophysics. *Adv. App. Prob.* **27**:943-959.

ROGUE WAVES 2008, Brest 13–14 October 2008

Extreme waves on current jets — are they freak?

Karina B. Hjelmervik and Karsten Trulsen

University of Oslo, Department of Mathematics, P.O.Box 1053 Blindern,
NO-0316 Oslo, Norway

It is well known that waves grow taller when they propagate against an increasing current. It is also well known that waves can be trapped inside an opposing current jet. These phenomena are often responsible for navigational problems in oceanic currents such as the Aghulas current, or in river estuaries or entrances of fiords during outgoing tides, or in tidal flows in the coastal zone.

In the presence of inhomogeneous currents, it becomes necessary to distinguish two different types of statistical distributions for surface waves, namely (1) distributions at each fixed location, and (2) distributions averaged over space, including regions with and without current. The first type of distribution is related to time series measured at fixed points, while the second type is more associated with spatial snapshots of the ocean surface.

If the inhomogeneous current is a priori known, we recommend using the first type of statistical distribution that is specific for each location. It then becomes unjustified to claim that large waves provoked by current refraction are freak waves, unless these waves also belong to the extreme tail of the particular probability distribution that applies at the specific location where these waves occur.

We have studied the statistical distributions of waves propagating against increasing collinear currents and current jets. Monte-Carlo simulations have been performed employing a nonlinear Schrödinger equation modified to include the effects of inhomogeneous current.

We find that application of the two types of statistical distributions may lead to opposite conclusions regarding the occurrence of freak waves on nonuniform currents. In particular, we anticipate that a time series of waves measured near the center of an opposing current jet will show more high waves and fewer freak waves than a time series measured away from the current jet.

Nonlinear Parameters of Wave Distribution to Characterize Freak Waves

*Seung-Ho Shin**, *Keyyong Hong**

Ocean Engineering Research Department, Maritime & Ocean Engineering Research Institute, KORDI
Daejeon 305-343, Korea*

ABSTRACT : *This study is carried out to investigate the nonlinear characteristics of field observed wave data acquired in the southwestern sea of Korean peninsula for 3 years. It is aimed to identify the correlation between nonlinear parameters and freak wave occurrence, which may eventually lead to freak wave forecasting based on wave spectra in real sea. The nonlinear parameters of ocean waves of skewness, atiltness, kurtosis and spectrum band width et al. are analyzed, and their relevance with component wave characteristics of significant wave height, maximum wave height and so on is examined. It is evident that with an exception of kurtosis, the parameters describing nonlinear characteristics of observed wave spectrum are feebly related to occurrence of abnormal maximum wave height, namely freak event. The kurtosis, which is a degree of peakness of mode of surface elevation distribution, shows strong relevance with freak event and we suggest a logarithmic formulation describing their correlation based on field wave data.*

INTRODUCTION

Various studies to inquire characteristics of freak waves were mainly attempted by theoretical and numerical method due to rare availability of reliable field wave data in open sea. However, it is essential that the laboratory development of freak wave phenomena is verified by the field wave data and its importance has been enhanced by the recent strong interest of freak wave forecasting in real sea.

In this study, we analyzed the field wave data in open sea

which were continuously observed in southwestern offshore of Korean peninsula (Fig. 1) from April 2003 to October 2006. Based on stochastic and spectral analysis of random wave characteristics, we identified the nonlinear parameters of wave spectra that govern the freak event like rogue waves.

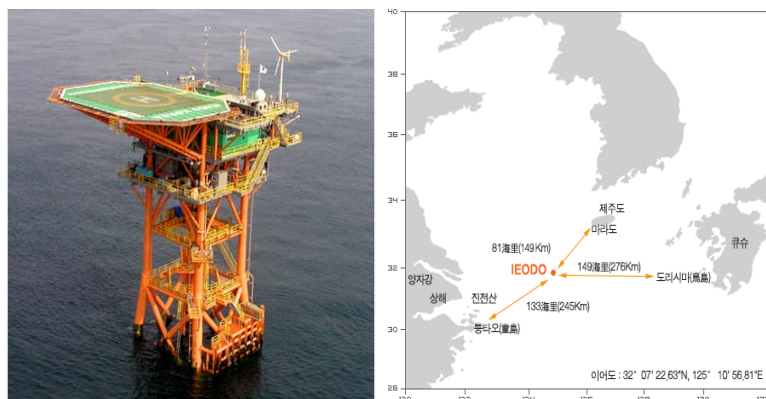


Fig. 1 Location of Ieodo Ocean Research Station

FIELD WAVE DATA

Ieodo Ocean Research Station is a complex ocean observation station located in southwestern offshore of Korea. Since the station started its operation in April 2003, it has collected the real time data necessary for maritime and fisheries observation, weather forecast and global environment watch.

Wave data acquired from the station are measured by MIROS Wave Radar[SM-001]. It continuously records oceanic and atmospheric information with a sampling rate of 5.116Hz. For the present analysis, the data collected from April 2003 to October 2006 was used and it consists of 40,227 sub sets which have 30 minutes recording length respectively.

KURTOSIS OF DISTRIBUTION OF SURFACE ELEVATION AND FREAK EVENT INDEX

The Jeodo wave data reveals distinguished correlation between nonlinear parameters and freak event from Chagwido wave data, which was measured by a moored buoy at relatively closed sea in southwestern part of Korean coast for a year. Shin et al.(2007) analyzed Chagwido wave data and investigated nonlinear parameters of observed random wave sets. They found that the freak event index, $H_{\max}/H_{1/3}$, has relatively close correlation to the kurtosis of distribution of surface elevation, which is represented by Eq. (1), than other nonlinear parameters of bandwidth of wave spectrum, Goda's spectrum peakness, skewness and atiltness of distribution of surface elevation.

$$K_t = \frac{1}{\eta_{rms}^4} \cdot \frac{1}{N} \sum_{i=1}^N (\eta_i - \bar{\eta})^4 \quad (1)$$

However, the correlation in Fig. 2 seems to be weak and it is hard to express it by a fitting curve. The weak correlation is partially contributed by low data sampling rate of 1.28Hz and imperfect motion of floating buoy in a steep high wave as freak waves

The relationship between kurtosis and freak event index of Jeodo wave data is shown in Fig 3. Upper, middle and lower one represents the result of wave data analysis for 2004, 2005 and 2006, respectively. Comparing to Chagwido wave data, it reveals much stronger correlation and it can be properly expressed by a logarithmic fitting function shown in Fig. 3. It prove that a precise data acquisition of waves is important to characterize the nonlinearity of surface elevation and its distribution, and then the kurtosis can be utilized as a forecasting index of freak waves in real sea.

ACKNOWLEDGEMENTS

This study has been carried out as a part of the Research Project 'PE0126A', 'PM0160A' and 'PN0115A'. Their support is gratefully acknowledged.

REFERENCE

- Shin, S. H. and K. Hong(2006), "A Study of the Appearance Characteristics and Generation Mechanism of Giant Waves", Journal of Korean Navigation and Port Research, Vol. 30(3), pp. 181-187(in Korean).
- Shin, S. H., K. Hong and J. S. Moon(2007), "Wave Data Analysis for Investigation of Freak wave Characteristics", Journal of Korean Navigation and Port Research, Vol. 31(6), pp. 471-478(in Korean).
- Faulkner, D. and Williams R. A.(1996), "Design for Abnormal Ocean Waves", RINA.
- Mori, N. and Janssen, P.(2005), "On Kurtosis and Occurrence Probability of Freak Waves", Submitted to Jour. Phys. Oceangra.

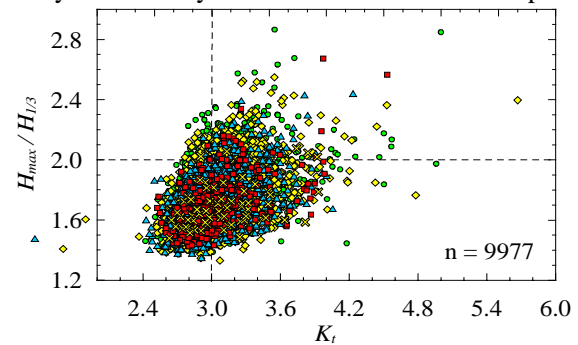


Fig. 2 The relationships between Kurtosis of distribution of surface elevation and $H_{\max}/H_{1/3}$ (sampling rate : 1.28Hz, Jeju)

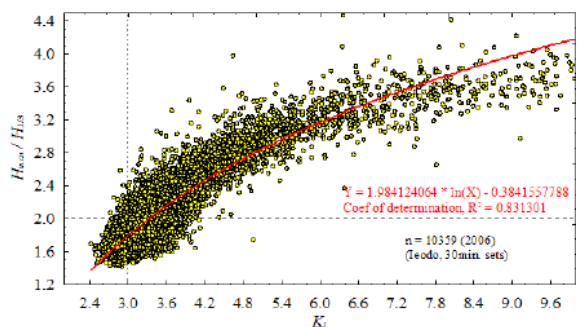
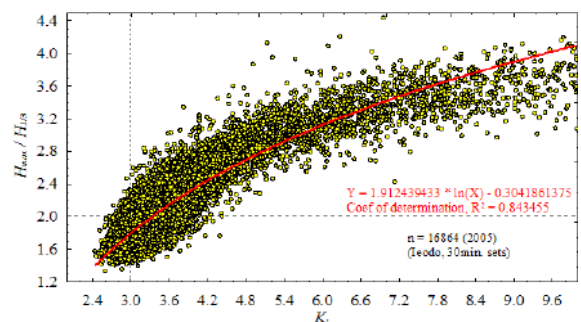
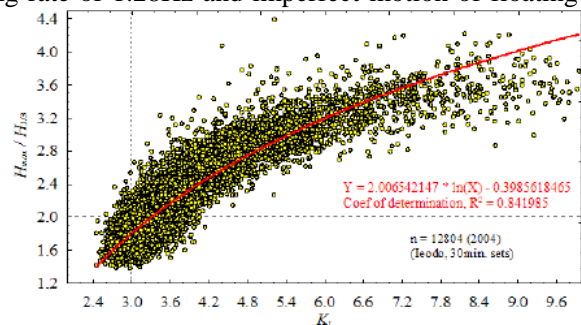


Fig. 3 The relationships between Kurtosis of distribution of surface elevation and $H_{\max}/H_{1/3}$ (sampling rate : 5.116Hz, Jeodo)



Sessions IV. Laboratory



Extreme value phenomena in optics: origins and links with oceanic rogue waves

John Dudley¹, Goëry Genty², Frédéric Dias³, & Benjamin Eggleton⁴

¹Institut FEMTO-ST, Université de Franche-Comté, Besançon, France

²Optics Laboratory, Tampere University of Technology, Tampere, Finland

³Centre de Mathématiques et de leurs Applications, ENS Cachan, Cachan, France

⁴CUDOS, School of Physics, University of Sydney, NSW 2006, Australia

jdudley@univ-fcomte.fr,

goery.genty@tut.fi, frederic.dias@cmla.ens-cachan.fr,

egg@physics.usyd.edu.au

Abstract. We present a numerical study of the evolution dynamics of “optical rogue waves”, statistically-rare extreme red-shifted soliton pulses arising from supercontinuum generation in highly nonlinear fibers.

1 Introduction

A central challenge in understanding extreme events is to develop rigorous models linking the complex generation dynamics and the associated statistical behaviour. Quantitative studies of extreme value phenomena, however, are often hampered in two ways: (i) the intrinsic scarcity of the events under study and (ii) the fact that such events often appear in environments where measurements are difficult. In this context, highly significant experiments were reported by Solli et al. in late 2007, where a novel wavelength-to-time detection technique has allowed the direct characterization of the shot-to-shot statistics in the extreme nonlinear optical spectral broadening process known as supercontinuum (SC) generation when launching pulses of long duration into a fiber with high nonlinearity [1]. Although this regime of SC generation is known to exhibit fluctuations on the SC long wavelength edge [2], it was shown that these fluctuations contain a small number of statistically-rare “rogue” events associated with an enhanced red-shift and a greatly increased intensity. Crucially, because these experiments were performed in a regime where modulation instability (MI) plays a key role in the dynamics, it has been possible to propose an important correspondence with the hydrodynamic rogue waves [3], whose origin has also been discussed in terms of MI or, as it is usually referred to in hydrodynamics, the Benjamin-Feir instability [4–6]. Although the links between optical and oceanic rogue waves will clearly require much further analysis, our objective here is to use a generalized nonlinear Schrödinger equation model to study the evolution dynamics of optical rogue wave (or rogue soliton) generation.

2 Dynamics of optical rogue waves

Our simulations use a generalized form of the well-known nonlinear Schrödinger equation suitable for modeling propagation of broadband unidirectional fields [7, 8]. Rogue wave dynamics would be expected whenever SC generation is induced from an initial stage of modulation instability, and we consider picosecond pulse excitation under similar conditions to previous numerical studies [1]. Specifically, we model 5 ps full width at half maximum gaussian pulses propagating in 20 m of photonic crystal fiber with zero dispersion at 1055 nm. Noise is included on the input field through a one-photon-per mode background and through a thermal spontaneous Raman scattering source term [2]. The general features of rogue soliton generation are shown in Fig. 1. Here, Fig. 1 (a) superposes the output spectra (gray traces) from an ensemble of 1000 simulations with different noise seeds, as well as the calculated mean (black line). The expanded view of the long wavelength edge in Fig. 1(b) allows us to clearly see the small number of rogue soliton events associated with a greatly increased red shift, and these particular events can be isolated using the technique developed in [1]. Specifically, for each SC in the ensemble, a spectral filter selects components above a particular wavelength on the long wavelength edge, and Fourier transformation then yields a series of ultrashort pulses of varying power depending on the position of the filter relative to the SC spectral structure. The frequency distribution of the pulse peak power then readily reveals the presence of statistically-rare high peak-power rogue solitons that have been fully captured because of their extreme shifts to longer wavelengths.

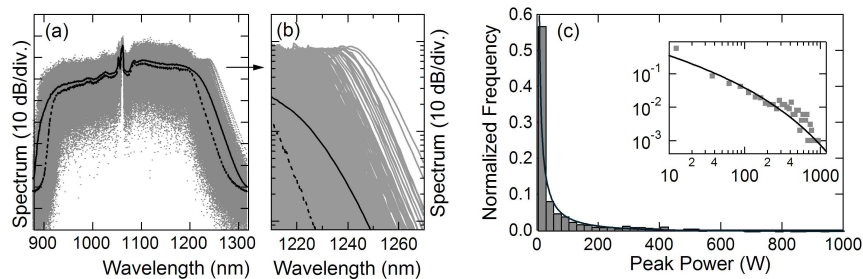


Fig. 1. (a) Results showing 1000 individual spectra (gray curves). The mean spectrum is shown as the solid black line. (b) Expanded view above 1210 nm. (c) Histogram of the peak power frequency distribution using 25 W bins. We plot normalized frequency such that bar height represents the proportion of data in each bin. The inset plots the results on a log-log scale, and also shows the fitted Weibull distribution (solid line).

Fig. 1(c) shows the histogram of the data using a filter at 1210 nm. The frequency distribution is clearly very skewed and the fraction of high power rogue solitons is extremely small with only 1 realization in the 1000 run ensemble

having a peak power exceeding 1 kW. Although a full treatment of the statistical properties of the rogue solitons is outside the scope of this paper, our preliminary analysis suggests that the histogram is well-fitted by a Weibull distribution, a class of “extreme value” probability density function that is commonly used to analyze events associated with large deviations from the mean and median [9]. This fit is shown as the solid line in Fig. 1(c).

Additional key features of the rogue soliton dynamics are shown in Fig. 2, where we compare the spectral and temporal evolution of two selected realizations in the ensemble. In particular, Fig. 2(a) illustrates the evolution of a “rogue” event associated with the generation of a 900 W peak power soliton centered around 1240 nm, whereas Fig. 2(b) shows the evolution for a case where the output spectrum is closer to the distribution median, and there is little spectral energy above 1210 nm.

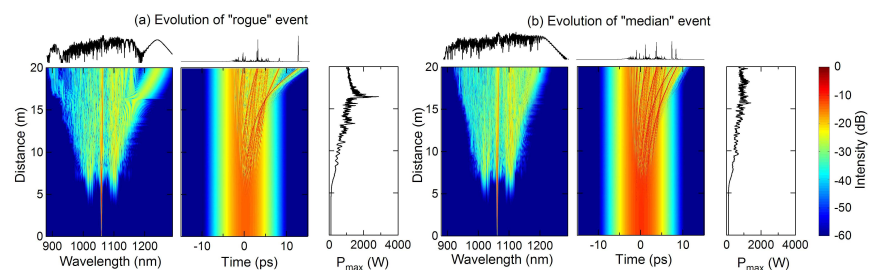


Fig. 2. Density plots of spectral and temporal evolution for: (a) a rare event leading to a rogue soliton (RS) and (b) a result close to the distribution median.

In both cases, however, the initial evolution is similar, with the growth of characteristic MI sidebands about the pump, and the development of a corresponding temporal modulation on the pulse envelope. Nonetheless, differences in the way in which the MI is seeded from the initial random noise leads to significant variation in the spectral and temporal evolution trajectories after a propagation distance of around 10 m. It is during this phase of the propagation that the modulated pulse envelope breaks up into individual soliton pulses, but we can see clearly how the rogue event is associated with the ejection of one particular high-power soliton pulse that extracts energy from the other soliton like pulses on the envelope, before clearly separating from the residual envelope in the time domain due to its significantly different group velocity. The exchange of energy between colliding solitons in the presence of the Raman effect has been the subject of much previous research [10, 11] and it is likely that this process plays a key role in the statistical excitation of rare rogue wave events in the case where supercontinuum generation arises from noise [1, 12]. The significance of the results shown in Fig. 2 is that they suggest that the study of the propagation

dynamics of an initially modulated input may allow this energy exchange process to be studied under controlled (rather than statistical) conditions. In fact, although we show only two particular results in this figure, a full analysis of the ensemble shows that the distinct spectral and temporal evolution trajectory shown in Fig. 2(a) is a characteristic feature of optical rogue soliton generation [13].

3 Conclusion

The study reported here has been motivated by the recent experimental observation of optical rogue waves, statistically rare soliton pulses generated on the long wavelength edge of a broadband SC spectrum. Our numerical simulations have provided insight into the distinctive features of these rogue soliton events. At this stage, it is clear that the links between optical and oceanic rogue waves will require much further analysis.

References

1. D. R. Solli, C. Ropers, P. Koonath, and B. Jalali, "Optical rogue waves," *Nature* **450**, 1054–1057 (2007).
2. J. M. Dudley, G. Genty, and S. Coen, "Supercontinuum generation in photonic crystal fiber," *Rev. Mod. Phys.* **78**, 1135–1184 (2006).
3. C. Kharif and E. Pelinovsky, "Physical mechanisms of the rogue wave phenomenon," *Eur. J. Mech. B Fluids* **22**, 603–634 (2003).
4. T. Benjamin and J. Feir, "The disintegration of wavetrains in deep water, Part 1," *J. of Fluid Mech.* **27**, 417–430 (1967).
5. A. Dyachenko and V. E. Zakharov, "Modulation instability of Stokes wave implies a freak wave," *JETP Lett.* **81**, 255–259 (2005).
6. M. Onorato, A. Osborne, and M. Serio, "Modulational instability in crossing sea states: A possible mechanism for the formation of freak waves," *Phys. Rev. Lett.* **96**, 014503 (2006).
7. G. Genty, P. Kinsler, B. Kibler, and J. M. Dudley, "Nonlinear envelope equation modeling of sub-cycle dynamics and harmonic generation in nonlinear waveguides," *Opt. Express* **15**, 5382–5387 (2007).
8. K. Blow and D. Wood, "Theoretical description of transient stimulated Raman scattering in optical fibers," *IEEE J. Quantum Electron.* **25**, 2665–2673 (1989).
9. S. Coles, *An introduction to Statistical Modeling of Extreme Values* (Springer-Verlag, London, 2001).
10. M. H. Frosz, O. Bang, and A. Bjarklev, "Soliton collision and Raman gain regimes in continuous-wave pumped supercontinuum generation," *Opt. Express* **14**, 9391–9407 (2006).
11. A. Peleg, "Intermittent dynamics, strong correlations, and bit-error-rate in multi-channel optical fiber communication systems," *Phys. Lett. A* **360**, 533–538 (2007).
12. J. M. Dudley, G. Genty, and B. J. Eggleton, "Harnessing and control of optical rogue waves in supercontinuum generation," *Opt. Express* **16**, 3644–3651 (2008).
13. D.-I. Yeom, J. A. Bolger, G. D. Marshall, D. R. Austin, B. T. Kuhlmey, M. J. Withford, C. M. de Sterke, and B. J. Eggleton, "Tunable spectral enhancement of fiber supercontinuum," *Opt. Lett.* **32**, 1644–1646 (2007).

Spectral characteristics of an extreme crest measured in a laboratory basin

Marios Christou¹, Kevin Ewans¹, Bas Buchner² & Chris Swan³

¹ Shell International Exploration & Production B.V.,
Kessler Park 1, Rijswijk 2288 GS,
The Netherlands.

marios.christou@shell.com and kevin.ewans@shell.com

² MARIN (Maritime Research Institute Netherlands),
Wageningen,
The Netherlands.

b.buchner@MARIN.NL

³ Department of Civil & Environmental Engineering,
Imperial College London,
London, SW7 2AZ, UK.

c.swan@imperial.ac.uk

Abstract. Spectral characteristics of extreme crests, measured in a laboratory basin are examined with the continuous wavelet transform. The analyses have provided further insight into the processes occurring in these extreme events. During the period of the extreme wave crest, spectral levels over all frequencies are substantially elevated by comparison with the average spectrum for the complete wave record. In previous studies, this was also observed in a similar analysis of the famous New Year wave event that occurred at the Draupner platform. The analyses also indicate that nonlinear effects are active during the crest event, second-order effects being particularly strong and indicating phase-locking of high frequency waves to freely-propagating waves with frequencies close to the spectral peak. These nonlinear effects appear to be strong only in the vicinity of the extreme crest. Comparisons are made against linear, second-order and fully nonlinear predictions of focused wave events, to substantiate the interpretation of the results.

1 Introduction

Insight into the behaviour and statistics of *rogue* or *freak* waves is important in the study of the behaviour of offshore platforms in survival conditions. Especially when there is a clear step in the response of the platform as function of the crest amplitude, such as the air-gap problem for fixed and floating platforms [13], the accurate determination of the *rogue* wave crests that are expected at a field location are important for the platform's survivability.

As a result, there are several theories that attempt to explain the occurrence of *rogue* waves to predict the largest crest elevations. Amongst these include

wave-current interactions, long-crested effects [9] and focusing of wave energy to form a *NewWave*-type group [18]; numerous examples of the latter are present in field measurements, an example being the famous New Year wave [10]. This paper will present laboratory measurements recorded in the Offshore Basin at MARIN [4] that are both unidirectional and incorporate random waves interacting with a current. The laboratory measurements will be compared to focused wave groups predicted by linear, second-order and fully nonlinear irregular wave models. The time histories of the water surface elevation produced from these four different sources will then be examined by spectral techniques such as the Short-Time Fourier Transform (STFT) and the Wavelet Transform. These spectral techniques will be employed with the aim of determining the degree of stationarity beneath the *rogue* wave event and examining the evolution of the wave spectrum. It will be demonstrated that extreme care is needed when interpreting the outputs of both the STFT and the Wavelet Transform. However, it will be shown that by comparing the results to spectra with known evolution it is possible to gain insight into the energy shifts beneath a *rogue* wave.

This paper continues with a brief summary of previous work in section 2 before summarising the laboratory investigation in section 3. The linear and nonlinear models are then introduced in section 4 and the spectral techniques are described in section 5. The results are then presented in section 6 before the final conclusions are drawn and the wider implications discussed in section 7.

2 Background

Several authors have reported extreme wave measurements in field and laboratory measurements. The most famous of these observations is the New Year's Wave as reported by Haver and Andersen (2000)[10] at the Draupner East platform. This sea state had a significant wave height of $H_s = 11.92\text{m}$ with a peak wave period of $T_p = 16.7\text{s}$ and the *rogue* wave had ratios of $\eta_c/H_s = 1.55$ and $H_{max}/H_s = 2.15$, where η_c is the crest elevation and H_{max} is the maximum wave height. Another example is the spatial analysis of extreme wave in a model basin by Buchner *et al.*(2007) [4]. In this paper it was shown that linear dispersion and second order theory could not explain the wave propagation towards this extreme wave crest.

The conventional FFT-based power spectral density has provided substantial insight into wave processes over many years, but more recently a number of authors have emphasised the additional insight that can be gained from the temporal spectral information available from a wavelet analysis [7, 15, 17]. The ability to examine the time-dependent spectral characteristics is important; several authors indicate that nonlinear wave-wave interactions are the cause of these extreme waves as a result of rapid shifting of wave energy in the spectrum, see Gibson and Swan (2007)[9].

Alternative approaches to examining temporal spectral characteristics include the Short-Time Fourier Transform (STFT) and the Hilbert-Huang Transform (HHT). The STFT consists of a Fourier Transform performed over a rel-

atively small time window. As such, it provides some information about both when and at what frequencies a signal event occurs, but with limited precision, determined by the size of the window. Cherneva and Guedes Soares (2005)[5] applied the technique, in conjunction with Hilbert Transform analyses, to analyse wave data recorded off the Portuguese coast, but it appears that more information on the temporal variability was gained from the Hilbert Transform analysis than from the STFT.

The HHT [11] is a data-adaptive technique. Firstly, an empirical mode decomposition (EMD) is performed, which identifies the specific local time scales and extracts them into Intrinsic Mode Functions (IMFs). A Hilbert transform of the IMFs is then performed, allowing an instantaneous frequency with which embedded events can be identified. Accordingly, the HHT does not have the same resolution difficulties as the STFT, and Velcheva and Guedes Soares (2007)[19] demonstrated the value of the technique in the examination of records with large wave events.

As with the STFT, the wavelet spectrum suffers from resolution difficulties, but unlike the STFT in which the time window is fixed for all frequencies, the wavelet spectrum has the advantage that the time window varies with frequency, providing constant frequency resolution but with increased time resolution (shorter time windows) at higher frequencies. In addition, the wavelet transform is readily extended to other spectral quantities, such as coherence and bi-coherence, providing additional time-dependent spectral features to be identified.

3 Laboratory Investigation

In Buchner *et al.* (2007)[4], a detailed description is given of the spatial measurements that were carried out; these are the basis of the present analysis. In this section a very brief summary of the earlier work is given as background. A unidirectional wave spectrum was generated with a significant wave height $H_s = 11.9\text{m}$ and a spectral peak period $T_p = 15.3\text{s}$ (JONSWAP $\gamma = 2.6$) at an angle of 15° to a current with velocity $V_c = 1.9\text{m/s}$ as demonstrated in Fig. 1. The laboratory investigation recorded several time histories of the water surface elevation at different spatial locations, as indicated in Fig. 2. Ewans & Buchner (2008)[8] built on the work of Buchner *et al.* (2007)[4] by analysing the spatial evolution of the *rogue* wave by employing the Wavelet Transform. They first demonstrated the sudden formation (within approximately 20m at full scale) and persistence (for approximately 160m) of the largest crest. They subsequently calculated the cross-spectral density based on the Wavelet Transform and concluded that the components around the peak frequency are freely propagating at the maximum event. Furthermore, they employed the bi-coherence based on the Wavelet Transform and ascertained that the second-order phase coupling was strong during the largest event and the high-frequency components are bound waves.

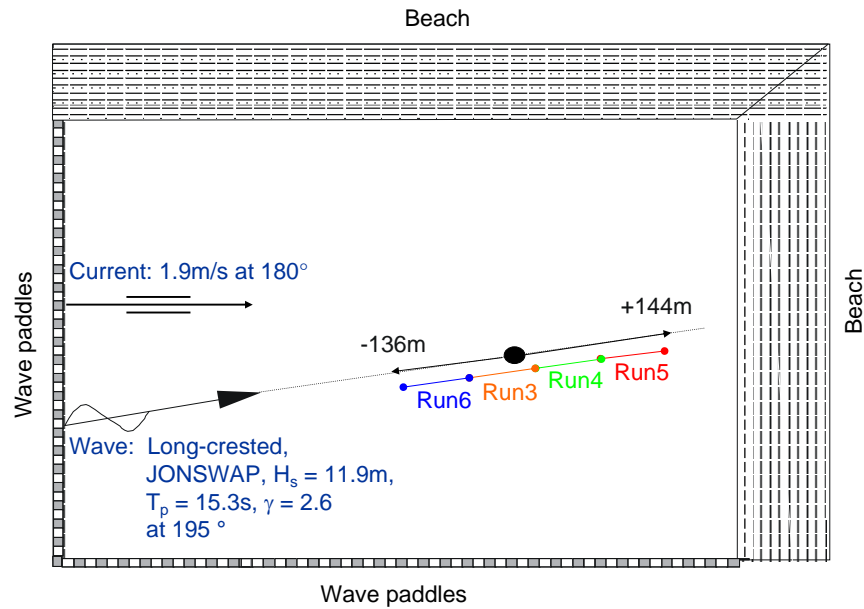


Fig. 1. Wave and current directions, original measurement location (black dot) and positions of the wave measurement frame for the four runs.

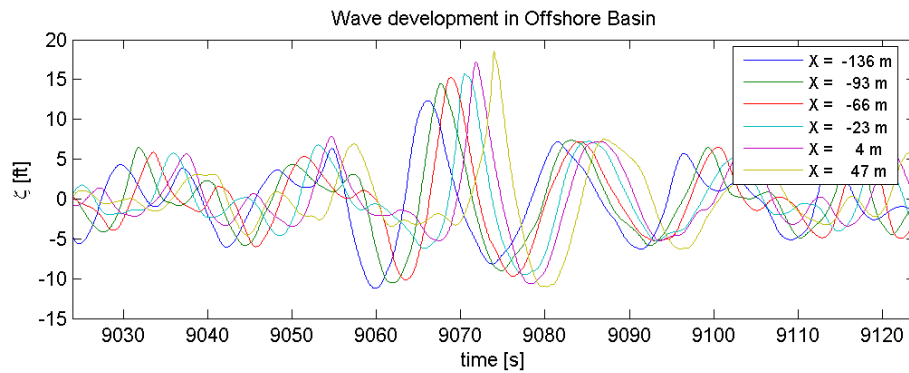


Fig. 2. Time histories of water surface elevation at different spatial locations; reproduced from Buchner *et al.* (2007)[4] and presented at full scale.

The present study only focuses on the time trace of the largest event that corresponds to the *rogue* wave at $x = 47\text{m}$ when converted from laboratory scale to full scale.

4 Linear and Nonlinear Models

This section briefly describes the linear and second-order irregular wave theories as well as the fully nonlinear model employed in the present study. The inputs to the linear and nonlinear models was a JONSWAP spectrum with the same peak wave period ($T_p = 15.3\text{s}$) and peak enhancement factor ($\gamma = 2.6$) as generated in the laboratory. However, rather than matching the significant wave height of the laboratory sea state, as a focused wave event was generated by the models it was thought more prudent to match the crest elevation predicted by the models with that from the experimental measurements of the *rogue* wave. The method by which this was achieved is discussed for the various models below. Furthermore, the current present in the laboratory investigation has not been included in the simulations.

4.1 Linear Random Wave Theory (LRWT)

The linear water surface elevation, $\eta^{(1)}$, can be simply considered as the summation of N components described by Airy theory [1]. This method is often referred to as Linear Random Wave Theory (LRWT) and is written as

$$\eta^{(1)} = \sum_{i=1}^N a_i \cos(k_i x - \omega_i t + \varphi_i), \quad (1)$$

where t is time and, for the i^{th} component, a_i is the amplitude, ω_i is the frequency and φ_i is the phase angle. A focused wave event is obtained by setting all $\varphi_i = 0$ rad and $x = 0$ m.

The linear input amplitude sum, A , is defined as the summation of all the amplitude components and for LRWT corresponds to the maximum crest elevation of a focused wave, η_c^{lrwt} . For LRWT, A is set equal to the crest elevation of the *rogue* wave as recorded in the laboratory, η_c^{lab} , which is expressed as

$$\eta_c^{lrwt} \equiv A = \sum_{i=1}^N a_i = \eta_c^{lab}. \quad (2)$$

The amplitude of each component, a_i , is scaled according to the JONSWAP spectrum.

4.2 Second-order Irregular Wave Theory

Most of the waves in a random sea are small and obey a linear model. However, the larger waves that determine the air-gap problem exhibit higher, steeper crests and shallower, broader troughs. This is accounted for by the second-order

correction terms as described in Sharma and Dean (1981) [16]

$$\eta^{(2)} = \eta^{(2)+} + \eta^{(2)-}, \quad (3)$$

$$\eta^{(2)+} = \frac{1}{4} \sum_i^N \sum_j^N a_i a_j K_{ij}^+ \cos(\psi_i + \psi_j), \quad (4)$$

$$\eta^{(2)-} = \frac{1}{4} \sum_i^N \sum_j^N a_i a_j K_{ij}^- \cos(\psi_i - \psi_j), \quad (5)$$

where $\psi_i = k_i x - \omega_i t + \varphi_i$, $\eta^{(2)+}$ and $\eta^{(2)-}$ are the second-order sum and difference terms with their corresponding kernels K^+ and K^- respectively. The total water surface elevation up to second-order is expressed as $\eta = \eta^{(1)} + \eta^{(2)}$. Once again, a focused wave event is obtained by setting all $\varphi_i = 0$ rad and $x = 0$ m.

As second-order theory includes sum and difference terms, it is no longer possible to set $A = \eta_c^{lab}$ as was done for LRWT. Furthermore, as the magnitude of the sum and difference terms cannot be determined *a priori*, the value of A must be determined iteratively until $\eta_c^{2nd} = \eta_c^{lab}$, where η_c^{2nd} is the maximum crest elevation of a focused wave up to second-order.

4.3 Fully Nonlinear Fourier-based Model

The present study also employs the Fourier-based model of Bateman *et al.* (2001)[3], hereafter referred to as BST. This model provides a highly efficient, fully nonlinear, directional wave model based on the Dirichlet-Neumann operator; the latter being similar to the G-operator proposed in two-dimensions by Craig & Sulem (1993)[6]. The inputs to the numerical model consist of the initial spatial representation of the water surface, $\eta(x)$, and the velocity potential on the water surface, $\phi(x, z = \eta)$, at some starting time, t_0 . Typically, these are defined by LRWT or second-order theory (as described above), well in advance of the focal time when the wave field is dispersed. At this stage the maximum water surface elevation will be small, and thus accurately described by linear or second-order irregular wave theory. The significant advantage of the BST model lies in its computational efficiency, which is due to the Dirichlet-Neumann operator that transforms the values of the velocity potential on the water surface to its spatial derivatives. This allows all the time dependent coefficients to be determined via a Fast Fourier Transform (FFT); the most important aspect of this increased efficiency being the ability to model realistic sea states, with high resolution in both the wave number and directional domains. The numerical model has been shown to be in very good agreement with the experimental measurements of Baldock *et al.* (1996)[2] and Johannessen & Swan (2001)[12]; the former involving unidirectional and the latter multi-directional focused waves. A full description of the numerical model with its implementation and validation can be found in Bateman *et al.* (2001)[3].

As with second-order theory, nonlinear increases in the water surface elevation cannot be determined *a priori*. Therefore, the value of A must be determined

iteratively until $\eta_c^{bst} = \eta_c^{lab}$, where η_c^{bst} is the maximum crest elevation predicted by BST. In the present study, this did not correspond to the focused wave event, but occurred slightly afterwards.

5 Spectral Analysis Techniques

5.1 Short-Time Fourier Transform (STFT)

The Short-Time Fourier Transform (STFT) simply performs a Fourier Transform over a smaller sample of a whole time signal. As this section is gradually translated from the beginning to the end of the whole time signal, the temporal evolution of the spectral frequency content can be determined. The STFT, $X(\tau, f)$, can be expressed as

$$X(\tau, f) = \int_{-\infty}^{\infty} x(t)w(t - \tau)e^{-j2\pi ft} dt \quad (6)$$

where $w(t)$ is a window function (a Tukey window with a ratio of taper to constant sections of 0.5 being employed in the present study), $x(t)$ is the time signal, f is the frequency and τ is the time shift. The spectrogram is defined as the square of the absolute STFT, that is $|X(\tau, f)|^2$. One disadvantage of the STFT is that there is a compromise between the resolution in time and frequency. If the resolution in time is high, then the resolution in frequency must necessarily be low and vice versa.

5.2 Wavelet Theory

The wavelet function, $\psi(t)$, has the following properties:

$$\int_{-\infty}^{\infty} \psi(t) dt = 0, \quad (7)$$

and

$$\int_{-\infty}^{\infty} |\psi(t)|^2 dt = 1. \quad (8)$$

The function can be dilated with a scale parameter, s , and translated in time by a shift parameter, p . Accordingly, the scaled and shifted wavelet function is given by

$$\psi_{s,p}(t) = \frac{1}{\sqrt{s}} \psi\left(\frac{t-p}{s}\right). \quad (9)$$

The continuous wavelet transform is the correlation of the signal $x(t)$ with the scaled and translated wavelet

$$W(s, p) = \int_0^{\infty} x(t) \psi_{s,p}\left(\frac{t-p}{s}\right) dt. \quad (10)$$

Following other authors [14, 15] we have chosen the complex Morlet wavelet for the analyses, which is a complex wave tapered with a Gaussian bell

$$\psi(t) = \frac{1}{\sqrt{\pi f_b}} e^{i2\pi f_c t} e^{-t^2/f_b}, \quad (11)$$

where f_b is a window width parameter, and f_c is the centre frequency. By comparison with a Gaussian function it can be recognised that $f_b = 2\sigma^2$, where σ^2 is the variance. In the analyses, $f_b = 1$, $f_c = 1.5$, and the wavelet is defined for an x -range of $[-8, 8]$. The centre frequency can be related to an effective frequency or “pseudo frequency”, f_{sig} , in signal space by

$$f_{sig} = \frac{f_c}{s\tau}, \quad (12)$$

where τ is the sampling interval, and the full width of the scaled wavelet function transformed to signal space TW is given by

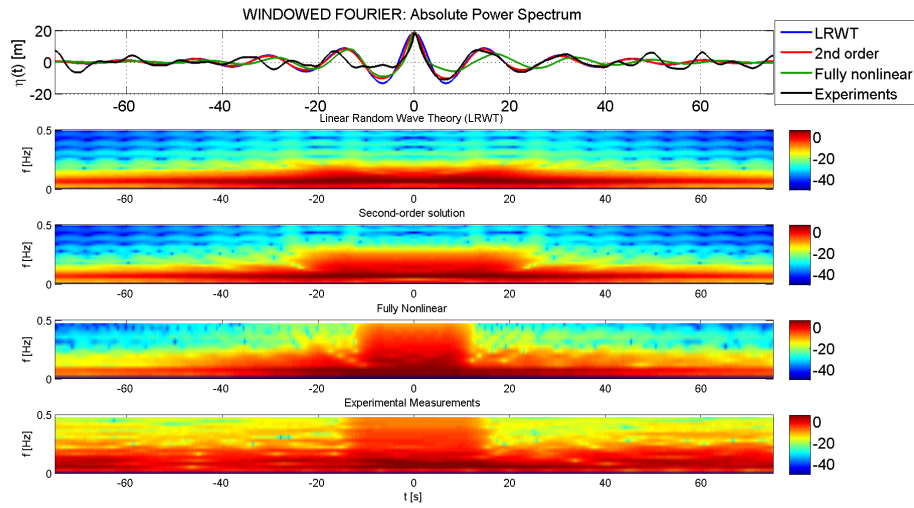
$$TW = \frac{2f_c}{f_{sig}}. \quad (13)$$

The advantage of the Wavelet Transform lies in the fact that each frequency component employs a different window width, which is a function of its period. This is in contrast with the STFT, which uses a constant window width for all frequencies. Another advantage of the Wavelet Transform is that it can produce reasonable temporal resolution for high-frequency components, whilst at the same time maintaining adequate resolution in frequency for low-frequency components.

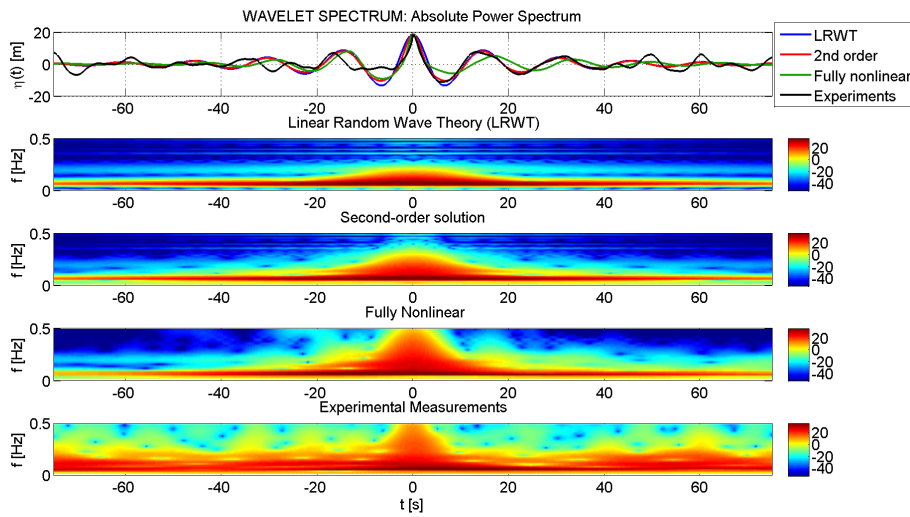
6 Discussion of Results

Fig. 3 presents the time histories of the water surface elevation as predicted by the linear, second-order and fully nonlinear models as well as that recorded in the laboratory. The time traces from the experimental measurements and the fully nonlinear model are shifted such that the maximum crest occurs at $t = 0$ s to facilitate the comparison with the analytical theories. Furthermore, Fig. 3 presents the power spectrums for the linear, second-order, fully nonlinear and experimental time traces as calculated using the STFT (subplot (a)) and the Wavelet Transform (subplot(b)). The STFT was calculated based on a window width of 51.2s, which was found to give the best compromise between frequency and time resolutions. Fig. 3 illustrates that the power spectra from the STFT and the Wavelet Transform are qualitatively similar, demonstrating the same trends. However, the Wavelet Transform is much more clearly defined, highlighting the disadvantages of the STFT in compromising between time and frequency resolutions and employing a constant window width for all frequencies.

It is very tempting to examine the STFT and Wavelet power spectrums for only the experimental measurements of the *rogue* wave. In so doing, the



(a) STFT spectrogram with a window width of 51.2s



(b) Wavelet power spectrum

Fig. 3. Time histories of the water surface elevation and power spectrums for linear, second-order, fully nonlinear models as well as experimental measurements.

conclusion would be that there is a very significant increase in the spectral density of all frequency components in the vicinity of the *rogue* wave event.

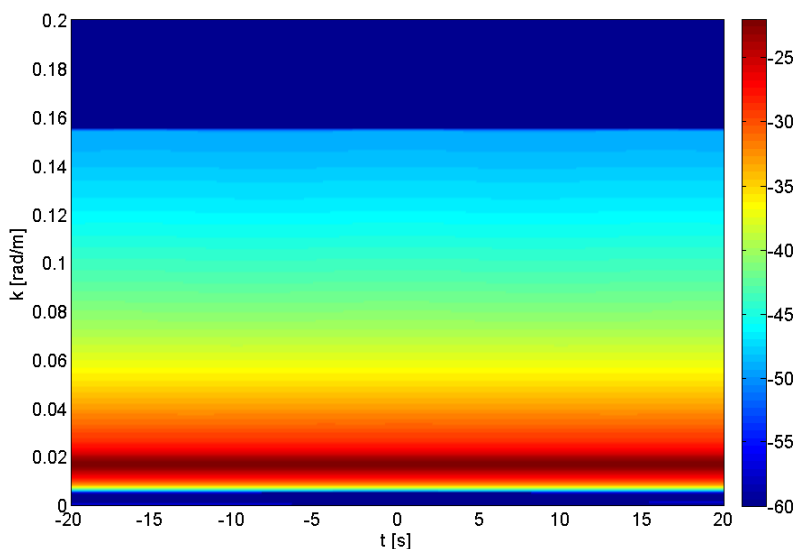


Fig. 4. Spectrogram produced by performing an FFT on the spatial water surface elevation at different times using Linear Random Wave Theory.

However, interpreting these STFT and Wavelet power spectrums at face-value can be misleading, as will be explained below.

Consider the power spectra obtained from the LRWT simulation. It is evident from Fig. 3 that the STFT and Wavelet analysis predict a power spectrum that evolves with time. However, linear theory assumes that all frequency components are present for all time and at all spatial locations. Furthermore, given that there are no second- or higher-order terms for LRWT, there is no modification of the underlying spectrum. Consequently, in theory, the spectrum obtained from a LRWT simulation is constant throughout time. Indeed, looking at a spatial water surface profile produced by LRWT and calculating the wave number spectrum at different times, the spectrogram in Fig. 4 is obtained. This illustrates a non-evolving power spectrum, as is expected theoretically from LRWT. Consequently, the STFT and Wavelet Transform applied to produce Fig. 3 are providing physically incorrect results.

To give an example of this phenomenon, consider a linear standing wave as produced by two regular waves propagating in opposite directions with frequency f_s and amplitude a_s . If you were to record a time history of the water surface elevation at an anti-node of the standing wave, this would measure a sinusoidal signal and an FFT would produce a spectrum with a spike at $f = f_s$ with an amplitude of $a = 2a_s$. If you were to now record the time history of the water surface elevation at a node of the standing wave, you would obtain a flat signal at zero and there would be no resulting spectrum. The spectrum produced

at the node of the standing wave is physically incorrect, as it is known that there are two regular waves present travelling in opposite directions. However, it is the phasing of the two waves that governs the location of the nodes and anti-nodes, but this cannot be ascertained without information from the spatial domain. Therefore, whilst the spectral technique applied is giving the correct mathematical interpretation, it is producing an incorrect physical explanation.

It can be argued that in the case of the standing wave, temporal and spatial information is available and that provides enough information to determine the wave's behaviour. However, whilst analytically and numerically a well resolved temporal and spatial description of the water surface elevation is readily available, it is extremely laborious to obtain in the laboratory and very rare to find it from field measurements. Therefore, the analysis chosen to examine wave data must be suitable for a time history of the water surface elevation at a single location, as is typically available from field measurements. Consequently, as demonstrated in the standing wave example, care must be taken when applying and examining the results of spectral analysis.

Despite this shortcoming of the STFT and Wavelet Transform, it is still possible to gain insight into the physical processes present within a *rogue* wave by employing these spectral techniques. This is done by comparing the power spectrums of the *rogue* wave with those obtained from simulations with known spectral evolution. One example of this is by employing LRWT, which, as described above, undergoes no spectral evolution. Another example is the second-order theory of Sharma & Dean (1981)[16]. In this case, whilst the water surface elevation has a low steepness, the second-order correction terms are negligible, and therefore, the power spectrum will be almost identical to that obtained from LRWT. However, as the steepness increases (such as in the vicinity of an extreme event), the second-order correction terms become more significant and the spectrum evolves to include the sum and difference bound components. Therefore, by comparing the power spectrums obtained from the experimental measurements to those calculated by linear and second-order irregular wave theories, it is possible to ascertain the physical processes occurring within the *rogue* wave.

This is precisely what is illustrated in Fig. 3. Focusing, for clarity, on the Wavelet power spectrum shown in Fig. 3(b), comparing the LRWT and second-order spectra highlights the contribution of the second-order correction terms. Far from the extreme event, $t = \pm 75\text{s}$, the two spectra are very similar, whilst in the vicinity of $t = 0\text{s}$, the increase in spectral density at the frequencies corresponding to the second-order sum terms is clearly evident. Comparing the fully nonlinear spectra with that from second-order, it is possible to ascertain the contribution of higher-order terms. In the vicinity of the largest crest elevation, this indicates an increase in the spectral density for the higher frequencies. This can be attributed to third-order resonant wave interactions as described by Gibson & Swan (2007)[9]. Finally, comparing the power spectra calculated from the experimental measurements of the *rogue* wave event and the fully nonlinear simulation, it is evident that in the vicinity of the largest event, the trends are very similar. This is surprising given the fact that the simulations do not include a

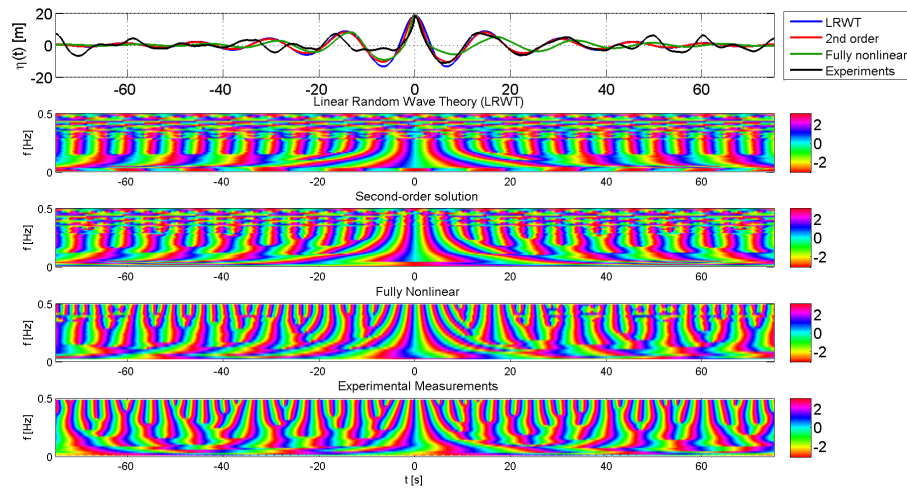


Fig. 5. Time histories of the water surface elevation and Wavelet phase for linear, second-order, fully nonlinear models as well as experimental measurements.

current and do not attempt to model the randomness of the sea state. However, this indicates that an amplification of the higher-frequency amplitude also occurs during the formation of a *rogue* wave event, and that this can be attributed, at least in part, to the third-order resonant wave interactions identified by Gibson & Swan (2007)[9].

The Wavelet Transform can also calculate the temporal evolution of the phase of each frequency component. This is illustrated by Fig. 5 for the linear, second-order and nonlinear models as well as the experimental measurements. This figure demonstrates that for all sources a large proportion of the frequency components come into zero phase with each other. This is to be expected for the linear and second-order simulations, given that a focused wave group was modelled, which by definition has zero phase for all components at $t = 0s$ ¹. However, for the fully nonlinear predictions and the experimental measurements, this was not expected given that the water surface profile is not perfectly focused. An aspect to particular note is the zero phase at $t = 0s$ for the higher frequencies, which have also seen a sudden amplification of their amplitude. This further supports the theory of a *rogue* wave appearing from the focusing of wave energy.

¹ In LRWT, for $f < 0.05Hz$ and $f > 0.3Hz$ the spectrum is not defined, which explains why the phase is non-coherent in these regions. A similar effect occurs for the second-order simulations.

7 Concluding Remarks

This paper has analysed the experimental measurements of Buchner *et al.* (2007)[4], who recorded a *rogue* wave in the Offshore Basin at MARIN. This analysis consisted of comparisons to focused wave groups generated by linear and second-order irregular wave theories and the fully nonlinear numerical model of Bateman *et al.* (2001)[3]. The Short-Time Fourier Transform and the Wavelet Transform were employed to examine the evolution of the wave spectrum in the vicinity of the *rogue* wave. It was demonstrated that both of these techniques predict an evolution of the linear wave spectrum, whilst this is known to be constant throughout time. It is, therefore, advisable to treat the output of these time-frequency spectral techniques with care. However, by comparing the spectral evolution beneath the *rogue* wave with that produced using linear, second-order and fully nonlinear models, it is possible to ascertain the contributions from different orders and the relative shifts of energy in the vicinity of the largest event. In so doing, it has been demonstrated that there is an amplification of the high-frequency amplitudes as the nonlinearity increases. Furthermore, the majority of the frequency components are shown to come into phase at the maximum event, which results in the focusing of wave energy, and supports one of the theories for the occurrence of *rogue* waves.

Acknowledgements

The authors gratefully acknowledge the support of Shell International Exploration and Production and MARIN.

References

1. **Airy, G. B.** "Wave and tides." *Encyclopedia Metropolitana*, 1845.
2. **Baldock, T. E., Swan, C., and Taylor, P. H.** "A laboratory study of nonlinear surface waves on water." *Philosophical Transactions of the Royal Society of London A*, Vol. 354 (1996), pp. 649–676.
3. **Bateman, W. J. D., Swan, C., and Taylor, P. H.** "On the efficient numerical simulation of directionally-spread surface water waves." *Journal of Computational Physics*, Vol. 174 (2001), pp. 277–305.
4. **Buchner, B., van Dijk, R. and Voogt, A.** "The spatial analysis of an extreme wave in a model basin." In *26th International Conference on Offshore Mechanics and Arctic Engineering (OMAE)*, 2007.
5. **Cherneva, Z. and Guedes Soares, C.** "Spectrogram analysis of the time frequency characteristics of ocean wind waves." *Ocean Engineering*, Vol. 32, No. 14–15 (2005), pp. 1643–1663.
6. **Craig, W. and Sulem, C.** "Numerical simulation of gravity waves." *Journal of Computational Physics*, Vol. 108 (1993), pp. 73–83.
7. **Elsayed, M. A. K.** "A novel technique in analyzing non-linear wave-wave interaction." *Ocean Engineering*, Vol. 33 (2005), pp. 168–180.

8. **Ewans, K. and Buchner, B.** “Wavelet analysis of an extreme wave in a model basin.” In *27th International Conference on Offshore Mechanics and Arctic Engineering (OMAE)*, 2008.
9. **Gibson, R. and Swan, C.** “The evolution of large ocean waves: the role of local and rapid spectral changes.” *Philosophical Transactions of the Royal Society of London A.*, Vol. 463 (2007), pp. 21–48.
10. **Haver, S. and Andersen, O. J.** “Freak waves – rare realizations of a typical population or typical realizations of a rare population?” In *Proceedings of ISOPE 2000, Seattle, USA*, 2000.
11. **Huang, N., Shen, Z., Long, S., Wu, M., Shih, H., Zheng, Q., Yen, N., Tung, C. and Liu, H.** “The empirical mode decomposition and the Hilbert spectrum for non-linear and non-stationary time series analysis.” *Proceedings of the Royal Society London A*, Vol. 454 (1998), pp. 903–995.
12. **Johannessen, T. B. and Swan, C.** “A laboratory study of the focusing of transient and directionally spread surface water waves.” *Proceedings of the Royal Society London A*, Vol. 457 (2001), pp. 1–36.
13. **Johannessen, T.B., Haver, S., Bunnik, T. H. J. and Buchner, B.** “Extreme wave effects on deepwater TLPs: Lessons learned from the Snorre TLP model tests.” In *Deep Offshore Technology (DOT) conference, Houston, November, 2006*.
14. **Krogstad, H. E., Magnusson, A. K. and Donelan, M. A.** “Wavelet and local directional analysis of ocean waves.” *International Journal of Offshore and Polar Engineering*, Vol. 10, No. 2 (2006), pp. 97–103.
15. **Liu, P. C.** “Is the wind-wave frequency spectrum outdated.” *Ocean Engineering*, Vol. 27 (2000), pp. 577–588.
16. **Sharma, J. N. and Dean, R. G.** “Second-order directional seas and associated wave forces.” *Society of Petroleum Engineering Journal*, Vol. 4 (1981), pp. 129–140.
17. **Shen, Z., Wang, W. and Mei, L.** “Finestructure of wind waves analyzed with wavelet transform.” *Journal of Physical Oceanography*, Vol. 24 (1994), pp. 1085–1094.
18. **Tromans, P. S., Anaturk, A. and Hagemeyer, P.** “A new model for the kinematics of large ocean waves—application as a design wave.” In *Proceedings of 1st Offshore and Polar Engineering Conference (ISOPE), Edinburgh*, Vol. 3 (1991), pp. 64–71.
19. **Veltcheva, A. D and Guedes Soares, C.** “Analysis of abnormal wave records by the Hilbert Huang Transform method.” *Journal of Atmospheric and Oceanic Technology*, Vol. 24 (2007), pp. 1678–1689.

Experimental and Numerical Study of Evolution of Statistical Properties of Unidirectional Narrow-Banded Steep Wave Groups

Lev Shemer¹, Anna Sergeeva², Alexey Slunyaev²

¹School of Mechanical Engineering, Tel-Aviv University, Tel-Aviv, Israel
Shemer@eng.tau.ac.il

²Institute of Applied Physics, RAS, Nizhny Novgorod, Russia
A.Sergeeva@hydro.appl.sci-nnov.ru, Slunyaev@hydro.appl.sci-nnov.ru

Abstract. Unidirectional random waves generated by a wavemaker in a 300-m-long wave tank are investigated experimentally. Spatial evolution of numerous statistical wave field parameters is studied. It is found that the frequency spectrum of the wave field undergoes significant variation in the course of its evolution along the tank; the values of all statistical wave parameters are strongly related to the local spectral width. The deviations of various statistical parameters from the Gaussian statistics increase with the width of the spectrum, so that the probability of extremely large (the so-called freak) waves is highest when the local spectral width attains maximum. It is found that the third-order random wave field model of Tayfun and Fedele [1] provides an appropriate description of the observed phenomena. The laboratory runs are reproduced through numerical simulations of the spatial form of the Dysthe equation. The simulation reproduce the wave shapes observed in laboratory, though for very steep waves some deviations in the computed wave shapes and the envelopes from those measured in the tank were observed at larger distances.

Keywords: unidirectional wave groups, laboratory experiment, water wave statistics, third-order statistical model; numerical simulations

1 Introduction

The kinetic wave theory serves as a basis for modern wave climate prediction. Kinetic theory of random ocean wave field is based on two fundamental assumptions: weak nonlinearity of waves and randomness of their phases [2, 3]. Theoretical investigations aimed at describing the statistical properties of nonlinear wave fields were originated in 1952 by Longuet Higgins [4], since then considerable progress was achieved by taking into account nonlinear effects (for recent results see [1, 5, 6,] and additional references therein). Beyond being of general scientific interest, the random wave field statistics determines the probability of high (freak) waves; the relation of

the spectral wave field characteristics to appearance of freak waves is thus of prior practical importance.

Numerous attempts have been made to explore the possibility to use deterministic nonlinear wave theories for forecast of evolution of a random wave field, and in this way for proving applicability (or restrictions) of the kinetic theory approach. These works reveal the crucial role of non-resonant interactions in the evolution of nonlinear random water waves. This understanding makes the experiments in a wave tank, where non-trivial exact resonances do not exist since only near-resonant-interactions between unidirectional waves are possible, a very convenient vehicle to study nonlinear random waves in laboratory conditions. Some experiments in a long wave tank have recently been performed on deep narrow-banded waves with random phases ([7] and references therein). These studies indicate that in spite of lack of exact resonances in a unidirectional wave field, nonlinear effects are essential and strongly affect the statistical properties of the wave field. Similar conclusions were reached in numerical simulations of deep and shallow water waves (see [8-10], among others).

In the present study we present results of an experimental investigation of random wave field evolution in a large wave tank, and compare them with the results obtained in an equivalent “numerical tank”. The use of numerical models instead of laboratory facilities enables studying random wave fields for a wide range of parameters, including over distances exceeding the lengths of available experimental installations and is thus obviously attractive. However, the ability of theoretical models to capture correctly wave dynamics requires experimental verification.

In Section 2 we briefly describe the experimental procedure and the way of generating initial conditions. The results of laboratory measurements are reported in Section 3. More details on the experiments and the data processing are given in [11]. In Section 4 the results of the numerical simulations are presented and compared with the experiments.

2 Experimental Facility and Procedure

The experiments were carried out in the Large Wave Channel (GWK) in Hanover that is about 300 m long, 5.0 m wide and 7.0 m deep. Water depth in the present experiments was set to be $h = 5$ m. A sand beach at the far end of the facility starts at the tank bottom at the distance $x = 270$ m and has a slope of 30° . The computer-controlled piston-type wavemaker is equipped with the reflected wave energy absorption system.

In the present experiments, the spatial evolution of numerous realizations of a wave field that all have identical initial frequency power spectra for the free wave components, but random frequency components' phases in each realization, is studied. To generate the wavemaker driving signal for each realization, we start with a deterministic Gaussian-shaped unidirectional wave group, with the surface elevation variation in time, $\eta(t)$, given by

$$\eta(t) = \eta_0 \exp\left(-\left(\frac{t}{mT_0}\right)^2\right) \cos \omega_0 t, \quad (1)$$

where $\omega_0 = 2\pi f_0 = 2\pi / T_0$ ($T_0 = 1.5$ s) is the carrier wave circular frequency, η_0 is the maximum wave amplitude in the group, and the parameter $m = 3.5$ defines the width of the group.

The spectrum of (1) also has a Gaussian shape with the relative width at the energy level of half of the maximum as

$$\frac{\Delta\omega}{\omega_0} = \frac{1}{m\pi} \sqrt{\frac{\ln 2}{2}} \approx 0.054. \quad (2)$$

To define an irregular wave pattern, the frequency spectrum of (1) was computed with the resolution of about 0.02 Hz. Then, for 60 most energetic harmonics random phases were assumed, while the amplitudes of other harmonics were set to be zero (for details see [11]). The resulting spectrum then defines a wave group of duration 51.2 s. This signal was repeated three times, yielding three nearly identical wave groups with the total extent of 153.6 s. To eliminate finite wavemaker displacement at the beginning and the end of the wave excitation period, and thus piston acceleration and velocity beyond the mechanically acceptable limits, windowing was used. As a result, two almost identical wave groups of duration 51.2 s were contained within these wave trains, and were used for the processing.

The chosen carrier wave period $T_0 = 1.5$ s in the linear approximation corresponds to the wave length $\Lambda_0 = 3.51$ m, therefore the dimensionless water depth $k_0 h = 8.95$, thus satisfying deep-water conditions for all wavenumbers with significant energy. The instantaneous water height is measured using 25 resistance type wave gauges at fetches ranging from 3.5 m to 214 m.

The maximum possible wave steepness within the group (1), $\varepsilon = \eta_0 k_0$, is adopted as the measure of nonlinearity of the wave field. Three experimental series were performed denoted as A (10 runs for $\varepsilon = 0.2$), B (46 runs for $\varepsilon = 0.25$) and C (13 runs for $\varepsilon = 0.3$). Visual observation of the wave field during initial runs performed with $\varepsilon = 0.3$ showed occasional wave breaking within the tank, phenomenon not accounted for in the deterministic model for wave field evolution used in Section 4. Thus, most experiments were carried out for conditions of series B.

3 Results of Experimental Data Processing

The spectral shape of the free wave component at the wavemaker was prescribed to be Gaussian. Due to the narrow-banded character of the spectrum $S(\omega)$, the 2nd and 3rd order bound waves may be easily identified in the initial frequency spectrum. In the initial stages of evolution, spectral widening around the carrier wave frequency $f_0 = 0.67$ Hz is observed up to the distance of about 100 m, or 30 carrier wave length Λ_0 as shown in Fig. 1. The characteristic frequency ω_m , the free wave spectral width, ν , and the spectral momenta m_j are defined as

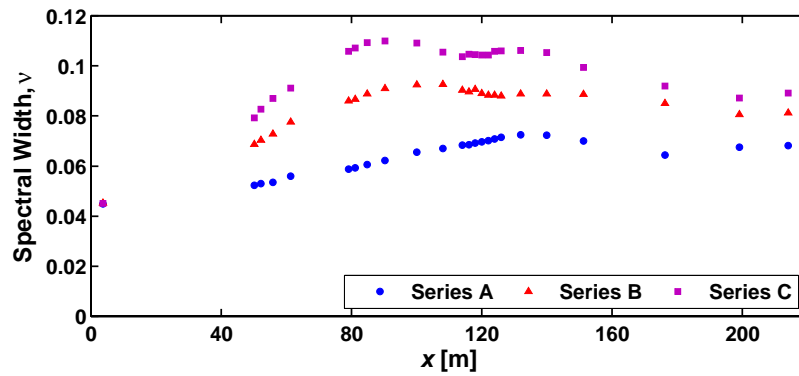


Fig. 1. Variation of the free waves spectral width along the tank.

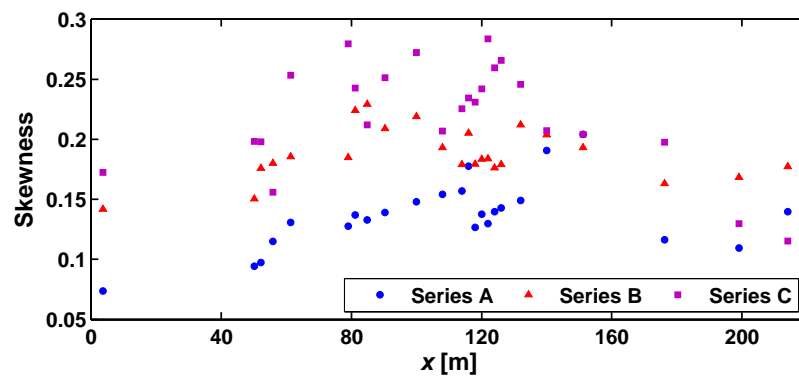


Fig. 2. Variation of the skewness along the laboratory tank.

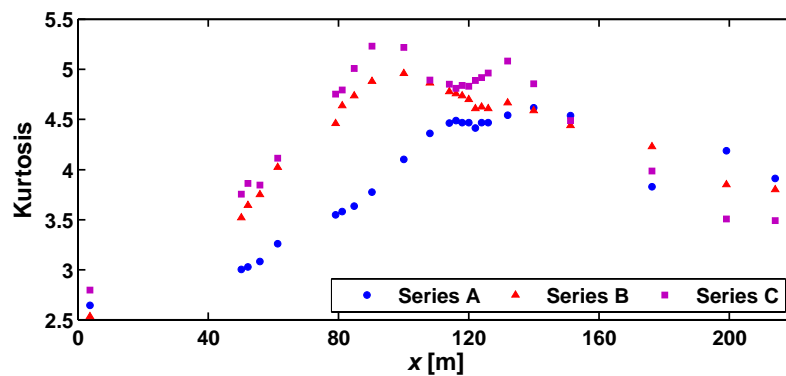


Fig. 3. Variation of the kurtosis along the laboratory tank.

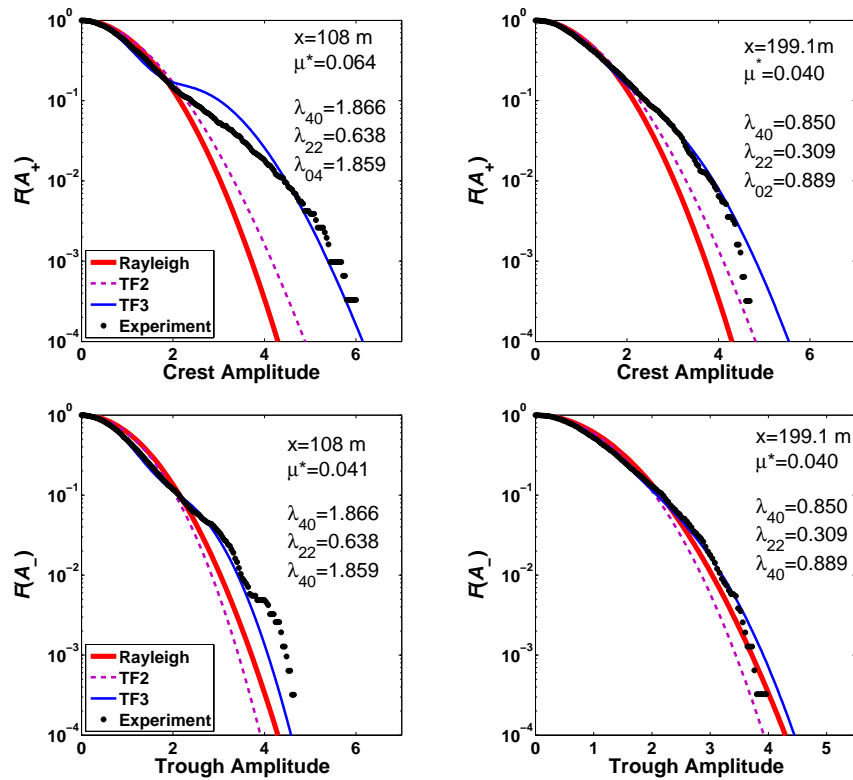


Fig. 4. Comparison of the experimentally measured wave crest and trough amplitude distributions with the Rayleigh and the 2nd (TF2) and the 3rd (TF3) order Tayfun and Fedele distributions [1], series B.

$$\omega_m = \frac{m_1}{m_2}; \nu = \sqrt{\frac{m_0 m_2}{m_1^2} - 1}; m_j = \int_{\omega_{\min}}^{\omega_{\max}} \omega^j S(\omega) d\omega, \quad (3)$$

where ω_{\min} and ω_{\max} define the limits of the free wave frequency domain. At the subsequent stages of the spatial evolution the spectrum "shrinks" again but still does not attain its initial shape at the distance of about 200 m, see Fig. 1. The characteristic frequency ω_m remains nearly constant along the tank.

The standard deviation, σ , skewness, λ_3 and kurtosis, λ_4 , of the surface elevation are defined in a standard way by

$$\sigma^2 = \langle \eta^2 \rangle, \quad \lambda_3 = \frac{\langle \eta^3 \rangle}{\sigma^3}, \quad \lambda_4 = \frac{\langle \eta^4 \rangle}{\sigma^4}. \quad (4)$$

For a normally distributed random wave field $\lambda_3 = 0$ and $\lambda_4 = 3$. The variations of λ_3 and λ_4 along the tank are presented in Fig. 2 and Fig. 3. It follows from Fig. 2 that the

skewness λ_3 , which characterizes the vertical asymmetry of the wave field, is positive and it increases when the nonlinear parameter ε becomes bigger.

The crest and trough amplitudes, A_+ and A_- , are calculated as a maximum / minimum of surface elevation between two zeros of the surface elevation. Both parameters are scaled by $m_0^{1/2}$. Fig. 4 shows their probability distributions at two fetches: at the distance corresponding to the maximum of the spectral width, and at the far end of the measuring domain. The distributions for both A_+ and A_- exhibit initial widening and then become narrower farther away from the wavemaker. For wave trough amplitudes, the distributions do not differ notably from the Rayleigh shape, except for the location with the maximum local spectral width at $x \approx 100$ m. Contrary to that, the wave crest amplitude probabilities exceed significantly the Rayleigh distribution. The difference in the behavior of crest and trough amplitudes is clearly related to the positive skewness as shown in Fig. 2.

The accuracy of the 2nd order (marked as TF2) and the 3rd order (marked as TF3) estimates of distributions for the wave crest probabilities according [1] is examined in Fig. 4. The values of the statistical parameters used for computing TF2 and TF3 curves are given in the corresponding figures (see [1, 11] for details). The figure demonstrates that the 2nd order model distribution TF2 underestimates the deviations from the Rayleigh curve as compared to the experimentally measured dependencies. The higher order TF3 distribution offers a much better description of the experimental results for the quite different spectral widths at both locations.

Wave height probability distributions were compared with the theoretical estimates similar to Fig. 4 for all experimental series (see [11]). The TF3 distribution seems to be quite accurate at the early stage of wave evolution, and at long fetches; the agreement with the experimental data deteriorates somewhat at the distance $x \approx 100$ m. The deviation from the Rayleigh distribution becomes especially evident for larger wave amplitudes.

4 Corresponding Numerical Simulation

The main motivation for carrying out numerical simulations corresponding to laboratory measurements was to clarify whether the simulations can accurately describe the evolution of individual nonlinear wave groups and of their statistical parameters along large distances. To carry out quantitative comparison with experiments in a wave tank, spatial evolution models, such as the spatial forms of the Dysthe or Zakharov equations [12-15], have to be applied. In this paper the spatial Dysthe model is used in the form:

$$i \left(A_x + \frac{2k_0}{\omega_0} A_t \right) + \frac{k_0}{\omega_0^2} A_{tt} + k_0^3 |A|^2 A - 8i \frac{k_0^3}{\omega_0} |A|^2 A_t - 2i \frac{k_0^3}{\omega_0} A^2 A_t^* - \frac{4k_0^3}{\omega_0^2} A \varphi_t = 0, \quad (5)$$

$$\varphi_{zz} + 4 \frac{k_0^2}{\omega_0^2} \varphi_{tt} = 0, \quad -h \leq z \leq 0,$$

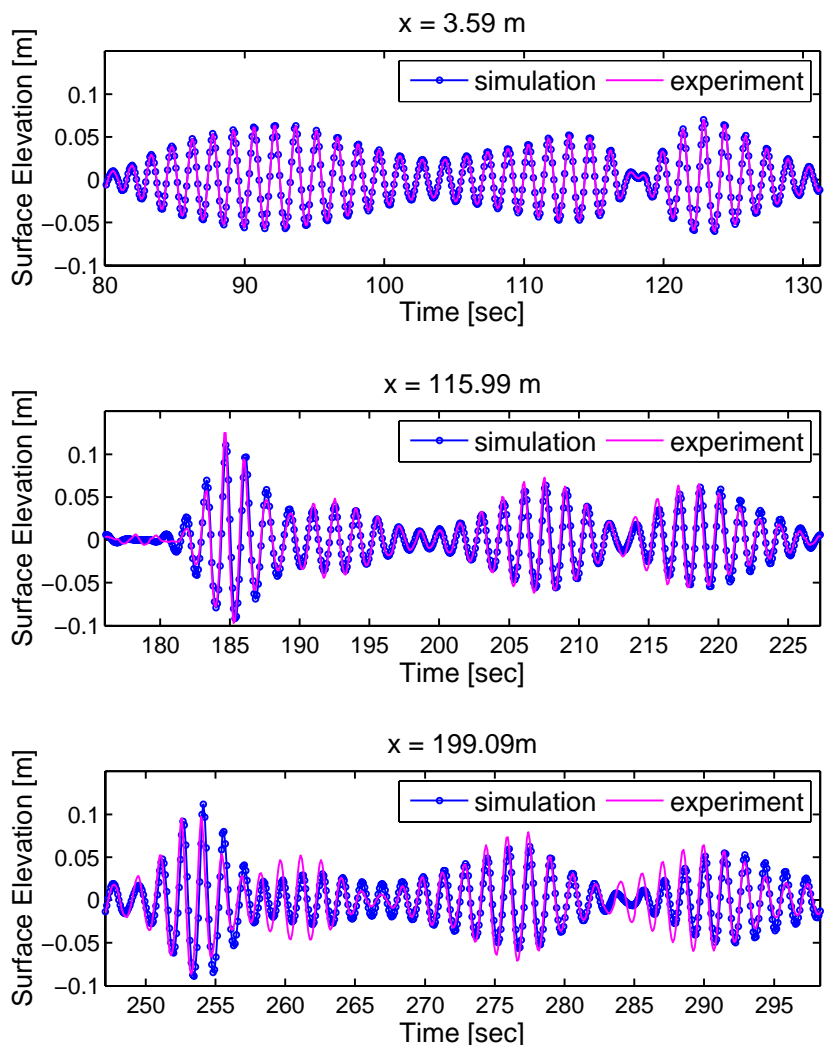


Fig. 5. Comparison of the measured and the simulated surface displacement variation in time for a single realization in series B at different locations.

$$\begin{aligned} \varphi_z &= -k \frac{\partial}{\partial t} |A|^2, & z = 0, \\ \varphi_z &= 0, & z = -h. \end{aligned} \tag{6}$$

Equations (6) define the boundary conditions at the surface, $z = 0$ and the water bed, $z = -h$. The surface displacement is computed taking into account the bound waves up to the 3rd order

$$\eta = -\frac{k_0}{\omega_0^2} \varphi_t + \operatorname{Re} \left[A \exp(i\omega_0 t - ik_0 x) + \left(\frac{k_0}{2} A^2 - \frac{ik_0}{\omega_0} A A_t \right) \exp(2i\omega_0 t - 2ik_0 x) + \frac{3k_0^2}{8} A^3 \exp(3i\omega_0 t - 3ik_0 x) \right]. \quad (7)$$

Some records of the experimental data exhibited well-distinguished long-wave oscillations, which may be due to seiches. To mitigate this effect, a long-wave filter was applied to remove the low frequencies from the experimental data, and in parallel, the first term on the right-hand-side of (7), which represents the induced long-wave component, was not used in computing η .

The series B of the laboratory runs was used for the comparison. The initial condition for the simulations is obtained through an iterative procedure, seeking for the complex envelope, $A(x, t)$, such that the reconstructed according to (7) temporal variation of the surface elevation is close to that measured in the laboratory tank at distance $x = 3.59$ m. Wave train duration of about 160 s was used for the comparison. The initial reconstructed wave field in each realization was indeed very close to the measured one (see Fig. 5, where records of a single individual realization with the duration 51.2 s are shown at various locations along the tank). Minor differences can be observed in the measured and the computed wave shapes, mainly at instants corresponding to the maximum surface displacement; two kinds of deviations can be specified: high-frequency oscillations (presumed to result from measurement noise) and the systematic underestimation of steep slopes for very high waves.

The 46 initial conditions were then simulated, retrieving computed $\eta(t)$ at distances corresponding to the probe locations in the tank. The numerical data was processed as described in Section 3, and the numerical and experimental results compared. The experimental and the simulated wave fields exhibit excellent agreement at short distances. At about $x \approx 100$ m large waves occur more often, and the difference in shapes for large surface displacements becomes more pronounced (Fig 5). Farther away from the wavemaker ($x > 100$ m) differences in wave envelopes become visible, as shown in Fig. 5, and they accrue, possibly as a result of accumulated error due lack of perfect agreement in the initial conditions.

Fig. 6 and Fig. 7 show the comparison for the main statistical parameters characterizing nonlinear effects, the skewness and the kurtosis. It is demonstrated that in general, the cumulant evolution is well described in simulations both for skewness and kurtosis. The wave asymmetry is slightly underestimated in the simulated initial conditions, resulting in some difference in the skewness values at $x=3.5$ m (see Fig. 6), whereas the initial values for the kurtosis in simulations and experiments coincide. According to Figs. 6 and 7, the numerical model underestimates the values of λ_3 and λ_4 up to the fetch of 130 m; the difference is especially pronounced around $x = 100$ m, possibly due to formation of high waves at this stage and the corresponding spectrum widening spectrum as discussed in Section 3. At longer distances ($x > 130$ m) the simulations slightly overestimate the cumulants.

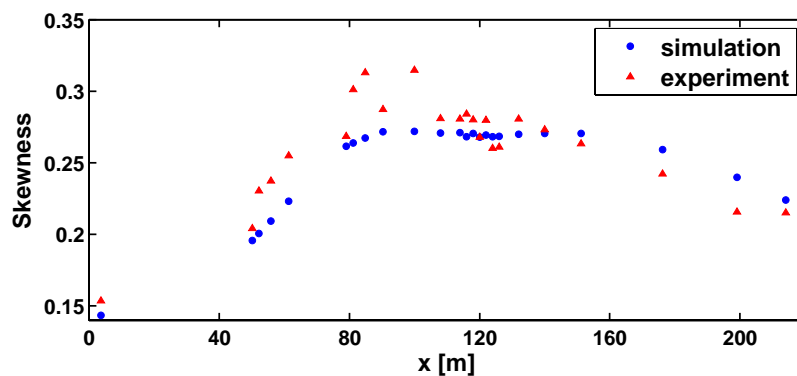


Fig. 6. Variation of the skewness along the tank, series B.

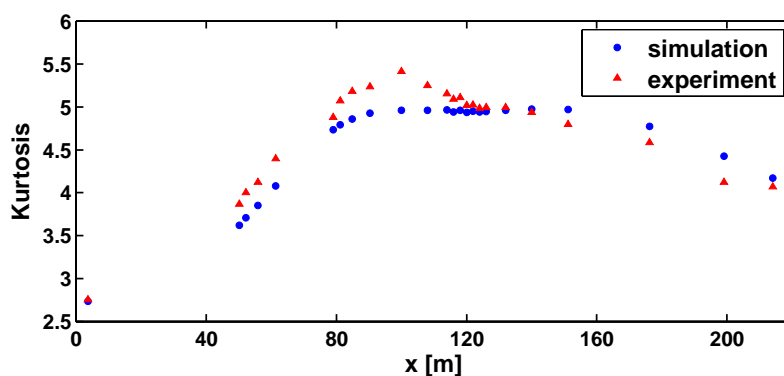


Fig. 7. Variation of the kurtosis along the tank, series B.

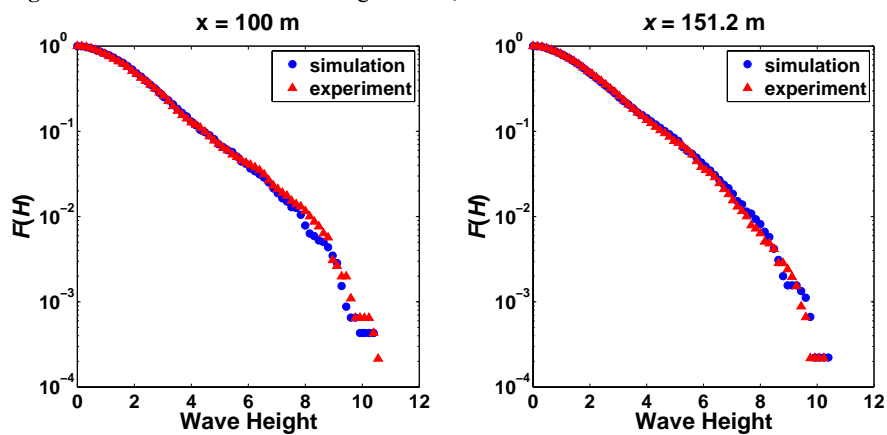


Fig. 8. Wave height distributions for the measured and simulated wave fields, series B.

Those minor differences notwithstanding, the wave height distributions derived from the experimental and the computed data manifest good agreement along the whole tank, see Fig. 8. This agreement applies both to the small-amplitude and the large-amplitude parts of the distributions, although occasional discrepancies may be observed for the largest waves, probably due to insufficient size of the ensemble.

5 Conclusions

Variation along the tank of various wave field parameters of random wave groups with a prescribed initial spectral shape is studied in laboratory measurements and by numerical simulations based on the spatial version of the Dysthe model. In general, very good agreement is obtained between the measurements and the computations. This statement is related to evolution of individual realizations along the tank, as well as to the spatial variation of important statistical parameters of the random wave field.

While the total energy of the wave field is approximately conserved, and the occasional breaking does not seem to cause significant dissipation, the spectral width undergoes essential variation in the evolution process. The initially narrow spectra become wider and attain maximum width at a certain distance from the wavemaker. The larger is the nonlinearity of the wave field, the more significant is the change in the spectral width and the shorter is the distance at which the widest spectrum is attained.

Statistical wave field parameters also exhibit spatial variation that is strongly related to the local spectral width. The kurtosis attains maximum, and the tails of probability distribution functions of the wave heights, wave crests and wave troughs attain maximum deviation from the Rayleigh distribution when the spectral width is maximum. For locally wider spectra, considerable deviations from the Rayleigh shape are observed not only for the distribution tails, but also for low values of crest and trough amplitudes, as well as for low wave heights. It appears that the 3rd order model distributions presented by Tayfun and Fedele [1] capture these phenomena adequately for the whole length of the tank and for all values of the nonlinear parameter ε , while the performance of the 2nd order statistical model is less satisfactory.

Numerical simulations of the random unidirectional wave field within the framework of the spatial Dysthe equation yield statistical parameters that at all locations are quite similar to those obtained in the experiments, exhibiting only minor dissimilarities; the difference in individual wave and envelope shapes is somewhat more noticeable. The latter becomes more pronounced after the more frequent occurrence of extremely large waves at the distance of about $x \approx 100$ m. The appearance of large waves that may result in breaking, as well as the spectrum widening at those locations may lead to inaccuracies in the wave dynamics description by the Dysthe model [12]. Alternatively, the decrease in the agreement between the experimental and the computed results with the distance from the wavemaker may be attributed to accumulation of error due to minor inaccuracies in the initial conditions.

Acknowledgments. We gratefully acknowledge the European Community support under the Access to Research Infrastructures Action of the Human Potential Programme (contract HPRI-CT-2001-00157) that made possible experiments in the Large Wave Channel (GWK) of the Coastal Research Center (FZK) in Hanover. The research is supported by grant # 3-3573 from the Israel-Russia Cooperation Program, by grant # 964/05 from the Israeli Science Foundation (ISF). The research of the Russian coauthors is supported by RFBR grants # 06-05-72011 and 08-02-00039, State Programme 2008-MO-04-06 and project Extreme Seas.

References

1. Tayfun M.A., Fedele F.: Wave height distributions and nonlinear effects. *Ocean Eng.* 34, 1631-1649 (2007).
2. Hasselmann K.: On the nonlinear energy transfer in a gravity wave spectrum. Part 1. General theory. *J. Fluid Mech.* 12, 481-500 (1962).
3. Zakharov V.: Statistical theory of gravity and capillary waves on the surface of a finite-depth fluid. *Eur. J. Mech. B/Fluids* 18, 327-344 (1999).
4. Longuet-Higgins M.: On the statistical distribution of the heights of sea waves. *J. Mar. Res.* 11, 245-266 (1952).
5. Naess A.: On the distribution of crest-to-trough wave heights. *Ocean Eng.* 12, 221-234 (1985).
6. Tayfun M.A.: Statistics of nonlinear wave crests and groups. *Ocean Eng.* 33, 1589-1622 (2006).
7. Mori N., Onorato M., Janssen P.A.E.M., Osborne A.R., Serio M.: On the extreme statistics of long-crested deep water waves: theory and experiments. *J. Geophys. Res.* 112, C09011 (2007) doi:10.1029/2006JC004024.
8. Onorato M., Osborne A., Serio M., Bertone S.: Freak wave in random oceanic sea states. *Phys. Rev. Lett.* 86, 5831-5834 (2001).
9. Janssen P.A.E.M.: Nonlinear four-wave interactions and freak waves. *J. Phys. Oceanography* 33, 863-884 (2003).
10. Pelinovsky E., Sergeeva A.: Numerical modeling of the KdV random wave field. *Europ. J. Mech. B/Fluids* 25, 425-434 (2006).
11. Shemer L., Sergeeva A.: An experimental study of spatial evolution of statistical parameters of unidirectional narrow-banded random wave field. *J. Geophys. Res.* 114, C01015 (2009), doi:10.1029/2008JC005077.
12. Shemer L., Kit E., Jiao Haiying: An experimental and numerical study of the spatial evolution of unidirectional nonlinear water-wave groups. *Phys. Fluids A* 14(10), 3380-3390 (2002).
14. Shemer L., Jiao Haiying, Kit E., Agnon Y.: Evolution of a nonlinear wave field along a tank: Experiments and numerical simulations based on the spatial Zakharov equation. *J. Fluid Mech.* 427, 107-129 (2001).
15. Slunyaev A., Pelinovsky E., Guedes Soares C.: Modeling freak waves from the North Sea. *Appl. Ocean Res.* 27, 12-22 (2005).
16. Shemer L., Goulitski K., Kit E.: Evolution of wide-spectrum wave groups in a tank: an experimental and numerical study. *Europ. J. Mech. B/Fluids* 26, 193-219 (2007).

Direct Measurements of Temporal Wave Field Evolution in a Laboratory Tank and Comparison with Strongly Nonlinear Simulations

Lev Shemer¹, Alexey Slunyaev², Boris Dorfman¹

¹School of Mechanical Engineering, Tel-Aviv University, Tel-Aviv, Israel
Shemer@eng.tau.ac.il

²Institute of Applied Physics, RAS, Nizhny Novgorod, Russia
Slunyaev@hydro.appl.sci-nnov.ru

Abstract. The evolution along a tank of unidirectional nonlinear wave groups with narrow spectrum previously studied in [1] is compared with numerical simulations based on weakly, strongly and fully nonlinear models. Measurements of the instantaneous surface elevation within the laboratory tank were carried out using digital processing of video-recorded sequences of images of the contact line movement at the tank side wall. Records of the measured surface displacements variation were obtained along the entire tank at different instants. The accumulated set of experimental data enables to compare directly the experimental data with the results of numerical simulations based on conventional numerical models which describe wave field evolution in time.

Keywords: unidirectional wave groups, narrow-banded wave groups, laboratory experiment, wave measurement, video image processing, strongly nonlinear numerical simulation

1 Introduction

Theoretical studies of nonlinear water waves are often performed by solving temporal evolution models. Contrary to that, in the laboratory as well as in the field experiments surface elevation variation with time is usually recorded at fixed locations. Attempts are sometimes made to translate the measured by point sensors frequency spectrum into the corresponding wave number (or wave vector in the two-dimensional case) spectrum. However, direct quantitative comparison of the frequency and the wave number spectra can not be carried out in a consistent way; due to nonlinearity the wave field contains not only free but also bound (locked) components; nonlinearity also affects the dispersion relation among the wave number and the frequency.

Spatial forms of numerical models are thus natural when used to reproduce laboratory experiments and to carry out quantitative comparison with the

measurements. The spatial version of the modified nonlinear Schrodinger (or Dysthe) equation, as well as the spatial version of the Zakharov equation were suggested and successfully applied for the description of laboratory experiments [2-4]. Nevertheless, it should be stressed that (mainly for historical reasons) the variety of available “temporal” numerical models is more extensive.

In this paper instantaneous “snapshots” of the whole wave field in a laboratory tank are used for direct comparison of the laboratory measurements and the results of simulation employing different numerical models (ranging from weakly to fully nonlinear); all models describe the temporal evolution of the wave field. Recently, the laboratory results reported in the present paper were compared with the solutions of both temporal and spatial versions of the Dysthe equation [1], emphasizing the differences in the temporal and spatial approaches. In particular, it was found that for the Dysthe equation both approaches are capable of describing the nonlinear effects observed during the evolution of a narrow-banded wave field; the temporal and spatial forms of the Zakharov equation [3, 5], which is free of the narrow-band assumption, may be used for a more accurate estimate of wave dynamics. It was also stressed in [1] that due to the difference between the phase and the group wave velocities, the separation between the free and the bound modes is much more pronounced when the spatial wave evolution (and, respectively, the frequency spectrum) is considered. This is an additional consideration that makes the spatial formulation of the wave field evolution problem more convenient for practical purposes.

Section 2 describes the experimental facility and the method of retrieving and processing sequences of the recorded video images, that yields wave shapes along the whole tank at different instances. In Section 3 the initial conditions are presented that are used for laboratory wave generation, as well as for the initiation of the numerical simulations. Section 4 reports on the results of the numerical simulations within the frameworks of the temporal form of the Dysthe equation with full linear dispersion taken into account [6], the High-Order Spectral Method [7], and the fully nonlinear method for solving the Euler equations in terms of conformal mapping following [8].

2 Measurements and Experimental Data Processing

The experiments were performed in the wave tank that is 18 m long, 1.2 m wide and has transparent side walls and windows at the bottom which allow viewing of the flow from various directions. The tank is filled to mean water depth of $h = 0.6$ m. Waves are generated by a computer-controlled wavemaker system. The instantaneous contact line shapes were recorded by a CCD video camera at a rate of 30 fps. The size of each frame is 640 by 480 pixels. The field of view of the camera located one meter from the tank wall spans 50 cm along the tank (see Fig. 1), so that the pixel dimension is about 0.8 mm. The camera is placed on a carriage to enable imaging of different regions of the tank. Advantage is taken of the high repeatability of the wave field excited by the computer-generated driving signal. In each consecutive recording session, the carriage is shifted along the tank, so that slightly overlapping images of the contact line movement along the whole experimental facility are obtained. At each

camera location every frame of the recorded video clip was processed separately. The instantaneous surface elevation at any fixed location can also be measured by resistance type wave gauges made of 0.3 mm platinum wire.

An example of a recorded image is presented in Fig. 1. While the contact line can be clearly identified visually, the image contains numerous additional features such as the tank supporting beam, objects in the laboratory beyond the tank, reflections, etc. An effective algorithm was developed to extract quantitative information from the recorded video clips that contain thousands of images like that in Fig. 1. The initial window is built in the first image of the series around a point that constitutes the center of the searching area and is chosen at or in a close vicinity to the desired curve. The vertical coordinate of the interfacial curve for every horizontal location is defined as the weighted average of the pixel intensities along the vertical extent of the window. Once all vertical coordinates within the window are calculated, the contact line shape within the window is approximated by a second order polynomial using the least mean square fit on the array of the detected points. The window is then shifted forward by one pixel in the direction given by the slope of the contact line, and the process is repeated. This process continues until the whole image is covered. More detailed description of the method is given in [1, 9].



Fig. 1. An example of the contact line image.

The present experimental approach was validated extensively using conventional resistance wire gauges at a number of locations along the tank and comparing with the data simultaneously acquired at the same distance by image processing technique. The difference between the instantaneous values of the surface elevation measured by the wave gauge located close to the tank's wall and by video image processing at various distances from the wavemaker always remains well below 1 mm and does not exceed the deviation between the outputs of different probes, see [9].

3 Initial Conditions

Laboratory experiments were performed for a wave group with Gaussian envelope generated by the wavemaker. The temporal variation of the surface elevation at the wavemaker has to the leading order the following form:

$$A(t) = A_0 \exp\left(-\left(t/mT_0\right)^2\right) \cos \omega_0 t, \quad (1)$$

where $\omega_0 = 2\pi/T_0$ ($T_0 = 1.5$ s) is the carrier wave circular frequency, $A_0 = 22$ mm is the maximum wave amplitude in the group, and the parameter $m = 3.5$ defines the width of the group. These parameters were chosen to enable nonlinear effects to become apparent.

The wave group satisfies the narrow-banded condition, $\Delta\omega/\omega \approx 0.54$, see [1], and also the deep-water condition $k_0 h \approx 5$, where k_0 is the carrier wavenumber, related to ω_0 through the deep-water linear dispersion relation, $\omega_0^2 = gk_0$; g is the acceleration due to gravity.

To start temporal wave simulation, the boundary condition (1) has to be transformed into the waveform at the initial instant, say $t = 0$. In [1], this transformation was done invoking the linear solution. A simpler approach is used here. Neglecting dispersion effects at distances corresponding to the length of the train, equation (1) leads to the following initial condition:

$$A(x, t = 0) = A_0 \exp\left(-\left(\frac{x-x_0}{mT_0 c_{gr}}\right)^2\right) \cos k_0(x-x_0), \quad (2)$$

where $c_{gr} \approx 0.54$ m/s is the carrier wave group velocity. The equation (2) describes the instantaneous wave field at the leading order at the instant prior to the group entrance to the tank. Since the spatial extent of the initial group is 6.3 m, in (2) $x_0 = 3.15$ m.

To compute the actual surface elevation, bound wave correction for finite-depth water up to the 3rd order [10] were taken into account

$$\begin{aligned} \eta = & -\frac{1}{4h}|A|^2 - \frac{i}{32(kh)^2}(AA_x^* - A^*A_x) + \text{Re}[A \exp(i\omega_0 t - ik_0 x) + \\ & + \left(\frac{k_0}{2}A^2 + \frac{i}{2}AA_x\right) \exp(2i\omega_0 t - 2ik_0 x) + \frac{3k_0^2}{8}A^3 \exp(3i\omega_0 t - 3ik_0 x)], \end{aligned} \quad (3)$$

where $A(x, t)$ is the complex wave amplitude associated with the Dysthe equation. Transform (3) takes into account the first harmonic (the carrier wave), the bound waves at the 2nd and the 3rd harmonics, and the long-wave bound correction that is represented by the two first items in (3).

The velocity potential on the free surface, $\varphi(x, t)$, required for the strongly and fully nonlinear numerical codes, is given by:

$$\varphi = -\sqrt{g/k_0} \text{Im}[A \exp(i\omega_0 t - ik_0 x)] \exp(k_0 \eta). \quad (4)$$

4 Numerical Simulations

The temporal wave evolution was solved within three numerical models: i) the Dysthe equation valid for deep water with full linear dispersion taken into account [6]; ii) the finite-depth High-Order Spectral Method of Dommermuth and Yue [7] (hereafter referred to as DY) with the nonlinear parameter $M = 6$; and iii) by means of the conformal mapping approach, developed by Dyachenko and Zakharov [8] (DZ hereafter), which is a fully-nonlinear spectral method for solving the potential Euler equations; its infinitively deep water version was used. All these models are derived for potential equations of ideal hydrodynamics and describe the linear dispersion without limitations (although different assumptions regarding the water depth are applied). The Dysthe model describes the evolution of wave group envelope under the assumption of weak nonlinearity and narrow spectrum. The DY model with $M = 6$ is often considered as a fully-nonlinear, since it takes into account higher-order nonlinear interactions. No details of the codes can be given here and may be found in the appropriate references; all are implemented using traditional approaches.

In the Dysthe simulations, (2) was used as the initial condition. To start simulations in the DY and DZ codes, nonlinear bound corrections (3) were taken into account, and the velocity potential was defined according to (4).

Surface displacement wave profile at $t = 0$, as well as the experimental measurements and the results of numerical simulations for three instants, $t = 14$ s, $t = 16$ s and $t = 18$ s, are shown in Fig. 2. The maximum duration of the wave propagation is limited by the size of the tank. Free wave envelopes obtained by inverting numerically the transform (3) are shown correspondingly in Fig. 3. The free wave envelope at $t = 0$ is actually the Gaussian wave envelope defined by (2).

The modification of the wave group shape in the course of its propagation along the tank is evident; it is caused by both the dispersive and the nonlinear effects. The effect of nonlinearity is manifested in the change of spectral shape, as discussed in [1]. The general agreement between the computations according to all models applied here and the experiments is quite satisfactory, but not perfect. The observed discrepancy between the numerical simulations, especially between the strongly nonlinear (DY) and the fully nonlinear (DZ) solvers, suggests that the nonlinear effects are manifested quite strongly during the evolution. On the other hand, a relatively simple weakly nonlinear Dysthe equation proves to be an adequate tool to describe the experiment.

The following explanations may be suggested for the minor differences found between the experimentally measured and the simulated wave fields. The most likely source for the discrepancy is that the initial condition for the numerical experiments is not exact. The translation of the wavemaker movement in time at $x = 0$ that results in (1) to the initial spatial distribution (2) is only approximate and neglects both dispersion and nonlinearity effects during the group propagation over a distance corresponding to its length.

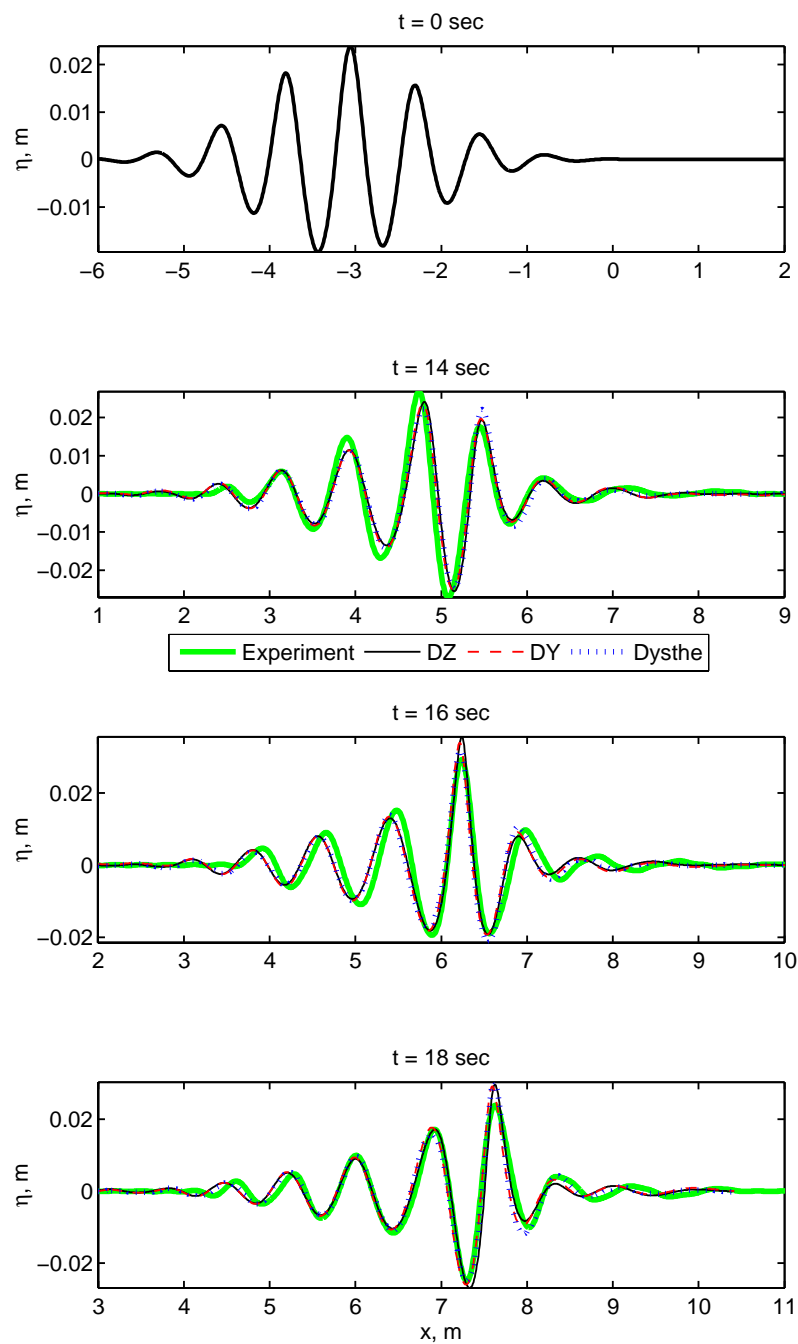


Fig. 2. Experimental (thick solid line) and simulated (thin solid line – DZ code, dashed line – DY code, dotted line – Dysthe code) surface displacement profiles at different instants.

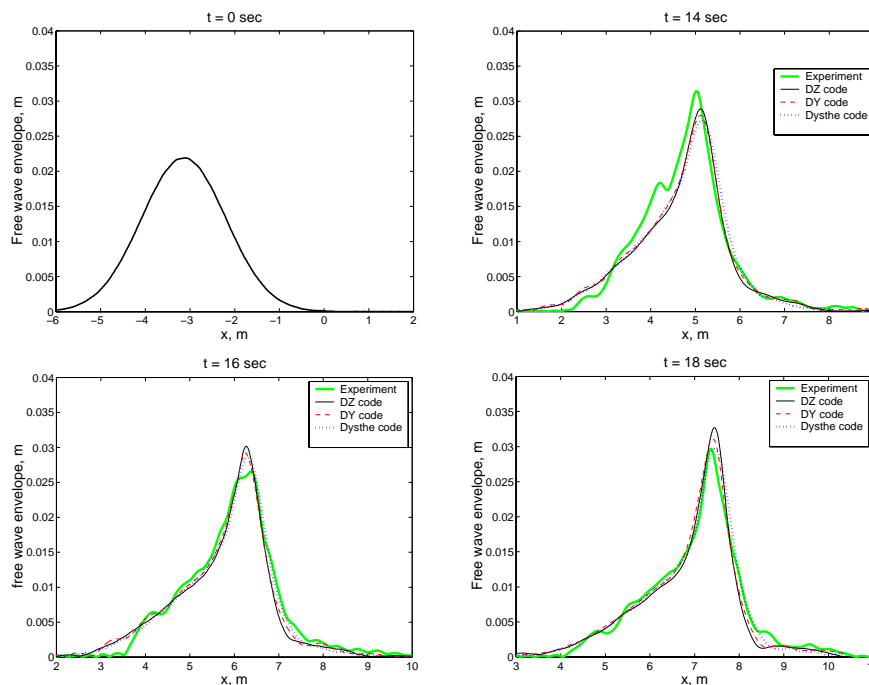


Fig. 3. Experimental and simulated free wave envelopes of surface displacement at different instants.

Comparison of those curves in Figs. 2 and 3 that correspond to the numerical simulations also suggests that the stronger is the nonlinearity of the model, the steeper individual waves it is capable to predict. Among the models employed in this study, the DZ model is the most (fully) nonlinear, the DY model with $M = 6$ describes up to 7-wave interactions, and the Dysthe equation takes into account only four-wave interactions.

Conclusion

The method of obtaining instantaneous distribution of surface wave displacement along the entire laboratory tank at various instances enables direct comparison of laboratory measurements with the results of numerical simulations performed within the framework of conventional models that describe temporal evolution of the nonlinear wave field. In this paper laboratory measurements of nonlinear wave dynamics of high-amplitude narrow-banded wave groups are quantitatively compared with the solutions of the weakly nonlinear Dysthe equation, the strongly nonlinear High-Order Spectral Method and the fully nonlinear Euler equations written in conformal variables. This approach provides a straightforward way to verify those

numerical models experimentally. In particular, to the best of our knowledge this is the first case when the solution of the Euler equations in conformal variables is compared with a laboratory experiment.

Acknowledgments. The research is supported by grant # 3-3573 from the Israel-Russia Cooperation Program, by grant # 964/05 from the Israeli Science Foundation (LS). The research for AS is supported by RFBR grants # 06-05-72011 and 08-02-00039, State Programme 2008-MO-04-06 and project Extreme Seas.

References

1. Shemer L., Dorfman B.: Experimental and numerical study of spatial and temporal evolution of nonlinear wave groups. *Nonlin. Proc. Geophys.* 15, 931-942 (2008).
2. Lo E., Mei C.C.: A numerical study of water-wave modulation based on a higher-order nonlinear Schrödinger equation. *J. Fluid Mech.* 150, 395-416 (1985).
3. Kit E., Shemer L.: Spatial versions of the Zakharov and Dysthe evolution equations for deep water gravity waves. *J. Fluid Mech.* 450, 201-205 (2002).
4. Shemer L., Kit E., Jiao H.-Y.: An experimental and numerical study of the spatial evolution of unidirectional nonlinear water-wave groups. *Phys. Fluids* 14, 3380-3390 (2002).
5. Zakharov V.E.: Stability of periodic waves of finite amplitude on the surface of a deep fluid. *J. Appl. Mech. Tech. Phys.* 9, 190-194 (1968).
6. Trulsen K., Kliakhandler I., Dysthe K.B., Velarde M.G.: On weakly nonlinear modulation of waves on deep water. *Phys. Fluids* 12, 2432-2437 (2000).
7. Dommermuth D.G., Yue D.K.P.: A high-order spectral method for the study of nonlinear gravity waves. *J. Fluid. Mech.* 184, 267-288 (1987).
8. Zakharov V.E., Dyachenko A.I., Vasilyev O.A.: New method for numerical simulation of a nonstationary potential flow of incompressible fluid with a free surface. *Europ. J. Mech. B/Fluids* 21, 283-291 (2002).
9. Dorfman B., Shemer L.: Video image-based technique for measuring wave field evolution in a laboratory wave tank, *Maritime Industry, Ocean Eng. and Coastal Resources*, 2, edited by: Guedes Soares C. and Kolev P.K., Taylor & Francis, London. 711-720 (2007).
10. Slunyaev A.V.: A high-order nonlinear envelope equation for gravity waves in finite-depth water. *JETP* 101, 926-941 (2005).

Statistical properties of mechanically generated surface gravity waves: a laboratory experiment in a 3D wave basin

M. Onorato¹, L. Cavaleri², O. Gramstad³, P.A.E.M. Janssen⁴, J. Monbaliu⁵, A. R. Osborne¹, M. Serio¹, C. T. Stansberg⁶, A. Toffoli⁷, and K. Trulsen³

¹ Dip. di Fisica Generale, Università di Torino, Via P. Giuria, 1, 10125 Torino, Italy
{onorato@ph.unito.it}

² ISMAR, Castello 1364/A, 30122 Venezia, Italy

³ Department of Mathematics, University of Oslo, P.O. Box 1053 Blindern, 0316 Oslo, Norway

⁴ ECMWF, Shinfield Park, Reading, U.K.

⁵ K.U.Leuven, Kasteelpark Arenberg 40, 3001 Heverlee, Belgium

⁶ Norwegian Marine Technology Research Institute A.S (MARINTEK), P.O. Box 4125 Valentinlyst, 7450 Trondheim, Norway

⁷ Det Norske Veritas, Veritasveien 1, 1322 Høvik, Norway

Abstract. A wave basin experiment has been performed in the MARINTEK laboratories, in one of the largest existing three-dimensional wave tanks in the world. The aim of the experiment has been to investigate the effects of directional energy distribution on the statistical properties of surface gravity waves. Different degrees of directionality have been considered, starting from long crested waves up to directional distributions with a spread of $\pm 30^\circ$ at the spectral peak. The results confirm that for long crested, steep and narrow banded waves, the statistical properties of the surface elevation substantially deviate from Gaussian statistics. As directional effects are taken into account, however, such deviations become less relevant. For broad directional spreading, in particular, waves are only weakly non-Gaussian.

1 Introduction

The statistical description of the surface elevation and, in particular, the occurrence for extreme waves is an important input for the design and operation of marine structures. In many practical application, it is a common practice to calculate the statistical properties of waves from a second-order approximation of the surface elevation, which includes the second-order bound contribution for each free wave mode [1]. Based on this approach, a number of probability density functions have been derived by several authors [2–5].

Despite the fact that the second-order approximation agrees with field measurements reasonably well [3], it does not include effects related to the dynamics of free waves. At third-order in wave steepness, though, there is a substantial change in the description of water waves. Whereas bound modes are still present,

resonant and non-resonant interactions between free waves are also possible and, as a consequence, wave amplitudes may change as the wave field evolves; the mechanism responsible for this is basically a generalization of the Benjamin-Feir instability [6] or modulational instability [7]. In this respect, numerical simulations of the Nonlinear Schrödinger equation [8] have shown that, for unidirectional waves, a substantial increase of the probability of occurrence of extreme waves takes place as waves are sufficiently steep and narrow banded (see also [9, 10]). Experimentally speaking, there has been a number of papers in which the role of the modulational instability on the statistical properties of long crested surface gravity waves was recognized [11–13].

Nevertheless, using numerical simulations of a modified Schrödinger equation in two horizontal dimensions, Onorato et al. [14] noted that the number of extreme wave events was reduced by increasing the directional spreading of the initial spectrum (see also [15, 16]). Because Schrödinger-type equations are a weakly nonlinear, narrow band approximation (both in frequency and in angle) of the Euler equations, it is *a priori* impossible to be sure that the results are correct when a large directional spreading is considered. In this respect, a confirmation of such results has recently been reported by Waseda [17], who performed laboratory experiments in a directional wave tank. Due to the narrow width of the tank, however, the results could be strongly affected by the reflection on lateral walls, especially when waves travel at a large angle with respect to the main direction of propagation. Here, we present a set of laboratory experiments that have been performed in one of the largest existing wave basin in the world. Our purpose is to study in details the transition region between the strongly non-Gaussian behavior of the surface elevation that characterize the long crested waves and the weakly non-Gaussian statistics that is typical of short crested seas and hence confirm previous experimental works [17].

The present paper is organized as follows. In Section 2 we describe the facilities and the experimental conditions. In Section 3 we discuss the influence of directional properties on the occurrence of extreme wave events. Concluding remarks are then included in last Section.

2 Facilities and experimental conditions

The experiments have been performed at the Marintek wave facilities in Trondheim, Norway. Waves have been generated in a large rectangular wave basin, where multiple tests are possible. The tank has dimensions $70\text{ m} \times 50\text{ m}$ and it is equipped with a system that is capable of changing the water depth. For the present experiment the water depth was fixed at 3 m . A multi-flap wavemaker capable of generating directional waves is fitted along the 70 m side of the basin (see [18] for more details).

The initial wave field was generated by using complex Fourier amplitudes, each with its modulus randomly chosen from a Rayleigh distribution around the “target” spectrum. The phases are randomly chosen from a uniform distribution between 0 and 2π . For the generation of input wave spectra the JONSWAP for-

mulation [19] has been used to model the wave energy in the frequency domain. We have chosen to describe the wave field with a peak period $T_p = 1$ s, which corresponds to a dominant wave length of 1.56 m. Two different types of experiments, *A* and *B*, characterized by two values of the Phillips parameter, α , and the peak enhancement factor, γ , have then been considered. The values of the input (imposed) spectral parameters, the significant wave height and the wave steepness of the two experiments *A* and *B* are summarized in Table 1.

Table 1. Imposed parameters in the experiments

<i>Exp.</i>	T_p [s]	α	γ	H_s [m]	$k_p H_s / 2$
<i>A</i>	1.0	0.014	3.0	0.06	0.13
<i>B</i>	1.0	0.016	6.0	0.08	0.16

A $\cos^N(\theta)$ function is then applied to model the energy in the directional domain. In order to consider different degrees of directional spreading, different values of the spreading coefficient N have been used, ranging from fairly long crested (large N) to short crested (small N) waves. The following values have been selected: $N = 840, 200, 90, 50, 24$.

In order to have enough waves to perform a significant statistical analysis, four realizations of the random sea surface from a given spectrum have been performed by using different sets of random amplitudes and phases; for each test, 20 minutes of wave records were collected, including ramp-up time. For the present tests we have analyzed the signals after 3 minutes, thus there are 17 minutes left which we would use for processing. In these tests, there is no second-order correction of input signals.

3 Experimental results

In the present section, we discuss some statistical properties of the measured wave fields. For convenience, we shall concentrate on the most nonlinear case, i.e. experiment *B* (see Table 1). Qualitatively, similar results have also been observed from the analysis of experiment *A*. A complete description of the experiments can be found in [18].

In figure 1, we present the kurtosis (λ_4), i.e. the fourth order moment of the probability density function, as a function of the distance from the wave maker for different values of the spreading coefficient N . The kurtosis provides information on the occurrence of extreme events and assumes value of 3 for Gaussian (linear) wave fields. For narrow directional distributions, i.e. long crested waves, the kurtosis gradually increases as waves propagate along the basin. It grows for about 15-20 wavelengths (middle of the basin), where it reaches its maximum. It is evident that departures from Gaussian statistics are particularly significant

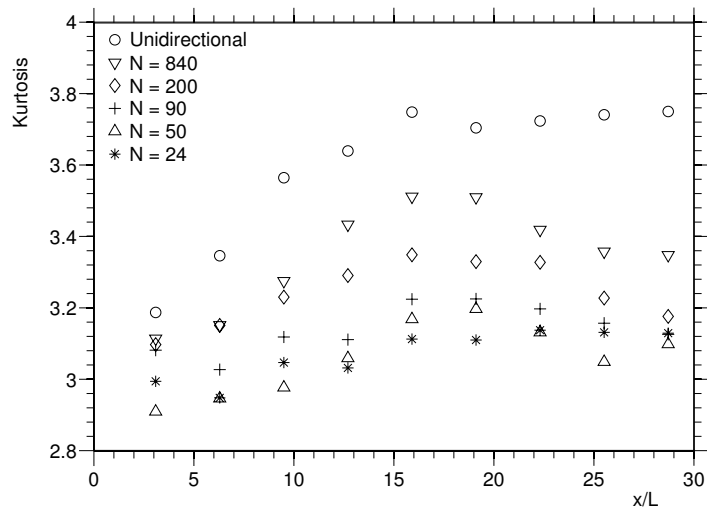


Fig. 1. Kurtosis as a function of distance from the wave maker for different values of N for experiment B .

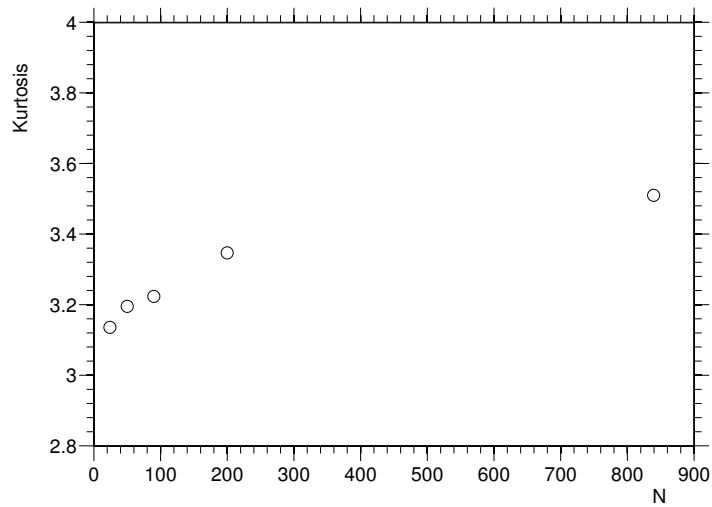


Fig. 2. Maxima of kurtosis as a function of N for for experiment B .

if waves are fairly long crested, while extreme waves occur less often for more short crested conditions (small N). This is clearly summarized in figure 2, where the maximum values of the kurtosis are shown as a function of the directional spreading. It is clear that the maximum of the kurtosis grows with N , i.e., it increases as waves become long crested.

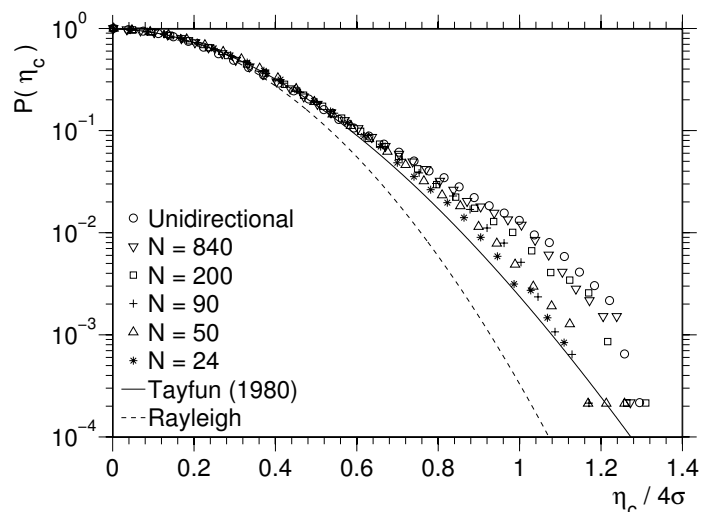


Fig. 3. Wave crest distribution at the probe of maximum kurtosis for for experiment *B*.

We now look at the probability density functions of the wave crests measured at the probe where the kurtosis reaches its maximum and compare them in figure 3 for different values of N ; the Rayleigh and Tayfun distribution [2], which is derived from a second order solution of the water wave problem under the narrow band approximation, are included as reference. The figure shows two important results: (i) for quasi-long crested waves, the appearance of extreme waves can be underestimated by an order of magnitude if linear or second-order theory (Tayfun wave crest distribution [2]) are considered; (ii) for large directional distribution, the probability of occurrence of extremes is well described by second-order theory.

4 Conclusions

We have presented a brief description of the statistical properties of surface gravity waves with special attention to the role of the angular distribution. The analysis has been based on a set of laboratory experiments conducted in one of

the largest directional wave tank in the world. Results have shown that the modulational instability process, which is regarded as one of the main mechanism for the formation of extreme waves in deep water, seems to be quenched when short crested waves are considered. A more detailed analysis of the aforementioned laboratory experiment can be found in [18].

References

1. LONGUET-HIGGINS, M.S.: The effect of non-linearities on statistical distribution in the theory of sea waves. *J. Fluid Mech.* **17** (1963) 459–480.
2. TAYFUN, M. A.: Narrow-band nonlinear sea waves. *J. Geophys. Res.* **85 C3** (1980) 1548–1552.
3. FORRISTALL, G.Z.: Wave crests distributions: Observations and second-order theory. *J. Phys. Ocean.* **30** (2000) 1931–1943.
4. PREVOSTO, M., KROGSTAD, H.E. & ROBIN, A.: Probability distributions for maximum wave and crest heights. *Coastal Engineering* **40** (2000) 329–360.
5. TAYFUN, M.A. & FEDELE, F.: Wave-height distributions and nonlinear effects. *Ocean Eng.* **34** (2007) 1631–1649.
6. BENJAMIN, T.B. & FEIR, J.E.: The disintegration of wave trains on deep water. *J. Fluid Mech.* **27** (1967) 417.
7. ZAKHAROV, V.: Stability of period waves of finite amplitude on surface of a deep fluid. *J. Appl. Mech. Tech. Phys.* **9** (1968) 190–194.
8. ONORATO, M., OSBORNE, A.R., SERIO, M. & BERTONE, S.: Freak wave in random oceanic sea states. *Phys. Rev. Lett.* **86** (2001) 5831–5834.
9. JANSSEN, P. A. E. M.: Nonlinear four-wave interaction and freak waves. *J. Phys. Ocean.* **33** (4) (2003) 863–884.
10. MORI, N. & JANSSEN, P. A. E. M.: On kurtosis and occurrence probability of freak waves. *J. Phys. Ocean.* **36** (2006) 1471–1483.
11. ONORATO, M., OSBORNE, A.R., SERIO, M., CAVALERI, L., BRANDINI, C. & STANSBERG, C.T.: Observation of strongly non-gaussian statistics for random sea surface gravity waves in wave flume experiments. *Phys. Rev. E.* **70** (2004) 067302.
12. ONORATO, M., OSBORNE, A.R., SERIO, M. & CAVALERI, L.: Modulational instability and non-gaussian statistics in experimental random water-wave trains. *Phys. of Fluids* **17** (2005) 078101–4.
13. ONORATO, M., OSBORNE, A., SERIO, M., CAVALERI, L., BRANDINI, C. & STANSBERG, C.T.: *b* Extreme waves, modulational instability and second order theory: wave flume experiments on irregular waves. *Europ. J. Mech. B/Fluids* **25** (2006) 586–601.
14. ONORATO, M., OSBORNE, A. R. & SERIO, M.: *a* Extreme wave events in directional random oceanic sea states. *Physics of Fluids* **14** (4) (2002) 25–28.
15. SOCQUET-JUGLARD, H., DYSTHE, K., TRULSEN, K., KROGSTAD, H.E. & LIU, J.: Distribution of surface gravity waves during spectral changes. *J. Fluid Mech.* **542** (2005) 195–216.
16. GRAMSTAD, O. & TRULSEN, K.: Influence of crest and group length on the occurrence of freak waves. *J. Fluid Mech.* **582** (2007) 463–472.
17. WASEDA, T. 2006 Impact of directionality on the extreme wave occurrence in a discrete random wave system. In: *Proc. 9th Int. Workshop on Wave Hindcasting and Forecasting*. Victoria, Canada (2006).

18. MIGUEL, O., CAVALERI, L., FOUQUES, S., GRAMDSTAD, O., JANSSEN, P.A.E.M., MONBALIU, J., OSBORNE, A.R., PAKOZDI, C., SERIO, M., STANSBERG, C.T., TOFFOLI, A. & TRULSEN, K. 2009 Statistical properties of mechanically generated surface gravity waves: a laboratory experiment in a 3D wave basin . *J. Fluid Mech.*, in press.
19. KOMEN, G.J., CAVALERI, L., DONELAN, M., HASSELMANN, K., HASSELMANN, H. & JANSSEN, P.A.E.M.: *Dynamics and modeling of ocean waves*. Cambridge University Press (1994).

TITLE: Extremely Narrow Spectrum and Freak Wave – an Abnormal Sea State
AUTHOR: Takuji Waseda, Hitoshi Tamura, Takeshi Kinoshita

ABSTRACT:

The evolution of random directional wave was investigated at the wave tank of the University of Tokyo, Institute of Industrial Sciences. By systematically changing the directional distribution of the random wave, we have discovered that the occurrence of freak wave rapidly diminishes as the directional spreading broadens. Closer look into the evolution of wave statistics and spectra revealed that the relative significance of non-resonant interaction (instability) over resonant quartet interaction gradually enhances as the directional spreading narrows. Based on this observation, we have extended the Benjamin-Feir Index (BFI) to take into consideration the deviation of the directional perturbation wave number from the resonance locus. With this index, the kurtosis, which is an indicator of freak wave occurrence, is not a monotonic function and has a peak around the most unstable condition. The result suggests that the probability of freak wave occurrence is high when a rare situation of directionally confined wind-sea is realized due to abnormal forcing (i.e. wind and current). This hypothesis will be tested against the recently conducted wind-wave coupled hind-cast run. At this point, we can only estimate the probability of such extraordinary circumstances because the sea-truth of the extreme wave event is not available for verification. We have initiated a five-year project to conduct a coordinated wave observation in the Kuroshio Extension area. A brief introduction of the planned observation will be made in the talk.

Nonlinear Modulations of Standing Long Gravity Waves in a Resonator

Alexey Slunyaev¹,
Alexander Ezersky², Dominique Mouazé², Wuttersack Chokchai²

¹ Institute of Applied Physics, Russian Academy of Sciences,
46 Ulyanov Street GSP-120, 603950 Nizhny Novgorod, Russia
Slunyaev@hydro.appl.sci-nnov.ru

² UMR CNRS 6143 "Morphodynamique Continentale et Côtière" (M2C)
Université de Caen-Basse Normandie
2-4 rue des Tilleuls, 14000 Caen, France,
Alexander.Ezersky@unicaen.fr

Abstract. Arising of modulations of surface gravity waves in a shallow water resonator under harmonic forcing is discovered in laboratory experiments. Different types of modulations are found. When certain conditions are satisfied (appropriate frequency and sufficient force of excitation) the standing waves become modulated, and the envelopes of standing waves propagate in the channel. Strongly nonlinear numerical simulations of the Euler equations are performed reproducing the modulational regimes observed in the laboratory experiments. The physical mechanism responsible for the occurrence of modulated waves is determined on the basis of the simulations; quantitative estimations are made with the help of a simplified weakly nonlinear theory.

Keywords: gravity waves, standing waves, resonator, modulations, three-wave interaction, shallow water

1 Introduction

Nonlinear instabilities of water waves are the source of large waves and wave patterns formation. The Benjamin – Feir (modulational) instability is suggested by a number of researchers as a possible and regular mechanism of rogue wave formation in the Ocean [1]. Meanwhile, theoretically proved instabilities may often be hardly observed in laboratory conditions, and perhaps ineffective in the conditions of a real sea. It takes wave time to enhance due to nonlinear interactions. Thus, limited sizes of laboratory facilities often make impossible direct observations of the nonlinear focusing effects when progressive waves are considered.

Standing waves, which may be understood as two counter propagating waves, are free of this drawback: the wave fetch may be much more than the size of laboratory

facility. Although the case of two wave systems may exhibit a more difficult dynamics [2, 3], in [4] they report that weakly nonlinear standing water waves are modulationally unstable only if the component traveling waves are modulation unstable.

The modulational instability is supported by satisfaction of the Lighthill condition

$$\omega''_0(k)\omega_2(k) < 0, \quad (1)$$

where $\omega_0(k)$ is the dispersion relation for linear waves, k is the wavenumber, and $\omega_2(k)$ is the nonlinear addition to the frequency, $\omega(k) = \omega_0(k) + \omega_2(k)|ka|^2$, a is the wave amplitude. When the water is sufficiently shallow, $kh < 1.363$, where h is the water depth, condition (1) is broken due to the change of sign of the nonlinear frequency correction, ω_2 , and the modulational instability vanishes.

In this paper we consider a shallow-water case, and the condition for the existence of longitudinal modulation instability (1) is not satisfied. In general, the stability analysis established for deep-water waves becomes trickier for shallow-water conditions, see recent study [5].

Condition (1) is relevant for weakly nonlinear quasi-sinusoidal progressive waves. As we show in this paper, nonlinear wave modulations of standing shallow water waves may significantly grow and lead to the formation of intense traveling envelopes of standing waves. We show that similar to (1), this effect is due to the combination of the shallow water dispersion and nonlinear frequency shift, what makes short-scale waves in resonance with long perturbations. In contrast to (1) this process is due to 3-wave interaction, what leads to other modulation growth rate as function of wave amplitude. Action of an external forcing enables resonator waves to get more energy. The described effect was first observed in laboratory (the facility is described in Section 2, and the laboratory measurements are summarized in Section 3), then reproduced by means of numerical simulations which are briefly described in Section 4. A more detailed description of the laboratory measurements and numerical simulations may be found in [6]. Section 5 represents a simplified theory which gives us quantitative estimate for the condition of the modulation occurrence onset.

2 Experimental Setup

The laboratory tests are carried out in a hydrodynamic channel, see Fig. 1. The length of the channel is $L = 15$ m, its width is 0.5 m, and the depth of the liquid layer is $h = 0.17$ m. A piston type wavemaker consisting of a vertical plate set in motion by a DC engine is placed at one end of the channel. The plate is moved in the horizontal direction by a harmonic law. Amplitude, B , and oscillation frequency, f , of the wavemaker could be changed. Free surface oscillations are registered by resistive wave gage placed at the end of the channel (see Fig. 1). Signals from the surface wave transducers and wavemaker displacement are recorded in a computer simultaneously for further data processing.

The channel used during the tests represents a resonator for surface gravity waves. Natural frequencies of resonator modes, f_n , are defined by the dispersion relation as

$$f_n = \frac{1}{2\pi} \sqrt{g \frac{\pi}{L} n \tanh\left(\frac{\pi}{L} nh\right)}, \quad n = 1, 2, 3, \dots, \quad (2)$$

where n numerates the modes, and g is the gravity acceleration.

The experiments are accomplished at the frequencies $0.34 \text{ Hz} < f < 0.48 \text{ Hz}$ corresponding to the excitation of modes with numbers $8 < n < 12$, hence, in the experiment we have the depth parameter $0.28 < kh < 0.42$, what breaks condition (1).



Fig. 1. The scheme of the experiments, (1) is the wavemaker, (2) is the transducer of horizontal displacement of wave maker, (3) is the resistive probe of a free surface displacement.

3 Observation of modulations in the laboratory tank

Three regimes were observed in the experiments. They are: 1) steady-state generation of nonlinear waves with constant amplitude; 2) regime with modulation, including chaotic modulation without wave breaking; and 3) regime with modulation accompanied by wave breaking. A map of these regimes on a plane (amplitude of oscillation of the wavemaker plate, B , versus oscillation frequency, f) is given in Fig. 2.

It is clear from the diagram that the wave modulation and breaking arise at smaller amplitudes of wavemaker oscillations if the excitation frequency does not coincide with the natural frequency of resonator modes (2).

Time series of the free surface displacement corresponding to the regular standing wave regime and regular modulation regime are presented in Fig. 3. An excitation of harmonics with frequencies multiple to the frequency of external forcing occurs for the regime without modulation. Consequently, a nonlinear steady wave is recorded (see Fig. 3a). For the regime with regular modulation the smallest period of the envelope wave (see Fig. 3b) was approximately equal to the period of basic mode of resonator, $1/f_1$, where $f_1 \approx 0.04 \text{ Hz}$. Besides, double modulated regular regime was observed, and also irregular (chaotic) wave dynamics with and without wave breaking, see these details in [6].

Sometime appearance of modulation in the channel needs a time. At the first stage of wave excitation steady nonlinear wave are generated. After a time (as rule 3 – 5 minutes) modulation may develop and maximal wave height in resonator became about two times more that before development of instability. Example of such processes is shown in Fig.4. A band pass filtering (high and low cut-off frequency)

was used to determine growing amplitudes of the spectral harmonics. The harmonics grow in amplitude from very small values, and when become of the magnitude of the fundamental harmonic, saturation takes place. The exponential function gives us the best fit approximation for the initial stage of the harmonic growth.

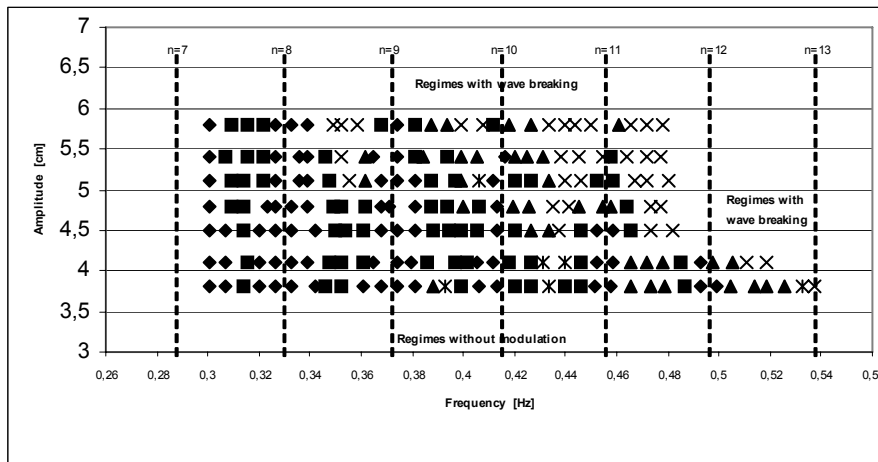


Fig. 2. The diagram of the regimes observed in the laboratory experiments (amplitude of the wavemaker, B , versus its frequency, f): rhombs – constant-amplitude standing waves; squares – regular modulated waves; triangles – chaotic wave modulation; stars – double modulation, crosses – wave breaking. The dashed lines show natural mode linear frequencies.

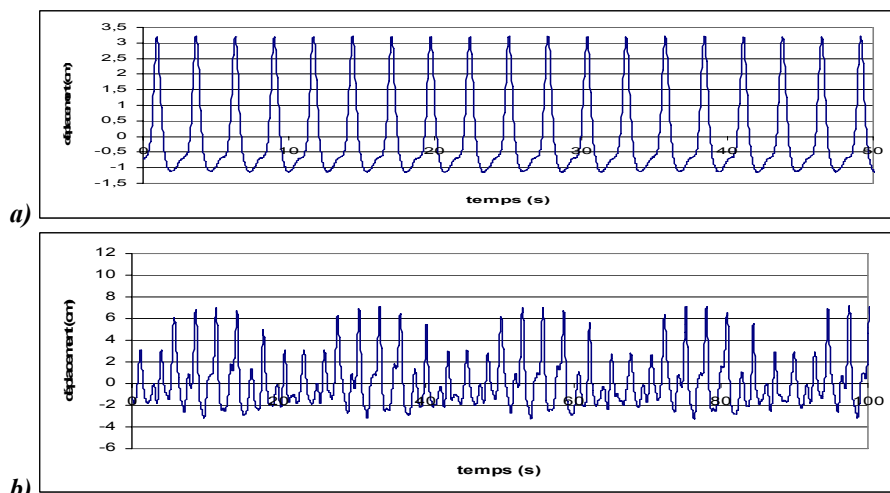


Fig. 3. Time series for different conditions of excitation: (a) the regime without modulation (amplitude $B = 45$ mm, $f = 0.3744$ Hz), (b) the regular modulation ($B = 48$ mm, $f = 0.3616$ Hz).

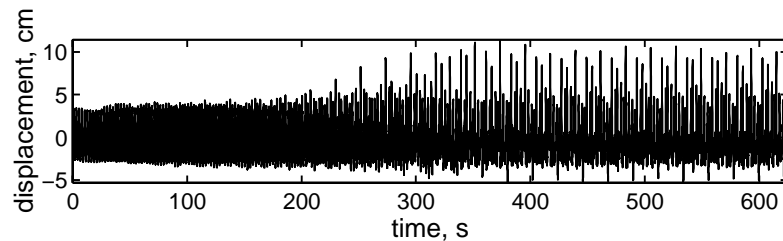


Fig. 4. Development of modulation from steady nonlinear waves. The excitation frequency $f=0.406$ Hz.

4 Numerical Simulation of the Modulations

The regimes, observed in the laboratory experiment, are reproduced in numerical simulations of primitive equations of ideal fluid. The potential Euler equations are solved with the help of the High-Order Spectral Method, HOSM, following [7]. The kinematic and dynamic boundary conditions on the free surface are written in form

$$\begin{aligned} \frac{\partial \eta}{\partial t} &= -\frac{\partial \Phi}{\partial x} \frac{\partial \eta}{\partial x} + \left(1 + \left(\frac{\partial \eta}{\partial x} \right)^2 \right) \frac{\partial \varphi}{\partial z} - \delta k^2 \eta, \\ \frac{\partial \Phi}{\partial t} &= -\eta - \frac{1}{2} \left(\frac{\partial \Phi}{\partial x} \right)^2 + \frac{1}{2} \left(\frac{\partial \varphi}{\partial z} \right)^2 \left[1 + \left(\frac{\partial \eta}{\partial x} \right)^2 \right] - P_a - \delta k^2 \Phi, \end{aligned} \quad (3)$$

where x and z are horizontal and vertical (upward) coordinates respectively, and t is time. Conditions $z = -h$ and $z = \eta(x, t)$ specify the water bed and the free surface displacement correspondingly. Function $\varphi(x, z, t)$ defines the velocity potential, and is obtained at every step of numerical integration through strongly nonlinear iterative solution of the Laplace equation with the potential at the surface specified by $\Phi = \varphi(x, z = \eta(x, t), t)$, see [7]. Term P_a in (3) denotes the atmosphere pressure; its variation in time is used to introduce wave excitation forcing. Damping effect was found important to obtain regular wave patterns. Coefficient $\delta = 0.0033 \text{ sec}^{-1}$ is chosen to have a better agreement between laboratory registration and simulations; it defines viscous wave dissipation.

A 30-meter computational domain with periodic boundary conditions is used in the numerical simulations of the 15-meter laboratory resonator. It is supposed, that $x = 0$ corresponds to the rigid wall of the laboratory resonator (where the gauge is situated, see Fig. 1), while $x = 15$ m corresponds to the other wall (position of the wave maker).

Regular standing wave (Fig. 3a, 5a) and regular modulated standing wave (Fig. 3b, 5b) regimes are reproduced by means of numerical simulations. On the spatio-

temporal diagram in Fig. 5b the traveling intense wave patterns are clearly seen, in contrast to Fig. 5a, where the wave field picture is uniform. Some wave shape asymmetry may be also observed due to the dissipation effect.

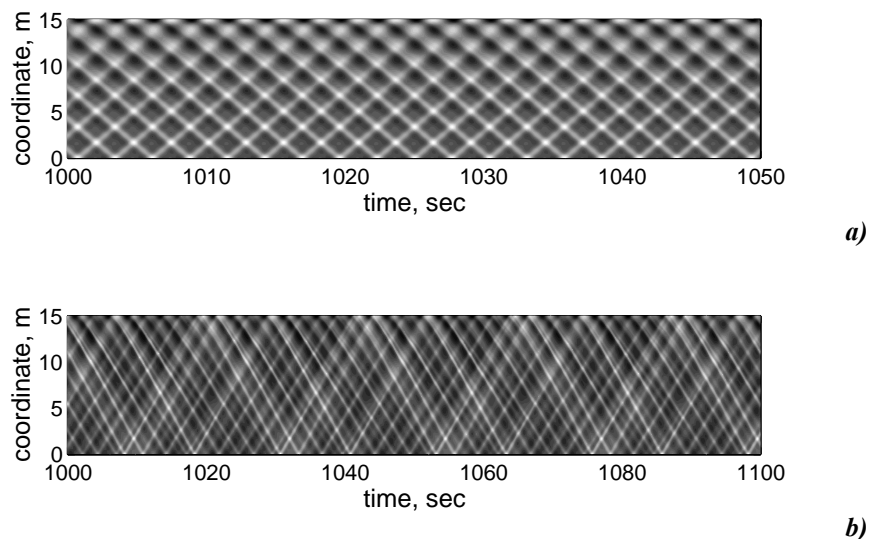


Fig. 5. Regular non-modulated waves (a) and standing wave modulation (b) observed in the numerical simulations, the spatio-temporal diagrams.

Strongly nonlinear numerical simulation of weakly perturbed standing waves showed that long modulations of standing waves lead to the growth of the excited sidebands, and also to the energy leakage to many low modes of the resonator. Then many modes of the resonator become excited, and the standing waves are strongly modulated. It is found that the growth rate of the excited spectral modes at the early stage corresponds to the three-wave interactions (see [6]). Thus, in contrast to the Benjamin – Feir modulational instability, three-wave interactions, which are common for the shallow-water waves, play the major role in the dynamics of modulated standing waves.

The diagrams of spatio-temporal spectra are obtained on the basis of the numerical simulation data as follows. First, the spatial Fourier transform of the surface elevation as function of space and time is performed. Then the temporal Fourier transform is applied to the modes of the spatial Fourier spectrum, represented by complex data time series. Thus, spatio-temporal spectrum $Sp(n, f)$ is obtained, where n is the mode number, and f is frequency. The length of a time series defines the frequency resolution, which is not less than 0.005 Hz for the presented figures. To render the intensity of the Fourier spectrum, Sp , every value of it (for the grid in the plane of modes and frequencies) is plotted by a filled circle with diameter, D , proportional to the amplitude of Sp in logarithmic scale; too small (insignificant) values of Sp are not plotted.

Fig. 6a shows the regime when modulations do not occur, while Fig. 6b demonstrate the case when modulations are developed. The horizontal dotted lines in Fig. 6 show the forcing frequencies, f , and also multiple values $2f$, $3f$, etc. The dash-dotted lines represent the exact linear dispersion (2), its shallow-water limit is given by the dashed straight lines. The solid straight lines in Fig. 6 are lined through the reference origin $(0, 0)$, and the point (n, f) , where $n = 9$ is the most excited mode at the forcing frequency f . Thus, this line on the spectral plane represents the phase velocity of the most excited standing wave.

The spots in Fig. 6a are discrete in both mode and frequency. The frequency discretization is due to the regular character of the record, and its interval is larger than the resolution. One driving frequency excites many modes. Fig. 6b represents the regime with modulations, and is quite different from Fig. 6a. There are much more energetic spots; the energy is spread along the curve of the shallow-water dispersion limit, and less – along the linear dispersion curve. For a given mode number the frequency spectrum is rather wide.

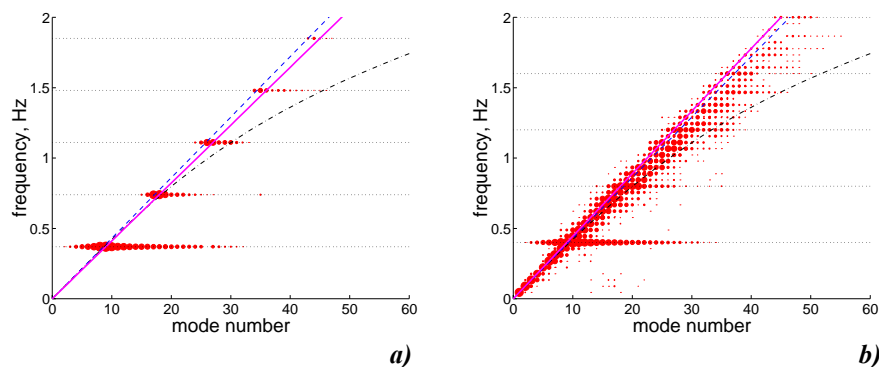


Fig. 6. Spatio-temporal spectral plane for the numerical experiment when standing wave modulations are not observed (a) and when regular modulations occur (b). The dash-dotted lines represent the exact linear dispersion, its shallow-water limit is given by the dashed straight lines. The horizontal dotted lines show the frequency and multiple frequencies of the excitation. The solid straight lines show the phase velocity of the most excited standing wave.

It is known, that in a 3-oscillator system with quadratic nonlinearity, lower frequencies may effectively get energy from the high-frequency oscillator (this process is exponential at its early stage, see [8]). It clearly follows from Fig. 6a, b, that modulations do not occur when the forcing wave velocity line (the straight lines in Fig. 6) is lower than the shallow-water limit of the dispersion. In the opposite, the modulations grow when the forcing wave velocity is higher than the long-wave speed (Fig. 6b). It may be concluded that the 3-wave resonance condition becomes fulfilled for the driving wave due to positive nonlinear frequency shift and for a number of low modes. The dynamics involves many wave triplets, thus the nonlinear energy exchange between them may be hard to interpret. Besides free waves, many bound waves are excited, proving that the waves are essentially cnoidal.

5 Weakly Nonlinear Theory for Shallow Water Resonances

As it is discussed in the previous part, the nonlinear three-wave interactions are responsible for the dynamics observed in laboratory experiments, and also in strongly nonlinear numerical simulations. Since the waves are essentially cnoidal, direct application of known theories for weakly nonlinear weakly modulated waves (including coupled equations describing quasi-sinusoidal waves) is not evident. Meanwhile, let us suppose that the effect of interaction between two counter propagating wave systems is of secondary importance, and that the heart of the observed instability is in the resonance between long perturbations and shorter nonlinear waves. Then let us consider a simplified weakly nonlinear dispersive shallow water theory for cnoidal waves, the Korteweg – de Vries equation (KdV)

$$\frac{\partial \eta}{\partial t} + c \frac{\partial \eta}{\partial x} + \gamma \eta \frac{\partial \eta}{\partial x} + \mu \frac{\partial^3 \eta}{\partial x^3} = 0, \quad c = \sqrt{gh}, \quad \gamma = \frac{3c}{2h}, \quad \mu = \frac{ch^2}{6}. \quad (4)$$

Equation (4) has stationary exact solutions, the cnoidal waves, expressed in terms of the Jacobi elliptic functions

$$\eta(x, t) = \frac{2a}{s^2} \left[dn^2 \left(\sqrt{\frac{\gamma a}{6\mu s^2}} (x - (c + V_{cn})t), s \right) - \frac{E(s)}{K(s)} \right] \quad (5)$$

(see for instance [9]), where K and E are complete elliptic integrals of the first and the second kinds,

$$K = \int_0^{\pi/2} (1 - s^2 \sin^2 \theta)^{-1/2} d\theta, \quad E = \int_0^{\pi/2} \sqrt{1 - s^2 \sin^2 \theta} d\theta. \quad (6)$$

The velocity of the cnoidal wave is defined by

$$V_{cn} = -\frac{\gamma a}{3s^2} \left(3 \frac{E(s)}{K(s)} + s^2 - 2 \right), \quad (7)$$

and the wave amplitude, a , is linked with the wave length, Λ , through relation

$$\Lambda = \sqrt{\frac{24\mu}{\gamma a}} s K(s). \quad (8)$$

The cnoidal waves may have strong vertical asymmetry, and amplitude parameter a has the meaning that the value $2a$ is equal to the wave height from the trough to the crest.

The “nonlinear” dispersion relation may be found after (7) and (8), and is given by formula (see [9])

$$\omega(k) - ck = -\mu k^3 \left(\frac{2K(s)}{\pi} \right)^2 \left(3 \frac{E(s)}{K(s)} + s^2 - 2 \right). \quad (9)$$

Parameter $0 \leq s \leq 1$ controls the strength of nonlinearity. Linear waves correspond to $s = 0$, then (9) transforms to $\omega(k) - ck = -\mu k^3$, which is the linear dispersion of the KdV equation (4). The right-hand-side term in (9) becomes zero or even positive when s is large enough. Thus, nonlinearity may give the opposite frequency shift than dispersion, and condition

$$3 \frac{E(s)}{K(s)} + s^2 - 2 = 0 \quad (10)$$

defines the nonlinear threshold when small-scale cnoidal waves may become in resonance with long linear waves.

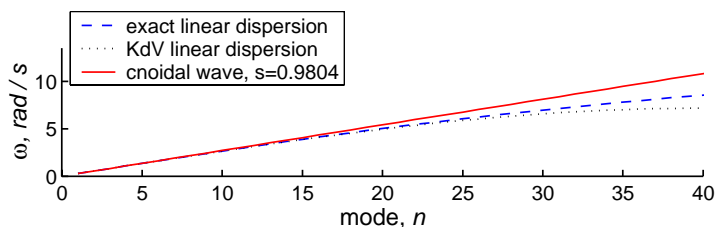


Fig. 7. Dispersion plane in terms of cyclic frequency versus mode number.

The dispersion curves for the conditions of the laboratory resonator, when condition (10) is fulfilled, are shown in Fig. 7. The solid line corresponds to the nonlinear frequency (9) of the cnoidal wave. It is straight and coincides with the long-wave limit of the linear water wave dispersion. The curve of linear dispersion provided by the KdV model (4) (dotted line) is quite close to the exact linear dispersion (2) shown by the dashed line.

Solution of (10) gives the value about $s \approx 0.98$; then the threshold wave amplitude when the nonlinear frequency correction in (9) is positive may be estimated as

$$a > \frac{2s^2 K^2 h^3}{3L^2} n^2 \approx 5.9 \frac{h^3}{L^2} n^2. \quad (11)$$

The strength of the three-wave nonlinear effects may be estimated with the help of the Ursell parameter, which may be defined as

$$Ur = \frac{a\Lambda^2}{h^3} = \frac{4aL^2}{n^2 h^3}. \quad (12)$$

The Ursell number is equal to 4, when the soliton solution of the Korteweg – de Vries equation is concerned (when nonlinearity and dispersion are of same order); estimate (11) results in the value of the Ursell number of about 74, what corresponds to a strongly nonlinear case.

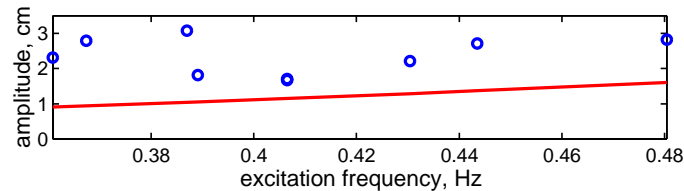


Fig. 8. Comparison of the estimated threshold wave amplitude (the curve) and the laboratory experiment (the circles). Experimental points correspond to the wave amplitude before development on the modulation in the system.

Comparison of the theoretical estimate with experimental data is given in Fig. 8. The solid line represents the condition (11), and the circles give the heights of measured standing waves divided by factor 4 (we suppose that a wave height is twice the amplitude, and that a standing wave height is twice the progressive wave height). It is important to note that the experimental data is not the marginal values, but the minimum wave amplitudes when modulations occur. Wave dissipation was clearly observed in the laboratory experiments and may also effect on the wave amplitude threshold. Thus, although the experimental points lie somewhat higher the theoretical curve, we conclude that the comparison in Fig. 8 proves rather good agreement between the observed phenomenon and theoretical estimates.

Acknowledgments. The experimental tests were supported by a French national scientific program called 'PLAMAR'. The research was supported for AS by RFBR grant 08-02-00039, State Programme 2008-MO-04-06 and project Extreme Seas.

References

1. Kharif, C., Pelinovsky, E., Slunyaev, A.: *Rogue Waves in the Ocean*, Springer-Verlag Berlin Heidelberg (2009).
2. Vlasov, S.N., Talanov, V.I.: *Wave self-focusing*. Institute of Applied Physics Press, Nizhny Novgorod (1997) (In Russian).
3. Griffiths, S.D., Grimshaw, R.H.J., Khusnutdinova, K.R.: Modulational instability of two pairs of counter-propagating waves and energy exchange in two-component media. *Physica D* 214, 1-24 (2006).
4. Bridges, T.J., Laine-Pearson, F.E.: Nonlinear counter propagating waves, multisymplectic geometry, and the instability of standing waves. *SIAM J. Appl. Math.* 64, 2096-2120 (2004).
5. Francius, M., Kharif, C.: Three-dimensional instabilities of periodic gravity waves in shallow water. *J. Fluid Mech.* 561, 417-437 (2006).
6. Ezersky, A., Slunyaev, A., Mouazé, D., Chokchai, W.: Occurrence of standing surface gravity waves modulation in shallow water. *Eur. J. Mech. B / Fluids*, Submitted (2009).
7. Dommermuth, D., Yue, D.K.P.: A high-order spectral method for the study of nonlinear gravity waves. *J. Fluid Mech.* 184, 267-288 (1987).
8. Rabinovich, M.I., Trubetskov, D.I.: *Oscillations and waves in linear and nonlinear systems*. Kluwer Academic Publisher, Dordrecht/Boston/London (1989).
9. Ostrovsky, L.A., Potapov, A.I.: *Modulated waves. Theory and applications*. Johns Hopkins Univ. Press., Baltimore (1999).

A deep-water beach for laboratory generation of abnormal waves

S. S. Denchfield¹, A. J. Murphy² and P. Temarel¹

¹ School of Engineering Sciences, University of Southampton, UK
 S.S.Denchfield@soton.ac.uk
 p.temarel@soton.ac.uk

² School of Marine Science and Technology, Newcastle University, UK
 a.j.murphy@newcastle.ac.uk

Abstract. The design of ships, as well as other marine structures, requires evaluation of wave-induced loads for their operational life. Ships often encounter abnormal waves in the open ocean during normal operational conditions. Research into how abnormal waves affect a ship is important, as they may cause severe damage or even loss of a ship.

The experimental method developed during this study uses an adjustable sloping beach, termed a “deep-water beach”, installed upstream of the target region in a wave tank to generate steep and breaking waves from a regular wave train. The deep-water beach was found to provide a means of readily generating different types of abnormal wave either singularly or reoccurring periodically, and in both deep and shallow water.

Preliminary tests were carried out placing a model yacht hull in the target region and measuring longitudinal force. Comparisons between forces measured in regular and abnormal waves (generated from the regular wave) indicate that steep waves induce longitudinal loads significantly larger than regular or breaking waves.

1 Nomenclature

d_b	Water depth at wave breaking (m)
d_0	Deep water depth (m)
f_d	Empirical scale factor for wave damping
H_b	Breaking wave height (m)
H_0	Deep water wave height (m)
I_r	Irribarren number
L	Wave length, generic (m)
L_0	Deep water wave length (m)
T_0	Deep water wave period (s)
α	Beach slope (degrees)
γ_b	$\frac{H_b}{d_b}$

2 Introduction

In the design of ships and other marine structures, it is common practise to account for wave-induced loads caused by regular and irregular waves. Furthermore, there is an increasing need to account for wave loads on marine structures subject to abnormal wave conditions in the open ocean. Specific accident investigations often rely on knowledge of abnormal wave conditions (e.g. Claughton (1984); Dahle and Kjaerland (1980); Faulkner and Williams (1997)) and research interest into abnormal conditions is readily apparent in recent literature, e.g. RINA (2005), as well as specific recent research into rogue waves, e.g. Olagnon and Prevosto (2004).

Although there are a number of numerical methods being researched to model abnormal waves, the highly abnormal and varied nature of these events means that in addition they are routinely investigated in physical experiments at model scale.

A variety of methods have been used to generate abnormal waves conditions in different experimental test facilities and are summarised below.

- Experiments in the breaking zone on beaches use radio-controlled models. Waves are mostly uncontrollable and unpredictable and testing is in breaking waves only (Claughton, 1984).
- The use of large amplitude regular waves in a wave tank is a simple method of generating breaking waves but few test facilities are able to generate waves of sufficiently high amplitude to achieve wave breaking (Claughton, 1984).
- A collapsing water column generates a single large or abnormal wave per test run. The wave is however not representative of a deep water abnormal wave (Claughton, 1984).
- A combination of horizontal and vertical constrictions in the wave tank can be used to increase the height of regular, progressing waves. Testing is in shallow water with limited model space (Dahle and Kjaerland, 1980).
- A wadedozer (bulldozer blade) can be mounted on the tow post to push a wall of water down the wave tank, producing a single breaking wave. It is not possible to test a model using this method (Hogben, 1976).
- A towed, submerged wing section generates a breaking wave but there is little control over the wave generated and a ship model cannot be used (Duncan (1981); Duncan (1983)).
- Sophisticated control of the wavemaker input signal can be used to superimpose regular wave packets at a specified location (e.g. Clauss (2002)).

While these methods have been successful at providing different abnormal waves in experimental tanks, this research seeks a further alternative that would permit the investigation of a range of different wave conditions on marine craft subject to abnormal waves while floating in deep water. The particular requirements of the method, which are not completely satisfied by any single method reviewed are:

- The structure subject to the abnormal waves should be floating in deep water attached to the tank towing carriage.
- A variety of different wave types must be generated in deep water with only minor adjustment to the experimental procedure or apparatus, using hardware that could be readily introduced into a standard towing tank. These wave types are:
 1. Steep but non-breaking waves
 2. Breaking waves
- The wavemakers need only be capable of generating regular wave-trains of one frequency at a time.
- The method used should be relatively simple and accurate

The method devised used a sloping tank bottom installed upstream of the target region so that it was between the wavemakers and the desired location of the abnormal event. This is henceforth referred to as a *deep-water beach*.

3 Types and generation of waves in deep and shallow water

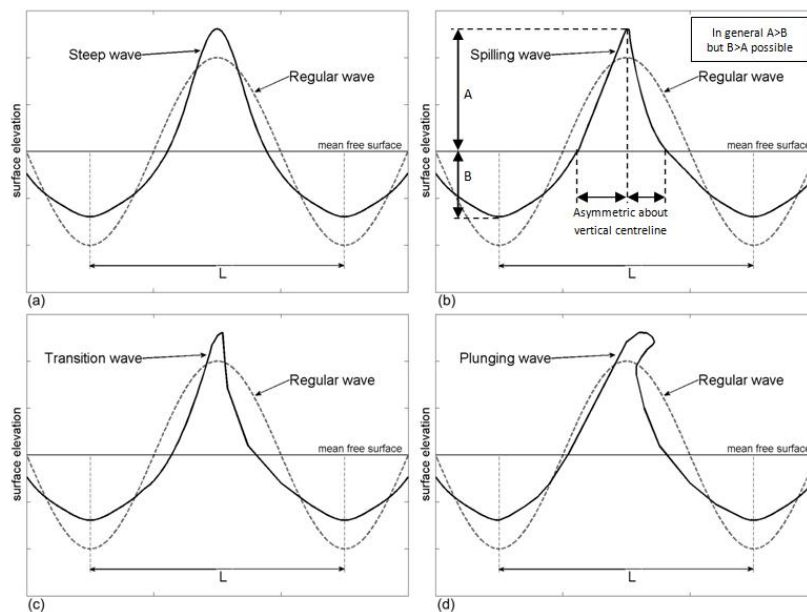


Fig. 1. Sketches showing the profiles of (a) steep (b) spilling (c) transition and (d) plunging waves (based on information from Cokelet (1977)) with the principal features of an abnormal wave profile defined on (b).

Figure 1(b) provides a general definition of an abnormal wave profile compared to a regular sinusoidal waveform. An abnormal wave of sufficient steepness will become a breaking wave (spilling or plunging). Furthermore, a transition wave type is defined because judging the difference between classing a wave as spilling or plunging is subjective.

The different types of breaking and non-breaking waves, indicated in Figure 1, can be formed as a regular wave train progresses over a sloping sea bed (Peregrine, 1983) and can also be present in deep water (Banner and Peregrine, 1993), with deep water defined by Equation 1 (Cokelet, 1977).

$$d_0 > 0.5L_0 \quad (1)$$

Jenkins (2001) uses the analogy between different types of breaking waves on beaches to make quantitative predictions of different types of breaking waves in deep water. This paper extends this analogy to generate different types of abnormal wave in deep water by using waves travelling from shallow water back into deep water, having been modified from regular to abnormal waves by the presence of the deep-water beach.

The success of the proposed method requires that waves generated in shallow water using the deep-water beach will persist into the deep water region beyond the end of the deep-water beach and not immediately return to a sinusoidal form. Preliminary tank experiments demonstrated the feasibility of this proposal, as a variety of steep and breaking waves persisted for a distance of one full wavelength into the deep water region beyond the end of a simple sloping tank bottom. Consequently, a more detailed investigation was commissioned.

4 Modification of regular waves advancing over a sloping seabed

To control the form of the wave at the end of the deep-water beach the incident wave properties, beach slope, and horizontal extent have to be correctly selected. The particular type of wave that will eventually form as it travels over a plane sloping beach is dependent on (Battjes, 1974):

1. The deep water wave steepness, defined here as $\frac{H_0}{L_0}$ and
2. The gradient of the sloping seabed, $\tan \alpha$.

These wave properties are incorporated into the Iribarren number, Ir , (Equation 2), which can be used to determine the type of wave that will be formed by a regular wave progressing over a sloping seabed as presented in Table 1 (corresponding to the wave types presented in Figure 1).

$$Ir = \frac{\tan \alpha}{(H_0/L_0)^{1/2}} \quad (2)$$

In the case of the breaking wave types, the limit of wave development is the point at which breaking occurs. In these cases, the local depth at which the wave

Table 1. Wave types formed as a regular wave progresses from deep water over a sloping seabed for different Iribarren numbers.

Abnormal Wave Type	Iribarren Number
Steep	$Ir = \textit{small}$
Spilling	$0.1 < Ir < 0.4$
Transition	$Ir \approx 0.4$
Plunging	$0.4 < Ir < 2.0$

is fully formed (and breaks) can be found through the use of the ratio of wave height to water depth at breaking ($\frac{H_b}{d_b}$). Generally the wave will break when the local depth is approximately equal to the local wave height, however a more precise estimate for breaking shows a weak linear dependency on the Iribarren number. Thus, while experimental observations show a certain amount of scatter (Battjes, 1974), the relationship can, for the purposes of engineering design, be expressed as in Equation 3, using γ_b , the breaking wave height to water depth ratio.

$$\gamma_b = 0.26Ir + 0.68 = \frac{H_b}{d_b} \tag{3}$$

Using the Iribarren number and its relationship to γ_b permits specification of the deep-water beach slope, the depth of water at its end, and the incident wave required to produce a given abnormal wave type. At low Iribarren numbers, steep waves can be formed. Alternatively a more precise knowledge (i.e. through numerical prediction) of how the wave develops from sinusoidal to breaking as it travels over the deep-water beach could be used to truncate the beach at the appropriate mid-development stage of the wave. In this way non-breaking, abnormally shaped waves will be present in the target location at the end of the deep-water beach.

5 The numerical and experimental generation of abnormal waves

To provide design guidelines for the deep-water beach, an engineering approach was used as no need was seen for a more sophisticated CFD approach. This involved numerical adaption of a high order Stream Function theory (Chaplin, 1980), selected because Stream Function theory provides good estimates for waves up to near breaking heights (Sarpkaya and Isaacson, 1981). The numerical approach used a discretisation of the sloping seabed into a series of steps. Adopting a quasi-static approach, a local wave profile was generated for each discrete step assuming constant local depth over the step. Connecting adjacent local wave profiles approximated the variation in wave profile over the slope. The approach was sufficiently accurate to design the experimental apparatus. During subsequent physical experiments empirical modifications to the method

were also made to account for the reduction in wave height as a function of tank length due to damping.

Using both the empirical relationships in Section 4 and this numerical approach, the dimensions of the deep-water beach were selected. The experimental arrangement used is presented in Figure 2. The deep-water beach was designed to allow the generation of a variety of abnormal waves by adjusting the beach gradient and its overall length, with the maximum length being 8.75m. Its construction was of rows of steel and wooden panels bolted to longitudinal steel bars. The number of rows was chosen to allow ease of assembly and flexibility of use. Wave probes (WP), located as shown in Figure 2, were used to record the wave profiles along the length of the deep-water beach and in the deep water beyond its end (i.e. beach cut-off). Table 2 provides the specifications of the deep-water beach and the incident regular wave characteristics tested.

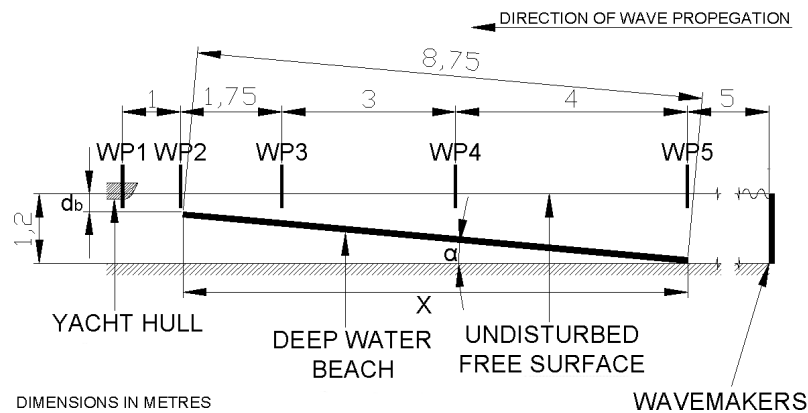


Fig. 2. Experimental set-up of the deep-water beach (all dimensions in metres).

Table 2. Parameters defining the incident wave characteristics and the beach specification for each abnormal wave type.

Abnormal Wave Type	H_0 (mm)	L_0 (m)	T_0 (s)	Ir	X (m)	α (degrees)	Slope
Steep	57	0.671	0.66	0.31	6.97	5.19	1:11
Spilling	84	0.656	0.65	0.35	8.00	7.13	1:8
Transition	56	0.659	0.65	0.43	8.66	7.13	1:8
Plunging	59	1.405	0.95	0.70	8.70	8.13	1:7

Table 3 provides a summary of the three sets of physical experiments undertaken with the deep-water beach.

Table 3. Summary of physical experiments.

Experiment	Objectives
Generation of different abnormal wave types	1) Comparison between experimental wave development over the beach and that anticipated using the adaption of Stream Function theory 2) Generate and examine different wave types in the deep water beyond the end of the deep-water beach
Measurement of longitudinal loads on a model yacht hull at a fixed location subject to regular, sinusoidal, deep-water head waves.	To provide a datum against which to compare the longitudinal loads induced by abnormal waves
Measurement of longitudinal loads on a model yacht hull at a fixed location in the deep water beyond the end of the deep-water beach, subject to abnormal head waves.	To assess the magnitude and time-variation of longitudinal loads in abnormal waves.

Figure 3 provides a comparison between the numerical and experimental wave profiles developing over the beach for a transition wave, including an allowance for wave damping.

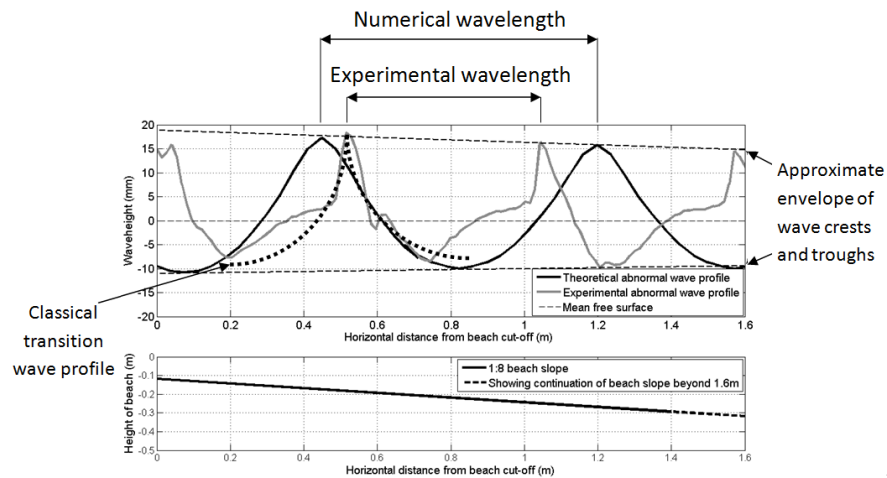


Fig. 3. Comparison of numerical and experimental wave profiles for a transition abnormal wave.

The damping factor used scales the height of the predicted abnormal wave to the same height as the experimentally-generated abnormal wave, i.e. $f_d = \max(H_{expt})/\max(H_{predicted})$. During this research the damping factor used was approximately 0.5. For the case presented in Figure 3, there is generally good correlation in shape between the numerical prediction by the modified Stream Function theory approach and the experimental wave profile, subject to the use of an appropriate value for f_d .

Therefore at a qualitative level there was a generally good correlation between the predicted shape of the wave development over the beach, if not a reliable agreement with the absolute height of the developing wave. Thus the adaptation of the Stream Function theory allowed specification of the slope and length of the beach to generate a desired type of wave.

Figure 4 compares the different wave profiles that were generated in the deep water beyond the end of the beach, namely at WP1 (see Figure 2).

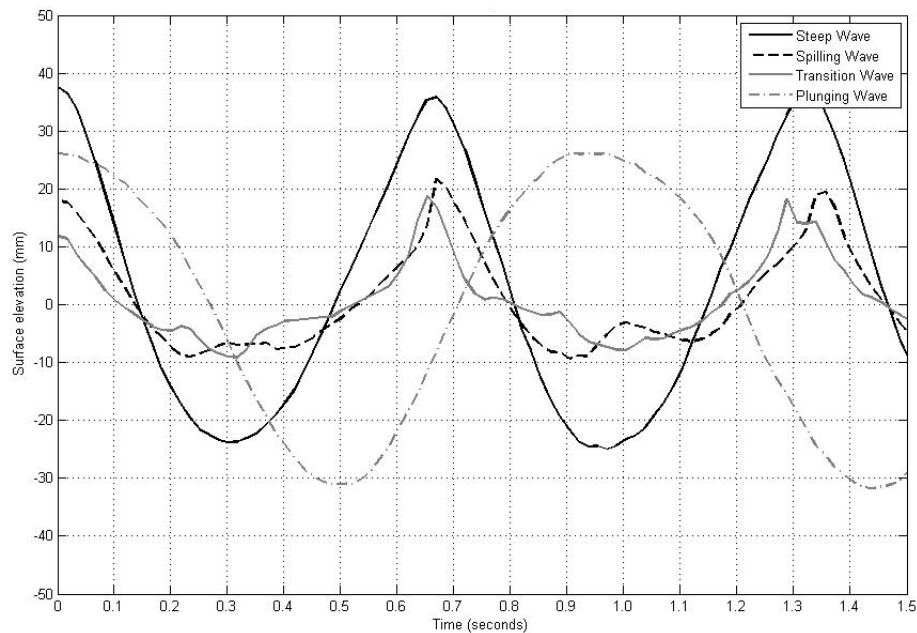


Fig. 4. Abnormal wave profiles measured in the deep water beyond the end of the deep-water beach at wave probe WP1.

As with the results of Figure 3, it is acknowledged that there was not always complete agreement between the calculated and generated wave profiles for each specified condition of the deep-water beach. However, the use of the deep-water beach was successful in generating different wave profiles which can be described as “abnormal” in comparison to the regular, sinusoidal, deep water waves used

to generate them. Furthermore, there is a qualitative agreement between the generated abnormal wave profile with variation in beach conditions. As the beach characteristics and regular incident waves used were varied as shown in Table 2, the generated wave profiles beyond the end of the beach clearly changed from steep to spilling, through transitional to a plunging wave.

As indicated in Table 3, the loads induced on a model ship hull were also investigated when subject to the different wave types. Figure 5 provides the longitudinal loads, per unit wave height, on a model yacht hull floating in deep water beyond the end of the deep-water beach, subject to a variety of different wave types. The loads induced by abnormal waves are presented together with the loads caused by the regular, sinusoidal incident wave that was used to generate the corresponding abnormal wave. The results indicate that a steep wave induced longitudinal loads significantly greater in magnitude than those due to the associated normal wave whereas a breaking wave caused longitudinal loads that are generally lesser in magnitude than those caused by the associated normal wave.

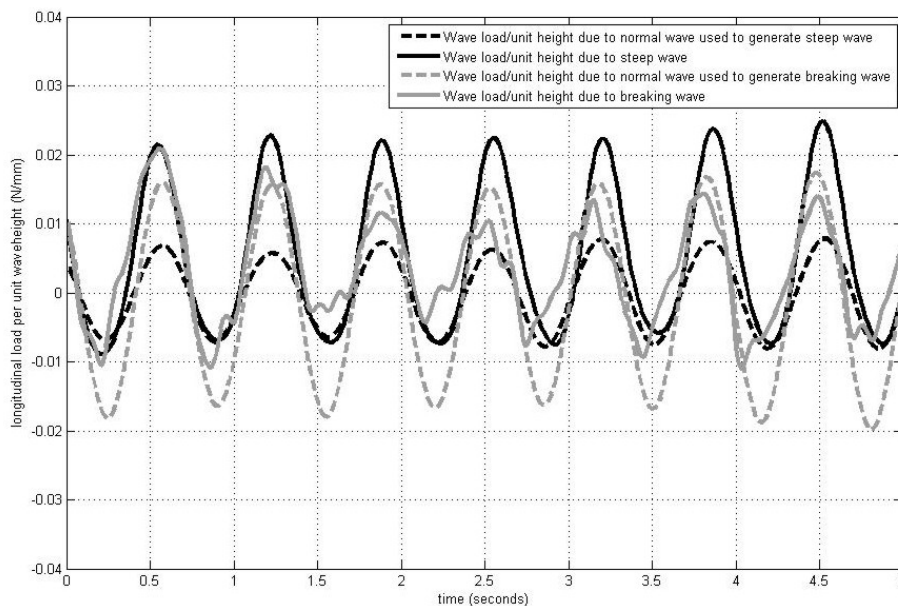


Fig. 5. Longitudinal load per unit wave height measured on yacht hull (see Figure 2) in normal (regular, sinusoidal, deep water waves) and the associated abnormal waves.

It is not necessarily possible to attach conclusive significance to the absolute values of the loads induced by the different abnormal waves. What is significant is the difference between the wave loads induced by abnormal waves and the associated regular deep water waves used to generate them. A principal focus of

this investigation was to provide a means of modifying regular waves to generate abnormal waves for the ultimate purpose of examining wave loads on marine structures in deep water. For the results in Figure 5 comparing the loads induced by the abnormal and associated regular waves, the waves leaving the wave paddles in each case are identical and the resulting difference in loads experienced by the yacht hull are due only to the modifications to the wave profile caused by the deep-water beach - as intended.

6 Conclusions

The deep-water beach did prove successful as a simple, versatile method for physically generating a variety of abnormal wave types in an experimental wave tank. In particular it provided an alternative means of generating abnormal waves where the wavemaker control system is unsophisticated, because only regular waves are needed as input. Furthermore, multiples of abnormal waves can be generated in a repeated series at a given location in the test tank by using a repeated sinusoidal wave train as the input. The persistence of the abnormal waves into deep water beyond the end of the deep-water beach also means this technique is suited to producing abnormal waves at deep water locations and, alternatively, judicious selection of wave parameters would allow use of the beach to generate shallow-water abnormal waves if required.

Preliminary investigations of the loads on a yacht hull have shown the loads in abnormal waves to differ from those in the associated regular waves. In addition the loads in steep waves are of a greater magnitude than those in breaking waves.

The numerical approach to deep-water beach design and specification, namely a basic adaption of Stream Function theory, showed a qualitative agreement with the waves produced in experiments and proved sufficiently accurate to allow the prototype deep-water beach design to be produced. Nevertheless, because of the simplicity of the numerical approach and noting other physical effects, e.g. wave damping, further research would be required to allow accurate quantitative prediction of the particular abnormal waves generated for a given beach specification and incident wave characteristics.

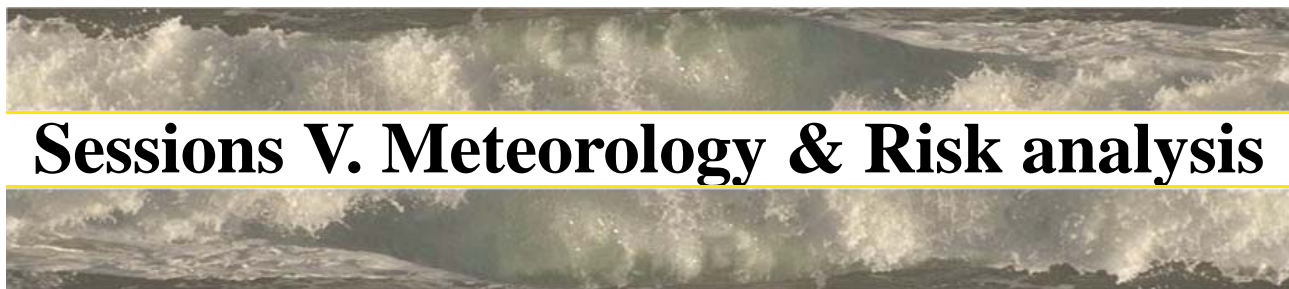
7 Acknowledgements

The authors would like to gratefully acknowledge the support from Lloyd's Register Educational Trust University Technology Centre in hydrodynamics, hydroelasticity and mechanics of composites.

The authors would like to thank Prof. J. R. Chaplin (University of Southampton, UK) for access and use of his High Order Stream Function computer program while conducting this research.

References

- M. L. Banner and D. H. Peregrine. Wave breaking in deep water. *Annual Review of Fluid Mechanics*, 25:373–397, 1993.
- J. A. Battjes. Surf similarity. In *4th Coastal Engineering Conference*, pages 466–480, 1974.
- J. R. Chaplin. Development of stream function wave theory. *Journal of Coastal Engineering*, 2:179–205, 1980.
- A. R. Cloughton. The dynamic stability of sailing yachts in large breaking waves. In *International Conference on Design Considerations for Small Craft*, 1984.
- G. Clauss. Dramas of the sea: Episodic waves and their impact on offshore structures. *Applied Ocean Research*, 24:147–161, 2002.
- E. D. Cokelet. Breaking waves. *Nature*, 267(5614):769–774, 1977.
- E. A. Dahle and O. Kjaerland. The capsizing of M/S Helland-Hansen: The investigation and recommendations for preventing similar accidents. *Transactions of the Royal Institution of Naval Architects*, 122:51–70, 1980.
- J. H. Duncan. An experimental investigation of breaking waves produced by a towed hydrofoil. *Proceedings of the Royal Society, London, Series A*, 377:331–348, 1981.
- J. H. Duncan. The breaking and non-breaking wave resistance of a two-dimensional hydrofoil. *Journal of Fluid Mechanics*, 126:507–520, 1983.
- D. Faulkner and R. A. Williams. Design for abnormal ocean waves. *Transactions of Royal Institution of Naval Architects*, 139:1–32, 1997.
- N. Hogben. The “wavedozer” - a travelling beam wavemaker. In *Proceedings of 11th ONR Symposium*, 1976.
- A. D. Jenkins. A stationary flow approximation for breaking wave crests and its application to the impact of extreme waves on vessels and offshore structures. In *Proceedings of 11th International Offshore and Polar Engineering Conference*, 2001.
- M. Ollagnon and M. Prevosto. *Proceedings of Rogue Waves*. 2004.
- D. H. Peregrine. Breaking waves on beaches. *Annual Review of Fluid Mechanics*, 15:149–178, 1983.
- RINA. *The Proceedings of International Conference on Design and Operation for Abnormal Conditions*, 2005.
- T. Sarpkaya and M. Isaacson. *Mechanics of wave forces on offshore structures, Chapter 4: Wave Theories*. 1981.



Sessions V. Meteorology & Risk analysis

Direct numerical simulation of waves subjected to an abrupt change of wind: evolution of spectra and kurtosis

S.Y.Annenkov & V.I.Shrira

Department of Mathematics, Keele University, UK

At present, forecasting of of freak wave probability is based upon modelling of wind wave evolution within the framework of the kinetic (Hasselmann) equation, which enables one to simulate wave spectra evolution, and then in operational forecasting regime to calculate the Benjamin-Feir index linked to the probability of freak events. In future it might become possible to carry out direct simulations of evolution of kurtosis using the integral equation derived by Janssen [Janssen (2003), (2004)]. However both the kinetic equation and the equation for kurtosis are based on the classical statistical theory of water waves, which assumes that a wave field is close to homogeneity, stationarity and gaussianity (e.g. [Komen et al.(1994), Zakharov *et al* (1992), Janssen(2004)]). In nature the wave fields are often subjected to strong external perturbations (sharp change of wind, inhomogeneous currents, etc), the reaction of a wave field to such perturbations cannot be described within the classical framework.

In the present work, reaction of a wind-wave field to a strong external perturbation (abrupt change of forcing) is studied by direct numerical simulation (DNS). We employ a particular DNS approach based on the integro-differential Zakharov equation [Annenkov & Shrira (2001)], which has been previously tested to give a good agreement with the kinetic equation where it is applicable [Annenkov & Shrira (2006)]. In all numerical runs, we start with low-intensity white noise, run the model under constant forcing for a sufficiently long time to allow the spectrum to develop, and then instantaneously increase or decrease the forcing. Although the classical kinetic theory cannot be applied to a strongly perturbed wave field, we have found that the main qualitative features of the adjustment to an abrupt change of forcing are correctly captured by the kinetic equation. There is, however, a key difference: the growth rate scale with $O(\varepsilon^4)$, not $O(\varepsilon^6)$ as predicted by the kinetic theory, indicating a $O(\varepsilon^{-2})$ timescale of the evolution, which is much faster than the $O(\varepsilon^{-4})$ timescale predicted by the kinetic equation. This implies that the evolution of random wave field on a fast (dynamic) timescale is a commonplace phenomenon, and wave modelling in the common situations

of rapidly changing or gusty winds, or presence of spatial inhomogeneities, should be radically revised. Higher statistical momenta also are shown to evolve on the dynamic $O(\varepsilon^{-2})$ timescale.

For developed waves the value of kurtosis is found to be nearly constant under the action of a constant wind. An abrupt increase of forcing leads to a fast decrease of kurtosis, which then increases again to a new quasi-equilibrium value, which has an approximately quadratic dependence on the intensity of forcing. The pattern of behaviour of wave field subjected to a sharp decrease of forcing is more complicated; depending on the external parameters several scenarios of evolution are possible.

References

- [Annenkov & Shrira (2001)] ANNENKOV, S. YU. & SHRIRA, V. I. 2001 Numerical modelling of water waves evolution based on the Zakharov equation. *J. Fluid Mech.* **449**, 341–371.
- [Annenkov & Shrira (2006)] ANNENKOV, S. YU. & SHRIRA, V. I. 2006 Direct numerical simulation of downshift and inverse cascade for water wave turbulence *Phys. Rev. Letters* **96**(20), 204501(4).
- [Janssen(2003)] JANSSEN, P. A. E. M. 2003 Nonlinear four-wave interactions and freak waves. *J. Phys. Oceanogr.* **33**, 863–884.
- [Janssen(2004)] JANSSEN, P. A. E. M. 2004 *The interaction of ocean waves and wind*, Cambridge University Press.
- [Komen et al.(1994)] KOMEN, G. J., CAVALERI, L., DONELAN, M., HASSELMANN, K., HASSELMANN, S. & JANSSEN, P. A. E. M. 1994 *Dynamics and modelling of ocean waves*, Cambridge Univ. Press.
- [Zakharov(1968)] ZAKHAROV, V. E. 1968 Stability of periodic waves of finite amplitude on the surface of deep water. *J. Appl. Mech. Tech. Phys.* **9**, 190–194.
- [Zakharov et al (1992)] ZAKHAROV, V. E., L'VOV, V. S. & FALKOVICH, G. 1992 *Kolmogorov Spectra of Turbulence I: Wave Turbulence*. Springer Series in Nonlinear Dynamics. 264 pp.

Occurrence and Breaking of Extreme Waves in Deep Water. A Stochastic Approach Revisit

Ioannis Alex. Papadimitrakis¹ and Frederic Dias²

¹National Technical University of Athens, School of Civil Engineering, Athens, Gr

ypapadim@central.ntua.gr

²Ecole Normal Supérieure de Cachan, Department of Mathematics, Paris, Fr

Frederic.Dias@cmla.ens-cachan.fr

Abstract. The occurrence of extreme waves in deep sea waters, and their breaking, is examined with the aid of a pdf model of joint amplitudes and frequencies. New wave breaking considerations allow kinematic, dynamic and maximum average slope concepts to be unified in a single breaking criterion that allows the more accurate determination of the limiting amplitudes that extreme waves can reach, incorporating the influence of non-linearity of the wave field and the premature wave breaking concept. The probability of extreme wave occurrence does not significantly depend on the sea spectrum bandwidth. The breaking probability of extreme waves increases with the inverse wave age, but its dependence on the latter parameter weakens, as the limiting crest height criterion is stiffened. The right variation of sea surface kurtosis, and of the Benjamin Fier Index, with the (inverse) wave age and their lower than unity values reconfirms their relation to the extreme wave occurrence.

1. Introduction

The presence of extreme waves and their breaking, in particular, threatens offshore structures and ships and may cause a lot of damage to them, possibly their destruction, and the loss of human lives. Quantitative information on the breaking of surface waves, in deep waters, is important in many aspects of oceanography, ocean engineering, marine hydrodynamics and environmental marine engineering, since wave breaking is the primary mechanism of wave energy dissipation and the major source of turbulence in the surface marine layer; it also enhances the exchange of gas, water vapor, momentum and energy between the atmosphere and the ocean. Large scale breaking may also cause the splitting of large oil slicks into smaller pieces, some of which enter the water column with the aid of the plunging crest tips. There, these smaller parcels either form water-in oil emulsions or dissolve in the water, forming oil-in water emulsions, or possibly adhere to other particles in suspension, causing in all cases great damage to the marine ecosystem.

Conventionally, extreme waves (known also as rogue or freak waves) are surface gravity waves whose heights are much larger than expected for a given sea state. Such picture is clearly seen in time records of sea surface height, during many storms, as for example in records from the Gorm and Draupner storms (Dysthe et al., 2005). Rogue waves are recognized when $H_h/H_s > 2$ or $H_c/H_s > 1.25$, although other authors have adopted values as low as 1.1, for the second inequality; here H_h , H_s , H_c are the wave height, the significant wave height and the crest wave height (or amplitude), respectively. The occurrence of rogue waves is also found, in the literature, to relate to other parameters that express either the sea surface characteristics or some of its properties, as the sea wave spectral bandwidth θ , a measure of the sea surface slope (as the rms slope, S_{rms} , or the significant slope, ξ), the sea surface kurtosis, C_4 , and the Benjamin Fier Index, BFI; C_4 appears to relate to BFI (Janssen 2005, 2003). Definitions of these quantities follow.

Extreme waves are formed by different mechanisms that have been described by various authors (see, for example, the excellent review by Dysthe et al. 2008), namely: a) by non-linear wave energy focusing caused by currents interacting with surface gravity waves, generated

locally or elsewhere and propagating either as swell or another sea, forming a mixed sea, b) by dispersive spatial-temporal focusing, i.e., by constructive interference of dispersive wave components in space and/or time (as in wave-wave interactions), c) in shallow coastal waters, by topographing focusing, via bottom diffraction and/or variable current refraction and by coastal or caustic reflection, and d) by non-linear instability mechanisms, as the Benjamin-Fier mechanism. In summary, rogue waves maybe generated by meteorological, dispersive and/or topographing focusing, wave-current and wave-wave interactions. The generation of rogue waves can also be experienced in laboratory experiments, where waves propagate along co-flowing and/or opposing currents (Wu and Yao, 2004).

Objectives of this study are: 1) the prediction of occurrence of extreme waves and their breaking, under various sea state conditions (expressed by the slope, ξ , and/or the wave age, c_p/U_{10}), using a stochastic model of the joint pdf of amplitudes and frequencies of sea waves described by Papadimitrakis (2005, called hereafter IP), and 2) the exploration of a possible relation of extreme wave occurrence with other established indices, as θ , S_{rms} or ξ , C_4 and BFI, using the above joint pdf model. Here, c_p is the phase speed of the dominant wave and U_{10} is the wind speed, measured at the height of 10 m above the mean sea level (MSL).

2. The stochastic model

The joint distribution of amplitudes and frequencies, $p(h, \omega)$, has been described in detail by IP. This model applies to both narrow- and broadband seas. Its spectral density, in terms of normalized amplitude, H , and frequency, Σ , is given by:

$$p(H, \Sigma) = 8H^2\Sigma^3 / \left\{ \pi^{1/2} (\theta^2 - 1)^{1/2} (\theta + 1) \right\} \exp \left\{ -H^2 \left[1 + (\Sigma^2 - 1)^2 / (\theta^2 - 1) \right] \right\}$$

$$H = h / (2m_0)^{1/2}, \quad \Sigma = \omega / (\alpha^{1/2} \omega_0), \quad (\omega_0 = m_2 / m_0)^{1/2}, \quad (\theta = m_0 m_4 / m_2^2)^{1/2}$$

$$\Sigma_p (= \alpha^{-1/2} \omega_p / \omega_0) = \left\{ \left[2 + (4 + 21\theta^2)^{1/2} \right] / 7 \right\}^{1/2} \quad (1, a, b, c, d, e, f)$$

where h , ω are the amplitude and radian frequency, m_i is the i th moment of the sea spectrum, and α is a positive coefficient, dependent also on θ , ω_0 and ω_p ; the subscript p refers to the spectral peak. Upon integration of $p(H, \Sigma)$ with respect to either Σ or H , the amplitude and frequency marginal densities are obtained, namely:

$$p(H) = [2/(\theta + 1)] F(B) H \exp(-H^2), \quad p(\Sigma) = 2(\theta - 1) \left\{ \Sigma / \left[\theta^2 - 1 + (\Sigma^2 - 1)^2 \right]^{1/2} \right\}^3$$

$$F(B) = 1 + erf(B^{-1}) + (B\pi^{-1/2}) \exp(-B^{-2}), \quad B = (\theta^2 - 1)^{1/2} / H \quad (2, a, b, c, d)$$

The first moment of $p(H)$ distribution provides the average amplitude, H_{av} , an exclusive function of bandwidth, θ , that also characterizes a given sea state. Detailed expressions of $p(H)$, $p(\Sigma)$ and H_{av} can be found in IP. Two more quantities of interest maybe obtained from $p(H, \Sigma)$ upon division of the latter by $p(H)$ or $p(\Sigma)$, respectively, namely the conditional frequency and/or amplitude probabilities, given as:

$$p(\Sigma|H) = p(H, \Sigma) / p(H) = \left\{ 4H\Sigma^3 / \left[\pi^{1/2} (\theta^2 - 1)^{1/2} \right] \right\} \cdot \exp \left[-H^2 (1 - \Sigma^2)^2 / (\theta^2 - 1) \right] \cdot F^{-1}(B_m)$$

$$p(H|\Sigma) = p(H, \Sigma) / p(\Sigma) \quad (3a, b, c)$$

The $p(H)$, $p(H|\Sigma)$ and/or $p(\Sigma|H)$ distributions are, particularly, important in exploring both the occurrence and the breaking of extreme waves.

3. Wave breaking considerations

Waves in the ocean travel in groups. The association of breaking waves, at sea, with wave group structures has been reported a long ago by Donelan et al. (1972). Assuming that the length of a rogue wave is comparable to the dominant wave length, λ_p , it follows that rogue waves are relatively steep. In a group of waves, when the wave at the peak of the group envelope becomes sufficiently steep {exceeding a threshold of critical steepness $(ak)_{cr}$ }, it will break. Thus, wave breaking (of the dominant wave) and rogue wave presence are intimately related (Gemrich, 2005).

For improving the understanding of wave breaking processes, it is necessary to focus on the proper criteria characterizing the occurrence of wave breaking, considering the accumulated knowledge from field and laboratory observations on this aspect. Papadimitrakis (2005) has described *how the breaking criteria of Phillips (1977) can be used* {in conjunction with his joint $p(H, \Sigma)$ pdf} *to generate* the analytical form of spectral wave breaking probability, $p_B(\Sigma)$, at any frequency Σ . These criteria describe the limiting amplitude, h_o , that a wave of frequency, ω , can reach (in the absence or presence of swell) before it breaks, but they have been modified (by IP) to properly account for surface drift current and non-linearity effects.

Of particular interest, in this study, is the variation of $p_B(\Sigma_p)$ as a function of an overall wave steepness, a parameter that characterizes locally the entire wave spectrum. Such a steepness

maybe represented by either $\xi \left[= m_0^{1/2} \omega_p^2 / (2\pi g) \right]$ or $S_{rms} \left[= g^{-2} \int_0^\infty \omega^4 S(\omega) d\omega \right]^{1/2}$. Here, g is

the gravitational acceleration and $S(\omega)$ represents the 1-D wave spectrum. It might be argued that $S_{rms} = c_2 \xi$, where the numerical coefficient c_2 is of $O(2\pi)$; its actual value depends on the form of the spectrum used to estimate S_{rms} .

As described in IP, $p_B(\Sigma_p)$ appears to increase dramatically with ξ ; furthermore, at frequencies $2\Sigma_p$ and $2.5\Sigma_p$ the corresponding $p_B(2\Sigma_p)$ and $p_B(2.5\Sigma_p)$ distributions lie below the $p_B(\Sigma_p)$ curve and vary slowly with c_p/u_* (u_* being the wind friction velocity), in agreement with the Banner et al. (2002) results. The latter authors have also explored the behavior of $p_B(\omega_p)$ distribution with the saturation function, $\sigma_f(\omega)$, which in terms of non-dimensional frequency, Σ , is given

as: $\sigma_f(\Sigma) \left[= (2g^2)^{-1} (\Sigma \alpha^{1/2} \omega_o)^5 S(\Sigma \alpha^{1/2} \omega_o) \right]$. Banner et al (2002) found that $p_B(\omega_p)$ increases

rather linearly in various $\sigma_f(\omega)$ regions, slower in the lower $\sigma_f(\omega)$ value region and more abruptly in the higher $\sigma_f(\omega)$ value region. The behavior of $p_B(\Sigma_p)$ distribution with $\sigma_f(\Sigma)$ is also explored in this study.

3a. Local maximum and average wave slope aspects

Combining the local limiting amplitude, h_o , with the corresponding wave number, it is possible to derive an expression for the local maximum slope, $S_{max}(\Sigma)$, at the corresponding frequency, Σ . As described in IP, these local slopes are reduced considerably, by the influence of surface drift, at frequencies remote from the spectral peak. Neglecting drift current effects, near the spectral peak, the maximum slope, at Σ_p , maybe written as: $S_{max,p} = S_{max}(\Sigma_p) \cong f/(2\alpha_i)$; here f is a function that accounts for the non-linearity of the wave field, and α_i is a constant that expresses the fact that a wave breaks (at the crest) when the real downward Lagrangian acceleration, a_i , reaches a value close to $0.39g$ (not $0.5g$). Various expressions for f have been provided by Longuet-Higgins (1975) and Longuet-Higgins and Fox (1978), and are summarized in IP. For $\xi \leq \xi_{max} = 0.0353$, $S_{max,p}$ remains ≤ 0.4432 . Since $S_{max,p} \cong f/(2\alpha_i)$, this

maximum slope appears to increase, with increasing ξ , from about 0.235 to 0.443 (when $\alpha_1 \approx 1.39$), consistent with field observations. It is noted that both Muller et al. (2005, cf. their Fig. 9) and Donelan and Magnusson (2005) have used as a critical steepness, $(ak)_{cr}$, for breaking waves (at the crest of a group envelope) the value of 0.3. Low overall steepness, ξ , may also reduce the maximum real acceleration, a_L , that an individual wave crest can reach, before it breaks, and thus lowers the local limiting slope, $S_{max}(\Sigma)$, at a particular frequency.

The breaking probability, $p_B(\Sigma_p)$, as a function of an overall wave steepness (say ξ), may also be obtained in terms of the local slope at the spectral peak frequency, $S_p = S(\Sigma_p)$, by estimating the probability of exceedance, $p(S_p > S_{max,p})$, of the local maximum slope there, $S_{max,p} =$

$S_{max}(\Sigma_p)$, namely: $p(S_p > S_{max,p}) = \int_{S_{max,p}}^{\infty} p(S_p) dS_p$. For accomplishing that, it is necessary to

estimate first the local maximum slopes, $S_{max}(\Sigma)$. These slopes, near the spectral peak (where the influence of surface drift is rather small), are given as: $S(\Sigma) = 2\sqrt{2}\pi\xi\Sigma^2(\Sigma^2H)$. Therefore, at the spectral peak: $S_p = S(\Sigma_p) = 2\sqrt{2}\pi\xi H = c_1 H$, where $c_1 = 2\sqrt{2}\pi\xi$. Hence, it follows that $S_{max,p} = S_{max}(\Sigma_p) = 2\sqrt{2}\pi\xi H_{o,p} = c_1 H_{o,p}$, where $H_{o,p}$ is the limiting normalized crest height at Σ_p . Following the rules of probability transformation, it is found that:

$$p(S_p) = c_1^{-1} p(H) \Big|_{H=c_1^{-1}S_p}, p(S_{max,p}) = c_1^{-1} p(H) \Big|_{H=c_1^{-1}S_{max,p}}, p(c_1^{-1}S_p) = p(H) \Big|_{H=c_1^{-1}S_p},$$

$$p(c_1^{-1}S_p) = c_1^{-1} [F(B_m)/(\theta+1)] 2(c_1^{-1}S_p) \exp(-c_1^{-2}S_p^2) \text{ and here } B_m = (S_p/c_1)(\theta^2-1)^{1/2}.$$

The average slope, $(kh)_{av}$, characterizing a wave field is obtained now by combining the average amplitude, h_{av} , and the wave number at the spectral peak frequency, k_p . In terms of ξ , $(kh)_{av}$ is written as: $(kh)_{av} = 2\sqrt{2}\pi\xi H_{av} = 8.886\xi H_{av}$. The average slope plays an important role in premature breaking, a concept that has also been described in IP. This premature breaking attribute, and its contribution in forming new unified breaking criteria, are further explored and utilized in this study, as described in section 5.

3b. Rogue wave occurrence and wave breaking relation

The common physical framework that rogue wave formation and the onset of wave breaking share is the energy focusing within non-linear wave groups. Frequently, a question arises as to what differentiates wave breaking from rogue waves. It appears that unidirectionality and directionality effects provide the link and/or the separating boundary between the two sides of the same generic mechanism, the non-linear (wave-wave) interactions within wave group structures. Other related questions that arise are: what are the occurrence rates of such steep waves (rogue waves, that is) and when do they break, whether the statistical joint distribution model of IP can be used to obtain the probability of occurrence of rogue waves, and whether the latter probability is less than $p_B(\Sigma_p)$, as indicated from field observations (Banner et al. 2002). Answers to these questions maybe provided with the aid of $p(H)$, $p(\Sigma|H)$ or $p(H|\Sigma)$ distributions, given previously. More specifically, taking into account the rogue wave definitions, in terms of either H_h or H_c , it is possible to evaluate the quantities: a) $p_B(\Sigma_p)$, b)

$p(H > 1.25H_s^n)$, c) $p_{orw}(\Sigma_p) = \int_{H_{cr}}^{\infty} p(H|\Sigma) dH \Big|_{\Sigma=\Sigma_p}$, d) $B_{orw,av} = \int_{H_{cr}}^{\infty} \int_0^{\infty} p(H|\Sigma) d\Sigma dH$ and e)

$p(H > H_{cr,b}) = \int_{H_{cr,b}}^{\infty} p(H)dH$. Here, $H_{cr} = n H_s^n$, $H_s^n (=2\sqrt{2})$ is the normalized significant wave height (using our definition of normalization), and $n = 0.0, 0.1, 0.2, \dots, 3.0$, Definitions of $H_{cr, b}$ are given in section 4.

4. Breaking of rogue waves

As described before, breaking of the spectral peak occurs when the local maximum slope $S_p > S_{max,p} \{ \cong f/(2\alpha_1) \}$, or alternatively when the limiting amplitude there $H_{o,p}$ exceeds the threshold value $H_{cr,b}^{ip} (\cong (4\sqrt{2}\pi\alpha_1\delta)^{-1} f$ (see also IP). Combining the arguments of Donelan and Magnusson (2005) and the results of IP expressing $S_{max,p}$ as above, and taking into account that the breaking rogue wave slope limit of 0.3 is well within the limits of $S_{max,p}$ variation (between 0.235 and 0.443), it follows that: $\pi H_{o,h} / \lambda_p \geq f / (2\alpha_1)$, $\pi H_s / \lambda_p = 0.1 (c_p / U_{10})^{0.35}$; here $H_{o,h}$ represents the height of a breaking rogue wave. Thus: $H_{o,h} / H_s \geq 10 [f / (2\alpha_1)] (c_p / U_{10})^{0.35}$. It is interesting to note that the application of the latter expression, with $c_p / U_{10} = 1.2$ or 0.3 (or less), yields $H_{o,h} / H_s \approx 4.5$ and 1.7, respectively. This implies that for mature wave fields, the wave height for breaking, $H_{o,h}$, must become very large (i.e. $> 4.5H_s$) compared to that required for less mature or young (and rather choppy, 3-D) waves for which $H_{o,h}$ needs to only exceed $1.7H_s$, a very sensible result. In terms of the significant slope, it appears that δ must exceed the values 0.03 and 0.074, respectively {when $\delta \cong 3.31 \times 10^{-2} (c_p / U_{10})^{-0.35}$ }. Using the normalization suggested by IP, for both $H_{o,h}$ and H_s , the non-dimensional limiting crest amplitude is written as: $H_{cr,b}^{dm} = 10\sqrt{2} \cdot (f / (2\alpha_1)) \cdot (c_p / U_{10})^{0.35}$ Both expressions of $H_{cr,b}^{ip}$ and $H_{cr,b}^{dm}$, characterizing the limiting amplitude of rogue waves, have been used in this study.

5. Breaking criteria. A revisit

The investigations of Wu and Yao (2004) and Wu and Nepf (2002) have added new insights, with respect to the breaking criteria that Phillips (1977) and Longuet-Higgins (1969) had suggested much earlier for spilling breaking and other types of wave breaking, in the presence or absence of swell. Among the three categories of breaking criteria used, namely the kinematic, dynamic, and the slope (or geometric) criterion, it appears that the kinematic one is the most fundamental. The dynamic criterion is also related to the maximum slope concept. It appears that the slope breaking criterion is related to other limiting (or maximum) average slope concepts (as described in IP). According to older field observations (Lake and Yuen, 1978), the average slope of a wave field, locally, cannot exceed the upper limit of about 0.28, that is: $(kh)_{av} = 2\sqrt{2}\pi\delta H_{av} = 8.886 \delta H_{av}(\theta) \leq 0.28$, although some other authors (e.g., Hsu et al. 1982) have argued that in non-linear bound wave fields this threshold may reach higher values, up to about 0.32. In summary, the breaking criteria, modified by the surface drift current effects and the non-linearity of the wave field expressed by f , have as follows:

$$\text{Kinematic: } \gamma c \leq u_{orb}^c + q_c \tag{4}$$

$$\text{Dynamic: } S_p > S_{max,p} \left\{ = a_L / g = f / (2\alpha_1) \text{ or } S_{max,p} = (f / 2\alpha_1) \left[1 - \alpha_o (c_p / u_*)^{-1} \right]^2 \right\} \tag{5(a, b, c)}$$

$$\text{Average slope: } S_{av} = 2\sqrt{2}\pi\delta H_{av}(\theta) \leq 0.28 \tag{6}$$

Here, q_c is the value of surface drift at the wave crest, and the coefficient α_o expresses the ratio of Eulerian surface drift and u_* , being of $O(0.5)$. The constant γ may take either of the following values: 1, 0.5, 0.75, or 1.5 depending on the type of breaking examined (e.g., spilling, plunging, etc.), and on whether the orbital velocity (at the wave crest), u_{orb}^c , on the RHS of the first inequality is compared with the phase velocity, c , or with the group velocity, C_g . Phillips (1977) and Longuet-Higgins (1969) has suggested $\gamma = 1$, for spilling breakers, whereas Wu and Yao (2004) have suggested $\gamma = 0.5$ (as $C_g = 0.5c$). On the other hand, Wu and Nepf (2002) have suggested $\gamma = 1.5$ for plunging breakers. The kinematic condition (1), with the aid of an expression providing the distribution of drift current along the mean wave profile (see also IP), leads to the determination of a critical frequency, ω_{cr} , above which all waves break, viz.: $\omega_{cr} / \omega_p = \gamma \left[1 - \left[(1 - ak)^2 - \gamma_1(2 - \gamma_1) \right]^{1/2} \right]^{-1}$, where: $\gamma_1 \approx 0.03(U_{10}/c_p)$ or $\approx \alpha_o (c_p / u_*)^{-1}$.

For $\omega_{cr} = \omega_p$, breaking of the dominant wave occurs and: $1 - \left[(1 - ak)^2 - \gamma_1(2 - \gamma_1) \right]^{1/2} = \gamma$.

Thus, in our formulation: $\gamma \leq 1$. In other words, for plunging breakers, u_{orb}^c must refer to the group velocity. Therefore, γ should have the value $0.5 \times 1.5 = 0.75$.

As mentioned before, the concept of limiting average slope leads to the notion of premature wave breaking, or stated it differently, for any given sea state (characterized by ξ , and/or U_{10}/c_p), a new local maximum slope $\xi_{max}^o \left[= 0.28 / \{2\sqrt{2}\pi\xi H_{av}(\theta)\} = 0.0315 H_{av}^{-1}(\theta) \right]$ can be obtained which, if exceeded, will cause the wave field to prematurely break, even if ξ (the slope characterizing the original sea state) is less than $\xi_{max} = 0.0356$; ξ_{max}^o cannot exceed the corresponding Stokes limit $\xi_{max}^s = 0.0505$. H_{av} is calculated {in the form of function $F_1(\theta)$, as described in IP} from knowledge of the wave spectrum. In this study, the spectral form proposed by Donelan et al. (1985), and slightly modified by Banner (1990), is used to estimate m_0, m_2 and m_4 , and hence θ , for selected values of either ξ and/or U_{10}/c_p , although other forms of the sea spectrum could also used for these calculations; ξ and/or U_{10}/c_p appear to be important parameters that characterize a given sea state. In the absence of swell, it is also possible to select only the value of U_{10}/c_p (perhaps, in the range proposed by Donelan et al. 1985) and then compute ξ from a chosen $\xi - U_{10}/c_p$, as that described above.

For a selected U_{10}/c_p value, ξ and the slope $B_{ef} = 4\pi\xi$ are estimated, γ_1 is examined whether it remains less or greater than: $1 - [B_{ef}(2 - B_{ef})]^{1/2}$ and proper values of both $\alpha_1 \{ = (f/2)(a_L/g) \}^{-1}$ and of $(ak)_{cr} \{ = B_{ef,cr}/c_p \}$ are determined as functions of f , γ and γ_1 ; $(ak)_{cr}$ expresses the maximum slope that a wave field can sustain for a given sea state. More specifically, if:

$$\text{A.} \quad \gamma_1 < 1 - [B_{ef}(2 - B_{ef})]^{1/2} \quad ; \quad a_L / g = 1 - \{(1 - \gamma)^2 + \gamma_1(2 - \gamma_1)\}^{1/2}$$

$$\alpha_1 = (f/2) \left[\{(1 - \gamma)^2 + \gamma_1(2 - \gamma_1)\}^{1/2} \right]^{-1}, \quad (ak)_{cr} = 1 - \{(1 - \gamma)^2 + \gamma_1(2 - \gamma_1)\}^{1/2} \quad 7(a, b, c)$$

Valid for: $\gamma_1 \leq 2$

$$\text{B.} \quad \gamma_1 > 1 - [B_{ef}(2 - B_{ef})]^{1/2} \quad ; \quad a_L / g = \left[2 + \gamma - \gamma_1 - \left[(2 + \gamma - \gamma_1)^2 - 2(1 + \gamma - \gamma_1)^2 \right] \right]^{1/2}$$

$$\alpha_1 = (f/2) \left[\left[2 + \gamma - \gamma_1 - \left[(2 + \gamma - \gamma_1)^2 - 2(1 + \gamma - \gamma_1)^2 \right] \right]^{1/2} \right]^{-1}$$

$$(ak)_{cr} = 0.5 \left[2 + \gamma - \gamma_1 - \left[(2 + \gamma - \gamma_1)^2 - 2(1 + \gamma - \gamma_1)^2 \right] \right]^{1/2} \quad 8(a, b, c)$$

Valid for: $\gamma_1 \leq 2$ and $\gamma - \sqrt{2} < \gamma_1 < \gamma + \sqrt{2}$

In both cases, B_{ef} and U_{10}/c_p should remain bound, viz.: $B_{ef} \leq 0.4432$ and $U_{10}/c_p \leq 66.67$. For $0.17 \leq \gamma_1 \leq 1.87$ or $5.7 \leq U_{10}/c_p \leq 61$, both of the inequalities: $1 - \{\gamma_1(2 - \gamma_1)\}^{1/2} \leq 0.4432$ and $\gamma - \sqrt{2} < \gamma_1 < \gamma + \sqrt{2}$ hold (for $\gamma = 0.5, .075, 1.0$). These relationships suggest that the local maximum steepness $(ak)_{cr}$ of rogue (or freak) waves maybe a function of the spectral bandwidth θ , as the latter is a function of ξ , provided that ξ and γ_1 are interrelated. This finding is consistent with the results of Wu and Yao (2004, cf. their Fig. 7) which show the decreasing trend of $(ak)_{cr}$ with increasing sea bandwidth. The results also suggest that α_1 is not a universal constant but a coefficient related to the maximum wave slope concept, in agreement with the findings of Longuet-Higgins (1986, 1985). The variation of a_L/g , with sea state, also indicates the a_L accelerations attained at the crest of large waves, under extreme conditions. Jenkins (2000) supports the idea that these accelerations may not exceed 0.5g (when the waves break), in contrast to the much larger values indicated by Fochesato et al. (2007). Yet, the former author claims that these large values represent the centripetal acceleration developed during the whirling around stage of the (plunging or projected) crest tip before it touches the forward face of the wave again (also Jenkins 2008-personal communication). Such explanation may imply that these large accelerations (of about 5-6g), reported in the literature, somehow resemble the upward trough accelerations, which according to Longuet-Higgins (1994, 1986, 1985) calculations may become unlimited. The loop under the crest of a wave (where a large acceleration develops), maybe thought of as a kind of wave trough. In shallow waters, because the breaking wave geometry is affected by wave directional spreading and focusing, it is possible that overturning rogue waves may have different properties depending on whether they are in the focusing or defocusing phase, at the breaking onset, a situation largely controlled by the maximum focusing angle and the water depth (Fochesato et al. 2007).

6. Probabilities of rogue wave occurrence and of breaking

These occurrence probabilities, and an average probability that characterizes the presence of rogue waves may be computed from the following relations:

$$p(H > H_{cr}) = \int_{H_{cr}}^{\infty} p(H)dH, \quad p_{orw}(\Sigma_p) = \int_{H_{cr}}^{\infty} p(H|\Sigma)dH \Big|_{\Sigma=\Sigma_p}, \quad B_{orw,av.} = \int_{H_{cr}}^{\infty} \int_0^{\infty} p(H|\Sigma)d\Sigma dH$$

The breaking probability of rogue waves is estimated by: $p(H > H_{cr,b}) = \int_{H_{cr,b}}^{\infty} p(H)dH$. Fur-

thermore, in order to conform with the max average slope restriction, at a given ξ , ξ_{max}^{θ} is calculated and examined as to whether it remains $\leq \xi_{max}^s$. If the initial $\xi \{=\xi(\theta)\}$ remains $\leq \xi_{max}^{\theta}$, the limiting amplitude $H_{cr,b}$ (at ω_p), corresponding to the initial ξ and the calculated f and α_1 values, is estimated. Yet, if $\xi(\theta) > \xi_{max}^{\theta}$, $\xi = \xi_{max}^{\theta}$ is set and a new value of $B_{ef,n}$ ($= 4\pi\xi_{max}^{\theta}$) is calculated and used for examining whether $B_{ef,n}$ satisfies the inequality of case A or case B. Using ξ_{max}^{θ} , a new value of f is estimated and another α_1 is obtained for use with $H_{cr,b}$, etc.

7. Results

Figure 1 shows the distribution of exceedance probability $p(H > H_{cr})$ against the numerical factor n (now in the range: $0 \leq n \leq 1.5$), with θ as a parameter. Figure 2 shows similar results for $p_{orw}(\Sigma_p)$. Figure 3 shows the exceedance probabilities $p_n(n)$ vs. n , estimated with the aid of C_4 , as suggested by Janssen (2003). Here: $p_n(n) = p(H_h > H_{cr,h}) = e^{-2n^2} [1 + C_4 B_H(n)]$,

$H_{cr,h} = 2H_{cr}$, $B_H(n) = 2n^2(n^2 - 1)$. Note that the (normalized) limiting wave height is given by: $H_{cr,h} = 2nH_s^n (= 4\sqrt{2}n)$, where now $n = 0, 1, 2, 3, 4$ or 5). On the side of this study, and for interpreting better the results obtained, the variation of θ with U_{10}/c_p is also shown in Figure 4. Figures 5(a, b, c) show the distributions of $p_B(\Sigma_p)$ vs. S_{rms} , or vs. the saturation function $\sigma_f(\Sigma)$ or vs. θ , with ξ as a parameter. Figure 6(a) shows the distribution of $p(S_p)$ as a function of inverse wave age, U_{10}/c_p , whereas Figures 6(b, c) show the exceedance probability $p(S_p > S_{p,max})$ vs. U_{10}/c_p or vs. θ , with ξ as a parameter. Figure 7 shows the breaking probabilities of extreme waves against U_{10}/c_p . Finally, Figures 8(a, b) show the variation of C_4 and BFI vs. U_{10}/c_p , whereas Figure 8c shows the variation of BFI vs. θ ; C_4 is calculated from the BFI, whereas the latter index is estimated with the aid of Goda's peakedness factor, Q_p , that can be expressed in terms of sea spectrum, viz.: $BFI = 2\pi\sqrt{2\pi}\xi Q_p$, $Q_p = (2/m_o^2) \int_0^\infty \omega S^2(\omega) d\omega$, $C_4 = (\pi/3\sqrt{3})BFI^2$.

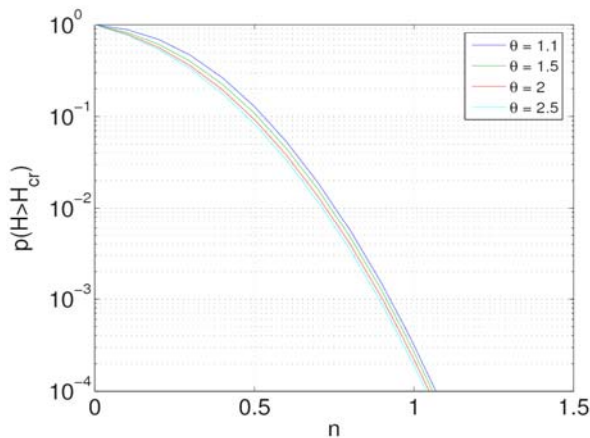


Fig. 1: Exceedance probability of crest height, using the marginal $p(H)$ density.

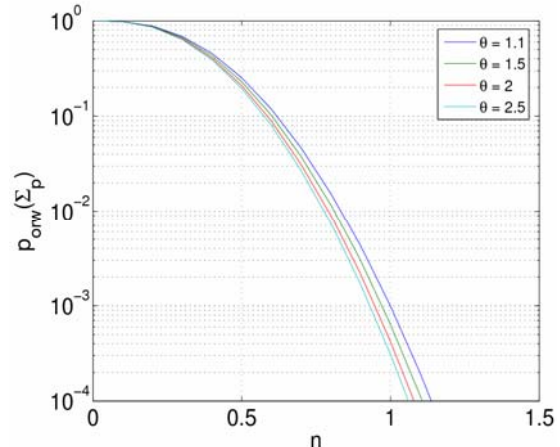


Fig. 2: Exceedance probability of crest height, using the conditional amplitude density.

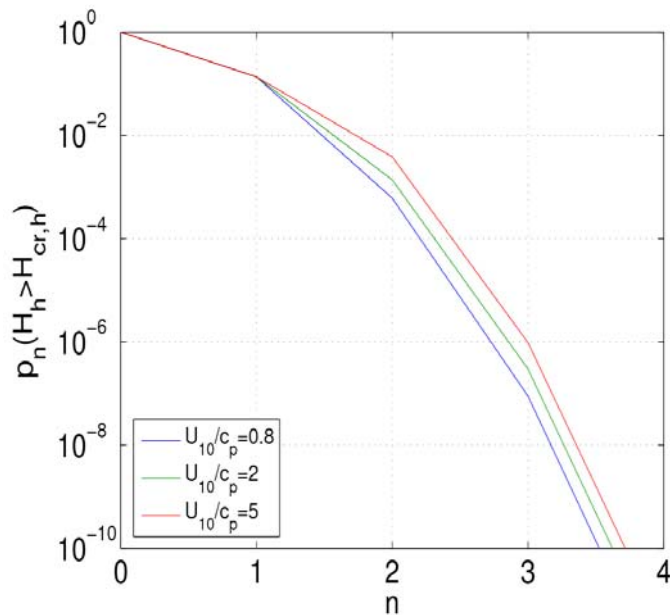


Fig. 3: Exceedance probability of wave height with the aid of C_4 for various U_{10}/c_p values.

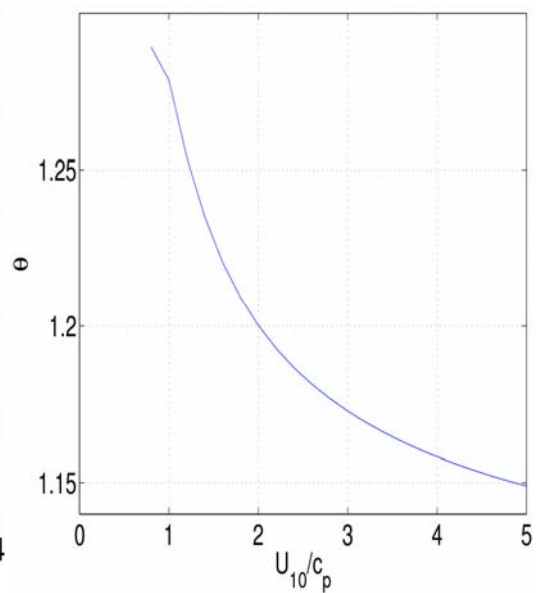


Fig. 4: Variation of θ against U_{10}/c_p .

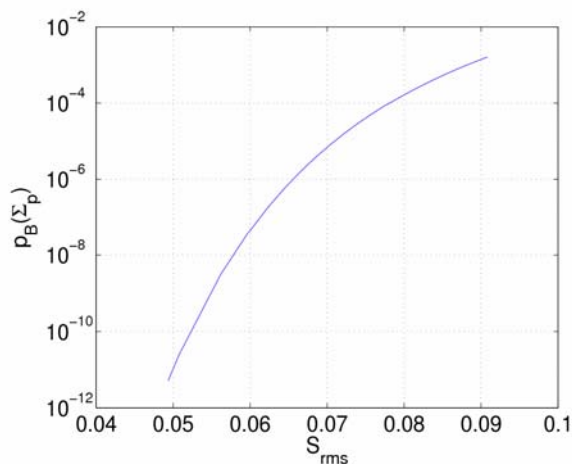


Fig. 5a: Probability of dominant wave breaking vs. the rms sea surface slope.

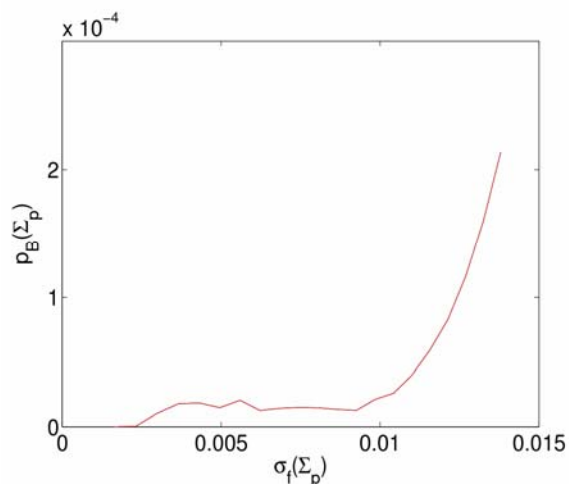


Fig. 5b: Probability of dominant wave breaking the saturation function.

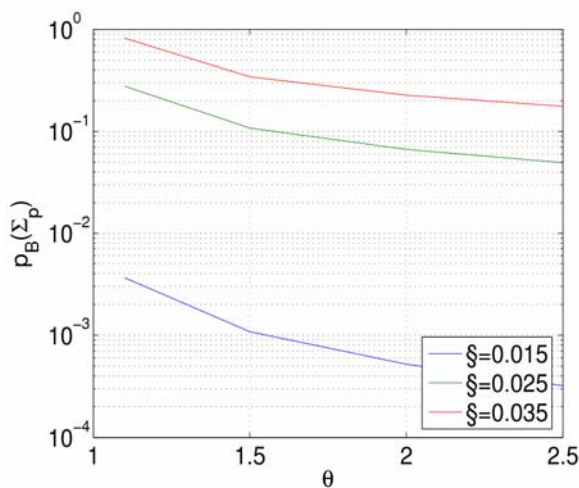


Fig. 5c: Probability of dominant wave breaking vs. sea surface bandwidth.

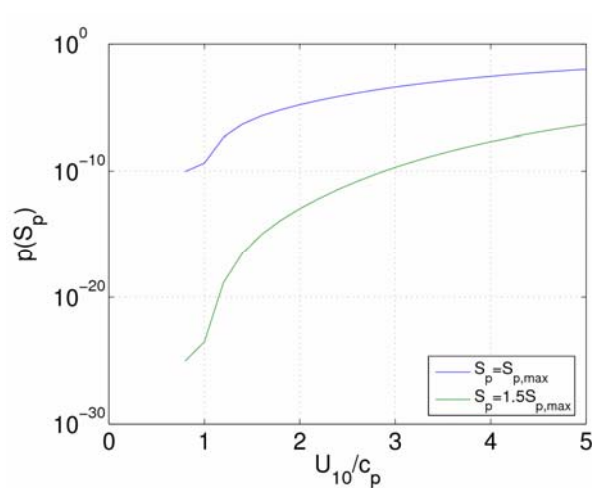


Fig. 6a: Probability distribution of peak slope, S_p , vs. the inverse wave age U_{10}/c_p .

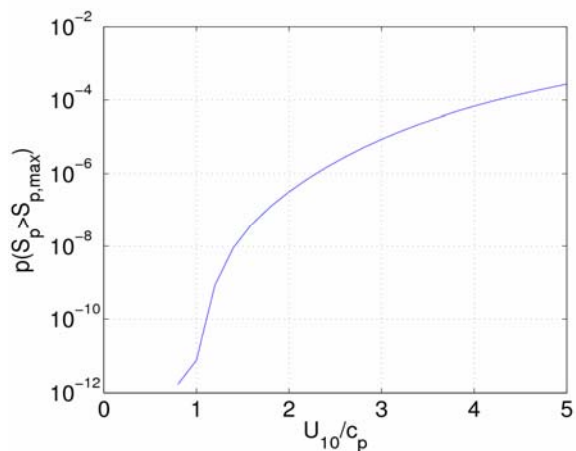


Fig. 6b: Exceedance probability of S_p vs. U_{10}/c_p .

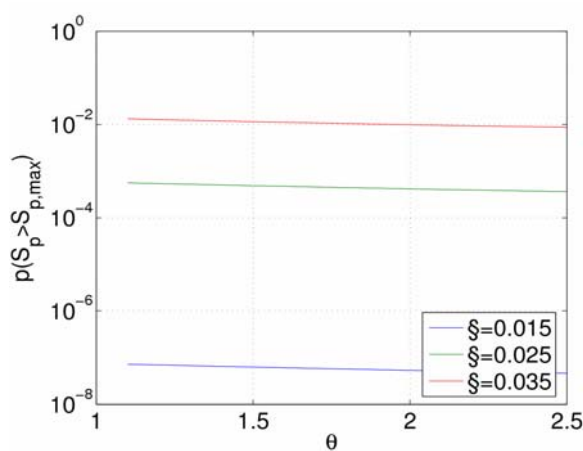


Fig. 6c: Exceedance probability of S_p vs. θ , with ξ as a parameter.

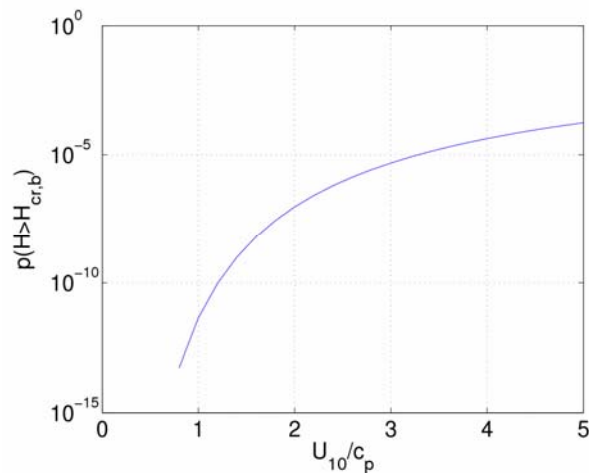


Fig. 7: Probability of rogue wave breaking vs. U_{10}/c_p .

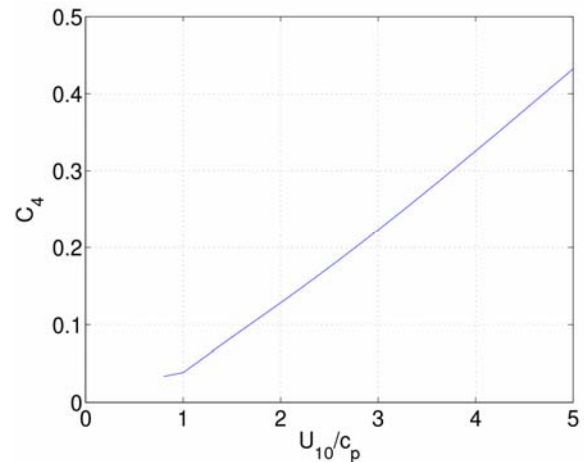


Fig. 8a: Distribution of kurtosis coefficient C_4 vs. U_{10}/c_p .

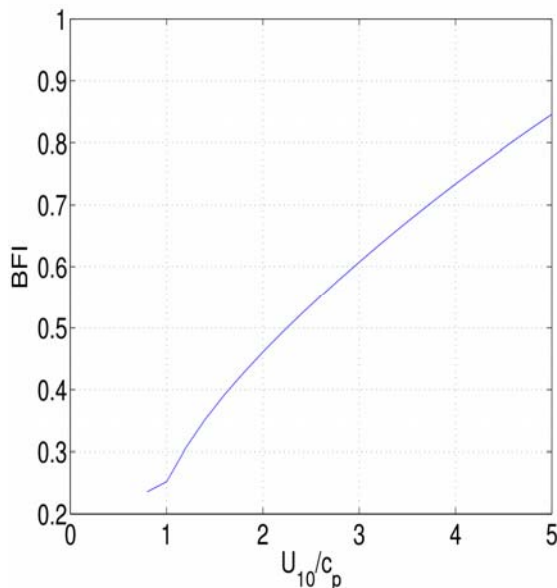


Fig. 8b: Variation of BFI against U_{10}/c_p .

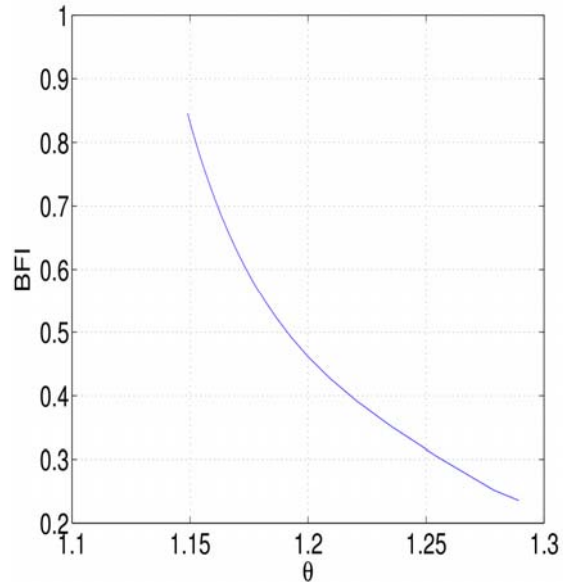


Fig. 8c: Variation of BFI against θ .

8. Concluding remarks

As seen from the various Figures, the statistical model of IP predicts the occurrence and breaking of extreme waves as a function of sea state, expressed in various ways (either by U_{10}/c_p or ξ , or by both, or θ , etc.). The model provides the right variation of key parameters associated with the occurrence of extreme waves, such as BFI and C_4 , with the sea state expressed by the above parameters. The model also yields the right variations of $p_b(\Sigma_p)$ with both $\sigma_f(\Sigma)$ and other parameters (S_{rms} , θ), in agreement with the Banner et al. (2002) and IP results. It also provides the breaking probabilities of extreme (rogue) waves.

The breaking probabilities of dominant waves and of rogue waves are estimated based on a new breaking criterion that unifies kinematic, dynamic and premature breaking concepts. With the above information available, the role of meteorological focusing in generating conditions producing rogue waves can be explored now in the Mediterranean basin, using a family of fully directionally resolved spectra wave models and reliable wind vector forecasts as well (as was done by Donelan and Magnusson, 2005 for the Atlantic ocean). Such work is in progress and, due to space limitation, it will be reported elsewhere in the future.

References

- Banner, M.L. (2005) Rogue waves and wave breaking-How are these phenomena related? *Proc. of 14th Aha Huliko'a Hawaiian winter workshop 2005*, 119-122.
- Banner, M.L., Geemrich, J.R. and Farmer, D. (2002) Multiscale measurements of ocean wave breaking probability. *J. Phys. Oceanogr.*, **32**, 3364-3375.
- Banner, M.L., Babanin, A.V., Young, I.R. (2000) Breaking probability for dominant waves on the sea surface. *J. Phys. Oceanogr.*, **30**, 3145-3160.
- Donellan, M.A. and Magnusson, A.K. (2005) The role of meteorological focusing in generating wave conditions. *Proc. of 14th Aha Huliko'a Hawaiian winter workshop*, 139-145.
- Donelan, M.A., Hamilton, J. and Hui, W.H. (1985) Directional spectra of wind-generated waves. *Phil. Trans. Royal Soc. London*, **A(315)**, 509-562.
- Donelan, M.A., Longuet-Higgins, M.S., Turner, J.S. (1972) Whitecaps. *Nature*, **239**, 449-451.
- Dysthe, K., Krogstad, H.E. and Muller, P. (2008) Oceanic rogue waves. *Annu. Rev. Fluid Mech.*, **40**, 287-310.
- Fochesato, C., Grilli, S. and Dias, F. (2007) Numerical modelling of extreme rogue waves generated by directional energy focusing. *Science Direct, Wave Motion*, 395-416.
- Janssen (2005) Nonlinear four-wave interactions and freak waves. *Proc. of 14th Aha Huliko'a Hawaiian winter workshop 2005*, 85-90.
- Janssen, P.A.E.M. (2003) Nonlinear four-wave interactions and freak waves. *J. Phys. Oceanogr.*, **33**, 863-884.
- Jenkins, A. (2000), Geometrical and kinematic properties of breaking waves in the framework of a stationary flow approximation. *Rogue waves 2000*, M. Olagnon and M. Athanassoulis (Eds.), Brest 29-30 November, 221-226.
- Gemmrich, J. (2005) On the occurrence of wave breaking. *Proc. of 14th Aha Huliko'a Hawaiian winter workshop 2005*, 123-130.
- Hsu, C.T., Wu, H.Y., Hsu, E.Y. and Street, R.L. (1982) Momentum and energy transfer in wind generation of waves. *J. Phys. Oceanogr.*, **12**, 929-951.
- Lake, B.M. and Yuen, H.C. (1978) A new model for non-linear wind waves. Part 1. Physical model and experimental evidence. *J. Fluid Mech.*, **88**, 33-62.
- Longuet-Higgins, M.S. (1986) Eulerian and Lagrangian aspects of surface waves. *J. Fluid Mech.*, **173**, 683-707.
- Longuet-Higgins, M.S. (1985) Accelerations in steep gravity waves. *J. Phys. Oceanogr.*, **15**, 1590-1985.
- Longuet-Higgins, M.S. and Fox, M.J.H. (1978) Theory of the almost highest wave. Part 2. Matching and analytic extension. *J. Fluid Mech.*, **85**, 769-786.
- Longuet-Higgins, M.S. (1975) Integral properties of periodic gravity waves of finite amplitude. *Proc. R. Soc. London*, **A(342)**, 157-174.
- Longuet-Higgins, M.S. (1969) On wave breaking and equilibrium spectrum of wind. *Proc. R. Soc. London*, **A(310)**, 151-159.
- Muller, P., Garret, C. and Osborne, A. (2005) Rogue waves. The fourteenth Aha Huliko'a Hawaiian winter workshop. *Oceanography I*, **18(3)**, 66-75.
- Papadimitrakis, I. (2005) On the probability of wave breaking in deep waters. *Deep-sea Research Part II*, **52**, 1246-1269.
- Phillips, O.M. (1977) The dynamics of the upper ocean. Cambridge Univ. Press.
- Wu, C.H. and Yao, A. (2004) Laboratory measurements of limiting freak waves on currents. *J. Geophys. Res.*, **109**, C12002, doi: 10.1029/2004JC002612, 18 pp.
- Wu, C.H. and Nepf, H.M. (2002) Breaking criteria and energy losses for three-dimensional wave breaking. *J. Geophys. Res.*, **107**, C10, 3177, doi: 10.1029/2001JC001077, 41-1 to 41-18.

Freak wave as a multivariable extreme (approach to estimation)

Leonid Lopatoukhin¹, Alexander Boukhanovsky²,

1 - St Petersburg State University, Dep. Oceanology,

2 - St Petersburg State University of Information
Technology Mechanics and Optics,

One of the most interesting extreme phenomenon is freak (or rogue) waves. Physical hypotheses of freak wave generation allow their arising in any place of an Ocean. Any metocean event described by a system of nonlinear thermo hydrodynamic equations possesses their own freaks. There is no common definition of a freak wave. The most simple is, that the wave with the height $h > 2h_s$ is freak. In this case of Rayleigh wave height distribution such a wave will be one from 3000. With the mean period 10s, such a wave will arise every 8 hours. It seems, that even the condition $h > 2.5h_s$ is too weak. Therefore, additional criteria concerns the wave form and it position among other waves are introduced. Freak waves have to posses some principal difference from extreme wave. Freak wave is unusual not by the height, but also by the form. This uncommonness specified by means set of parameters; e.g., $h > 2.4h_s$, $\text{crest} > 0.65h$, unusual steepness δ of a wave and (or) it front or back slope, deep trough (twice as greater than preceding and subsequent waves), etc. Not all of these parameters are realized simultaneously.

The approach regarded freak wave as multivariable random event is needed. As the first approach two dimensional version of BOLIVAR (see: World Meteorological Organisation WMO/TD-No. 1041, 2000, JCOMM Technical Report) method is used. The background of this method is a set of stochastic models for short-term, annual, synoptic and year-to-year variability of waves. The details of approach, comparison with other methods and known freak wave records will be presented.

Numerical study of the sea state in the Kuroshio Extension region at the time of an accident

Hitoshi Tamura¹, Takuji Waseda^{1,2} and Yasumasa Miyazawa¹

1 Frontier Research Center for Global Change/JAMSTEC
2 Department of Environmental & Ocean Engineering/The Univ. of Tokyo

In the past few decades, a number of vessels have been shipwrecked in the Kuroshio Extension (KE) region, which is notorious for the occurrence of freak waves. Our aim was to investigate the sea state at the time of an accident in this region. We were particularly interested in the effect of ocean currents on wave statistics and the probability of freak waves in realistic situations. We therefore investigated the results of a hindcast simulation produced by a third-generation wave model based on WAVEWATCH III. We implemented the SRIAM method (Komatsu and Masuda, 1996) for efficient and accurate computation of the nonlinear energy transfer function. In addition, we used reanalysis data from the Japan Coastal Ocean Predictability Experiment (JCOPE) to specify the states of the Kuroshio and Kuroshio Extension. The wave model was driven by 6-hourly wind stress estimated from the NCEP/GFS reanalysis, and the 1-day mean current field from the JCOPE.

We investigated a recent accident in the KE region. On June 23, 2008, the Suwa-Marun No. 58, a fishing boat with 20 crew members, encountered abnormal waves twice off Cape Inubosaki in the KE region, and sank approximately 10 minutes after being hit by the initial wave. At the time of writing, the Japan Coast Guard was still investigating the accident.

Our hindcast simulation indicated that the significant wave height could have reached over 3 m around the accident location (indicated by the white circle in Fig. 1). In addition, the wave spectrum was composed of a low-frequency swell from the Pacific and the southern part of Japan, and a high-frequency local component, implying that the wave field at the accident site included both wind waves and swell. Moreover, ocean current may have played a role, because a branch of the meandering Kuroshio may have influenced the sea state in the accident location. A detailed analysis of the sea state, including the spectral shape, is discussed in this presentation.

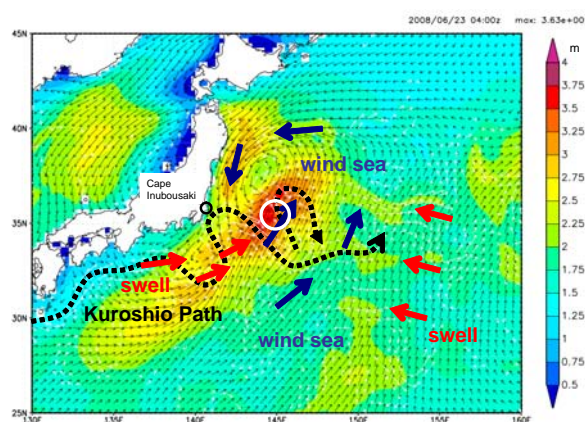


Fig. 1. Instantaneous plane view of the significant wave height and peak direction at the time of the accident. Black dotted line represents the Kuroshio path.

RISK ANALYSIS CONCENTRATED ON WAVE CREST KINEMATICS.

Søren Peter Kjeldsen
Trondheim Maritime Academy.
Ladehammerveien 6. – 7004 Trondheim. NORWAY.
E-mail: peter.kjeldsen@stfk.no

Abstract.

The present investigation deals with a risk analysis of two severe marine accidents, and associated model experiments in a wave tank. A numerical model is used to predict the kinematics in the crests of extreme breaking waves. A good knowledge of wave crest kinematics in these deep water plunging breakers is paramount for safety of lives at sea.

1. Introduction.

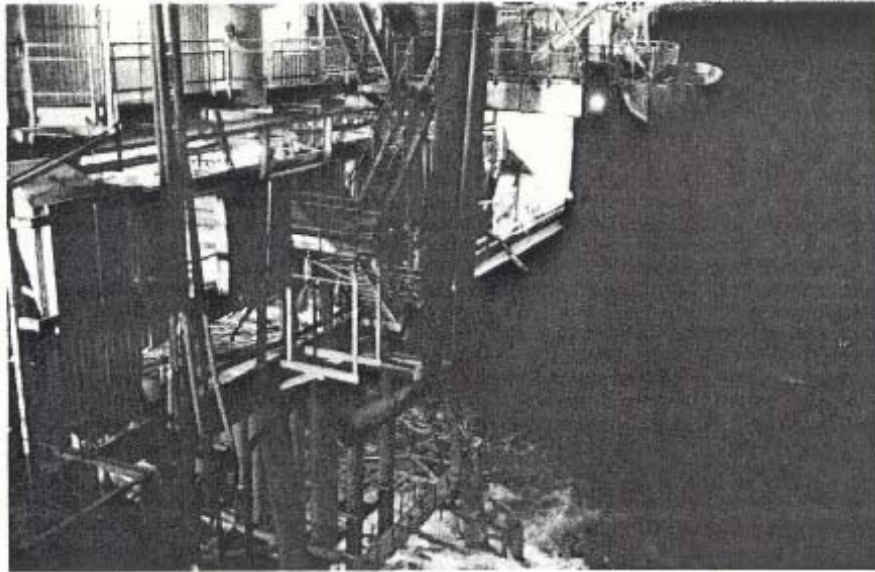
It turns out that the crest particle velocities in sea waves are the most important parameters to consider, even more important than extreme wave heights. In order to focus on crest particle velocities in a risk analysis, the start will be to estimate the probability of a certain sea state in a gale, and further to estimate the amount of breaking waves in this sea state. Actual measurements at sea or in model test tanks can be used to map the vertical distributions of both crest particle velocities, and crest particle accelerations. From such distributions several mathematical models can be used to predict the wave forces on fixed or floating marine structures. The resistance of marine structures to extreme wave forces, can be regarded as a time-dependend random variables, degraded by corrosion, marine growth in the water line and fatigue. Finally the probability of failure can be computed in the risk analysis. However several events of failure might occur at sea with equal probabilities, but the consequences of such failures will in many cases differ significantly. Thus in a risk analysis, also the consequences must be estimated and calculated for instance in terms of economic losses. The present publication deals with an analysis of 2 severe marine accidents, and the consequences of these accidents.

2. Velocities in Breaking Waves.

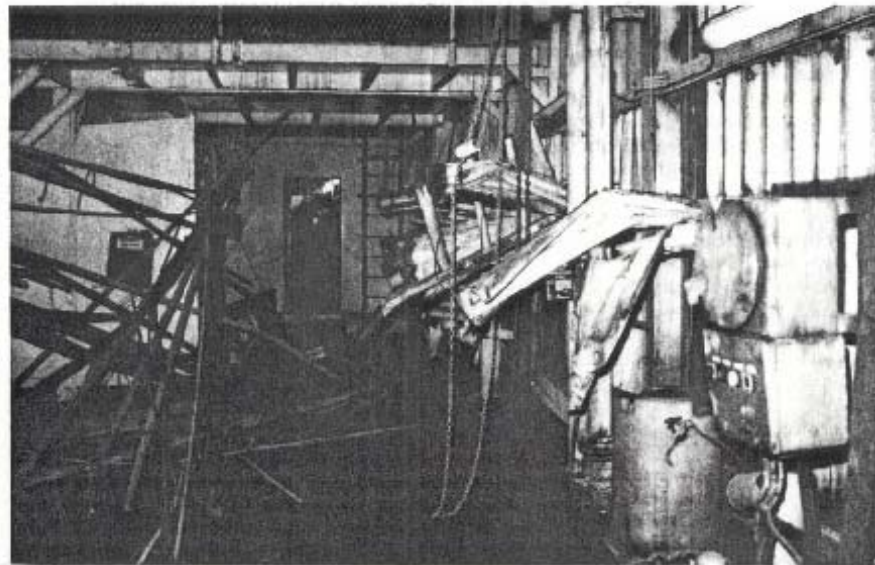
In Fig 1 the inception and further development of breaking is shown in a spilling breaker. Breaking waves in this “**SPILLING-mode**“, are very common both in deep and shallow waters. The breaking starts when the local crest particle velocity in the very top of the wave exceeds the wave phase velocity. Then a very small water jet is developed in the crest, and when this jet hits the front of the wave, air is entrained and a pattern of eddies and entrained air rolls further down on the front of the wave. It can be seen in Fig. 1, that the duration of breaking in such a spilling breaker is quite large. The experimental investigation described below showed, that inception of breaking in random generated irregular waves in deep waters could occur for wave steepnesses as low as: **$H/L = 0.05$** , where H is the wave height in front of the wave, and L is the wave length.



Fig. 1. Development of a spilling breaker.
From the FILM: "BREAKING WAVES" by Kjeldsen & Olsen.



. A freak wave removed a thin metal sheet above deck level at the 2/4-A platform at EKO-FISK. This Figure shows the typical situation viewed from outside.



View from inside.

Fig. 2. On the 3rd of January 1984 a high elevated freak wave hit the superstructure on the EKOFISK platform 2/4-A. (From KJELDSEN 1984.)

3. The Ekofisk Damage.

On the 3rd of January 1984 a high elevated freak wave hit the superstructure on the EKOFISK platform 2/4-A more than 20 m above the mean water level. The wave came from a direction different from the wind direction and hit the superstructure in a violent impact. This superstructure was not designed to resist wave forces. The result was that a very thin metal sheet was removed and the whole control room on the platform was flooded. The large horizontal steel beams supporting the deck was also bended. The damages are shown on Fig 2. All electricity was lost and oil production was stopped for a number of days, leading to economic losses. No people was hurt in this accident.

4. Experimental Investigation.

In order to map such wave forces on fixed and floating marine structures, a large experimental programme was performed by KJELDSEN, TØRUM & DEAN 1986 in the ocean basin at Marintek in Trondheim in Norway. The drag- and lift-forces in extreme waves were measured on a vertical column representing one of the legs on the EKOFISK steel jacket. The obtained results represent also the wave forces on the column on a floating semisubmersible platform, if relative motion is taken into account.

The experimental set-up was designed to measure shear forces and bending moments in the local zone from the lowest wave through up to the zone for the maximum run-up on the column above the top of the wave crest. 26 shear force transducers were installed in the vertical column. In addition two 3-axis current meters and 3 wave gauges were installed to measure the wave patterns and kinematics. These experiments were performed in irregular deep water waves with prescribed wave spectra. A total of 87 experiments were performed. Time series from the particular experiment, in which the maximum shear forces were measured are shown in Fig, 3. Here it can be seen that the largest forces were measured in a breaking wave **A** with a nearly vertical front, and not in the larger non-breaking wave **B**, that followed the breaking wave as wave number 2 in a wave group. It was further observed that this particular breaking wave developed as a plunging breaker in deep water. Violent wave impacts of short duration (a few milliseconds) were also measured on vertical steel plates in an additional experiment.

It is well known that such deep water waves breaking in the “**PLUNGING-Mode**” creates the largest forces on ships and the largest problems for their manoeuvres.

5. Numerical model of kinematics in breaking waves.

The offshore industry has used the Wheeler stretching method to predict wave kinematics above mean water level in non-breaking waves. However experiments have shown that this method predicts kinematics only in waves of low steepness. For more steep extreme waves, this method is not sufficient. In order to predict wave kinematics in very steep non-breaking waves, and in breaking waves in the “**PLUNGING-mode**”, a numerical model is developed, see KJELDSEN, VINJE, MYRHAUG, BREVIG 1980. This particular model is calibrated against experiments. A wave-wave interaction experiment showed that an interaction between only 2 waves was sufficient to generate a plunging breaking wave in deep water. An example of results obtained in the numerical model is shown in Fig 4.

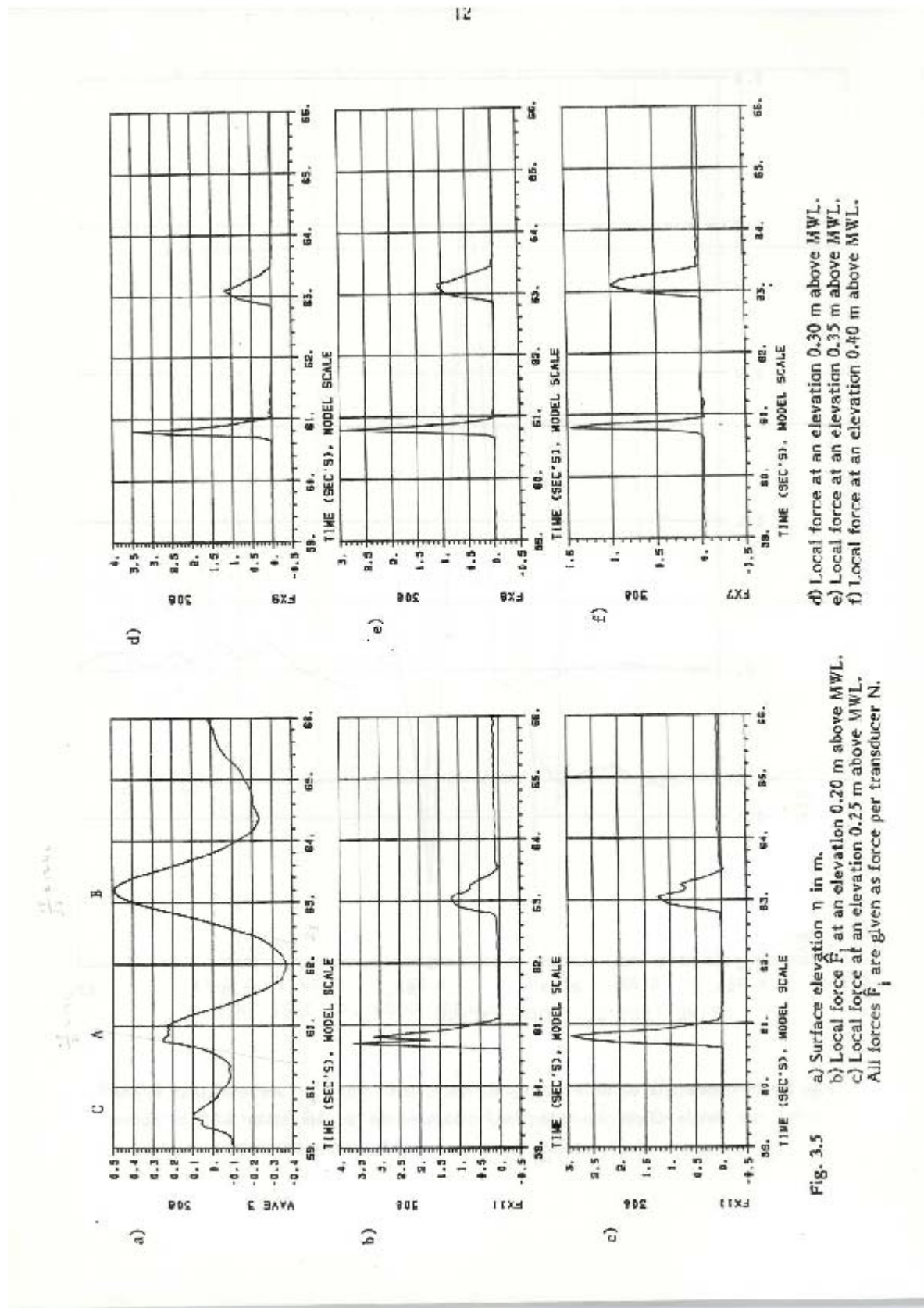


Fig. 3.5 a) Surface elevation η in m.
 b) Local force \hat{F}_i at an elevation 0.20 m above MWL.
 c) Local force at an elevation 0.25 m above MWL.
 All forces \hat{F}_i are given as force per transducer N.

Fig. 3. Time series of surface elevation and drag forces measured above mean water level.

Wave A is a plunging breaker, wave B is a non-breaking wave.

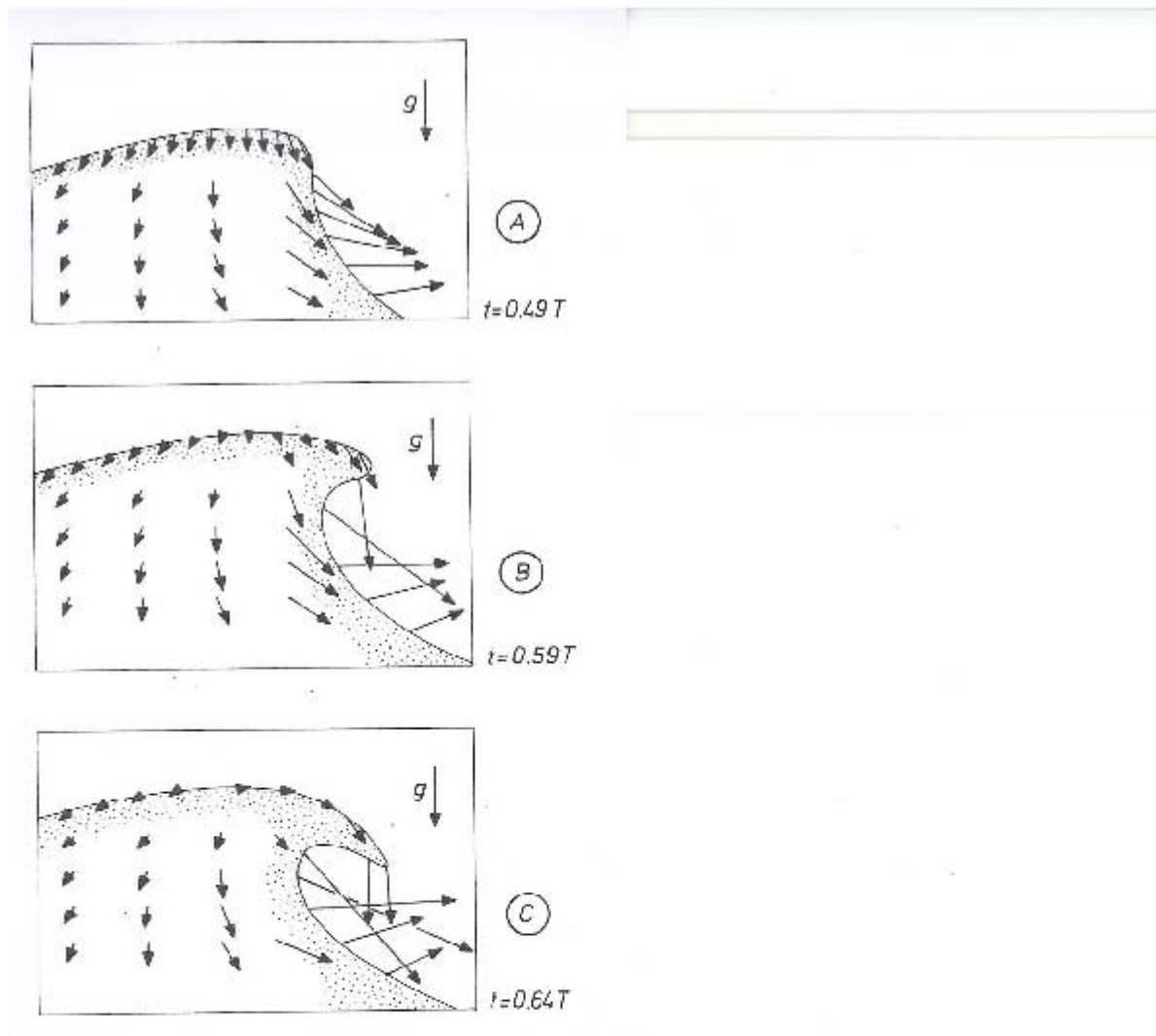


Fig. 4. Simulation of local particle accelerations in a deep water plunging breaker. The vertical arrow indicates the gravity acceleration $g = 9.81 \text{ m/sec}^2$. Local particle accelerations attain values up to 3 g.

5. The accident with the trawler "GAUL".

On the 8th February 1974 the british trawler "GAUL" disappeared in the Barents Sea.

At that time it was a very heavy gale and a significant wave height close to 15 m.

A strong easterly wind meet a current from the opposite direction. Under such conditions it is well known, and confirmed by experiments that breaking waves in deep waters at sea transits from a "SPILLING-mode" to a "PLUNGING-mode", see KJELDSEN & MYRHAUG 1980.. No emergency call was ever given It is assumed that "GAUL" was hit by one or two plunging breakers in succession, got a large heeling angle more than 60 degrees and finally lost water tight integrity.

. A very large SAR-operation with navy vessels and aircrafts participating,was performed, but nothing was found. 36 people onboard lost their lives. Fig 5 shows the trawler "GAUL". 1997 the wreck was found in 300 m water depth with some open fish doors on the starboard side. A very sudden capsizing had occurred.



Fig 5. The british trawler "GAUL". (From A.R. JACOBSEN 2002.)

6. Conclusions.

1. – Many scientists are aware of the fact, that it is not the highest waves that creates the largest responses on ships and platforms. In many cases it is the breaking waves with nearly vertical walls of water that creates the largest responses and the largest difficulties for manoeuvres.
2. – It is of paramount importance to map the wave crest kinematics, and the probabilities associated with them, in order to perform a reasonable risk management.

3. – The performed experiments showed that inception of breaking in deep water random generated irregular waves, in some cases took place when wave steepnesses were as low as $H/L = 0.05$.

7. References

- Jacobsen A.R. 2002: "Disaster- Unsolved problems from the Barents Sea" Aschehoug & co (in Norwegian)
- Kjeldsen S.P., Olsen G.B. FILM "BREAKING WAVES".
- Kjeldsen S.P., Tørum A., Dean R.G. 1986: "Wave Forces on Vertical Piles caused by 2- and 3-dimensional Breaking Waves" Proc. 20th International Conference on Coastal Engineering, Taipei, Taiwan.
- Kjeldsen S.P., Vinje T., Myrhaug D., Brevig P., "Kinematics of Deep Water Breaking Waves" Paper No 3714. Proc. 12th Offshore Technology Conference. Houston. Texas. 1980.
- Kjeldsen S.P. 1984: "Dangerous Wave Groups" Norwegian Maritime Research. Vol 2. pp 4-16.
- Kjeldsen S.P., Myrhaug D, 1980 "Wave-wave Interactions, Current-Wave Interactions, and resulting Extreme Waves and Breaking Waves" Proc. 17th International Conference on Coastal Engineering. Sydney. Australia.
- Kjeldsen S.P. 2008: "Training and Experience with SAR-operations in the Barents Sea". SAR-Conference. Brest France. October 2008.

7. Acknowledgements.

We acknowledge permission from PHILLIPS to publish the photos shown in Fig. 2., and the support from STATOIL, HYDRO and The Royal Norwegian Council for Scientific and Industrial Research for supporting the experimental programme.

Kurtosis and “Extreme” Wave Probabilities in Very Young Wind-Generated Seas

Donald T. Resio, ERDC-CHL, Vicksburg MS, USA

Charles E. Long, ERDC-CHL, Duck NC, USA

Several recent studies have hypothesized that the probability distribution of large individual wave heights in ocean waves can be linked to the “Benjamin-Feir Index (BFI),” which provides a simplified prediction of the kurtosis of the wave height distribution. Observations also appear to support the existence of this type of a relationship; however, the link between the BFI, kurtosis, and large wave probabilities is much more tenuous when directional spreading is considered, with the general consensus being that increased directional spreading leads to decreased kurtosis.

In a presentation at the 10th Workshop on Wave Hindcasting and Forecasting held in Oahu, Hawaii, Janssen et al. (2007) use data from ECMWF to develop a relationship between wave age and kurtosis in ocean areas of the world and an associated increase in the ratio of the largest individual wave in a sample to the significant wave height. However, the wave age of the samples used there were essentially all greater than about 0.6. Since the dependency of kurtosis, and consequently the likelihood of very large wave, is shown to be a strong function of decreasing wave age near this limit, it is interesting to examine a set of data specifically collected at very short fetches to extend our understanding of this behavior. As described in Long and Resio (JGR, 2007), a detailed measurement program (using an array of surface-piercing capacitance gages) was undertaken in Currituck Sound to study waves in complex, short-fetch areas. Information from this study covers a range in wave ages from about 0.25 to 2.0 and provides an independent check of previous results as well as extending the range to lower wave ages. As shown in Long and Resio, the observed spectra exhibit large variations in spectral peakedness (frequency bandwidth) and in directional spreading. In all, this data set provides information for over 1,000,000 individual waves, along with a detailed analysis of the spectral characteristics accompanying these probabilities.

At this time, we have completed analyses of one quarter of the data. Our results suggest that, although the frequency bandwidth is quite small for some of the samples, we do not observe a substantial increase in the probabilities of large waves. It is possible that the relatively broad directional spreading (with typically bimodal spectral tails) prevents the kurtosis and the large-wave probabilities from increasing significantly. At the conference, we will present results for the complete set of analyses along with comparisons to various theoretical predictions.

Forecasting Extreme Waves in Practice

Anne Karin Magnusson
Norwegian Meteorological Institute, 5007 Bergen, Norway
a.k.magnusson@met.no

Abstract. An expert team at met.no in Bergen has been forecasting severe storms for Ekofisk since 1991, and for Valhall since 2004. Both oil fields are situated in central North Sea, about 30 km apart, and both are subject to subsidence, so that lower parts of the deck have increased probability of being subject to waves compared to initial design criteria. Risk reducing actions are therefore developed to ensure among other safe human activity on lower construction levels. Forecasting the extremes is today, for the Ekofisk eXtreme Wave Warning system (EXWW), focused on forecasting the significant wave height. Experience with 3 different in-situ measuring wave sensors at Ekofisk through monitoring of more than 100 storms has shown significant differences between sensors, showing a need for standardized methods in wave measurements, and that great care must be taken in extracting exact scientific relations for Rogue waves. It is also shown that forecasting significant wave height in extreme storms is still a challenge.

1. Introduction

“Rogue waves”, “freak waves” or “extreme waves” have in the past 10-15 years become common knowledge, in the sense that “everybody” knows they occur at times. The probable height of these and their cause is still a topic for research, with no proven relationships, therefore, activity at sea still relies on forecasting of significant wave height (H_s). An analogy is found in wind forecasting, where it is known that it is the gusts that provoke damages, but, extreme gusts, like extreme waves, are confined to small areas, and time and exact place for occurrence is not predictable with today’s knowledge. Methods for forecasting higher probability of occurrence are under consideration both for winds and for waves, but for the time being it is the average quantities like maximum 10 minute wind speed or 20 minutes significant wave height that are forecasted for the special users.

Forecasting the highest significant wave (H_s) in an energetic storm is also a challenge, as will be exemplified later. An expert team at the Norwegian Meteorological Institute (met.no) in Bergen has been monitoring and forecasting extreme waves for Ekofisk since 1991. Ekofisk is a platform complex, operated by ConocoPhillips, situated in the central North Sea (N56.5, E3.2, see Figure 1 and Figure 2). The extraction of oil in the ground under the platforms makes the soil deep below the sea bottom compress, making the platforms subside slowly. The subsidence varies geographically; at some platforms the subsidence has been of the order of 10m since start of production in 1971. Different actions to reduce the risk of wave impact on higher levels of the platforms have been taken: jack-up, that is elongation of the legs of some platforms by 6m (1987); installation in 1989 of a 100m high concrete wall, approximately 30 meters above mean sea level, to surround and protect the

central processing platform (2/4-T, the 'Tank'); Water injection; building of new platforms in a east going axis from the old complex (Ekofisk II, started in 1998); decommissioning of platforms north of the tank, and the tank.

On 12th December 1990, the most severe storm ever recorded at Ekofisk made numerous damages on platforms in the North Sea. H_s was measured at the maximum to 13.2m with a Waverider buoy, a value at the order of a 30-50 year return period. It induced the start of EXWW, Ekofisk eXtreme Wave Warning, where an expert team updates special forecasts every 3 hours in severe storms.

In the first years of EXWW, the necessary risk reducing actions offshore could be taken at 3 hours pre-warning. Since 2-3 years, new procedures include demobilisation of some platforms, which in the most severe cases will need complete demobilisation, requiring about 1000 people to be flown onshore. This is due to take many hours. Therefore actions around this demobilisation must be started already 2-3 days before culmination in a storm. This decision is of course an important one to take, with high economic consequences. There are a number of uncertainties to be considered when deciding when to do what in the extreme storms. A combination of statistics and experience is used by the companies to decide what level of H_s to use for different actions. Forecasting skill on H_s is one of the important values to know. Different studies have been carried out to quantify the forecast skill of the forecasters and the models. Some results are presented hereunder.

Validation of forecasts needs high quality of measurements. Ekofisk has now four different wave sensors (Figure 2) that send data in real time to a server at met.no, making Ekofisk one of the best wave instrumented offshore site in the world. The real time monitoring and the validation work performed have shown high short time variability in the measurements, and considerable differences in between the measuring systems, and this is presented in the following section.

Rogue waves are for waves like the ultimate 'gusts' in the wind. Knowledge on the heights and forces involved is still un-complete, as there are only few quality controlled measurements of the most exceptional ones, the most famous being the Draupner wave on 1st January 1995. Statistics between rogue wave events and parameters that are suggested to be related to events have failed to prove any relations, (Olagnon and Magnusson, 2004, and Krogstad et al, these proceedings). But this is not surprising, since we know that a singular extreme wave in a sea state may happen in an area but not at a measuring site. This is known because of damages at high levels of constructions, while records are not made of similar heights at measuring sites. Statistics from a limited number of high storms will therefore probably not give certain relationships.

Forecasting the extreme significant wave height in intense and severe storms is a challenge of its own. An example of prognoses during the storm on 9th November 2007 is given hereunder to demonstrate this.

2. The wave sensors

Phillips Petroleum Norway, now ConocoPhillips, have recorded waves at or in the vicinity of the Ekofisk complex since 1980. Different sensors have been used, and mounting locations on the complex have changed through time. In the years 1991 to 1993, environmental data were available through modem. Since 1993 data have been transferred in real time through internet. The first winter season (1991-1992) learnt us that the wave data from two height measuring systems (an EMI radar and a Plessey radar) were largely affected by lee effects from the tank (Figure 2). High focus was thereafter put on good quality wave measurements, because forecast skills are highly dependent on measuring feedback. A WAMOS (www.oceanwaves.de) was installed to measure directional wave spectra at 2/4-K, and two new sites were chosen for 2 down looking lasers (Optech lasers), one at flare South, with good exposure to waves from east-west direction, and one at flare North, with relatively good exposure to northerly directions, and also from the east and west sectors. This paper only deals with the wave measurements from the in-situ systems (wave profilers). The two Optech lasers have given relatively good measurements in the period 1995-2005, although with known problems of possible reflection of waves from the tank in northerly situations at the northern flare, and sea spray from the platform legs in the vicinity of both sensors when waves are large, not always as much as seen in the picture in Figure 3 showing the southern part of the Ekofisk complex during a storm.

Due to decommissioning of the platforms North of the tank, the sensor at flare North was replaced in 2005 with a new system of 4 lasers in an array on the bridge between 2/4-K and 2/4-B (Krogstad et al, these proceedings). The bridge is oriented East-West, with open sector towards North and South. Waves from westerly sector may be subject to interference with the 2/4-B platform, which is about 80 meters away. The sensor at flare South was replaced with a MIROS down-looking radar altimeter, a Miros Range Finder (MRF).

A non-directional waverider buoy has been measuring free-field waves since 1980. Data return from this system is quite high. Batteries are changed outside the winter season, a procedure started after a stormy winter not allowing for replacement for a long time.

3. Quality of measurements

Experience from monitoring the wave data from different sensors during storms in real time has given useful knowledge on quality of wave measurements. Discussions with system providers have also revealed that sampling and filter techniques are used to filter inevitable bad samples occurring from time to time. This results in apparently good and smooth wave profiles, from which detail wave information can be extracted. Details about this filtering is outside the scope of this paper, but some points seem necessary to report here in view of the validation results given, and in perspective of the conferences goal, getting more knowledge about rogue waves.

The measurements of significant wave height from the waverider buoy (WR) have always been looked at as reference data, although it is a wave-follower. Waves are measured as un-skewed (Magnusson et al, 1999), but wave height from crest to trough will still be correct, and so is the significant wave height considered to be. It has been reported earlier that buoys may disappear under the water surface at approach of high crests (probably steep and very high crests). In 2006 new software was installed at Ekofisk to treat the Waverider data in real time. For a period there were very noisy data, out of range or invalid. It appeared that when the buoy was submersed, the datastream from the buoy to the receiving station at the platform was broken. The missing data were filled with default numbers (large negative), being part of the analysis, and making large erroneous data. The solution adopted then by the system provider was to filter the data in real time to keep the reporting as continuous as possible. Despite this discrepancy the Waverider buoy is still regarded as a reference at Ekofisk.

The MIROS altimeter (MRF) is seen to give lower maximum H_s in storms compared to the WR (Figure 3), also in directions where there are no sheltering effects expected. WR data have also been compared to measurements from a SAAB altimeter at Valhall, (Figure 4), operated by BP. The same discrepancy is observed to WR data. Correlation is good but slope of regression lines shows that H_s at the Waverider is about 10% higher than at the down looking sensors at Ekofisk and at Valhall 30 km away. Through a meeting with MIROS we learnt that a spike removal filter was running on the raw data from the MRF to ensure stable data return in real time. In Figure 5 we see a picture of an extreme wave passing the construction supporting the bridge north of the sensor at Flare South, causing a lot of sea spray (and green water in this case). H_s is not known at time of picture, but probably somewhere between 10 and 12m. Sea spray is believed to occur (and to cause erroneous data) even when waves are lower. The spike removal is necessary, but it also filters too large acceleration in data, smoothing high crests. This alters the statistics of the wave crests, and may be part of the cause giving lower H_s values when waves are steep. The discrepancy is seen through all ranges of H_s . Not surprisingly, because steep waves occur in all ranges of H_s . A more thorough investigation is necessary to quantify the discrepancies in wave profiles and H_s values.

The LASAR, a system of 4 lasers in an array mounted on the bridge between 2/4-B and K, were configured by Mark Donelan and no filtering is used on the raw data, which are sampled at 5Hz. The measuring procedure gives unfortunately a lot of spikes. The lasers used in this configuration are from the same manufacturer (Optech) as the sensors used at Flare South and North in the period 1995 to 2005, but the new sensors in the LASAR system have lower intensity due to more restrictive rules (related to eye-safety). So far the analysis of storm data has shown that significant wave height can be higher with the LASAR system than with the WR but the difference is not quantified yet.

4. Variability in Hs

All 3 sensors at Ekofisk measuring the wave profile at 2 and 5 Hz show similar behaviour in short time variability of Hs, see example from the Andrea storm 8th to 9th November 2007 in Figure 6. Hs values can differ by 2 meters (20%) from one 20 minute record to the next from the same sensor. Just after midnight measurements vary between roughly 6.5 and almost 10m, regardless of sensor. To demonstrate the variability we have evaluated the one-, two- and three-hourly running means of Hs from the WR in the same period of time shown in Figure 6, and the standard deviation between the Hs values within these intervals. The evolution of these averages are shown in Figures 7, 8 and 9, with envelopes at the standard deviations. Maximum Hs in storms decreases from 11m (the maximum 20 minutes value) to Hs (1-hrly)=10 m, Hs (2-hrly)= 9.6 m, and Hs (3-hrly) = 9.54m. The mean and maximum standard deviation of data included in the data within the period of time shown in the figures changes from respectively 0.57 m and 1.75m in the one-hourly data to 0.78m and 1.23m in the 3-hourly data.

5. Validation of ECMWF forecasts in 9m-storms or larger

Because of new safety procedures at Ekofisk and Valhall, an exact forecast of highest significant wave height in a storm is necessary 3 days ahead of the culmination time of the storm. A threshold of 9 m in the forecasted Hs at culmination, 3 days in advance, is used for triggering special preparedness offshore and onshore within the companies (ConocoPhillips and BP). In very extreme storm events, up to around 1000 persons must be flown to shore from the Ekofisk Complex, and around 200 persons from Valhall to shore. New platforms are being built that will soon make demobilisation unnecessary. Until then, there is high interest in the forecast skills.

The most important question for deciding which thresholds to use for the different actions to be taken are: how accurate is the forecaster's prediction at three and two days in advance? How accurate are the long range forecasting models in extreme storms? To answer these questions, forecasts given in storms that gave around 9m or more at Ekofisk in the period 2000-2007 were analysed. There are not that many cases with Hs above 9m at Ekofisk. We can count 38 such storms since 1980, six winter seasons had none, while two had four. Tools and models for forecasting are under continuous improvement, so that doing statistics on model prognoses many years back in time is not relevant for forecast uncertainty today. The number of real time data has also increased in this period through increasing number of satellites and regular flights measuring wind, temperature and humidity in the atmosphere and wind and waves on the sea surface.

Validation has been performed on forecasts issued every 3 hours during EXWW storms, but before the unmanning of the platforms was relevant, EXWW forecasts were not issued more than 15-24 hours ahead of culmination. Results of the validation of these warnings issued in storms with wave height higher than 9 meter in the period

1991 till today, 30 in number, show a forecasting skill (here being the average error between max forecasted and max observed 20 minutes H_s) varying between -.2 and -.5m in average up to 24 hours ahead of the maximum in storm. The wave model prognoses run at met.no have larger errors, varying from a deficit of 1 meter in average up to 24 hours before, and of 2 meters up to 60 hours ahead of culmination. The wave and atmospheric models at met.no are run over a limited area up to 60 hours, with higher resolution than the global models run at ECMWF. Error statistics for the ECMWF forecasts of significant wave height at Ekofisk are shown in Figure 10. Maximum values of forecast are extracted regardless of timing, some storms had stored output every 3 hours, but standard was 6 hours. The storms considered are from January 2002 to March 2007. All errors are shown with different symbols for different runtimes up to 96 hrs ahead of maximum in Figure 11.

Several updates of the model system at ECMWF have been made. For instance going from about 55 km resolution to 25 km resolution in January 2006. Figure 11 shows that the storm after this improvement in resolution gave high score in November 2006, but other storms thereafter showed again a deficit of 2 meters and more.

The fact is that one never really will be sure of if an extreme situation is well forecasted in advance. Consistency in forecasts from the different meteorological institutes permits to evaluate the probability of a development by looking at the similarities and consistencies. There are also different probabilistic forecasts produced that may help in the decision making, but some more analysis has to be done on the value of these to make use of them in offshore operations and this service in special.

In the next section the different forecasts in the Andrea storm are presented.

6. The Andrea-storm

The form and development of a depression, including the propagation direction across the sea area of interest is very important for what the culmination height will be. Spectral shape parameters that may be used for extreme wave warning will also be dependent on this development.

The Andrea storm, which name was given for the EXWW services only, must be said to be well forecasted. The severity was quite well predicted, in that H_s at the 9 to 10 meter level were modelled 2-3 days ahead, though with variations from one run to the next available 6 or 12 hours later. EPS (Ensemble Prediction System) runs from ECMWF gave early storm wave height culmination at 9 to 10 meter level at Ekofisk with high probability already 4 days in advance. An example is given in Figure 12, showing wind speed, H_s and T_p EPS-forecasts starting at the 6th November 2007 at 12 UTC. These prognoses are available around 10-12 hours after analysis time, in this case 54 hours before culmination in storm.

Figure 13, 14 and 15 demonstrates how varying the storm development was predicted from one run to another. In Figure 13 two different predictions of H_s from ECMWF

are compared (+84 and +96 hours). Although Hs is 9 meters at Ekofisk in both cases, the area of 9m in the +96 hours forecast (blue lines and colouring) is relatively correct compared to analysed fields, but in the forecast 12 hours later (+84 hours, red lines and colouring) the strongest field is forecasted to be more to the west, reflecting another storm development. Figure 14 shows 3 different model prognoses for situation on 8th November 2007 at 18 UTC (ECMWF; met.no's WAM50km, which is WAM run with 50km resolution with winds from a 20 km resolution atmospheric model (HIRLAM20); WAM10km which has 10 km resolution and is forced with winds from HIRLAM with 12km resolution). All these predictions were available around two and a half days before maximum in storm, and they all predict the storm maximum to be located W - NW of Ekofisk (5, 8 and 9,5m) while the maximum occurred closer to the Norwegian coast.

Closer to storm culmination (+33 hours) all 3 models agree more on where the maximum will occur. ECMWF gives 9 meters in an area NE of Ekofisk. The coarse met.no WAM model (50km) gives 10 m in almost same area, and the fine grid model WAM10km peaks above 11m just North of Ekofisk at that time. Figures 7-9 show that there is a higher degree of severity between 03 and 09 UTC on November 9th. The closer to culmination time, the closer to the Norwegian Coast the maximum wave field is. WAM10km evaluates maximum Hs to be 11.5-12 m in the Norwegian trench NE of Ekofisk on the 9th at 06 UTC, with between 10 and 10.5m at Ekofisk. Which is quite close to the observed maxima, but slightly above the maximum one-hourly averaged Hs from WR.

7. Conclusive remarks

The Andrea storm was what we can call a well forecasted storm. Long in advance (3-5 days) predictions from ECMWF, both deterministic and from the Ensemble Prediction System (EPS), gave values of maximum Hs in the storm close to what was observed. It underpredicted the 20 minutes maximum value, but was close to the 3 hourly average value. Finer resolution models run at met.no gave Hs predictions slightly higher, comparing better with running average values of Hs over shorter period (one hourly).

The Andrea storm was a challenge to predict even if forecasts were good in average. Risk reducing actions had to be taken 2-3 days in advance, and the value of expected maximum 20 minutes value of Hs is used as criteria.

Small differences in atmospheric developments of a severe storm may give large differences in significant wave height at one location (50-100%). Large differences (not quantified herein) in the spectral shapes may be expected, and probably also in the wave profile statistics (crest, trough, steepness). Analysis of an extreme wave event is dependent on a good storm track history.

Wave measurements are seen to be sensor dependent. The analysis of wave data from the different sensors at Ekofisk and Valhall Ekofisk demonstrates the need of an improved description of spike removals from the system providers, and of standardisations in wave data sampling.

8. Acknowledgements

Thanks to Jean Bidlot at ECMWF for providing the ECMWF forecasts for Ekofisk in the period 2002-2007.

9. References

Magnusson A.K., M.A. Donelan, and W.M. Drennan, (1999): "On estimating extremes in an evolving wave field". Coastal engineering 36, pp 147-163.

Olagnon M. and Magnusson, A.K., (2004): "Sensitivity Study of sea parameters in correlation to extreme wave occurrences". Proceedings of ISOPE, 2004.

Olagnon M. and van Iseghem, S. (2000): "Some observed characteristics of sea states with extreme waves". Proceedings of 10th International Offshore and Polar Engineering Conf., ISOPE, 3, pp. 84-90.

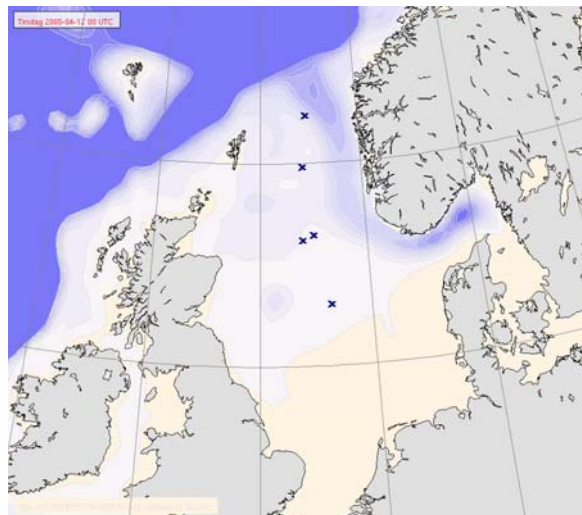


Figure 1 Ekofisk in central North Sea (N56.5,E3.2), southernmost point in Figure), operated by ConocoPhillips, and Valhall (N56.3,E3.4, close to Ekofisk), operated by BP. Isolines for bottom topography. Grid lines every 5 degrees.

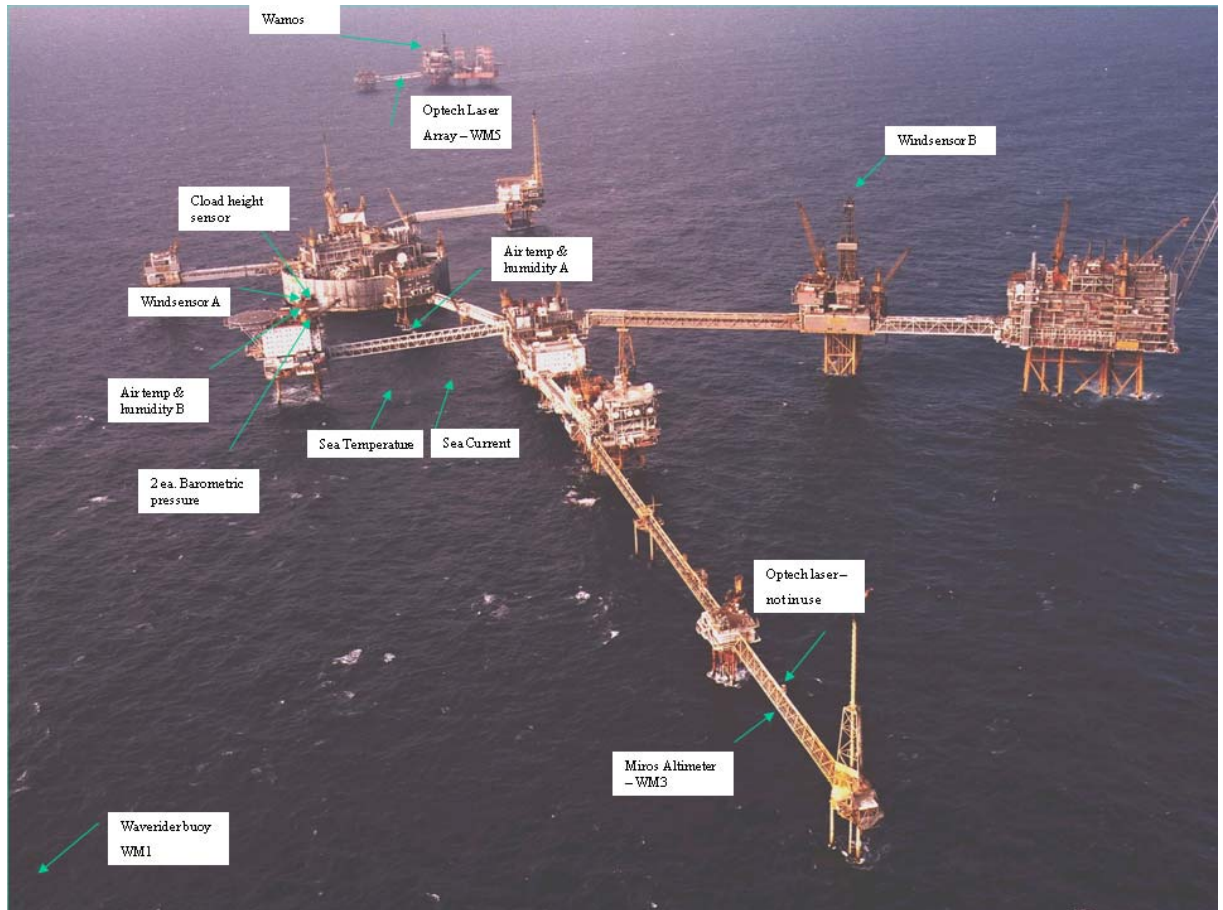


Figure 2 The platform complex Ekofisk (N 56°30', E 3°12'), and instrumentation for environmental data, viewed from south. The two platforms in the east branch are built in 1999 and 2002. The central platform 2/4-T, also called the Tank, is the platform inside the concrete wall that was put in place in 1989. The wall has a diameter of 120 meters, is 100 meters high of which about 30 meters are above mean sea level. In the north we see the two platforms 2/4-K and 2/4-B, with the bridge in between where the new LASAR system is mounted.

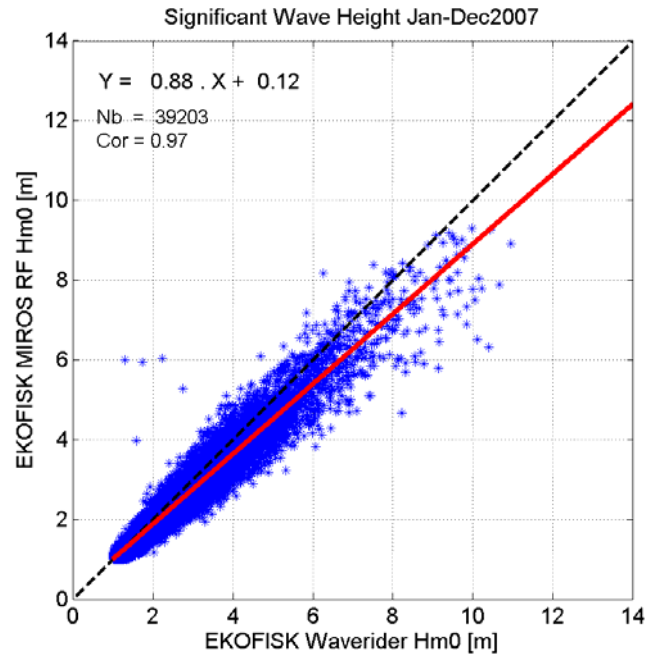


Figure 3 Comparison between significant wave height H_s ($H_s > 1\text{m}$) from the Waverider and the MIROS Range Finder (MRF) at Ekofisk, for the period 2007.

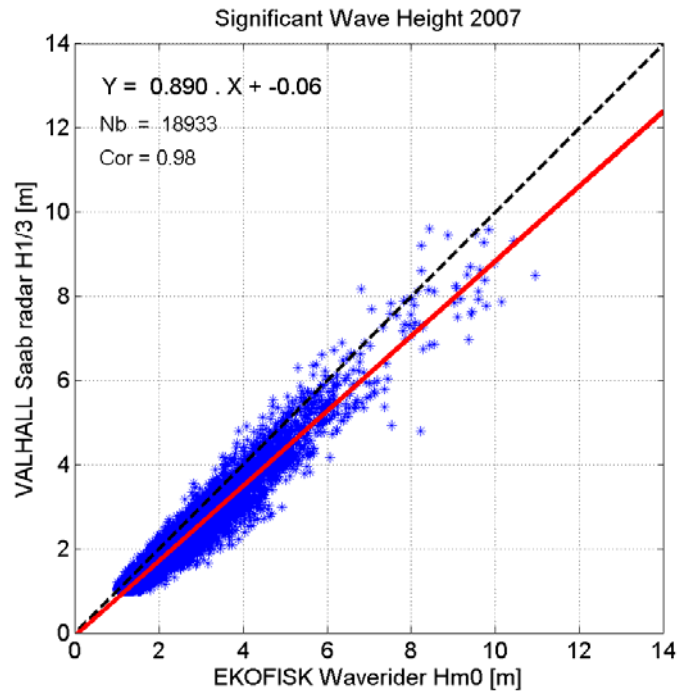


Figure 4 Comparison between H_s (>1m) from the Waverider at Ekofisk and the Saab radar at Valhall in 2007.



Figure 5 Flare South is the tower to the left in the picture. An extreme wave breaks through the support of the bridge just north of the site where one down-looking wave

sensor (Optech laser at the time of the picture) is mounted.

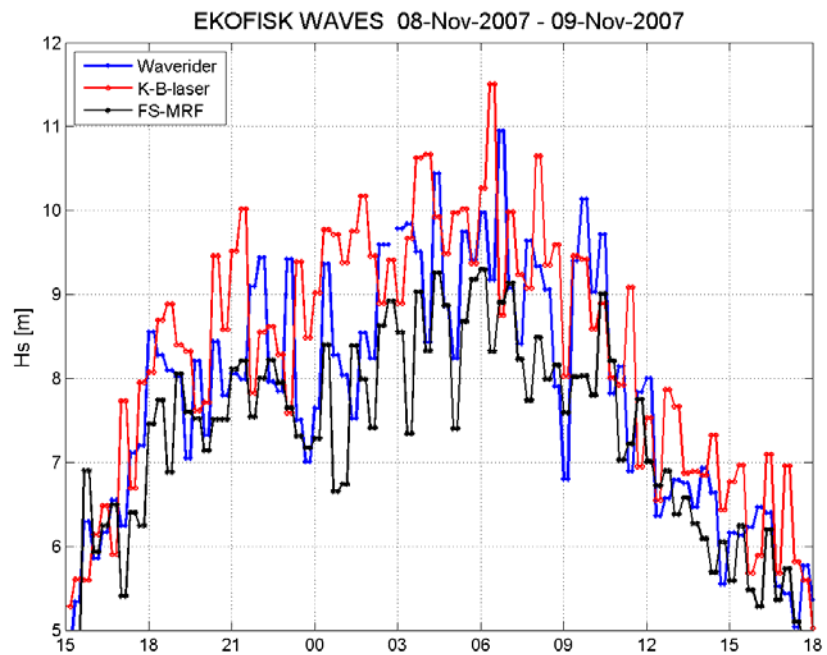


Figure 6 Example of a storm record (9th November 2007, the Andrea storm at Ekofisk) showing how significant wave height from the 3 sensors at Ekofisk vary with time. Hs can vary with almost 2m (20%) from one measurement to the next.

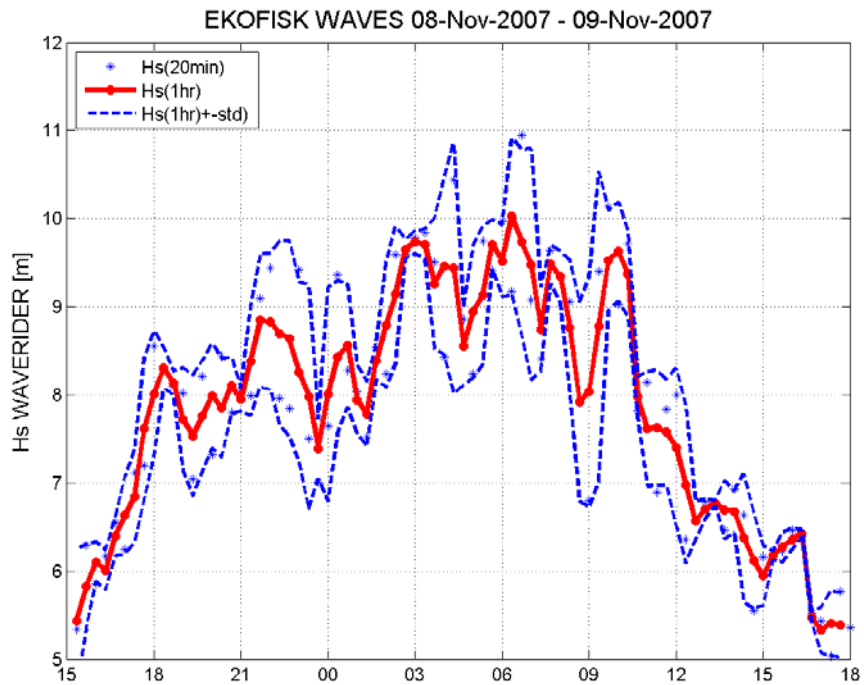


Figure 7 One hourly running averages of the Waverider during the Andrea storm at Ekofisk, 9th November 2007. Blue dots: 20 minutes records, Red line: one hourly running average on the 20 minutes significant wave heights from the Waverider. Blue stippled lines: the one hourly averages +/- the standard deviation between the 3 records in each hourly average.

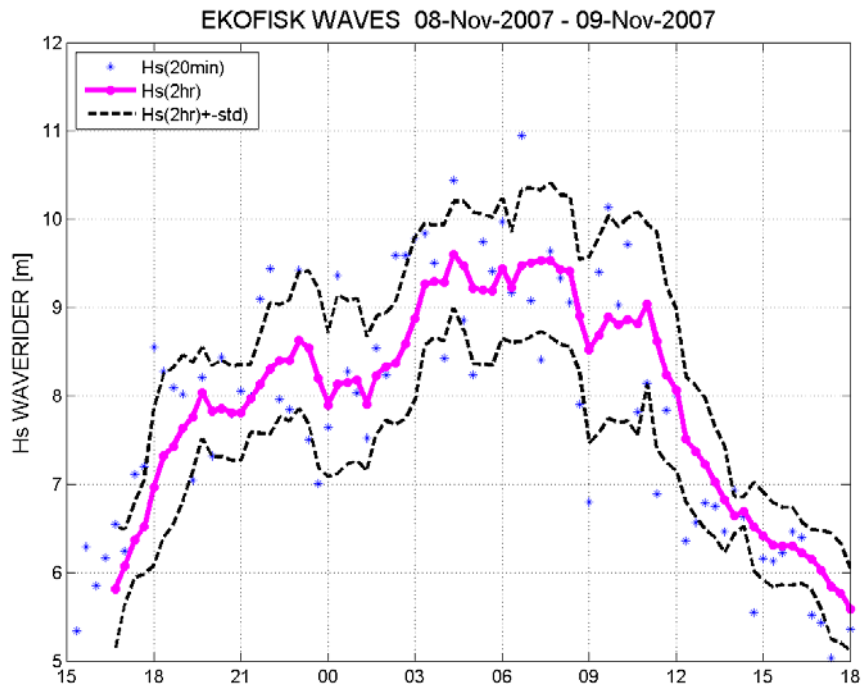


Figure 8 Two hourly running averages of the Waverider during the Andrea storm at Ekofisk, 9th November 2007. Blue dots: 20 minutes records, Magenta line: 3-hourly running average on the 20 minutes significant wave heights from the Waverider. Black stippled lines: the 3-hourly averages +/- the standard deviation between the 3 records in each 3-hourly average.

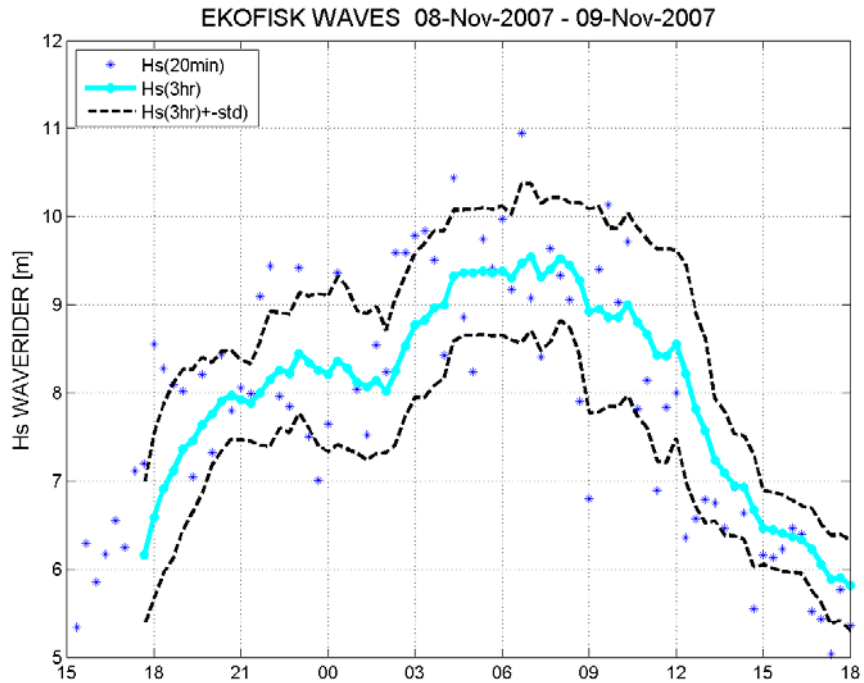


Figure 9 Three hourly running averages of the Waverider during the Andrea storm at Ekofisk, 9th November 2007. Blue dots: 20 minutes records, Cyan line: 3-hourly running average on the 20 minutes significant wave heights from the Waverider. Black stippled lines: the 3-hourly averages +/- the standard deviation between the 3 records in each 3-hourly average value.

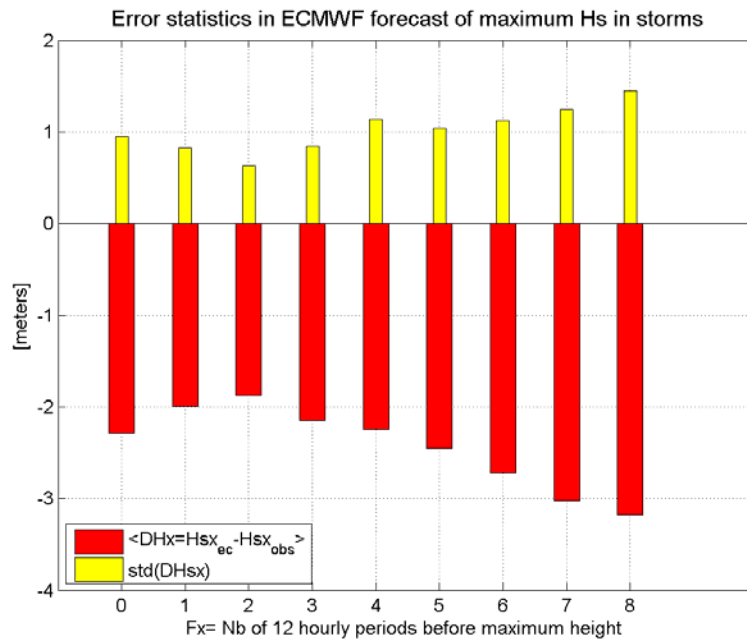


Figure 10 Validation of the wave model prognoses from ECMWF in storms with culmination height 9 meter or more, up to 4 days ahead. Storms from the period 2002 to March 2007. Only maximum Hs is used, time of maximum may vary up to 12 hours to observed value. Red bars: mean error in forecasted maximum in storm. Yellow bars: standard deviation of the difference.

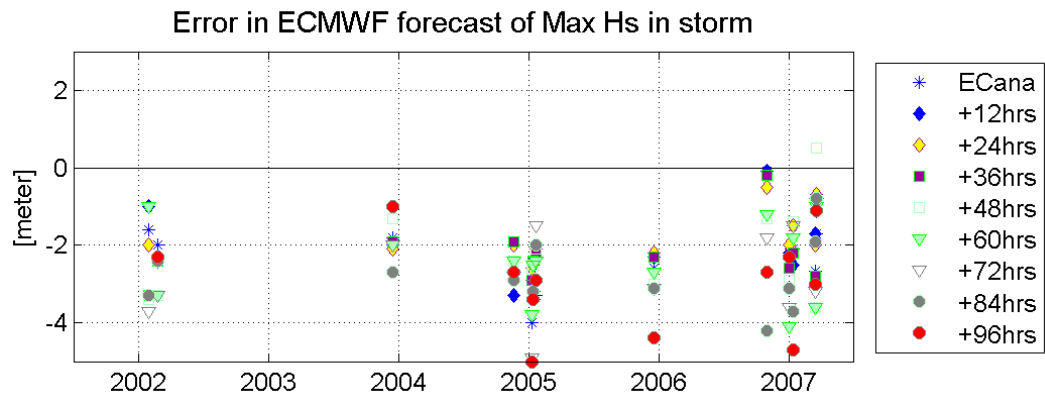


Figure 11 Validation of the wave model prognoses from ECMWF in storms with culmination height 9 meter or more, in the period 2002 to March 2007. Only maximum Hs is used (from the quality controlled data and using 20minutes values), time of maximum may vary up to 12 hours to observed value. Different symbols for different start times of the model, up to 4 days ahead.

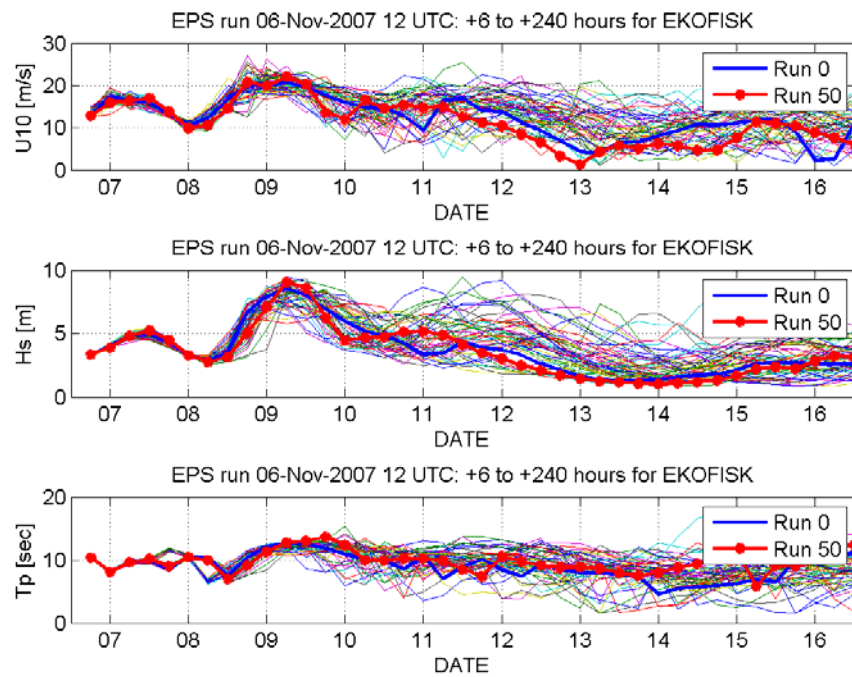


Figure 12 ECMWF EPS prognoses of wind speed, Hs and peak period (Tp) at Ekofisk, giving high probability for Hs around 9m on 9th of November. These results were available just before midnight on the 7th, around 54 hours before culmination.

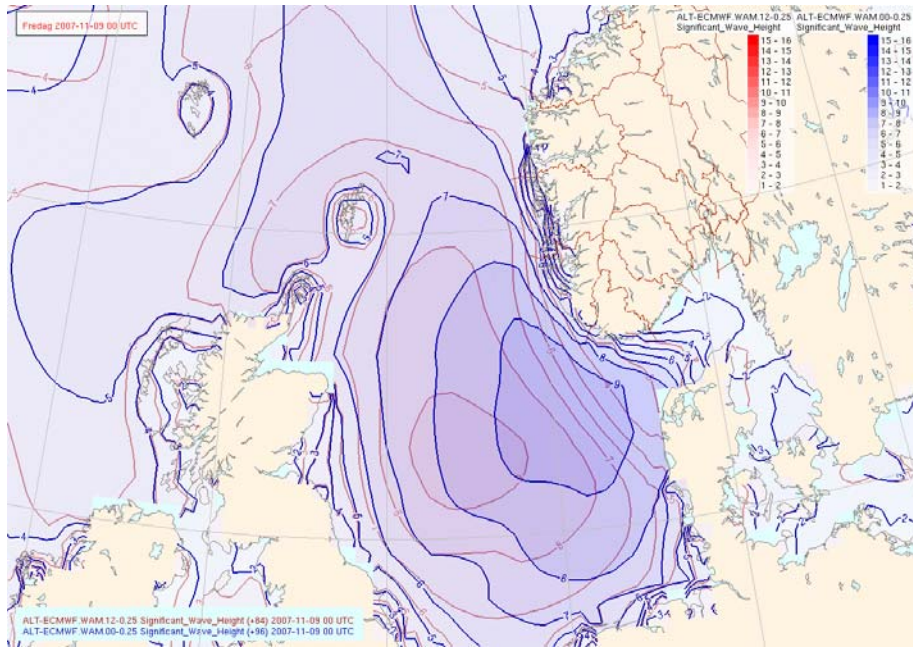


Figure 13 Significant wave height at 9th November 2007 at 00 UTC in the +84 hours (red lines, isolines every meter) and +96 hrs (blue lines) from ECMWF. The oldest is the closest to analysed fields (maximum 20 minutes and one-hourly values from the Waverider at Ekofisk are 11m and 10m respectively).

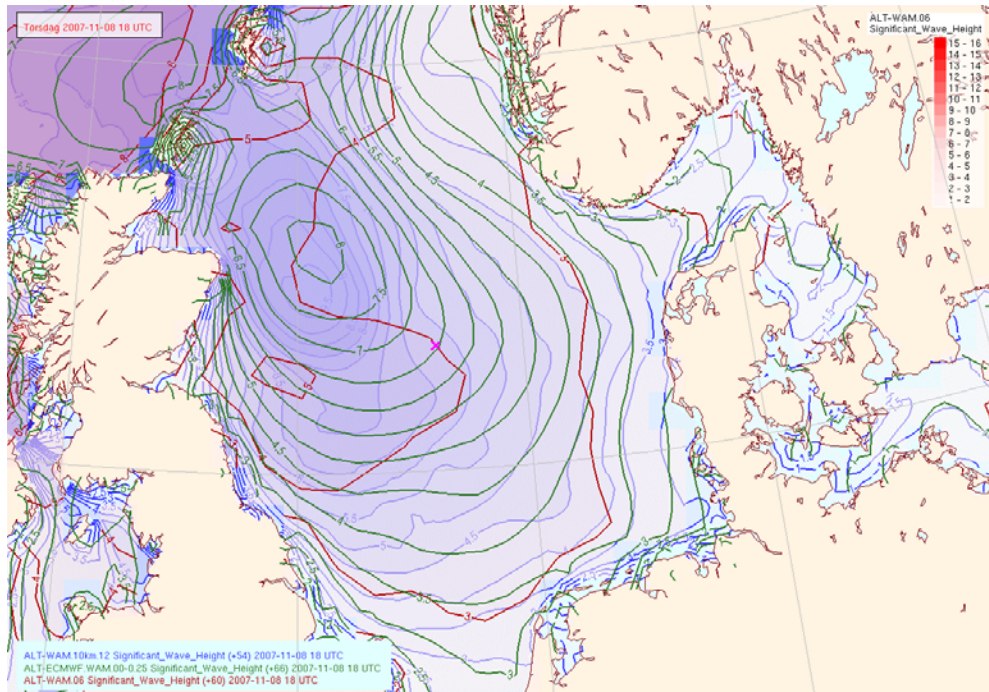


Figure 14 Significant wave height at 8th November 2007 at 18 UTC in the +54 hours from WAM10km (blue lines, isolines every half meter, max Hs= 9.5m), and +66 hrs from ECMWF (green lines, max Hs = 8m), and +60 hours from met.no's WAM 50km (max Hs =5m). Here the storm maxima are all in western part of the North Sea.

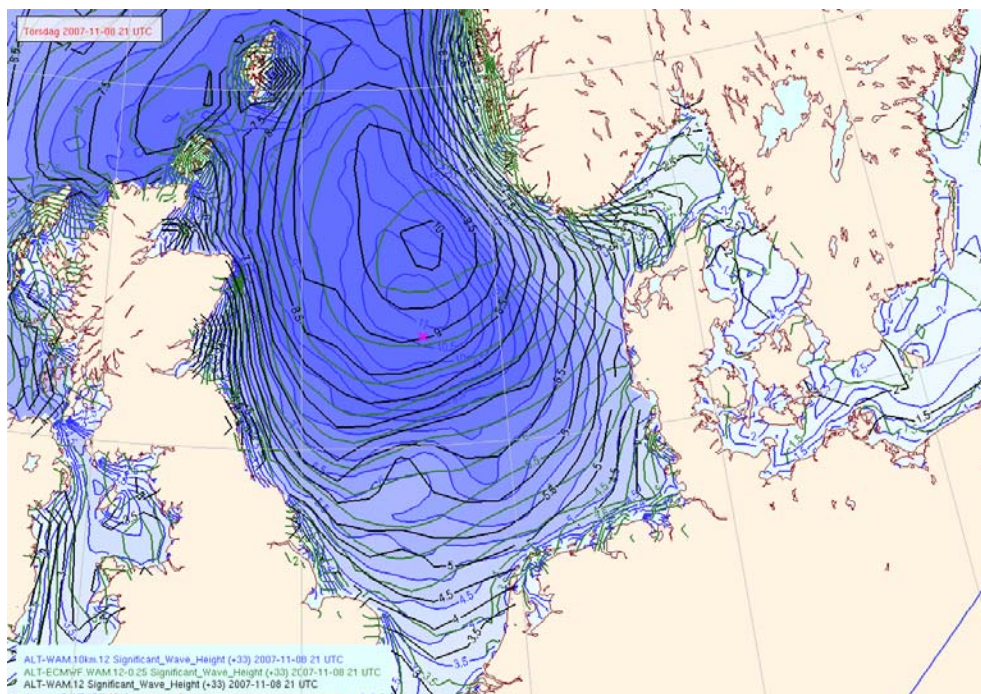


Figure 15 Significant wave height (isolines every half meters) on 8th November 2007 at 21 UTC in the +33 hours forecasts from the ECMWF model (green lines, max Hs is 9m), the Norwegian coarse WAM model (dark blue, max Hs is 10m), and the Norwegian fine grid (WAM 10km) model (light blue, max Hs is 11m). Ekofisk location is indicated with a red cross.

 Mean and std of 1-2-3 hourly averages of Hs_waverider
 Maximum Hs (Waverider) = 10.95m

	1hr	2hr	3hr
Hsmean_x	10.03	9.60	9.54
Mean(std)	0.57	0.72	0.78
Max(std)	1.75	1.27	1.23

Implications of Non-linear Waves for Marine Safety

Elzbieta M. Bitner-Gregersen¹, Alessandro Toffoli¹, Miguel Onorato²
and Jaak Monbaliu³

¹ Det Norske Veritas Research & Innovation, Veritasveien 1,
N-1322 Høvik, Norway
elzbieta.bitner-gregersen@dnv.com
alessandro.toffoli@dnv.com

² Università di Torino, Via Giuseppe Verdi 8,
I-10124 Torino, Italy
onorato@ph.unito.it

³ Hydraulics Laboratory K.U.Leuven, Kasteelpark Arenberg 40,
B-3001 Leuven, Belgium
Jaak.Monbaliu@bwk.kuleuven.be

Abstract. It is well established that the modulational instability enhances the probability of occurrence for extreme events if waves are long crested, narrow banded and sufficiently steep. As a result, substantial deviations from commonly used second-order theory-based distributions can be expected. However, the coexistence of directional wave components can suppress the effects related to the modulational instability. To get better insight into the effect of wave directionality and its implication for design work, numerical simulations based on the truncated potential Euler equations were used. The analysis has been concentrated primarily on the wave crest distribution.

1 Introduction

Extraordinarily extreme waves, often called *rogue* or *freak* waves, have been subject to much attention in the last decade. Although the existence of these waves themselves has generally not been questioned, neither circumstances under which these waves occur nor their physical nature were well understood. Recently, our knowledge of ocean waves has considerably advanced. A number of extreme wave studies have been conducted theoretically [14]), numerically [22, 23, 30], experimentally [24, 25]) and based on the field data [3, 4]. The completed EU research project MaxWave (2003), Rogue Waves (2000 and 2004) Workshops, the Hawaii Workshops on extreme waves (2005 and 2007) as well as the RINA conferences on “Design and Operation for Abnormal Condition I, II and III” held in 1997, 2001 and 2005 in London, have made significant contribution to better understanding of rogue waves; however, several important questions are still not answered.

More systematic investigations of extreme and rogue wave mechanisms, such as bimodal seas, directional energy spreading, spatial description, effects of water depth, and

wave-current interaction, are still lacking. There is also a need for more field data to study rogue waves in the ocean. These investigations are essential for reaching consensus about probability of occurrence of rogue waves which is mandatory for evaluation of possible revision of classification society rules which do not include explicitly rogue waves today [2].

A number of physical mechanisms to explain the extreme and rogue wave phenomena have been suggested in the last decade. These include: wave-current interactions, linear Fourier superposition (frequency or angular linear focussing), and nonlinear interaction and modulational instability. Much attention has recently been given to the study of modulational instability of free wave packets [14, 22, 24, 25]. This instability can develop when waves are long crested, i.e. unidirectional, narrow banded and in infinite water depth, and lead to the formation of exceptionally large waves, far beyond the ones described by second-order theory. Several findings suggest that statistical properties of surface gravity waves (particularly the occurrence of extreme wave events) are substantially affected by modulational instability [9, 19, 25, 30, 36]. However, in the case of more realistic sea states, where wave components with different directions of propagation coexist (i.e. short crested wave fields), the effect of the modulational instability is notably reduced [9, 23, 37, 38].

Understanding of implications of wave directionality on statistical properties of the surface elevation is important for design work. To get better insight into the effect of wave directionality, numerical simulations based on the truncated potential Euler equations have been used in the present study. The effect of various directional spreading conditions on the modulational instability and hence on statistical properties of the surface elevation has been investigated. The analysis has been concentrated primarily on the wave crest distribution and results are compared with distributions based on the second-order theory, which are commonly used in design practice. The results are discussed in perspective to the current design and operational criteria of marine structures within a framework of the risk-based design approach.

2 Current Design Practice

The design practice has been moving over the last decades towards a more consistent risk based approach. The risk based approaches are based on the modern reliability methods [18], and are used for design and safety assessment of marine structures. The reliability methods allow quantifying in a probabilistic way the uncertainties in the different parameters that govern the structural integrity. This allows reliability assessment of structural components or a structure. Further reliability-based design of a structural component (or a structure) provides a means to satisfy target reliability with respect to specific modes of failure. The probabilistic approach can be used for calibration of partial safety factors in the development of LRFD codes, and for development of acceptance criteria for structural designs, confer DNV CN 30.6 (1992) [5], ISO 2394 [13] and Skjong et al [29].

Within modern reliability theory [18] the failure criterion is expressed in terms of a limit state function, $g(\cdot)$, which may have any form in general and is a function of n ran-

dom variables $\mathbf{X}=(X_1, X_2, \dots, X_n)^T$ that describe the failure set ($g < 0$), the failure surface ($g = 0$), and the safe set ($g > 0$). Thus, the probability of failure is

$$P_F = P(g(X_1, X_2, \dots, X_n) \leq 0) \quad (1)$$

with the corresponding reliability index β defined as

$$\beta = -\Phi_n^{-1}(P_F) \quad (2)$$

where Φ_n denotes the standardized cumulative normal distribution function.

Note that a reliability index obtained by a structural reliability analysis is a nominal value, which depends on the analysis models and uncertainties included, rather than an absolute reliability value, which may be given a frequency interpretation.

Structural Reliability Analysis (SRA) allows application of physical first principles, and complex distribution models for the stochastic variables. By SRA we can quantify the failure probability, and determine sensitivity measures for parameters that govern the structural integrity.

The traditional format of classification societies' rules for ships is mainly prescriptive, and the link to an overall safety objective is not always transparent. IMO [11, 12] has developed Guidelines for use of the Formal Safety Assessment (FSA) methodology in rule development which will support development of risk-based goal-oriented regulations.

When discussing impact of extreme waves on the marine structures a distinction can be made between ship structures and offshore structures. Even though the same basic principles prevail for hydrodynamic loads on ships and offshore structures, actual problems and methods for assessing these loads in the design stage are quite different. Further, as ships are sailing they are exposed to varying wave environment. Therefore, different wave data, and to some extent different wave models, are used for defining design and operational conditions for these two classes of structures.

To have a clear and consistent approach for determining design loads, we need to define the limit state categories and the scenarios we design for. In the offshore industry the following well proven terminology is applied which is starting to be accepted also within the shipping industry:

- *Ultimate Limit State (ULS)* corresponding to the maximum load carrying resistance;
- *Fatigue Limit State (FLS)* corresponding to the possibility of failure due to the effect of cyclic loading;
- *Serviceability Limit State (SLS)* corresponding to the criteria applicable to normal use or durability;
- *Accidental Limit State (ALS)* corresponding to the ability of the structure to resist accidental loads and to maintain integrity and performance due to local damage or flooding;

In the design process, ship structural strength and ship stability are calculated, following international standards, in extreme events with an occurrence of once in every 20 years (Ultimate Limit State, ULS). Recently an increase of the return period to 25 years has been suggested and applied. ALS (Accidental Limit State) checks cover grounding, collision and fire and explosion. ALS does not include a check for severe weather events. Limited knowledge about rogue waves and particularly ship behaviour in these waves, as well as a lack of information about the probability of ships encountering such waves, precludes their explicit inclusion in operational and design practice for ship structures.

Offshore structures (including FPSOs) follow a different approach and are designed for the 100-year return period (ULS). The Norwegian offshore standards (NORSOK Standard [22]) takes into account extreme severe wave conditions by requiring that a 10000-year wave does not endanger the structure integrity (ALS). However, extended knowledge about extreme and rogue waves and marine structures' behaviour in them is necessary to reach consensus within the offshore industry on wave models for the prediction of extreme and rogue waves and design scenarios to be included in a possible ALS check.

An extended knowledge about extreme and rogue waves, in particularly their probability of occurrence and ship structures behaviour in them is mandatory for evaluation of possible revision of classification society rules and for providing a consistent approach combining new information about extreme and rogue waves in a design perspective, see Bitner-Gregersen et al [2]. So far, consensus about the probability of occurrence of rogue waves has not been reached either a consistent risk-based approach has been proposed.

Statistical characteristics of the sea surface like skewness and kurtosis as well as the wave crest distribution will need to be a part of the risk-based approach. Today the second-order theory-based Forristall crest distributions (2d and 3d) [8] are commonly used in design practice, e.g. DNV RP-C205 [6].

3 Numerical Simulations

In the case of constant water depth ($h=\infty$ in this study), the velocity potential $\Phi(x,z,t)$ of an irrotational, inviscid, and incompressible liquid satisfies the Laplace's equation everywhere in the fluid. The boundary conditions are such that the vertical velocity at the bottom ($z=-\infty$) is zero, and the kinematic and dynamic boundary conditions are satisfied for the velocity potential $\Psi(x,y,t)=\Phi(x,y,\eta(x,y,t),t)$ on the free surface, i.e., $z=\eta(x,y,t)$, [40]. The expressions of the kinematic and dynamic boundary conditions are as follows:

$$\Psi_t + g\eta + \frac{1}{2}(\Psi_x^2 + \Psi_y^2) - \frac{1}{2}W^2(1 + \eta_x^2 + \eta_y^2) = 0 \quad (3)$$

$$\eta_t + \Psi_x\eta_x + \Psi_y\eta_y - W(1 + \eta_x^2 + \eta_y^2) = 0 \quad (4)$$

where the subscripts denote the partial derivatives, and $W(x,y,t)=\Phi_{z|z=\eta}$ represents the vertical velocity evaluated at the free surface.

The time evolution of an initial surface elevation can be calculated from Eqs. (3) and (4). For this study, we have used the higher order spectral method (HOSM), which was independently proposed by West et al [39]) and Dommermuth and Yue [7]. A comparison of these two approaches [4] has shown that the formulation proposed by Dommermuth and Yue (1987) [7] is less consistent than the one proposed by West et al [39]; the latter, therefore, has been applied for the present study. The advantage of HOSM in comparison to others methods is that it allows simulating a large number of random realizations of the surface elevation, within a reasonable computational time, without limitations in terms of the spectral bandwidth.

HOSM uses a series expansion in the wave slope of the vertical velocity $W(x,y,t)$ about the free surface. Herein we have considered a third-order expansion so that the four-wave interaction is included [31, 32]; note, however, that the solution is not fully nonlinear. The expansion is then used to evaluate the velocity potential $\Psi(x,y,t)$ and the surface elevation $\eta(x,y,t)$ from Eqs. (3) and (4) at each instant of time. All aliasing errors generated in the nonlinear terms are removed (see [31, 39] for details). The time integration is performed by means of the four-order Runge–Kutta method with a time step $\Delta t=T_p/200$ (T_p is the spectral peak period). A concise review of HOSM can be found in [31].

For the construction of the initial conditions, a directional wave spectrum $E(\omega,\theta)=S(\omega)D(\theta)$ is used, where $S(\omega)$ represents the frequency spectrum and $D(\theta)$ is the frequency-independent directional function. The initial surface elevation $\eta(x,y)$ is calculated by first moving to a wavenumber spectrum with linear dispersive relation, and then applying the inverse Fourier transform with the random amplitude and phase approximation (see [36] for details). As it is frequently used for practical applications, the JON-SWAP formulation [15] is herein adopted to describe the energy distribution in the frequency domain. In the present study, for convenience, we have chosen a peak period $T_p=1$ s, which corresponds to a dominant wavelength $\lambda_p=1.56$ m, a significant wave heights $H_s=0.08$ m, a peak enhancement factor $\gamma=6.0$; such a sea state is characterized by a wave steepness $k_p H_s/2 = 0.16$, where k_p is the wavenumber associated to the spectral peak. Note that the choice of the peak period is arbitrary, and any other wave period representing wind sea could have been applied. For the description of the directional domain, a $\cos^N(\theta)$ angular spreading function has been adopted. Several directional conditions have been considered, ranging from long crested (large N) to short crested (small N) conditions. The following values of the spreading coefficient N have been used: N = 840, 200, 90, 50, 12, 2.5. A more detailed description of such experiments can be found in [37].

For the present numerical experiments, a space domain of 14 m x 14 m has been considered with a mesh of 256 x 256 nodes. The initial surface has been let evolve according to Eqs. (3) and (4) for 60 peak periods and output surfaces have been stored every 6 peak periods. In order to have statistically significant results, about 100 repetitions of the wave surface have been performed with identical spectral density but different random amplitudes and phases.

4 Skewness and Kurtosis

In the following section, we discuss the effect of directional spreading on the skewness λ_3 , and kurtosis λ_4 , of the surface elevation. Whilst the first describes the degree of vertical asymmetry, the latter refers to the occurrence of large wave events. For a Gaussian, linear, random process, the following values should be expected: the skewness $\lambda_3=0$; and the kurtosis $\lambda_4=3$. In Figs. 1 and 2, the maximum values recorded during the temporal evolution of the surface elevation of the skewness and kurtosis are shown as a function of the directional spreading coefficient N .

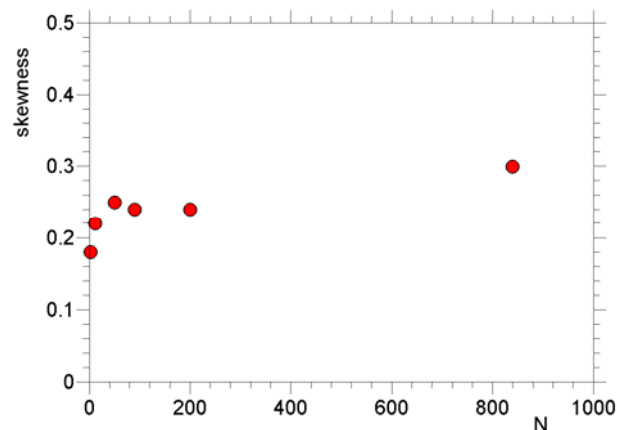


Fig. 1 Skewness (λ_3) as a function of the directional spreading coefficient N .

It is rather well established that ocean waves are not symmetric. Consequently, the skewness of real waves significantly deviates from the one expected in linear wave theory. This is clearly observed from the simulations of Eqs. (3) and (4). Note that, as already shown by Mori et al [20], the skewness is mainly dominated by the second-order interactions [16], while modulational instability has only a weak effect on the vertical asymmetry of the wave profile. In this respect, we observed that the skewness is consistent with the value expected from second-order theory, which is of about 0.24 for a wave steepness of 0.16. When waves become short crested, however, the skewness is slightly reduced as a consequence of the reduction of the second-order interaction [35].

The present findings are in agreement with previous investigations of the statistical properties of the surface elevation (Mori et al 2007 [20], Toffoli et al 2008a and 2008b [37,38]) which indicate that the skewness is mainly dominated by the second-order bound contribution (second-order theory). Therefore, the skewness is only weakly affected by the modulational instability.

On the other hand, the kurtosis is significantly affected by the modulational instability. For long crested conditions, this results in strong deviations from linear (Gaussian) and second-order statistics, where the kurtosis is expected to be close to 3. However,

when waves become short crested, the effect of the modulational instability is substantially reduced. In particular, for broad directional spreading conditions (wind sea), extreme waves do not seem to be more frequent than the second-order theory predicts. This result is consistent with previous numerical simulations of Schrödinger-type equations [30] and laboratory experiments [26, 38].

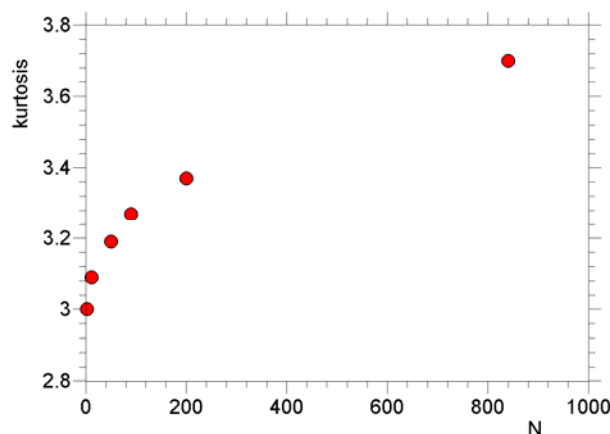


Fig. 2 Kurtosis (λ_4) a function of the directional spreading coefficient N.

5 Wave Crest

Today it is common practice to describe the surface elevation by using second-order wave theory, from which probabilistic models for the sea surface, crests and troughs can be developed (for example, [8, 28, 33, 34]). Among them, the wave crest distributions proposed by Forristall [8] are frequently used for engineering applications. When waves are long crested, however, extreme waves can occur more often than in second-order wave theory and, as a consequence, the tail of the wave crest distribution can deviate from second-order based distributions; for example, the underestimation of the second-order based distribution at low probability levels (e.g. $P(\eta) < 0.001$) can be of about 20% [37]. This is also clearly shown in Fig. 3, where the wave crest distribution from the simulations of Eqs. (3) and (4) is presented for different degree of the directional spreading and compared with the Rayleigh distribution and the Tayfun one [33].

Deviations from second-order distribution are gradually suppressed when the directional distribution broadens. As observed for the kurtosis, the effect of the modulational instability is negligible for broad directional wave fields. In such conditions, second-order based wave crest distributions describe the simulated sea states reasonably well. As shown in Fig. 4 in particular, the Forristall distributions (2d and 3d) [8] seem to provide an appropriate description of the wave crest in broad directional wave fields (see also [38]).

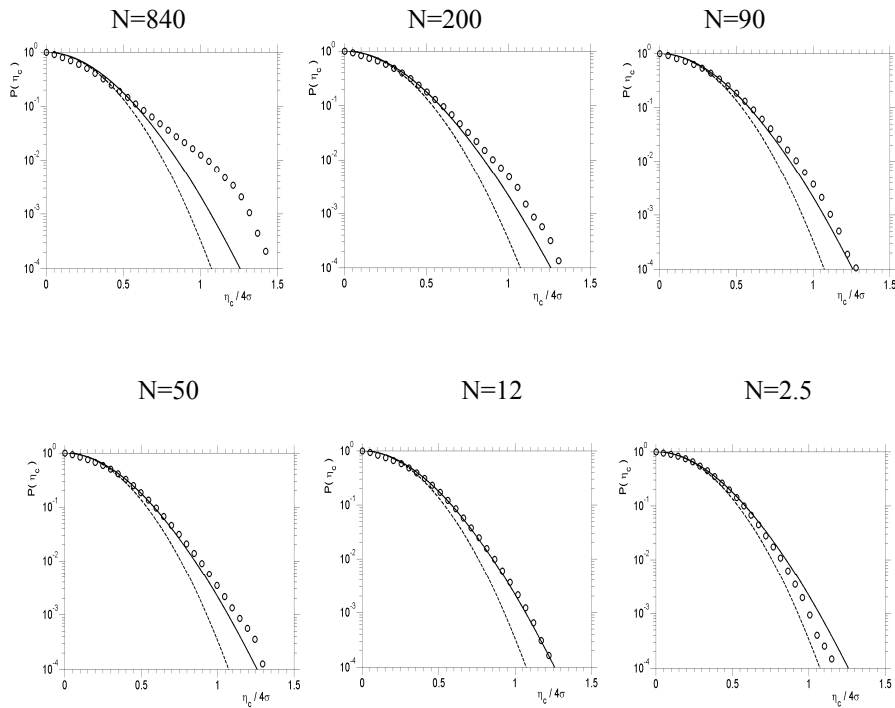


Fig.3 Wave crest distributions; o simulations -Tayfun (1980), -- Rayleigh.

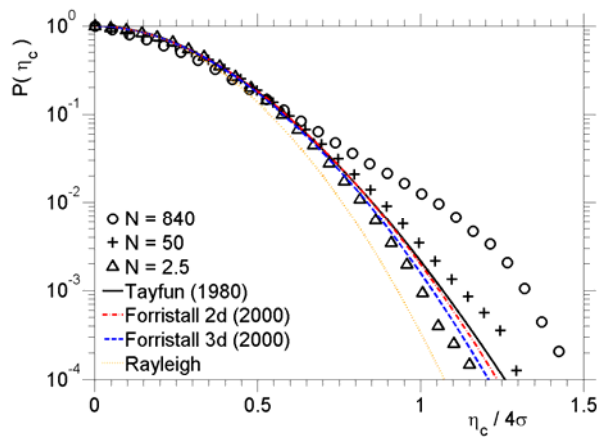


Fig.4 Wave crest distributions.

DNV RP C-205 (2007) [6] recommends that typical values of the directional spreading coefficient for wind sea are $N=2$ to $N=4$; whilst for swell $N \geq 6$ is more appropriate. According to DNV RP C-205 the directional spreading of swell can also be modelled by a Poisson distribution [1, 17].

Following the current DNV RP C-205 recommendations the present results strongly indicate that for deep water and locations where wind sea is present the modulational instability does not affect significantly the second-order theory-based wave crest distributions. However, for locations where only an energetic swell is present a wave crest distribution may largely deviate from the second-order theory-based crest distributions due to the modulational instability.

6 Conclusions

The study presents the effect of wave directionality on sea state characteristics like the skewness and kurtosis and on the distribution of wave crest. The effect of the modulational instability is reduced when directionally spread wave components are present, in particular, the kurtosis decreases significantly. Both the skewness and kurtosis values do not diverge largely from the ones expected for second-order waves for broad directional wave fields. Further, for the directional spreading coefficient $N=2.5$ the distribution of wave crest coincides satisfactory with the second-order-theory based distribution of Forristall [8] used in current design practice. These findings are consistent with previous simulations of the modified non-linear Schrödinger equations [23, 30] and laboratory experiments [26, 38].

It should be noticed that the study is limited to deep water and to one generation mechanism of rogue waves, the modulational instability. The presented solution is not fully nonlinear. Further, the existing knowledge about wave directional spreading models may have some deficiencies. Therefore more detailed investigations of meteorological and oceanographical conditions in which extreme and rogue waves occur is essential for reaching a firm conclusion on applicability of the second-order-based distributions in design practice. A comparison of the second-order-based crest distribution of Prevosto et al [28] with numerical simulations is also called for.

These investigations are essential for reaching consensus about probability of occurrence of rogue waves which is mandatory for evaluation of possible revision of classification society rules which do not include explicitly rogue waves today [2].

Acknowledgement

The work presented was performed within the EC Marie Curie Network "Applied stochastic models for ocean engineering, climate and safe transportation" SEAMOCS (contract MRTN-CT-2005-019374). The numerical simulations with the HOSM model were partly performed by using the K.U. Leuven's High Performance Computing (HPC) facilities.

References

1. Bitner-Gregersen, E. M. and Hagen, Ø.: Directional Spreading in Two-Peak Spectrum at the Norwegian Continental Shelf. *Proceed. of the 21st Inter. Conf. on Offshore Mechanics and Arctic Eng. (OMAE 2002)*, June 23-28, Oslo, Norway (2002).
2. Bitner Gregersen, E. M., Hovem, L. and Hørte, T.: Impact of Freak Waves on Ship Design Practice. *Proceedings MAXWAVE Final Meeting*, Geneva, Switzerland, October 8-10 (2003).
3. Bitner-Gregersen, E. M. and Magnusson, A. K.: Extreme Events in Field Data and in a Second Order Wave Model. *Proc. Rogue Waves 2004 Workshop*, October 20-32, Brest, France (2004).
4. Clamond, D., Francius, M., Grue, J., and Kharif, C.: Long Time Interaction of Envelope Solitons and Freak Wave Formations, *Europ.J. Mech. B-Fluids*, 25 (2006) 536–553.
5. DNV CN30.6: Structural Reliability Analysis of Marine Structures, Høvik, Norway, July (1992).
6. DNV RP-C205: Environmental Conditions and Environmental Loads. Høvik, Norway, April (2007).
7. Dommervuth, D. G. and Yue, D. K. P.: A High-order Spectral Method for the Study of Nonlinear Gravity Waves, *J. Fluid Mech.*, 184 (1987) 267–288.
8. Forristall, G. Z.: Wave Crest Distributions: Observations and Second Order Theory. *J.Phys. Oceanogr.*, 30 (2000) 1931-1943.
9. Gibson, R. S., Swan, C., Tromans, P. S.: Fully Nonlinear Statistics of Wave Crest Elevation Calculated Using a Spectral Response Surface Method: Application to Unidirectional Sea States. *J. Phys. Oceanogr.*, 379 (2007) 3–15.
10. Gramstad, O. and Trulsen, K.: Influence of Crest and Group Length on the Occurrence of Group Length. *J. Fluid Mech.*, 582 (2007) 463–472.
11. IMO: Interim Guidelines for the Application of Formal Safety Assessment (FSA) to the IMO Rule Making Process. Maritime Safety Committee, 68th session, June (1997); and Marine Environment Protection Committee, 40th session, September (1997).
12. IMO: Guidelines for Formal Safety Assessment for the IMO Rule Making Process. IMO/Marine Safety Committee 74/WP.19, (2001).
13. ISO 2394: General Principles on Reliability for Structures.
14. Janssen, P. A. E. M.: Nonlinear Four-Wave Interaction and Freak Waves, *J. Phys. Ocean.*, 33, (2003) 63–884.
15. Komen, G., Cavaleri, L., Donelan, M., Hasselmann, K., Hasselmann, H., Janssen, P.: *Dynamics and Modeling of Ocean Waves*. Cambridge University Press, Cambridge (1994).
16. Longuet-Higgins, M. S.: The effect of non-linearities on statistical distribution in the theory of sea waves, *J. Fluid Mech.*, 17 (1963) 459–480.
17. Lygre, A. and Krogstad, H.: Maximum Entropy Estimation of the Directional Distribution in Ocean Wave Spectra, *J.Phys. Ocean.*, Vol 16, (1986).
18. Madsen, H. O., Krenk, S. and Lind, N. C.: *Methods of Structural Safety*. Prentice-Hall, Englewood Cliffs, NJ 07632, (1986).
19. Mori, N. and Yasuda, T.: Effects of High-Order Nonlinear Interactions on Unidirectional Wave trains. *Ocean Engineering* 29 (2002) 1233–1245.
20. Mori, N., Onorato, M., Janssen, P.A.E.M., Osborne, A.R. & Serio, M.: On the Extreme Statistics of Long-Crested Deep Water Waves: Theory and Experiments. *J. of Geophys. Res.* 112 (C9), C09011 (2007).
21. NORSOK (2007) Standard N-003: Action and action effects, Rev. 2, http://www.standard.no/pronorm-3/data/f/0/03/78/7_10704_0/N-003d2r2.pdf.
22. Onorato, M., Osborne, A., Serio, M. and Bertone, S.: Freak Wave in Random Oceanic Sea States. *Phys. Review Letters*, 86:25 (2001) 5831–5834.

23. Onorato, M., Osborne, A. R., and Serio, M.: Extreme Wave Events in Directional Random Oceanic Sea States, *Phys. Fluids*, 14 (2002) 25–28.
24. Onorato, M., Osborne, A. R., Serio, M., and Cavaleri, L.: Modulational Instability and Non-Gaussian Statistics in Experimental Random Water-Wave Rains, *Phys. Fluids*, 17, 078101, doi:10.1063/1.1946769, (2005).
25. Onorato, M., Osborne, A., Serio, M., Cavaleri, L., Brandini, C., Stansberg, C.: Extreme Waves, Modulational Instability and Second Order Theory: Wave Flume Experiments on Irregular Waves. *European Journal of Mechanics B/Fluids*, 25 (2006) 586–601.
26. Onorato, M., Cavaleri, L., Fouques, S., Gramstad, O., Janssen, P.A.E.M., Monbaliu, J., Osborne, A.R., Pakozdi, C., Serio, M., Stansberg, C.T., Toffoli, A. and Trulsen, K. : Statistical Properties of Mechanically Generated Surface Gravity Waves: a Laboratory Experiment in a 3D Wave Basin . *J. Fluid Mech.*, in press (2009).
27. Petrova, P., Cherneva, Z. and Guedes Soares, C.: Distribution of Crest Heights in Sea States with Abnormal Waves. *Applied Ocean Research*, 28 (2006) 235–245.
28. Prevosto, M., Krogstad, H., and Robin, A.: Probability Distributions for Maximum Wave and Crest Heights, *Coast. Eng.*, 40 (2000) 329–360.
29. Skjong, R, E Bitner-Gregersen, E Cramer, A Croker, Ø Hagen, G Korneliussen, S Lacasse, I Lotsberg, F Nadim and Ronold, K.O.: “Guidelines for Offshore Structural Reliability Analysis – General” DNV Report No 95 – 2018 (1995).
<http://research.dnv.com/skj/OffGuide/SRAatHOME.pdf> 1
30. Socquet-Juglard, H., Dysthe, K., Trulsen, K., Krogstad, H. and Liu, J.: Distribution of Surface Gravity Waves during Spectral Changes. *J. Fluid Mech.*, 542 (2005) 195–216.
31. Tanaka, M.: A Method of Studying Nonlinear Random Field of Surface Gravity Waves by Direct Numerical Simulations, *Fluid Dyn. Res.*, 28 (2001) 41–60.
32. Tanaka, M.: On the Role of Resonant Interactions in the Short-Term Evolution of Deep -Water Ocean Spectra. *J. Phys. Oceanogr.*, **37:4** (2007) 1022-1036.
33. Tayfun, M.: Narrow-Band Nonlinear Sea Waves. *J. Geophys. Res.*, 85:C3 (1980) 1548–1552.
34. Tayfun, M. A. and Fedele, F.: Wave-Height Distributions and Nonlinear effects, *Ocean Eng.*, 34 (2007) 1631–1649.
35. Toffoli, A., Onorato, M., and Monbaliu, J.: Wave Statistics in Unimodal and Bimodal Seas from a Second-Order Model. *Eur. J. Mech. B-Fluid*, 25 (2006) 649–661.
36. Toffoli, A., Onorato, M., Bitner-Gregersen, E. M., Osborne, A.R. and Babain, A.V.: Surface Gravity Waves from Direct Numerical Simulations of the Euler Equations: A comparison with second order theory. *Ocean Eng.*, 35:3-4 (2008a) 367-379.
37. Toffoli, A., Bitner-Gregersen, E. M., Onorato, M. and Babain, A.V. Wave Crest and Trough Distributions in a Broad-Banded Directional Wave Field. *Ocean Eng.*, 35 (2008b) 1784–1792.
38. Waseda, T.: Impact of Directionality on the Extreme Wave Occurrence in a Discrete Random Wave System. *Proceedings of the 9th International Workshop on Wave Hindcasting and Forecasting*, Sept. 24-29, Victoria, Canada (2006).
39. West, B. J., Brueckner, K. A., Janda, R. S., Milder, D. M., and Milton, R. L.: A New Method for Surface Hydrodynamics, *J. Geophys. Res.*, 92 (1987) 11803–11824.
40. Zakharov, V. E.: Stability of Periodic Waves of Finite Amplitude on the Surface of a Deep Fluid, *J. Appl. Mech. Tech. Phys.*, 9 (1968) 190–194.

Rogue waves 2008

Brest, 13-14-15 October 2008

Since the Rogue Waves 2000 and 2004 workshops, researchers have pursued activity in the proposition of models and descriptions that can improve our understanding of rogue waves. The Brest Rogue Waves 2008 workshop gathered again many scientists and engineers to an opportunity to confront and discuss their views on the subject. It provided an assessment of the State of the Art of research on those matters, and was one more step forward towards efficient mitigation measures.

Keywords: ocean waves, extremes, rogue waves, freak waves.

Rogue waves 2008

Brest, 13-14-15 octobre 2008

Depuis les colloques Rogue Waves 2000 et 2004, la recherche s'est poursuivie pour la proposition de modèles susceptibles d'améliorer notre compréhension des vagues scélérates. Le colloque Rogue Waves 2008 a de nouveau rassemblé à Brest de nombreux scientifiques et ingénieurs qui ont pu y confronter et discuter leurs positions sur le sujet. Les dernières avancées dans le domaine ont pu y être évaluées, et un nouveau pas a été ainsi fait vers des mesures appropriées face au risque de ces événements.

Mots-clés : vagues, extrêmes, vagues anormales, vagues scélérates.

